Alma Mater Studiorum – Università di Bologna

DOTTORATO DI RICERCA

BIOCHIMICA

Ciclo XX

Settore/i scientifico disciplinari di afferenza: BIO/10

Biochemistry in Healthy and Neoplastic Human Tissues: Metabolic Alteration Revealed by HR-MAS Nuclear Magnetic Resonance Spectroscopy

VALERIA RIGHI

Coordinatore Dottorato
Prof. Giorgio Lenaz

Relatori
Dott. Vitaliano Tugnoli
Prof.ssa Adele Mucci

Esame finale anno 2008

Alma Mater Studiorum – Università di Bologna

DOTTORATO DI RICERCA

BIOCHIMICA

Ciclo XX

Settore/i scientifico disciplinari di afferenza: BIO/10

Biochemistry in Healthy and Neoplastic Human Tissues: Metabolic Alteration Revealed by HR-MAS Nuclear Magnetic Resonance Spectroscopy

VALERIA RIGHI

Coordinatore Dottorato
Prof. Giorgio Lenaz

Relatori
Dott. Vitaliano Tugnoli

Prof.ssa Adele Mucci

Esame finale anno 2008

Ai miei Genitori

A mio Fratello Fabio

CONTENTS

ABBREVIATIONS

Ac	Acetate
AAG	Gastric Atrophy Autoimmune
Ala	Alanine
Asp	Aspartate
Arg	Arginine
Asn	Asparagines
At	Glycerol-3-phosphate acyltransferases
Bet	Glycine-betaine
^{13}C	Carbon 13
CHESS	Chemical Shift Selective saturation standard
Ck	Choline kinase
CNS	Central Nervous System
Cho	free Choline
ChoCC/tCho	Choline Containing Compounds or total Choline
Chol	Cholesterol
COSY	COrrelation SpectroscopY
CPMG	Carr-Purcell-Meiboom-Gill
Cr	Creatine
Ct	Cytidylyltransferase
CT	Computed Tomografy
Cys	Cysteine
D2O	Deuterated water
1D	one-Dimensional
2D	two-Dimensional
E	Ethanolamine
FA	Fatty Acids
FID	Free Induction Decay
FT	Fourier Trasformer
GABA	γ-AminoButyric Acid
α-, β-Glc	α-, β-Glucose
Gln	Glutamine
Glu	Glutamate
Glx	Glutamine plus Glutamate
Gly	Glycine

G-Gly	Glycine intermediate
GPC	Glycerophosphocholine
GPE	Glycerophosphoethanolamine
GSH	γ-Glutamylcysteinylglycine, glutathione
^{1}H	Proton
His	Histidine
HPF	High Power Field
HR-MAS	High-Resolution Magic Angle Spinning
HMBC	Heteronuclear Multiple Bond Correlation
HMQC	Heteronuclear Multiple Quantum Coherence
HSQC	Heteronuclear Single Quantum Coherence
HTau	HypoTaurine
Ile	Isoleucine
Lac	Lactate
LED	Longitudinal-Eddy current Delay
Leu	Leucine
Lip	Lipids
Lpl	Lysophospholipase
Lys	Lysine
MRI	Magnetic Resonance Imaging
MRS	Magnetic Resonance Spectroscopy
Met	Methionine
Man	Mannitol
MM	MacroMolecoles or bonded amino-acids
Myo-Ino	*Myo*-Inositol
NAA	*N*-acetylAspartate
NMR	Nuclear Magnetic Resonance
β-OHBut	β-hydroxybutyrate
Pap	Phosphatidate phosphohydrolase
PCA	Principal Components Analysis
PCr	Phosphocreatine
PC	Phosphocholine
PE	Phosphoethanolamine
PEG	Polyethylene glycol
Ph	Phospholipids
Phe	Phenylalanine
Pla	Phospholipase A

Plc	Phospholipase C
Pld	Phospholipase D
PLS-DA	Partial Least Squares-Discriminant Analysis
PNET	Primitive NEuroectodermal Tumor
PRESS	Point Resolved Spectroscopy
Pro	Proline
Ptc	Phosphocholine cytidylyl-transferase
RCC	Renal Cell Carcinoma
Scy-Ino	Scyllo-Inositol
Suc	Succinate
Tau	Taurine
TG	Triglycerides
Thr	Threonine
TMA	Tetramethylammonium
TOCSY	TOtal Correlation SpectroscopY
Tyr	Tyrosine
UDP	Uridine diphosphate
UMP	Uridine monophosphate
Val	Valine
VOI	Volume of interest
WHO	World Health Organization

SUMMARY

This thesis is focused on the metabolomic study of human cancer tissues by *ex vivo* High Resolution-Magic Angle Spinning (HR-MAS) nuclear magnetic resonance (NMR) spectroscopy. This new technique allows for the acquisition of spectra directly on intact tissues (biopsy or surgery), and it has become very important for integrated metabonomics studies. The objective is to identify metabolites that can be used as markers for the discrimination of the different types of cancer, for the grading, and for the assessment of the evolution of the tumour. Furthermore, an attempt to recognize metabolites, that although involved in the metabolism of tumoral tissues in low concentration, can be important modulators of neoplastic proliferation, was performed. In addition, NMR data was integrated with statistical techniques in order to obtain semi-quantitative information about the metabolite markers. In the case of gliomas, the NMR study was correlated with gene expression of neoplastic tissues.

Chapter 1 begins with a general description of a new "omics" study, the metabolomics. The study of metabolism can contribute significantly to biomedical research and, ultimately, to clinical medical practice. This rapidly developing discipline involves the study of the metabolome: the total repertoire of small molecules present in cells, tissues, organs, and biological fluids. Metabolomic approaches are becoming increasingly popular in disease diagnosis and will play an important role on improving our understanding of cancer mechanism. **Chapter 2** addresses in more detail the basis of NMR Spectroscopy, presenting the new HR-MAS NMR tool, that is gaining importance in the examination of tumour tissues, and in the assessment of tumour grade. Some advanced chemometric methods were used in an attempt to enhance the interpretation and quantitative information of the HR-MAS NMR data are and presented in **chapter 3**. Chemometric methods seem to have a high potential in the study of human diseases, as it permits the extraction of new and relevant information from spectroscopic data, allowing a better interpretation of the results.

Chapter 4 reports results obtained from HR-MAS NMR analyses performed on different brain tumours: medulloblastoma, meningioms and gliomas.

The medulloblastoma study is a case report of primitive neuroectodermal tumor (PNET) localised in the cerebellar region by Magnetic Resonance Imaging (MRI) in a 3-year-old child. *In vivo* single voxel ^{1}H MRS shows high specificity in detecting the main metabolic

alterations in the primitive cerebellar lesion; which consist of very high amounts of the choline-containing compounds and of very low levels of creatine derivatives and *N*-acetylaspartate. *Ex vivo* HR-MAS NMR, performed at 9.4 Tesla on the neoplastic specimen collected during surgery, allows the unambiguous identification of several metabolites giving a more in-depth evaluation of the metabolic pattern of the lesion. The *ex vivo* HR-MAS NMR spectra show higher detail than that obtained *in vivo.* In addition, the spectroscopic data appear to correlate with some morphological features of the medulloblastoma. The present study shows that *ex vivo* HR-MAS ^{1}H NMR is able to strongly improve the clinical possibility of *in vivo* MRS and can be used in conjunction with *in vivo* spectroscopy for clinical purposes.

Three histological subtypes of meningiomas (meningothelial, fibrous and oncocytic) were analysed both by *in vivo* and *ex vivo* MRS experiments. The *ex vivo* HR-MAS investigations are very helpful for the assignment of the *in vivo* resonances of human meningiomas and for the validation of the quantification procedure of *in vivo* MR spectra. By using one- and two dimensional experiments, several metabolites in different histological subtypes of meningiomas, were identified. The spectroscopic data confirmed the presence of the typical metabolites of these benign neoplasms and, at the same time, that meningomas with different morphological characteristics have different metabolic profiles, particularly regarding macromolecules and lipids.

The profile of total choline metabolites (tCho) and the expression of the Kennedy pathway genes in biopsies of human gliomas were also investigated using HR-MAS NMR, and microfluidic genomic cards. ^{1}H HR-MAS spectra, allowed the resolution and relative quantification by LCModel of the resonances from choline (Cho), phosphorylcholine (PC) and glycerolphorylcholine (GPC), the three main components of the combined tCho peak observed in gliomas by *in vivo* ^{1}H MRS spectroscopy. All glioma biopsies depicted an increase in tCho as calculated from the addition of Cho, PC and GPC HR-MAS resonances. However, the increase was constantly derived from augmented GPC in low grade NMR gliomas or increased PC content in the high grade gliomas, respectively. This circumstance allowed the unambiguous discrimination of high and low grade gliomas by ^{1}H HR-MAS, which could not be achieved by calculating the tCho/Cr ratio commonly used by *in vivo* ^{1}H MR spectroscopy. The expression of the genes involved in choline metabolism was investigated in the same biopsies. High grade gliomas depicted a significant upregulation of choline kinase and phospholipase C, as well as a downregulation of the cytidyltransferase gene, the balance of these being consistent with the accumulation of PC. In the low grade

gliomas, Phospholipase A and lysophospholypase were upregulated and Phospholipase D became downregulated, supporting the accumulation of GPC. The present findings offer a convenient procedure to classify accurately glioma grade using ^{1}H HR-MAS, providing in addition the genetic background for the alterations of choline metabolism observed in high and low gliomas grade.

Chapter 5 reports the study on human gastrointestinal tract (stomach and colon) neoplasms. The human healthy gastric mucosa, and the characteristics of the biochemical profile of human gastric adenocarcinoma in comparison with that of healthy gastric mucosa were analyzed using *ex vivo* HR-MAS NMR. Healthy human mucosa is mainly characterized by the presence of small metabolites (more than 50 identified) and macromolecules. The adenocarcinoma spectra were dominated by the presence of signals due to triglycerides, that are usually very low in healthy gastric mucosa. The use of spin-echo experiments enable us to detect some metabolites in the unhealthy tissues and to determine their variation with respect to the healthy ones. Then, the *ex vivo* HR-MAS NMR analysis was applied to human gastric tissue, to obtain information on the molecular steps involved in the gastric carcinogenesis. It is possible to identify glycine, alanine, free choline and triglycerides as possible molecular markers related to the human gastric mucosa differentiation from pre-neoplastic to neoplastic conditions. A microscopic investigation was also carried out in order to identify and locate the lipids in the cellular and extra-cellular environments. Correlation of the morphological changes detected by transmission (TEM) and scanning (SEM) electron microscopy, with the metabolic profile of gastric mucosa in healthy, gastric atrophy autoimmune diseases (AAG), *Helicobacter pylori*-related gastritis and adenocarcinoma subjects, were obtained. These ultrastructural studies of AAG and gastric adenocarcinoma revealed lipid intra- and extra-cellularly accumulation associated with a severe prenecrotic hypoxia and mitochondrial degeneration.

A deep insight into the metabolic profile of human healthy and neoplastic colon tissues was gained using *ex vivo* HR-MAS NMR spectroscopy in combination with multivariate methods: Principal Component Analysis (PCA) and Partial Least Squares Discriminant Analysis (PLS-DA). The NMR spectra of healthy tissues highlight different metabolic profiles with respect to those of neoplastic and microscopically normal colon specimens (these last obtained at least 15 cm far from the adenocarcinoma). Furthermore, metabolic variations are detected not only for neoplastic tissues with different histological diagnosis, but also for those classified identical by histological analysis. These findings suggest that the same subclass of colon carcinoma is characterized, at a certain degree, by

metabolic heterogeneity. The statistical multivariate approach applied to the NMR data is crucial in order to find metabolic markers of the neoplastic state of colon tissues, and to correctly classify the samples. Significant different levels of choline containing compounds, taurine and myo-inositol, were observed. Particularly, in this case, the presence of lipids it is not a marker of the tumor or of the grade of malignity.

Chapter 6 deals with the metabolic profile of normal and tumoral renal human tissues obtained by *ex vivo* HR-MAS NMR. The spectra of human normal cortex and medulla show the presence of differently distributed osmolytes as markers of physiological renal condition. The marked decrease or disappearance of these metabolites and the high lipid content (triglycerides and cholesteryl esters) is typical of clear cell renal carcinoma (RCC), while papillary RCC is characterized by the absence of lipids and very high amounts of taurine. This research is a contribution to the biochemical classification of renal neoplastic pathologies, especially for RCCs, which can be evaluated by *in vivo* MRS for clinical purposes. Moreover, these data help to gain a better knowledge of the molecular processes envolved in the onset of renal carcinogenesis.

RIASSUNTO

Lo scopo di questa tesi è stato di effettuare uno studio di metabolomica (scienza relativa al pool dei metaboliti a basso peso molecolare presenti in un tessuto o in un fluido biologico) eseguito su neoplasie umane, attraverso l'utilizzo della *ex vivo* High Resolution-Magic Angle Spinning (HR-MAS) Nuclear Magnetic Resonance (NMR) spectroscopy. Questa tecnica permette di ottenere spettri direttamente sul tessuto (ottenuto per biopsia o in seguito ad intervento chirurgico) senza nessun pretrattamento, ed è diventata molto importante per studi metabonomici, relativi all'integrazione del metaboloma con una robusta elaborazione statistica. Dopo aver identificato i pattern metabolici di vari tessuti e organi umani sani e quelli delle rispettive neoplasie di differente tipo e grado istologico, l'obbiettivo è stato quello di ricercare nel tessuto tumorale i metaboliti che potessero assumere il significato di markers delle neoplasie, in relazione anche al grado e all'evoluzione del tumore stesso, con evidenti implicazioni cliniche (diagnosi, trattamento e prognosi). Inoltre, si è cercato di individuare quei metaboliti, che anche se presenti in basse concentrazioni, appaiono tuttavia coinvolti nel metabolismo tumorale, e possono essere anch'essi importanti modulatori della proliferazione neoplastica. Come anticipato, per gli studi metabonomici, i risultati NMR sono stati integrati con analisi statistiche per ottenere informazioni semiquantitative sui marker metabolici. Nel caso dei gliomi lo studio di risonanza è stato inoltre correlato con l'espressione genica di enzimi coinvolti nel pattern delle "coline" a livello del tessuto neoplastico. La scelta delle "coline" si è resa indispensabile essendo ampiamente dimostrato che il ciclo di Kennedy è coinvolto in modo determinante nel processo tumorale.

Il **capitolo 1** presenta una introduzione generale alla metablomica. Lo studio del metabolismo tumorale può contribuire significativamente alla ricerca biomedica e in definitiva alla pratica medico-clinica, rendendo disponibili informazioni molecolari relative all'insorgenza ed alla progressione della neoplasia. Il rapido sviluppo di questa disciplina riguarda lo studio del metaboloma, cioè l'insieme delle piccole molecole presenti in cellule, tessuti, organi, e fluidi biologici. L'approccio metabonomico è diventato sempre più popolare nella diagnosi di malattie e avrà un ruolo importante nel migliorare la comprensione nei meccanismi molecolari coinvolti nell'insorgenza e nello sviluppo delle neoplasie umane. Nel **capitolo 2**, vengono riportate in dettaglio le basi della spettroscopia NMR. In particolare viene descritta la tecnica HR-MAS, che ha acquisito fondamentale importanza nell

valutazione dei profili metabolici che caratterizzano le neoplasie umane e le differenziano dai rispettivi tessuti funzionale. Nel **capitolo 3** sono descritti alcuni metodi chemometrici avanzati, utilizzati per migliorare l'interpretazione e le informazioni quantitative dei dati spettroscopici ottenuti con l'HR-MAS. La combinazione dei dati biochimico-spettroscopici con l'elaborazione statistica nello studio delle malattie umane, permette non solo l'estrazione di nuove e rilevanti informazioni dai dati ottenibili con la spettroscopia NMR, ma anche una migliore interpretazione degli stessi assegnando una significatività statistica ai marker biochimici ipotizzati.

Nel **capitolo 4** sono presentati i risultati ottenuti attraverso l'analisi *ex vivo* HR-MAS NMR eseguita su differenti tipi di tumori cerebrali. Il primo tipo di neoplasia cerebrale riportata si riferisce al medulloblastoma, neoplasia a prevalente incidenza infantile. In particolare viene discusso il "case report" di un PNET (Neuro Ectodermal Primitive Tumour) localizzato nella regione cerebellare MRI (Magnetic Resonance Imaging) in un bambino di tre anni. La spettroscopia *in vivo* single voxel ^{1}H MRS ha mostrato alta specificità nel rilevare le principali alterazioni metaboliche nella lesione cerebellare, come un alto contenuto dei composti contenenti colina e una ridotta quantità di creatina ed *N*-acetilaspartato. La *ex vivo* HR-MAS ^{1}H NMR, eseguita a 9.4 Tesla sul campione neoplastico prelevato durante l'operazione, permette di identificare diversi metaboliti dando una approfondita e più ampia valutazione del pattern metabolico della lesione. Gli spettri HR-MAS mostrano che i dettagli spettrali sono maggiori rispetto a quelli che si ottengono dallo spettro *in vivo*. In più i dati spettroscopici sembrano essere correlati con alcune caratteristiche morfologiche del medulloblastoma. Lo studio mostra come l'*ex vivo* HR-MAS è capace di migliorare fortemente le possibilità cliniche della *in vivo* MRS e puo essere utilizzata in combinazione con la spettroscopia *in vivo* per scopi clinici. Tre sottotipi istologici di meningioma (meningoteliale, fibroso e oncocitico), neoplasia extracerebrale a carattere prevalentemente begnina, sono stati analizzati mediante spettroscopia *in vivo* ed *ex vivo*. L'analisi *ex vivo* HR-MAS NMR ha permesso una accurata descrizione del profilo metabolico ed facilitano l'interpretazione e l'assegnazione dei segnali degli spettri *in vivo* dei diversi meningiomi e anche la validazione del procedimento di quantificazione degli spettri *in vivo*. Utilizzando esperimenti mono- e bidimensionali, sono stati identificati diversi metaboliti nei differenti sottotipi istologici. I dati spettroscopici confermano la presenza di metaboliti tipici delle neoplasie benigne, e nello stesso tempo che i meningiomi con differenti caratteristiche morfologiche presentano un pattern metabolico diverso soprattutto per quanto riguarda componenti riferibili a macromolecole e lipidi.

Il profilo metabolico dei composti contenenti colina e l'espressione genica del ciclo di Kennedy in biopsie umane di gliomi sono stati studiati utilizzando la spettroscopia HR-MAS NMR e sonde dedicate per lo studio di geni specifici. Lo spettro ^{1}H HR-MAS permette la risoluzione e la relativa quantificazione attraverso un software particolare (LCmodel) delle risonanze della colina (Cho), fosforilcolina (PC) e glicerofoforilcolina (GPC), le tre componenti principali del singolo picco delle coline totali (tCho) osservato negli spettri *in vivo* di gliomi. Tutte le biopsie di glioma mostrano una aumento delle tCho, calcolato come somma delle risonanze rilevabili in HR-MAS di Cho, PC e GPC. Tuttavia il principale dato è relative all'aumento della GPC nei gliomi di basso grado e dall'aumento di PC nei gliomi di alto grado. Il comportameno di questi metaboliti permette una netta discriminazione tra gliomi di alto e basso grado con l'HR-MAS, situazione che non può essere ottenuta calcolando il rapporto tCho/Cr che comunemente viene considerato con la spettroscopia *in vivo*. Sulle stesse biopsie è stata studiata l'espressione genica del pattern enzimatico coinvolto nel metabolismo delle coline. I gliomi di alto grado mostrano una significativa up-regulation dell'enzima colina kinasi e fosfolipasi C, mentre mostra una down-regulation del gene che codifica per l'enzima citidil-trasferasi; l'andamento dell'espressione di questi enzimi giustifica l'accumulo della PC rilevato nella spettroscopia. Nei gliomi di basso grado, la fosfolipasi A e la lisofosfolipasi sono up-regulated, mentre la fosfolipasi D è down-regulated, spiegando in modo analogo l'accumulo di GPC. Questo studio presenta un'adatta procedura per classificare accuratamente il grado del glioma utilizzando l'HR-MAS, a condizione che parallelamente sia valutato il back-ground genetico alla base delle alterazioni del metabolismo delle coline osservato nei gliomi di basso e alto grado.

Lo studio di neoplasie umane dell'apparato gastrointestinale è presentato nel **capitolo 5**. Le caratteristiche dei profili metabolici della mucosa gastrica sana, della mucosa affetta da gastrite per infezione da *Helicobacter Pilory*, della mucosa affetta da una condizione preneoplstica quale la gastrite atrofica autoimmune (AAG) e dell'adenocarcinoma gastrico sono analizzate utilizzando spettroscopia *ex vivo* HR-MAS NMR. Il profilo metabolico della mucosa gastrica sana e affetta da *Helicobacter Pilory* è risultato molto simile.Le due situazioni sono caratterizzate dalla presenza di più di 50 metaboliti. Al contrario gli spettri di adenocarcinoma sono dominati dalla presenza di risonanze dovute a lipidi, trigliceridi in particolare. Il contenuto di questi ultimi è basso o quasi assente nella mucosa sana. Inoltre il tessuto affetto da AAG ha mostrato un pattern molecolare intermedio fra la situazione funzionale e quella neoplastica. L'uso della sequenza spin-echo ha permesso di rilevare alcuni metaboliti distintivi del tessuto neoplastico e di evidenziare la loro variazione rispetto al sano.

L'analisi HR-MAS applicata al tessuto gastrico ci ha fornito quindi informazioni su alcuni possibili step molecolari coinvolti nel processo della carcinogenesi gastrica. È stato infatti possibile identificare alcuni metaboliti che appaiono particolarmente significativi quali glicina, alanina, colina libera e trigliceridi come possibili marker legati alla differenziazione della mucosa gastrica a partire da una condizione sana, attraverso la condizione preneoplastica fino ad arrivare a quella neoplastica. È stata effettuata anche una indagine microscopica per localizzare i lipidi (i trigliceridi rilevati con L'HR-MAS) nei tessuti gastrici sani, affetti da AAG e da adenocarcinoma. Lo studio ha avuto come obbiettivo di correlare i cambiamenti morfologici, rilevati con la microscopia elettronica a trasmissione (TEM) e a scansione (SEM), col profilo metabolico della mucosa gastrica sana, dell'AAG, della gastrite dovuta a H. pylori e dell'adenocarcinoma. Gli studi ultrastrutturali della AAG e dell'adenocarcinoma gastrico rivelano che l'accumulo di lipidi, sotto forma di "goccioline lipidiche" (lipids bodies) avviene sia negli spazi intra- che in quelli extra-cellulari ed è associato ad una forte ipossia prenecrotica e ad una degenerazione mitocondriale.

Nel capitolo viene riportata anche un'accurata analisi del profilo metabolico del tessuto sano e neoplastico del colon utilizzando la spettroscopia *ex vivo* HR-MAS NMR in combinazione con metodi statistici: Principal Component Analysis (PCA) e Partial Least Squares Discriminant Analysis (PLS-DA). Lo spettro NMR della mucosa sana presenta un profilo metabolico diverso rispetto al tessuto neoplastico e anche rispetto al tessuto prelevato a 15 cm di distanza dalla zona tumorale e definito macroscopicamente eistologicamente sano. Inoltre le variazioni metaboliche sono rilevate non solo tra carcinomi con diversa diagnosi istologica, ma anche per carcinomi che presentano la stessa diagnosi istologica. Questo suggerisce che la stessa sottoclasse tumorale è caratterizzata da un certa eterogeneità metabolica. L'analisi multivariata applicata ai dati NMR è stata determinante per identificare i marker metabolici del tumore del colon e per classificare correttamente il campione. Variazioni significative sono state osservate nelle quantità relative di metaboliti quali coline, taurina e mio-inositolo. I lipidi in questo tratto gastrointestinale non risultano essere un marker tumorale o del grado di malignità.

Il lavoro riportato nel **capitolo 6** presenta la caratterizzazione del profilo metabolico di parenchima renale umano funzionale e neoplastico ottenuto mediante *ex vivo* HR-MAS NMR. Gli spettri di campioni chirurgici renali relativi alle zone corticali e midollari mostrano una diversa distribuzione dei metaboliti ad attività osmotica (osmoliti). La marcata diminuzione o assenza dei metaboliti e un elevato contenuto di lipidi (trigliceridi e esteri del colesterolo) è tipica dei carcinomi renali a cellule chiare, mentre i carcinomi papillari sono caratterizzati da

assenza di lipidi e un elevato livello di taurina. Questa ricerca fornisce un contributo biochimico-molecolare ad una migliore comprensione delle patologie neoplastiche renali, soprattutto dei carcinomi a cellule chiare. Crea inoltre le premesse biochimiche fondamentali per future applicazioni cliniche della spettroscopia *in vivo*. Inoltre questi dati contribuiscono a migliorare la conoscenza del processo molecolare che è alla base della carcinogenesi renale.

Chapter 1

INTRODUCTION TO METABOLOMICS

GENERAL INTRODUCTION

The final decades of the twenteth and the beginning of the twenty-first centuries, have witnessed a revolution in biomedical research that has made it possible to move from the study of single genes, single mRNA transcripts, single proteins, or single metabolites to studies that encompass entire genomes, transcriptomes, proteomes, and metabolomes (Figure 1).

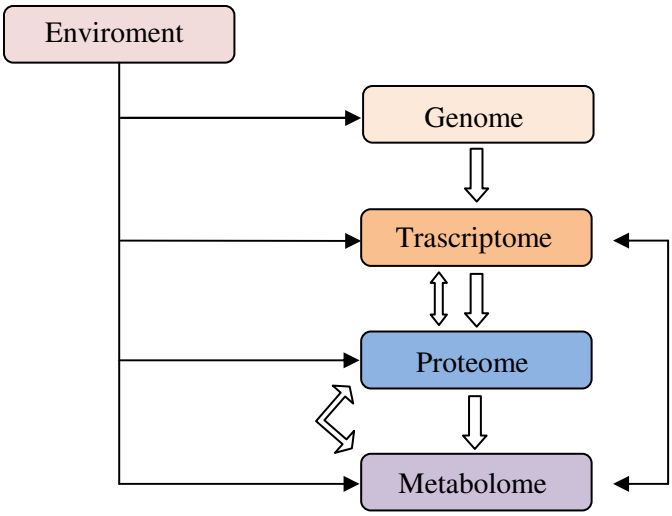

Figure 1. The biological organization of the '-omes'. The classical view of biological organization is to consider the flow of information from the genome to the transcriptome, to the proteome and then the metabolome. However, each tier of organization depends on the other, so a perturbation in one network can affect another. Furthermore, the environment has a important impact not only on the expression and concentrations of transcripts, proteins and metabolites, but also on the genome by selecting for adaptive changes in subpopulations of cells within a tumour. Metabolomics can potentially investigate much more than normal metabolism and metabolic disorders, it can also be used to monitor changes in the genome or to measure the effects of downregulation or upregulation of a specific gene transcript.

Since the finalization of the sequencing of the human genome, the main goals of functional genomics have been to determine the role of the products of newly identified genes, as well as to determine those that might be therapeutically targeted. So far, functional genomic strategies have largely centred on gene-expression studies (transcriptomics) or protein profiles (proteomics) (1-3). These approaches have led to several successes in the field of cancer biology, such as the identification of new tumour subtypes, as well as transcriptional and protein biomarkers for certain types of cancer (4-8). Also, metabolomics, the study of metabolism at the global, has the potential to contribute significantly to biomedical research

and, ultimately, to clinical medical practice. This rapidly developing discipline involves the study of the metabolome, the total repertoire of small molecules present in cells, tissues, organs, and biological fluids. Metabolic activity can also be quantified, as various analytical tools have been developed to measure concentrations of low-molecular-weight metabolites. This is a particularly challenging task as low-molecular-weight metabolites represent a diverse range of chemicals. Perhaps the best description of this approach was offered by Steve Oliver of Manchester University, who used the term 'metabolomics' to describe "the complete set of metabolites/low-molecular-weight intermediates, which are context dependent, varying according to the physiology, developmental or pathological state of the cell, tissue, organ or organism" (9). This definition arose from the term that was originally used to describe a powerful tool for phenotyping yeast mutants (9).

Although '-omic' technologies are complementary, analysis of the metabolome is an especially useful approach for identifying pathways that are perturbed in a given pathology, when compared with the transcriptome and proteome. Measuring metabolite concentrations is a more sensitive approach than following the rates of chemical reactions directly. Metabolic control analysis has demonstrated that although changes in enzyme concentrations and activities ('the proteome') have a small impact on metabolic fluxes (the rate of which metabolite passes through a given metabolic pathway), changes in flux have a significant impact on metabolite concentrations (10-12). This is because the control of the metabolic flux of a pathway is spread across all the enzymes present in the pathway, rather than being controlled by a rate determining step. Furthermore, there is not necessarily a good quantitative relation between mRNA concentrations and enzyme function, but as metabolites are downstream of both transcription and translation, they are potentially a better indicator of enzyme activity (13) (Figure 2). Metabolomic approaches also generate highly reproducible data sets. One disadvantage is that the number of metabolites that exist in a mammalian tissue is probably far smaller than the number of transcripts that are present in the mammalian transcriptome. Therefore, a given metabolite pattern can reflect several genomic changes. It is also not a trivial matter to connect the genome to the metabolome, complicating attempts of using metabolomics as a functional genomics tool in cancer research. Metabolomic approaches, however, will become increasingly popular in disease diagnosis and will have an important role in improving our understanding of the mechanisms of cancer.

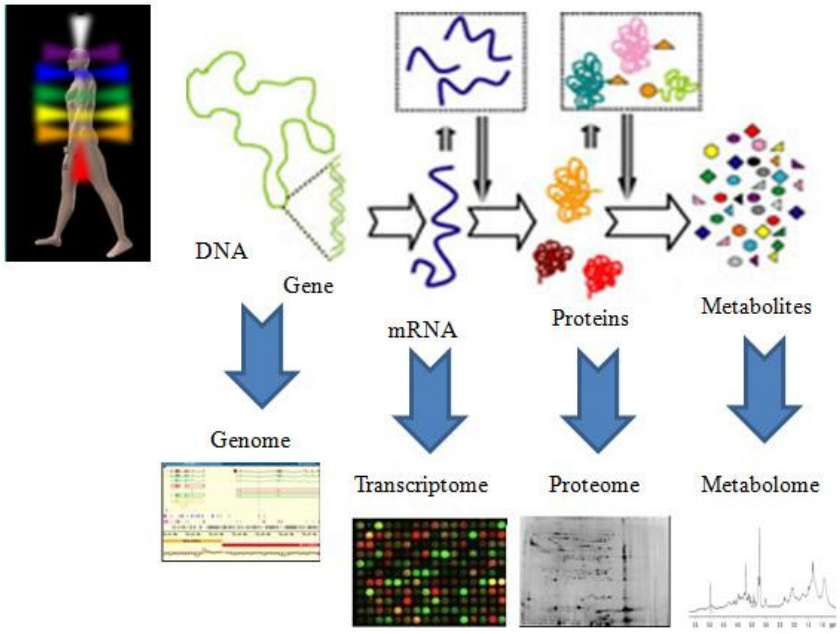

Figure 2. The "Omics" sciences are characterized by complex data sets of related phenomena each of which taken as a whole constitute a picture of an organism. Different techniques are used to analyze the different "omics" sciences.

The use of metabolic profiling to follow systemic changes in multicellular organisms has led Jeremy Nicholson to coin the word 'metabonomics'. He defines metabonomics as "the quantitative measurement of the multivariate metabolic responses of multicellular systems to pathophysiological stimuli or genetic modification" (14). In addition to the terms 'metabolomics' and 'metabonomics', researchers have felt it necessary to distinguish the types of analytical techniques used in these approaches (15). 'Metabolic profiling' has been proposed as a means of measuring the total complement of individual metabolites in a given biological sample, whereas 'metabolic fingerprinting' refers to measuring a subclass of metabolites to create a 'bar code' of metabolism (16,17).

Metabolomics can be used to monitor tumour growth and regression, and can therefore increase our understanding of pathogenic mechanisms as well as improve monitoring of treatment regimens. It has already been used to analyse the function of Hypoxia Inducible Factor-1β in tumours and to monitor the progression of therapy-induced apoptosis in gliomas. Metabolomic analysis is therefore a promising approach to identify biomarkers that could be used in the non-invasive monitoring of anticancer therapies, particularly those that induce

apoptosis. This could also be used as a non-invasive tool for monitoring tumours progression in animal models, which cannot be achieved using histology, transcriptomics or proteomics. One drawback is that the number of metabolites that can be detected *in vivo* (directly on patients) is relatively small at present, making it difficult to determine exactly which metabolic pathways underlie a detected alteration. *In vitro* metabolomic studies, performed on the aqueous extracts of human tissues, have also demonstrated several differences between tumour types, in terms of various biochemical pathways (18,19) (Table I).

Table I. Example of metabolic biomarker of human tumors.

Metabolite	Metabolic function	Associated tumours/characteristics
Alanine	In conjunction with lactate, increases in tissues during hypoxia; made by transamination of pyruvate to prevent further increases in lactate (20)	Brain tumours, including metastasis, gliomas, meningiomas and neuroepithelial tumours, clear cell renal carcinomas.
ChoCC	Include free choline, phosphocholine, glycerophosphocholine and phosphatidilcholine; these are key constituents of phospholipid bilayer cell membranes	Levels change during apoptosis and necrosis; the tumour types that these changes have been found in include brain, sarcomas, prostate and hepatoma.
Glycine	An amino acid and an essential precursor for *de novo* purine synthesis	Decreased following disruption of Hypoxia Inducible Factor (HIF-1) signalling pathway.
Lactate	An end product of anaerobic glycolysis	Increases rapidly during hypoxia and ischaemia; poorly vascularised tumours have a low intracellular pH as a result of increased lactate production; increased rates of lactate production have been associated with a range of tumours and, in particular, certain types of neoplasms (21)
Myo-Inositol	Involved in osmoregulation and volume regulation	Increased in colon adenocarcinoma, glioma, schwannomas,ovarian carcinoma, astrocytoma and endometrial cells, decreased in breast tumours
Taurine	Important in osmoregulation and volume regulation; hypotaurine is also an antioxidant and might protect cells from free-radical damage	Increased in squamous-cell carcinoma, prostate, cancer and liver metastasis
Fatty Acids	Constituents of cell membranes	Increased in glioma cells undergoing apoptosis and in dedifferentiated and pleomorphic liposarcomas

Hence, metabolomics offers a particularly sensitive method to monitor changes in a biological system, through observed changes in the metabolic network. Different analytical techniques are utilized in metabolomic studies, including gas chromatography (GC), liquid chromatography (HPLC) and HPLC with electrochemical detection, mass spectrometry (MS)

and nuclear magnetic resonance (NMR) spectroscopy. In particular MS and NMR are used as tools to monitor changes in tumour metabolism (22,23) (The NMR *in vitro* was performed on the aqueous extracts obtained from the human tissues; the *ex vivo* was performed on the human specimens without any pretreatment; and *in vivo* was performed directly on healthy and functional tissues and organs of the human body). Such metabolomic approaches are being used to profile cell lines, tumours and systemic metabolism in human cancer tissue *ex vivo* and *in vivo*, and will provide another functional genomic tool for cancer research (24).
Understanding disease processes through metabolic profiling is not a new concept and the NMR spectroscopy has been widely used as metabolic profiling tools since the early 1970s (25-27). NMR spectroscopy has also been used to differentiate between different cancer cell lines (18,19) and to monitor metabolic processes that occur in cancer cells. There are numerous reasons for employing NMR as a primary tool for structure based metabolomic investigations, many of which are the same as those that have attracted structural biologists to NMR. Modern NMR makes it possible to perform rigorous structural analysis of many metabolites in crude extracts, cell suspensions, intact tissues, or whole organisms. Structural determination of known metabolites using various one-dimensional (1D) and two-dimensional (2D) NMR methods is straightforward, whereas *de novo* structural analysis of unanticipated or even unknown metabolites is also feasible. In addition to popular high-sample-throughput applications, NMR is particularly powerful for metabolite structural determinations, including the atomic positions of isotopic labels (*e.g.*, ^{13}C, ^{15}N, or ^{2}H) in different isotopomers generated during stable isotope tracer studies (28-31). These latter applications provide detailed maps of biochemical pathways or networks (32,33). As a result, metabolic pathways can now be systematically mapped by NMR with unprecedented speed. Using NMR-based approaches, 20–40 metabolites can typically be detected in tissue extracts, and 100–200 can be detected in urine samples.

Today a new technique, called high-resolution magic angle spinning (HR-MAS) ^{1}H NMR spectroscopy, can produce *ex vivo* high-resolution spectra from intact tissue (34-37). A biopsy or post-mortem sample of intact tissue is spun at an angle to the applied magnetic field. The spinning results in a significant improvement in the resolution of the spectrum obtained. This approach has several advantages over NMR spectroscopy of tissue extracts. The results from the *ex vivo* HR-MAS ^{1}H NMR spectroscopy investigations of tumors have demonstrated the importance of being able to separate out co-resonant metabolites. It is also being used to confirm the metabolic events measured, *in vivo*, using MRS.

References

1. Chu S, DeRisi J, Eisen M, Mulholland J, Botstein D, Brown PO, Herskowitz I. The transcriptional program of sporulation in budding yeast. *Science* 1998; **282**: 699-705.
2. Shalon D, Smith SJ, Brown PO. A DNA microarray system for analyzing complex DNA samples using two-color fluorescent probe hybridization. *Genome Res.* 1996; **6**: 639-645.
3. Klose J, Nock C, Herrmann M, Stühler K, Marcus K, Blüggel M, Krause E, Schalkwyk LC, Rastan S, Brown SD, Büssow K, Himmelbauer H, Lehrach H. Genetic analysis of the mouse brain proteome. *Nature Genet.* 2002; **30**: 385-393.
4. Golub TR, Slonim DK, Tamayo P, Huard C, Gaasenbeek M, Mesirov JP, Coller H, Loh ML, Downing JR, Caligiuri MA, Bloomfield CD, Lander ES. Molecular classification of cancer: class discovery and class prediction by gene expression monitoring. *Science* 1999: **286**, 531-537.
5. Moch H, Schraml P, Bubendorf L, Mirlacher M, Kononen J, Gasser T, Mihatsch MJ, Kallioniemi OP, Sauter G. High-throughput tissue microarray analysis to evaluate genes uncovered by cDNA microarray screening in renal cell carcinoma. *Am. J. Pathol.* 1999; **154**: 981-986.
6. Celis JE, Celis P, Ostergaard M, Basse B, Lauridsen JB, Ratz G, Rasmussen HH, Orntoft TF, Hein B, Wolf H, Celis A. Proteomics and immunohistochemistry define some of the steps involved in the squamous differentiation of the bladder transitional epithelium: a novel strategy for identifying metaplastic lesions. *Cancer Res.* 1999; **59**: 3003-3009.
7. Seow TK, Ong SE, Liang RC, Ren EC, Chan L, Ou K, Chung MC. Two-dimensional electrophoresis map of the human hepatocellular carcinoma cell line, HCC-M, and identification of the separated proteins by mass spectrometry. *Electrophoresis* 2000; **21**: 1787-1813.
8. Voss T, Ahorn H, Haberl P, Dohner H, Wilgenbus K. Correlation of clinical data with proteomics profiles in 24 patients with B-cell chronic lymphocytic leukemia. *Int. J. Cancer* 2001; **91**: 180-186.
9. Oliver SG. Functional genomics: lessons from yeast. *Phil. Trans. R. Soc. Lond.* 2002; **357**: 17-23.
10. Kell DB, Westerhoff HV. Towards a rational approach to the optimization of flux in microbial biotransformations. *Trends Biotehnol*. 1986; **4**: 137-142.
11. Fell DA. *Understanding the Control of Metabolism* Portland Press, London; 1996.
12. Mendes P, Kell DB, Westerhoff HV. Why and when channeling can decrease pool size at constant net flux in a simple dynamic channel. *Biochim. Biophys. Acta* 1996; **1289**: 175-186.
13. ter Kuile BH, Westerhoff HV. Transcriptome meets metabolome: hierarchical and metabolic regulation of the glycolytic pathway. *FEBS Letts.* 2001; **500**: 169-171.
14. Nicholson JK, Wilson I. Understanding 'global' systems biology: metabonomics and the continuum of metabolism. *Nature Rev. Drug Discov.* 2003; **2**: 668-676.

15. Chung YL, Stubbs M, Griffiths JR. *Metabolic Profiling, its Role in Biomarker Discovery and Gene Function Analysis* Harrigan GC, Goodacre R. (eds). Kluwer Academic Publishing: Dordrecht 2003; 83-94.
16. Fiehn O. Combining genomics, metabolome analysis and biochemical modeling to understand metabolic networks. *Comp. Funct. Genomics* 2001; **2**: 155-168.
17. Fiehn O. Metabolomics the link between genotypes and phenotypes. *Plant Mol. Biol.* 2002; **48**: 155-171.
18. Florian CL, Preece NE, Bhakoo KK, Williams SR, Noble MD. Characteristic metabolic profiles revealed by 1H NMR spectroscopy for three types of human brain and nervous system tumours. *NMR Biomed.* 1995; **8**: 253-264.
19. Florian CL, Preece NE, Bhakoo KK, Williams SR, Nobel MD. Cell type-specific fingerprinting of meningioma and meningeal cells by proton nuclear magnetic resonance spectroscopy. *Cancer Res.* 1995; **55**: 420-427.
20. Ben-Yoseph O, Badar-Goffer RS, Morris PG, Bachelard HS. Glycerol 3-phosphate and lactate as indicators of the cerebral cytoplasmic redox state in severe and mild hypoxia respectively: a 13C- and 31P-n. m. r. study. *Biochem J.*1993; **291**: 915-919.
21. Preul MC, Caramanos Z, Collins DL, Villemure JG, Leblanc R, Olivier A, Pokrupa R, Arnold DL. Accurate, noninvasive diagnosis of human brain tumors by using proton magnetic resonance spectroscopy. *Nature Med*. 1996; **2**: 323-325.
22. Oliver SG, Winson MK, Kell DB, Baganz F. Systematic functional analysis of the yeast genome. *Trends Biotechnol.* 1998; **16**: 373-378.
23. Nicholson JK, Lindon JC, Holmes E. 'Metabonomics': understanding the metabolic responses of living systems to pathophysiological stimuli via multivariate statistical analysis of biological NMR spectroscopic data. *Xenobiotica* 1999; **29**: 1181-1189.
24. Griffin JL, Shockcor JP. Metabolic profiles of cancer cells. *Nat. Rev. Cancer* 2004; **4**: 551-561.
25. Devaux PG, Horning MG, Horning EC. Benyzloxime derivatives of steroids; a new metabolic profile procedure for human urinary steroids. *Anal. Lett.* 1971; **4**: 151.
26. Horning EC, Horning MG. Human metabolic profiles obtained by GC and GC/MS. *J. Chromatogr. Sci.* 1971; **9**: 129-140.
27. Fan TW. Metabolite profiling by one- and two-dimensional NMR analysis of complex mixtures. *Prog. Nucl. Mag. Res. Spectrosc.* 1996; **28**: 161-219.
28. Fan X, Bai J, Shen P. Diagnosis of breast cancer using HPLC metabonomics fingerprints coupled with computational methods. *Conf. Proc. IEEE Eng. Med. Biol. Soc.* 2005; **6**: 6081-6084.
29. de Graaf AA, Mahle M, Mllney M, Wiechert W, Stahmann PHS. Determination of full 13C isotopomer distributions for metabolic flux analysis using heteronuclear spin echo difference NMR spectroscopy. *J. Biotechnol.* 2000; **77**: 25-35.

30. Lu D, Mulder H, Zhao P, Burgess SC, Jensen MV, Kamzolova S, Newgard CB, Sherry AD. 13C NMR isotopomer analysis reveals a connection between pyruvate cycling and glucosestimulated insulin secretion (GSIS). *Proc. Natl. Acad. Sci. USA* 2002; **99**: 2708-2713.
31. Fan TW-M, Lane AN. Structure-based profiling of metabolites and isotopomers by NMR. *Prog. NMR Spectrosc.* 2007. In press.
32. Dauner M, Bailey JE, Sauer U. Metabolic flux analysis with a comprehensive isotopomer model in *Bacillus subtilis*. *Biotechnol. Bioeng.* 2001; 76:144-156.
33. Forbes NS, Meadows AL, Clark DS, Blanch HW. Estradiol stimulates the biosynthetic pathways of breast cancer cells: detection by metabolic flux analysis. *Metab. Eng.* 2006; **8**: 639-652.
34. Cheng LL. Lean CL, Bogdanova A, Wright SC Jr, Ackerman JL, Brady TJ, Garrido L. Enhanced resolution of proton NMR spectra of malignant lymph nodes using magic angle spinning. *Magn. Reson. Med*. 1996; **36**: 653-658.
35. Chen JH, Enloe BM, Fletcher CD, Cory DG, Singer S. Biochemical analysis using high-resolution magic angle spinning NMR spectroscopy distinguishes lipoma like well differentiated liposarcoma from normal fat. *J. Am. Chem. Soc.* 2001; **123**: 9200-9201.
36. Millis K, Weybright P, Campbell N, Fletcher JA, Fletcher CD, Cory DG, Singer S. Classification of human liposarcoma and lipoma using *ex vivo* proton NMR spectroscopy. *Magn. Reson. Med.* 1999; **41**: 257-267.
37. Tomlins A, Foxall PJ, Lynch MJ, Parkinson J, Everett JR, Nicholson JK. High resolution magic angle spinning ^{1}H nuclear magnetic resonance analysis of intact prostatic hyperplastic and tumour tissues. *Anal. Comm*. 1998; **35**: 113-115.

Chapter 2

NUCLEAR MAGNETIC RESONANCE

GENERAL INTRODUCTION

Nuclear Magnetic Resonance (NMR) Spectroscopy is a powerful tool for the structure determination of organic compounds, biomolecules and natural compounds, for the study of tissue extracts or intact tissues, and for the obtainment of detailed three-dimensional maps of the human body and organs. In the field of biomedicine, the two areas of NMR are represented by Magnetic Resonance Imaging (MRI) and by the multi-branched Magnetic Resonance Spectroscopy (MRS), where MRS is the acronym utilized in place of NMR. MRI uses the strong signal from water protons (^{1}H) to provide a detailed anatomical maps and has proven to be an indispensable tool for both researchers and clinicians, but its specificity in defining the pathology is limited to only some diseases. More diagnostic information can be obtained by MRS because it can detect the much weaker signals from nuclei as proton, carbon and phosphorous of metabolites.

When MRS is applied to a small volume of interest (VOI) of an organ, exploiting the localization techniques employed in MRI, it is known as *in vivo* MRS. The *in vivo* MRS studies are focused on organs (muscles, liver, brain, breast and prostate) the study of which has been made accessible through the use of appropriate coils for the acquisition of the signals. *In vivo* MRS, owing to the low resolution experimentally obtainable, allows to detect and quantify the changes in concentration of a limited number of metabolites as lactate (Lac), *N*-AcetylAspartate (NAA), Creatine (Cr) plus phosphocreatine (PCr) and choline containing compounds (ChoCC) (1-4), and it can be used when the NMR molecular marker of the tissue states are well established by means of a detailed biochemical study. This important goal can be accomplished by the spectroscopic analysis on tissue extract, by *in vitro* MRS studies that can be performed both on water soluble and on lipid fractions (5-14), giving an overall profile of the metabolites present in the tissues (15). The biochemical detail attainable is far higher than that characteristic of *in vivo* MRS, and this renders *in vitro* studies extremely important for the correct interpretation of *in vivo* spectra (16-20). In these last years it has became possible to further improve the metabolite picture of a tissue, by using the *ex vivo* MRS directly on tissues specimens.

A new technique, HR-MAS NMR (High Resolution Magic Angle Spinning Nuclear Magnetic Resonance), working under magic-angle-spinning conditions (21-33), permits to obtain spectra on samples, which are otherwise troublesome for classical high-resolution,

much better than that of *in vivo* spectra. *Ex vivo* HR-MAS NMR represents another powerful tool, whose potentiality and relations with *in vivo* and *in vitro* MRS measurements have to explored (34-37).

BASIC PRINCIPLES

NMR is a spectroscopic technique (38-40) based on a quantum property of nuclei called spin I, described as an intrinsic angular momentum of quantum particles, that can only assume integer or half-integer values (0, 1/2, 1, 3/2,…). The quantum angular momentum of particle with spin I is given by:

$$L=\hbar[I(I+I)]^{1/2}$$

where $\hbar=1.054x10^{-34}$Js is the Planck constant (h) divided by 2π. Nuclei also possess a magnetic moment μ proportional to their spin angular momentum L, through a constant characteristic for each nucleus called magnetogyric ratio γ (in units of rad $s^{-1}T^{-1}$), in the equation:

$$\mu = \gamma\hbar[I(I+I)]^{1/2}$$

NMR spectroscopy can be in principle applied to all nuclei with spin I≠0. The nuclei possessing I=1/2 are generally more easily studied than those having I>1/2[41] because they give sharper lines. The most important nuclei for organic chemists and biochemists are ^{1}H, ^{13}C, ^{15}N,^{19}F and ^{31}P, which all have I=1/2. ^{1}H, ^{19}F, and ^{31}P are the most receptive nuclei, being characterized by both high isotopic percentages and high γ. Conversely, ^{13}C and ^{15}N are less abundant (1.1% and 0.37%) and have low γ, hence are less facile nuclei. When a static magnetic field B_0 (in units of T-Tesla) is applied, the energy levels of a nucleus with spin I become 2I+1. For instance, for a spin ½ the energy levels are two, the corresponding spin states are denoted as α and β (Figure 1) and are related to the parallel (low energy) and antiparallel (higher energy) orientation of the magnetic moment μ with respect to the B_0 field.

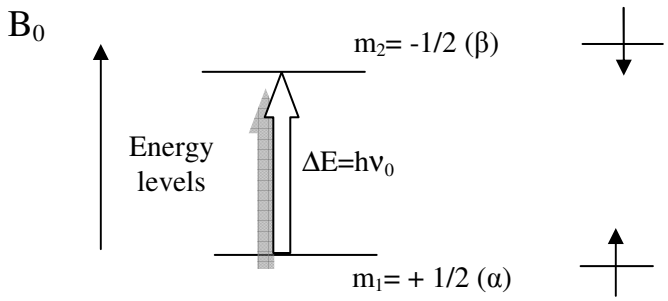

Figure 1: Energy separation between nuclear spin states.

The energy difference between the spin energy levels is equal to $h\nu_0$ (Planck's law) where ν_0 is referred to as Larmor frequency (of the order of MHz). Over a large number of spins at thermal equilibrium, the lower energy state is slightly more populated than the higher one, and a net magnetization M_0 of the sample (longitudinal magnetization) is present parallel to the applied B_0 field direction (z axis). The application of the radio-frequency field B_1, close to the Larmor frequency ν_0, perpendicular to B_0 and turned on for a short time (pulse), causes the rotation of M_0 around the B_1 direction towards a plane perpendicular to B_0 (the xy plane) and permits the creation of a transverse magnetization, the detection of which generates the NMR signal (Figure 2).

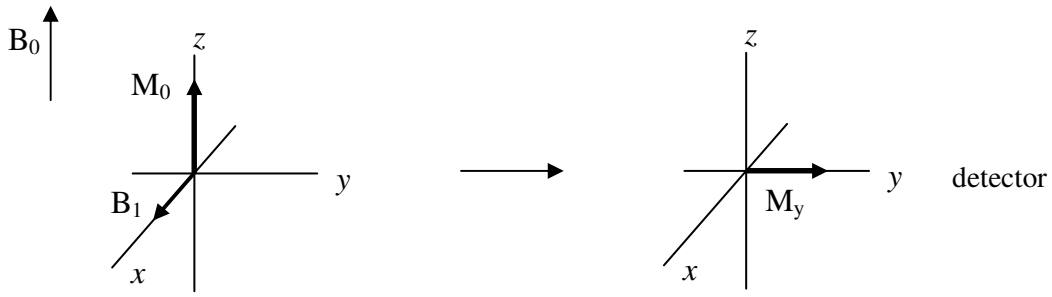

Figure 2. Outline of the simplest NMR experiment in the rotating frame.

After the perturbation caused by B_1 the magnetization relaxes to its equilibrium. The reconstruction of the longitudinal magnetization towards equilibrium is characterized by a time constant called longitudinal relaxation time T_1, whereas the decay of the transverse magnetization is characterized by another time constant called transverse relaxation time T_2.

The effect of T_2 on the FID and the signals is shown in Figure 3. To reach the desired signal-to-noise ratio is often necessary to add more FIDs, waiting an appropriate delay (dependent on T_1) between subsequent acquisitions to ensure that the magnetization has relaxed to its equilibrium value.

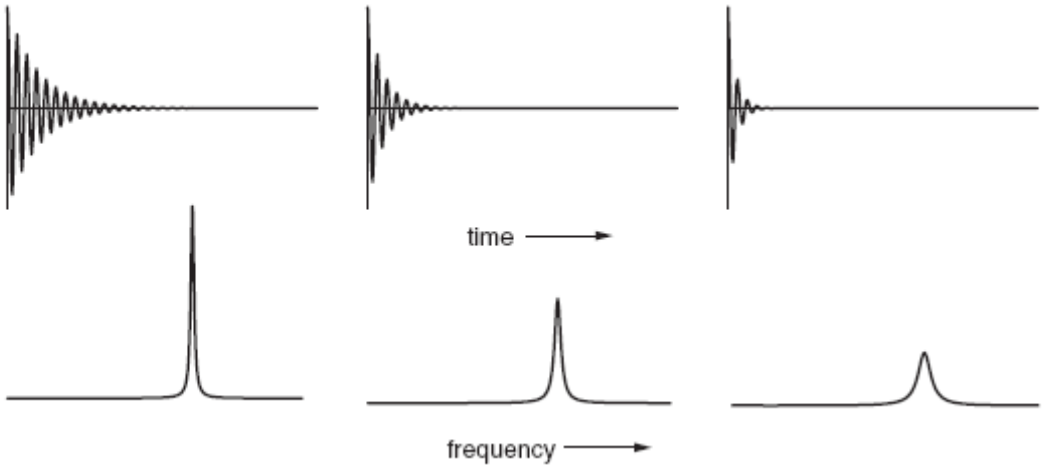

Figure 3. Illustration of the fact that the more rapidly the FID decays the broader is the line in the corresponding spectrum. A series of FIDs are shown at the top of the figure and the corresponding spectra are below, all plotted on the same vertical scale. The integral of the peaks remains constant, so as they get broader the peak height decreases.

This signal, called FID (free induction decay), has to be processed with the Fourier transform (FT) algorithm to became interpretable, giving a spectrum consisting in a plot of signal intensity as a function of frequency (Figure 4).

Figure 4. From FID (a) to spectrum (b) through FT transformation. Fourier transformation is the mathematical process which takes us from a function of time (the time domain), such as a FID, to a function of frequency, *i. e.* the spectrum.

The actions performed by the NMR spectrometer, pulses and delays of very precise lengths, can be programmed and constitute as a whole what is generally called a pulse sequence. Pulse sequences can be represented by simple diagrams in which pulses are denoted

by boxes of different lengths and are separated by time intervals which have to be accurately chosen in relation to specific NMR parameters. The simplest pulse is that commonly used to record ^{1}H NMR spectra. (Figure 5)

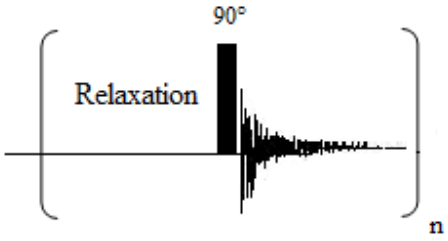

Figure 5. Pulse sequence scheme for acquisition of ^{1}H NMR spectrum. The index n indicates the repetition times of the sequence and will be omitted later.

^{13} Carbon Nuclear Magnetic Resonance Spectroscopy

The element carbon consists of a stable isotopes ^{12}C and ^{13}C with 98.9% and 1.1% natural abundance, respectively. Only the ^{13}C nucleus has a magnetic moment and has a spin I=1/2 while the ^{12}C nucleus of the major isotope is non magnetic. The main difficult in ^{13}C NMR is the low natural abundance of the carbon 13 nucleus (1.108%) and its low gyro-magnetic ratio γ. Low natural abundance and small gyro-magnetic ratio are the reason why ^{13}C NMR is much less sensitive (1.59%) than ^{1}H NMR (100%). The acquisition of ^{13}C is used for determine the structure of compounds. The ^{13}C chemical shift scale spans some 250 ppm. Because the ^{13}C nucleus is isotopically rare, it is extremely unlikely that any two adjacent carbon atoms in a molecule will both be ^{13}C. As a consequence ^{13}C-^{13}C coupling is not observed in ^{13}C NMR spectra, *i. e*. there is no signal multiplicity or splitting in a ^{13}C spectrum due ^{13}C-^{13}C coupling.

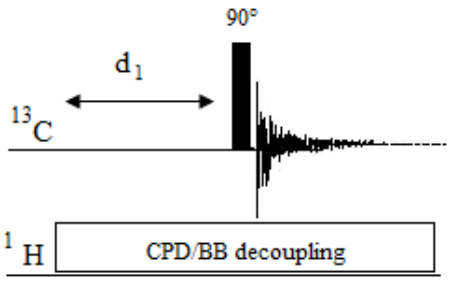

Figure 6. ^{1}H decoupled ^{13}C and then acquired the ^{13}C signals.

^{13}C couples strongly to any protons which may be attached ($^{1}J_{CH}$ is typically about 125 Hz fro saturated carbon atoms in organic molecules). Spin coupling to one or more protons complicates the interpretation of the ^{13}C spectra and thus it is normally removed using a variety of proton decoupling techniques (Figure 6). All decoupling procedures are based on the same principle, the broadband irradiation of all proton resonances with a high-power amplitude-modulated and monochromatic ^{1}H frequency. The irradiation saturates the Boltzman energy levels of the proton spectrum, removing the macroscopic magnetization of all protons and making the scalar proton couplings disappear from the ^{13}C spectrum. There are two main proton decoupling methods: broad band decoupling (BB) and composite pulse decoupling (WALTZ). They differ in the type of modulation of the proton frequencies. Whereas BB uses a continuous irradiation of proton frequencies with a train of rectangular pulses of identical duration and opposite phase (41) composite pulse decoupling uses blocks of ^{1}H pulses of different pulse lengths and phases (42) WALTZ sequences are more efficient than BB, allowing decoupling ^{13}C spectra using less decoupler power and diminishing also the potential dielectric heating of the sample.

NMR PARAMETERS

The structural identification of compounds is encoded into three principal spectral parameters: chemical shifts (δ, ppm), the spin-spin coupling constants (J, Hz) and the signal areas. The spectral shape is also dependent on the longitudinal and transverse relaxation times, T_1 and T_2, respectively.

Chemical shift

When a molecule is placed in a B_0 field, the molecular electron distribution shields the applied magnetic field with respect to the nuclei, and being this distribution generally anisotropic, the magnetic field experienced by nuclei at different sites is slightly different, as well as their Larmor frequencies (*i.e.* their signals in the NMR spectrum). This phenomenon is called *chemical shift* and, in principle, we expect to find, in the NMR spectrum of a certain isotope, a different signals for each chemically different nucleus. These differences are very low in the MHz scale and spectroscopists prefer to express them in terms of *part per million* (δ, ppm) with respect to a reference compound, which varies from nucleus to nucleus. For instance, for ^{1}H, ^{13}C and ^{29}Si spectroscopy the reference, when organic solvents are employed,

is tetramethylsilane (TMS) whose ^{1}H ,^{13}C and ^{29}Si NMR signals are placed at $\delta = 0$ ppm in the corresponding chemical shift scales. In the case of water solutions the reference is sodium 2,2-dimethyl-2-silapentane-5-sulfonate (TSP). The chemical shift is very informative on the chemical environment of a given nucleus and permits the identification of the chemical groups present in a molecule. For organic compounds, ^{1}H NMR signals are found in the range of 0-16 ppm (43), whereas ^{13}C signals span approximately from 0 to 250 ppm [41, 43], ^{19}F signals from +50 to -280 ppm (with respect to δ of trichlorofluoromethane set equal to 0), ^{31}P signals from +250 to -180 ppm (with respect to δ of 85 % phosphoric acid set equal to 0) and ^{15}N signals from +500 to -400 ppm (with respect to δ of nitromethane set equal to 0). The chemical shift range is different for the different nuclei, being dependent on the atomic number of the elements specie.The literature reports collections of chemical shifts for the most important metabolites (44-45) that can be used for assignment purposes.

Coupling constant

NMR signal of nuclei with spin I=½ posses a fine structure that is due to the interaction among nearby spins, mediated by bonding electrons and it is referred to as spinning coupling or scalar coupling constant, denoted J and given in Hz unit. The J coupling is an intramolecular interaction, independent of the applied magnetic field and is denoted as homonuclear and heteronuclear if the spins are of some or different isotopic type, respectively. The J coupling constants are shared between couples of spins. A group of spins coupled together is called spin system. The signal multiplicity of a nucleus in a spin system depends on the number of spins coupled with it and on the values of the coupling constants.

The more observed proton-proton coupling constants *J*(H,H) are those over two and three bonds ^{2}J(H,H) and ^{3}J(H,H), respectively. The geminal coupling constants ^{2}J(H,H) are observed only in the case of diastereotopic methylene protons. For the ^{3}J a further dependence on the dihedral angle, expresses by a Karplus type relaxations, is found: the ^{3}J value is larger for an angle of 180°, smaller for an angle around 90° and reaches a relative maximum at 180°. The one-bonded ^{1}J(C,H) are the largest carbon-proton couplings, hence the more easily observed, whereas ^{3}J(C,H) are usually higher than ^{2}J(C,H) (41,43,46,47). The *J* coupling are strongly dependent on the chemical structure in terms of geometry and constitution. The factors which influence more the values of coupling constants are γ of coupled nuclei, hybridization, bond length, bond angle, substituent electro-negativity. The phenomenon of

spin coupling is not restricted to carbon and proton, but involves other interesting nuclei such as ^{31}P and ^{19}F,the presence of which can further complicate proton and carbon spectra.

Integrated area

The area of NMR signals is directly proportional to the number of nuclei generating it, providing that an adequate delay between subsequent scans has to be used to allow for longitudinal relaxation. The estimate of the number of nuclei can be obtained from signal height only when comparing singlets of the same width at half height. Signal width is inversely proportional to transverse relaxation time, which, in turn, depends on molecular motion. Slowly tumbling molecules posses short T_2 and give broad signals.

The peculiar advantage of NMR spectroscopy is based on its ability to identify a wide range of compounds present in complex mixtures, owing to the flexibility in the experimental implementation which, in turn, permits the choice among a great number of experiments in order to establish molecular connectivity and spatial relationships.

High Resolution NMR in solution

Liquid or powdered samples (*e. g.* those derived from perchloric acid -PCA- extraction and lyophilisation or from lyphophilic extraction) are usually dissolved in a suitable deuterated solvent, such as D_2O or $CDCl_3$. The usage of deuterated solvents permits to minimise the huge proton signals coming from the solvent itself, that can obscure the weaker ones from the solute. It also provides the deuterium lock signal utilised in high-resolution NMR for magnetic field stabilisation. When D_2O is used signals coming from OH, NH and SH groups are lost due to proton-deuterium exchange. To avoid this effect a H_2O/D_2O 9/1 mixture is generally used, and suitable solvent suppression techniques employed.

HR-MAS (High Resolution Magic Angle Spinning)

High-resolution NMR spectra of biological samples have been usually obtained from homogeneous clear liquid extracts of tissues or cells. Recently, a new technique, HR-MAS, which stands for high-resolution magic-angle spinning, has been introduced. HR-MAS NMR can be considered a hybrid technique between solid-state NMR and classical solution state NMR. It uses, similarly to solid-state NMR, the magic angle spinning (MAS), (48) but it retains the classical solution NMR experiments. Similar to solution NMR, HR-MAS NMR

involves direct polarization transfer and not cross-polarization transfer (CP-MAS) (49) between ^{1}H and heteronuclei (^{13}C or ^{15}N), thus distinguishing it from CP-MAS experiments on true solid state.

In liquids, molecules do not generally experience significant motional restriction and tumble at rates faster than the NMR observation frequency. Thus, significant spectral broadening effects due to the fact that the molecules are not motionally free are averaged, resulting in narrow spectral lines. In tissues, restriction of molecular motions and areas of different magnetic susceptibility result in spectral broadening that is not effectively averaged. In this type of sample, interactions such as dipolar couplings and chemical shift anisotropy produce spectral broadening with an angular dependence of $(3\cos^2\theta\text{-}1)$, where θ is the angle between the static magnetic field and the inter-nuclear vector responsible for the interaction. It is known that if a sample is spun mechanically, at a rate faster than the spectral broadening originating from these interactions, and at the magic angle of 54.7° (which meets the criterion of $[3\cos^2(54.7°)\text{-}1 = 0]$, the contribution from these interactions to the broadening of spin-one-half nuclei NMR bands can be significantly reduced (50,51).

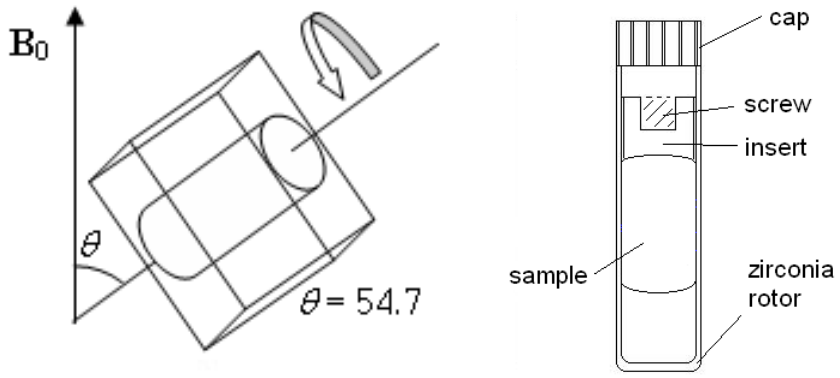

Figure 7. Schematic representation of HR-MAS probe (left); HR-MAS rotor (right).

A rotor, which is filled with the tissue sample, is placed in a stator block. This rotor is spun at the magic angle at an appropriate frequency and the RF coil in the stator block allows for the application of high-frequency pulses to the sample and serves as a receiver coil thereafter. Nowadays, a magnetic field gradient coil, aligned along the magic angle axis, can also be included to allow NMR experiment in which gradients are used to select specific spin coherences or to allow the measurement of diffusion properties of the substances present.

HR-MAS uses dedicate probeheads capable of studying the samples in rapid rotation (3÷15 kHz) around an axis 54.7° tilted with respect to that of the static magnetic field (B_0) (Figure 7). These probeheads drastically reduce contribution from dipolar couplings, chemical shift anisotropy, and susceptibly distortions, providing high-resolution spectra from semisolid samples, such as tissues. The quality of the obtained spectra is comparable to that obtained from aqueous extracts, and the acquisition techniques used are those employed in high-resolution NMR in solution. The advantage is that of carrying out measurements on intact tissues specimens (34,23), without any pretreatment, enabling the extractions step to be omitted, and aqueous and lipid fractions to be detected simultaneously, enhancing the possibility of identifying biochemical markers with diagnostic and prognostic value. After the first application of HR-MAS NMR on human tissue specimens, some articles on *ex vivo* HR-MAS spectroscopic studies on different organ tissues have appeared (52-64).

In order to evidence the quality of the spectra obtained with the HR-MAS probe with respect to those obtained using high resolution probe, I report in Figures 7 and 8 the spectra of kidney tissue samples. The sample for the high resolution probe was prepared by putting a piece of kidney directly in a 5mm glass tube. It is evident (see Figure 7 and 8) the better resolution obtained with HR-MAS.

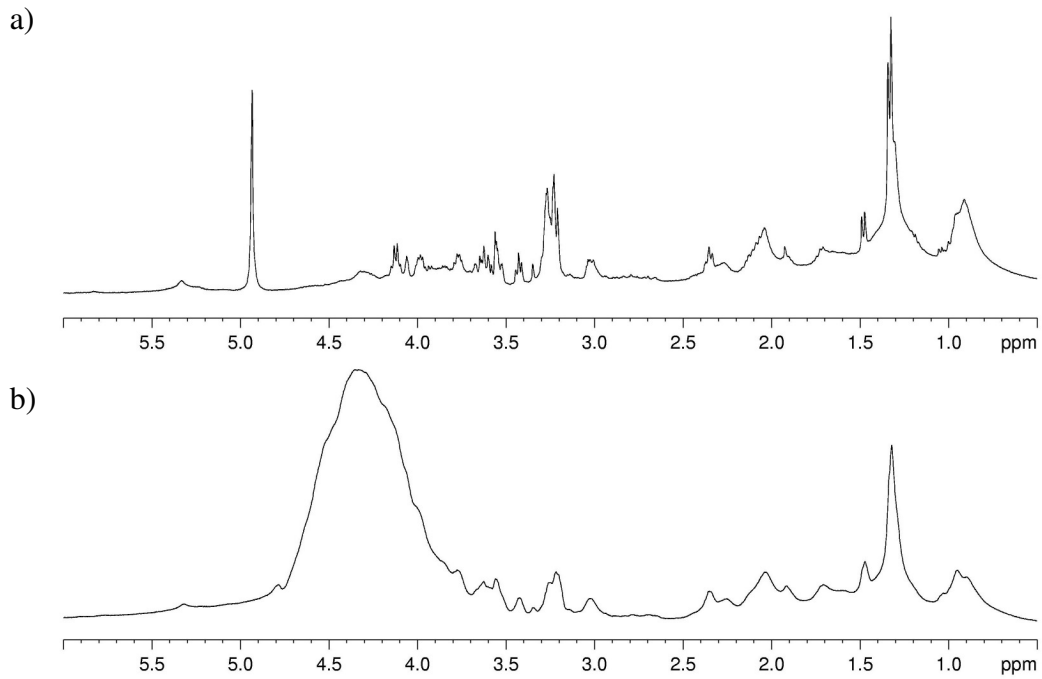

Figure 7. 1D proton NMR spectra of kidney obtained with water-presaturation pulse sequence with composite pulse to a) HR-MAS probe and b) High Resolution probe.

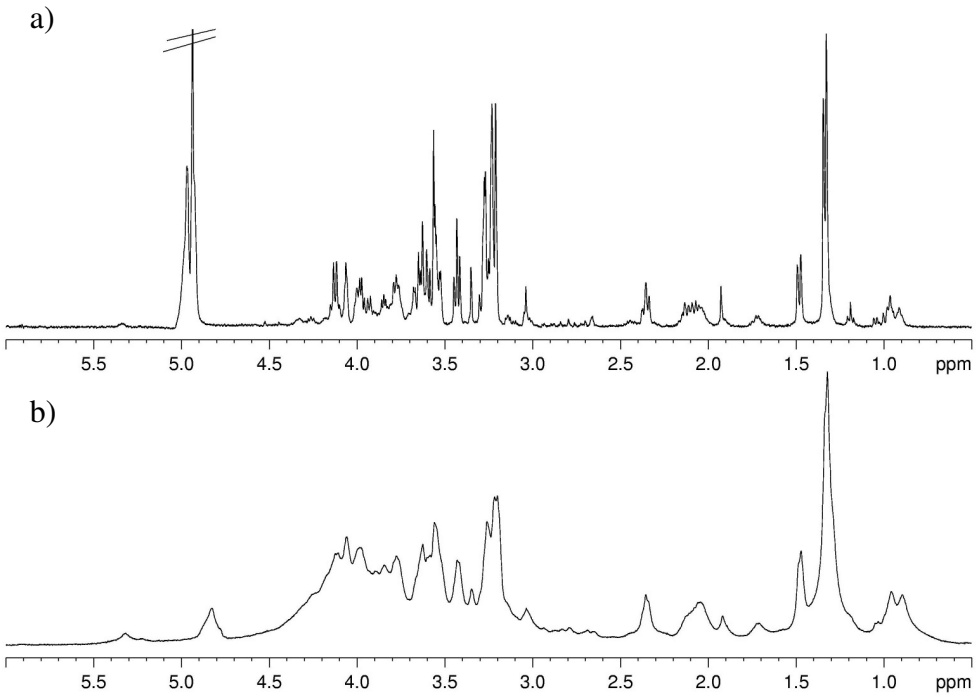

Figure 8. 1D proton NMR spectra of kidney obtained with CPMG sequence with total spin-echo time $2n\tau$=360 ms, to a) HR-MAS probe and b) High Resolution probe.

Sample Selection and Treatment

One major advantage of HR-MAS NMR spectroscopy is that the sample preparation is straightforward and relatively fast, although this still has to be carried out manually. Samples of as little as ~ 20 mg can be prepared (65). The original samples healthy or neoplastic (the tissues are to be considered healthy or neoplastic only when the histological examination confirms the macroscopic finding, mainly when these studies are undertaken for the first time) are to be put rapidly in liquid nitrogen and stored at -85°C until NMR analyses. The samples can be preserved up to 3 months without observing changes in the spectra, and the measurements should be taken within this period. Immediately before NMR analysis, the tissue sample is cut to have suitable dimensions and flushed with D_2O to eliminate residual blood (thus reducing the iron content, with the aim to improve the homogeneity, and in turn the water suppression) and to add deuterium as nucleus for the lock system. The specimens are then transferred into the MAS zirconia rotors (4 mm OD) that are available in different capacities (12, 50, 90 μL), and are chosen in relation to the sample amount. A Teflon perforated insert is used to restrict the volume, to eliminate bubbles, and to improve the homogeneity of the sample. The insert is closed by a screw, then the rotor by a cap the star

shape of which provides the driving for the rotor (see Figure 7). The rotor are generally spun at frequencies between 2000 and 6000 Hz, when working on tissues. This is dependent on the spectrometer frequency and is chosen so that spinning side bands will be located outside the spectral region of interest, i.e. at an observation frequency of 400 MHz, a 4000 Hz rotation frequency is chosen in order to make sure that spinning side bands lie outside the 10 ppm ^{1}H NMR spectral window. Maintenance of tissue integrity is the limiting factor in the selection of rotation speed. Signal line-widths decrease and signal intensities consequently increase with increasing spinning speed and these effects are reversible when returning to lower spinning speeds. However, after rotation at frequencies of about 8000 Hz, it has been found that spectral line widths remain sharper after returning to lower speeds, indicating some breakdown of cell structures, with the concomitant release and higher mobility of metabolites. Reasons for this are the moderate centrifugal forces if the tissue sample is not well packed into the rotor (66).

The temperature in the MAS NMR experiments can be adjusted over a wide range and the current commercially available standard cooling devices, temperatures of 1-10° C are easily achieved. Especially for experiments which take long times, such as 2D acquisitions or extended sets of 1D experiments, it is advisable to cool the specimen in the rotor to temperatures below room temperature. Several studies have been performed at temperatures of 10-30° C, but it has been recommended that experiments be carried out at 4° C, to maintain stability over a longer period. It is very important to keep the tissue temperature as low as possible, since the intracellular reaction rates in the tissue increase 2-4 fold when the temperature is increased by 10° C. The rotor temperature is regulated using gas flow, the temperature of which can be adjusted. Although most published studies cite an operating temperature, it might not always accurately reflect the sample temperature, since it simply reflects that of the cooling gas. Higher spinning speeds can induce considerable frictional heating (24) and hence this provides an additional need for sample cooling. It is always important when carrying out HR-MAS NMR spectroscopic studies of tumor samples, to obtain data in a period as short as possible. Samples should be snap-frozen in liquid nitrogen straight after tumor excision in order to avoid *post mortem* changes (67-69). When defrosting samples for MAS NMR, tumor metabolism is not interrupted as is the case when carrying out freeze-clamped extraction studies. Therefore, it is best to defrost and process tumor samples in an ice bath and to keep the time short before the sample is placed in the rotor and kept at a low temperature. Although some studies have reported that sample freezing affects the NMR

profile of tissue metabolites (67,70), there is the need to keep the surgery to NMR experiment time at room temperature as short as possible, and, until further practical improvement, snap freezing and low temperature storage are the only real possibilities.

The measurements reported in the present thesis, unless otherwise indicated, are carried out maintaining the temperature of the sample at 278° K. Sample and instrument preparation takes about 20 min.

NMR EXPERIMENTS

One-Dimensional NMR Spectra

The NMR experiments utilized to obtain HR-MAS spectra of tissues are the same as those used in solution. A generally employed basic set of experiments is formed by:

1. The 1D ^{1}H NMR experiment with suppression of the residual HDO/H_2O (Figure 9): it generates a spectrum containing signals from metabolites, macromolecules, and lipids It is necessary to suppress the water signal because its high intensity can obscure the resonances of the other components. Among several approaches that can be adopted (71), the presaturation one is that preferred by us. It consists in the irradiation of the HDO/H_2O signal with a weak radiofrequency field B_1 (50 Hz) for some seconds prior to the acquisition of the ^{1}H spectrum (Figure 10). This method is more selective than others, but it is not recommended when peaks from protons involved in chemical exchange processes with water are studied, because their signals are reduced or lost.

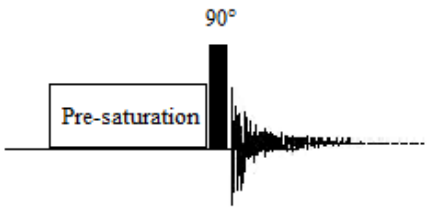

Figure 9. Pulse sequence scheme for acquisition of ^{1}H NMR spectrum with low power pre-saturation of water signal during the relaxation delay.

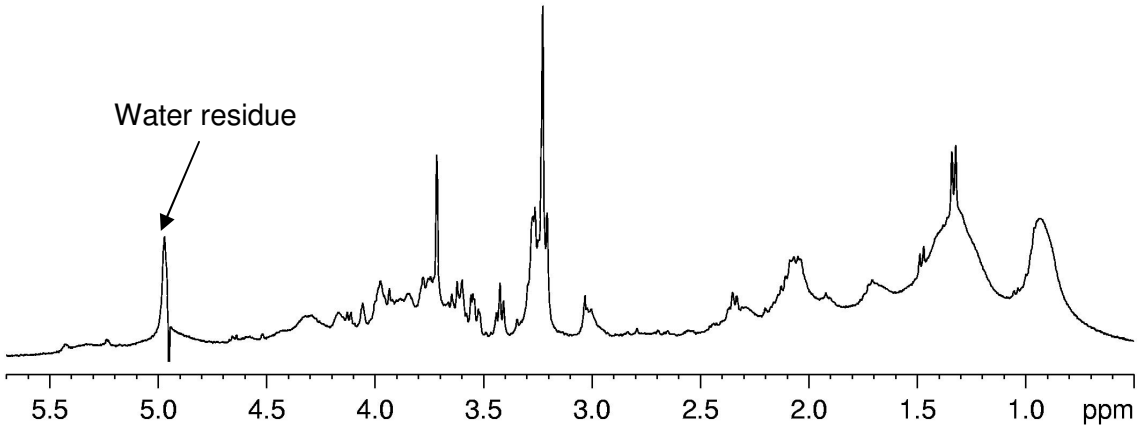

Figure 10. 1D proton NMR spectra of healthy gastric mucosa obtained with water-presaturation pulse sequence with composite pulse.

2. The water-suppressed spin-echo experiment (Carr-Purcell-Meiboom-Gill, CPMG) (72) (Figure 11): it acting as a T_2 filter cuts off signals from macromolecules and lipids, leaving only signals from small metabolites (Figure 12). The experiment employs the pulse sequence:

[d_1-90°-(τ-180°-τ)$_n$-AQ]

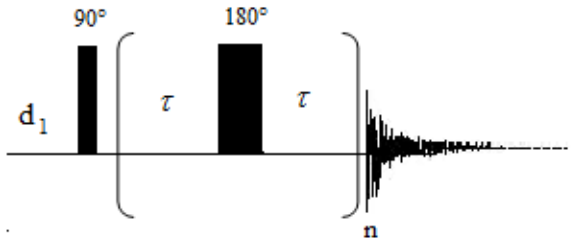

Figure 11. Pulse sequences for the spin echo (T_2 filter).

where d_1 is the relaxation delay, 2τ is the echo time, and AQ the acquisition time. The 90° pulse creates a transverse magnetization that decays during the spin-echo period (τ-180°-τ)$_n$.

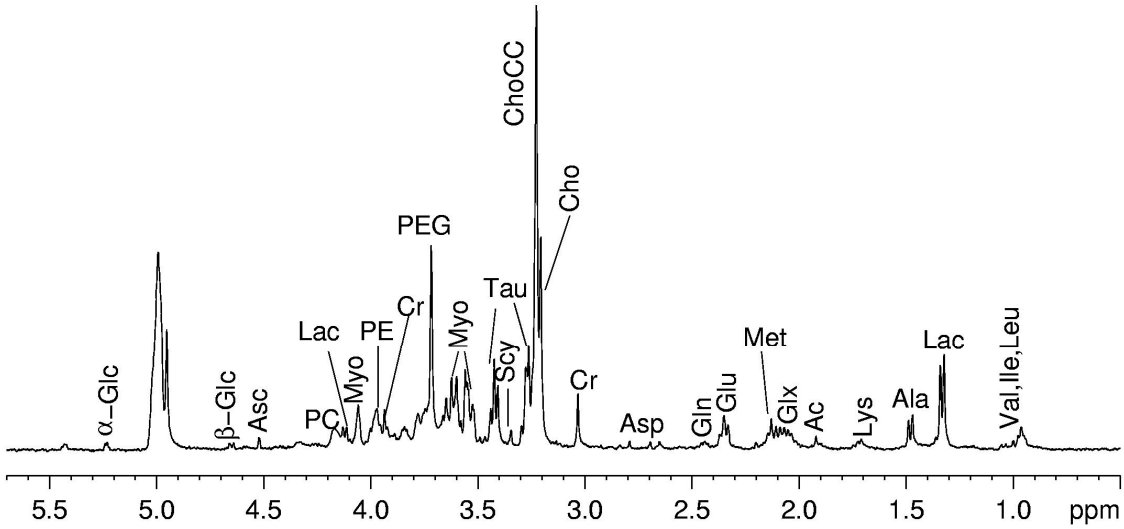

Figure 12. 1D proton NMR spectra of healthy gastric mucosa obtained with CPMG sequence with total spin-echo time 2nτ=360 ms.

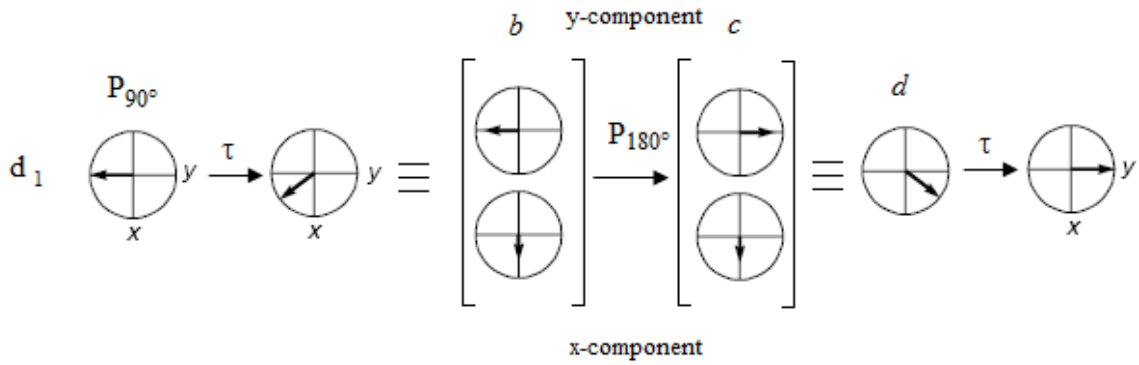

Figure 13. Example of magnetization behavior in the spin-echo sequence.

After the delay (d1), P90° generates a My magnetization that precedes during τ; this magnetization can be resolved into y- and x-components as shown in *b*. The 180° pulse applied on the x-axis has not effect on the x-component of the magnetization; in contrast the y-component is rotated by 180° in the yz-plane, ending up along the opposite axis. The individual components after the 180° pulse are shown in *c*, and the corresponding vector is shown in *d*. The effect of the 180° pulse on the x-axis is to reflect the vector in the xz-plane. During the second time τ the vector precesses in the same direction (Figure 13). At the end of the sequence the vector always ends up along the y-axis, regardless of the time τ and the offset Ω; the sequence is said to "refocus the offset (or shift).

Macromolecules having short T_2 [T_2 can be estimated by the half-height line width $l_{w1/2}$ by the equation $l_{w1/2}=1/(\pi T_2)$] should be completely relaxed and filtered out. The total echo time $2n\tau$ can be varied in relation to the T_2 of the macromolecules. The water suppression irradiation is used during d1 and in my experiments this parameter was set to 1.5 s.

3. The gradient-based stimulated-echo pulse sequence (with bipolar-gradient pulse pairs and longitudinal-eddy current delay, LED) (73) (Figure 14): it generates a spectrum in which signals coming from slowly diffusing molecules are retained at expenses of those from low molecular weight metabolites, which are, in turn, reduced (Figure 15). The experiment employs the following pulse sequence:

[d_1-90-g_1-δ-180-g_2-δ-90-g_3-Δ-90-g_1-δ-180-g_2-δ-90-g_4-d_{21}-90-AQ]

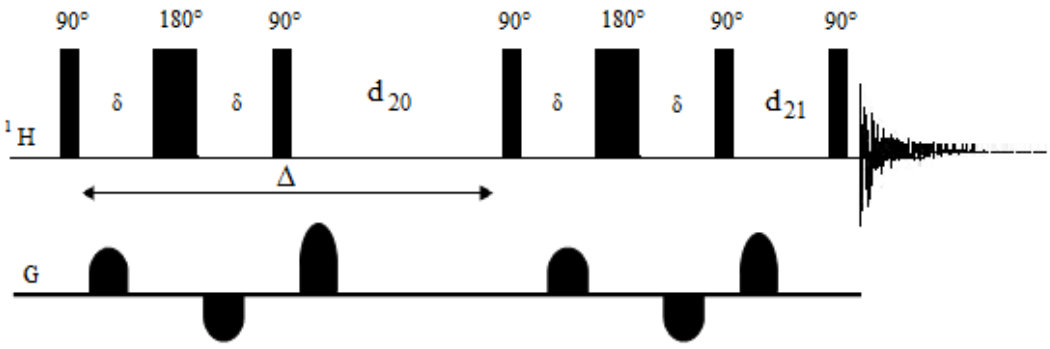

Figure 14. . Pulse sequences for diffusion-edited spectra.

where $g_2= -g_1$, the diffusion time $d_{20}= \Delta$-90-δ-180-δ-90 and d_{21} is the eddy-current time. The correct selection of d_{20} and the gradient strength permits to filter out signals from fast moving small molecules and to retain only macromolecules.

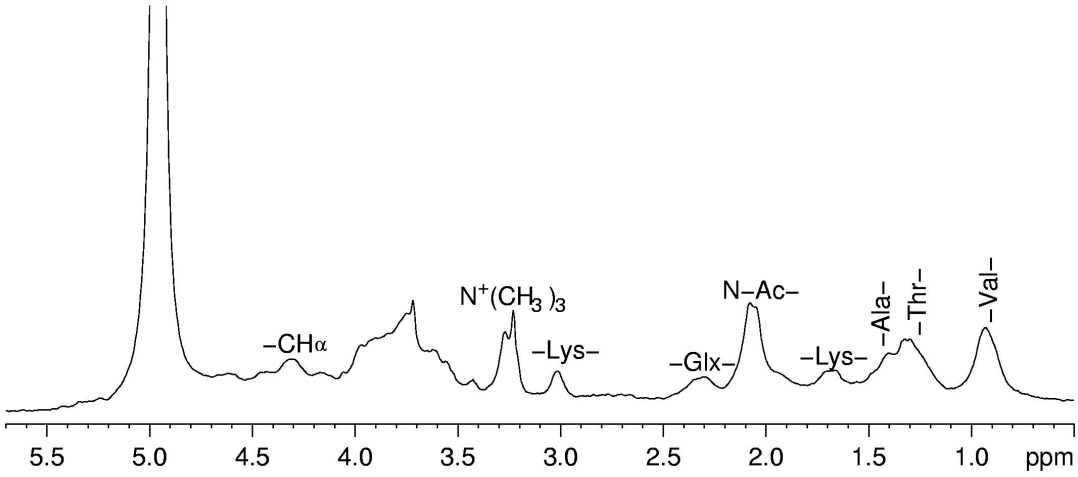

Figure 15. 1D proton NMR spectra of healthy gastric mucosa obtained with diffusion edited spectrum obtained with Δ=200 ms, δ=4 ms and gradient strength of 32 G/cm.

These last two experiments exploit the different relaxation and diffusion properties of small metabolites with respect to macromolecules and lipids. The accurate choice of the spin-spin relaxation delay 2nτ and of parameters influencing diffusion (gradient-field pulse duration δ, gradient strength, and diffusion time Δ) enables two complementary sets of signals, corresponding to narrow and broad components, to be isolated.

The acquisition of a diagnostic set (comprehensive of 1, 2 and 3) of 1D HR-MAS spectra requires about 30 min. In the case of scarcely overlapping signals the chemical shifts and coupling constants of metabolites can be derived by direct inspection of the spectrum. The comparison of the data obtained with those reported in the literature, taking into account that pH can influence the chemical shifts, can lead to the identification of some compounds. Nevertheless, NMR spectra of intact tissues or biological extracts show generally a complex profile due to the overlapping of resonances of a wide type of molecules. Crowded spectra can be analysed to a greater degree through the use of two-dimensional techniques.

Two-Dimensional NMR Spectra

2D NMR spectra can be a valuable aid in elucidating complex NMR spectra, permitting identification of unknown compounds mainly by analyzing their spin-spin correlations through chemical bonds.

In NMR the signal is recorded as a function of one time variable and then Fourier transformed to give a spectrum which is a function of one frequency variable. In two-dimensional NMR the signal is recorded as a function of two time variables, t_1 and t_2, and the

resulting data Fourier transformed twice to yield a spectrum as a function of two frequency variables. The general scheme for two-dimensional spectroscopy is:

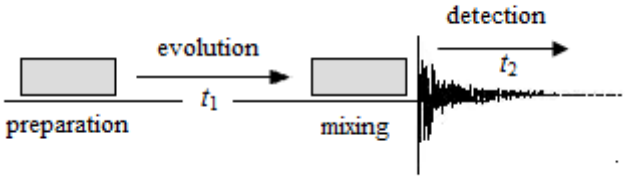

In the first period, called the preparation time, the sample is excited by one or more pulses. The resulting magnetization is allowed to evolve during t_1. Then another period follows, called the mixing time, which consists of a further pulse or pulses. After the mixing period, the signal is recorded as a function time variable, t_2. This sequence of events is called a *pulse sequence* and the exact nature of the preparation and mixing periods determines the information found in the final 2D spectrum. It is important to realize that the signal is not recorded during the time t_1, but only during the time t_2 at the end of the sequence.

The two-dimensional signal is recorded in the following way. First, t_1 is set to zero, the pulse sequence is executed and the resulting free induction decay recorded. Then the nuclear spins are allowed to return to equilibrium. t_1 is then set to Δ_1, the sampling interval in t_1, the sequence is repeated and a free induction decay is recorded and stored separately from the first. Again the spins are allowed to equilibrate, t_1 is set to $2\Delta_1$, the pulse sequence repeated and a free induction decay recorded and stored. The whole process is repeated again for $t_1 = 3\Delta_1$, $4\Delta_1$ and so on until sufficient data is recorded, typically 50 to 500 increments of t_1. Thus recording a two-dimensional data set involves repeating a pulse sequence for increasing values of t_1 and recording a free induction decay as a function of t_2 for each value of t_1.

Among the plethora of 2D experiments found in the literature, the most effective, and thus most commonly employed, for the identifications of metabolites in mixtures are COrrelation SpectroscopY (COSY) (74), TOtal Correlation SpectroscopY (TOCSY) (75,76), and Heteronuclear Single Quantum Coherence (HSQC) (77) or Heteronuclear Multiple Quantum Coherence (HMQC) (78) experiments.

COSY (79-81) experiment (Figure 16), and its variants, is one of the most popular and useful of all two-dimensional experiments. It is a homonuclear experiment, mostly used for analyzing proton spectra. During t_1 the spin system evolves under the effect of *J* couplings and chemical shifts, the second 90 degree pulse transfers spin information between pairs of coupled nuclei which is detected during t_2. The Spectra are 2D plots in which signals

corresponding to the 1D spectrum are on the diagonal, whereas off-diagonal peaks, called cross-peaks, are found between pairs of coupled spins (Figure 17). These correlations are usually due to connections through two and three bonds, but long-range connectivities can sometimes be observed.

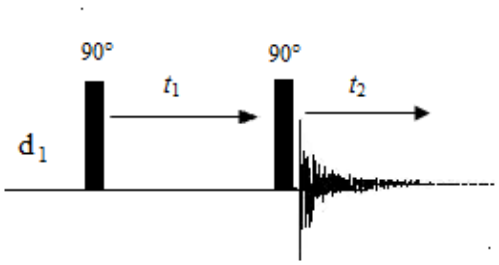

Figure 16. Pulse sequence for homonuclear COSY experiment. d_1 relaxation delay, t_1 evolution time, t_2 acquisition time.

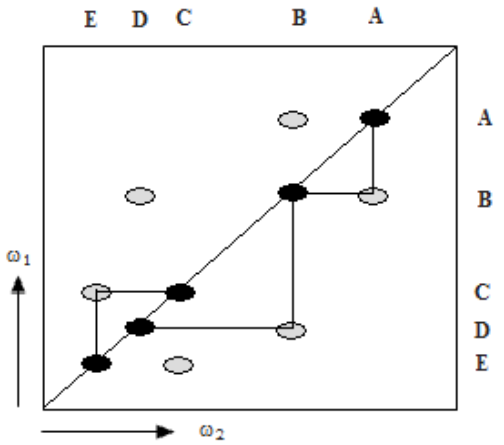

Figure 17. Schematic COSY spectrum, indicating how it is used to determine the chemical shifts of coupled spin. In this example there are five spins, A-E. *Diagonal peaks*, are filled and *cross peaks* are unfilled. Diagonal peaks have the same frequency coordinates (chemical shifts) in each dimension, whereas for cross peaks the coordinates are different. The appearance of the cross peak at ω_1 frequency of B and the $\omega_2$frequency of A indicates that A and B are coupled. Using the same interpretation for the other peaks, we find that B is further coupled to D. Similarly, C is coupled to E. Overall, the COSY spectrum allow us to trace out the network of coupled spins in the molecule.

As example of the used of COSY in the characterization of the gastric mucosa are shown in Figure 18.

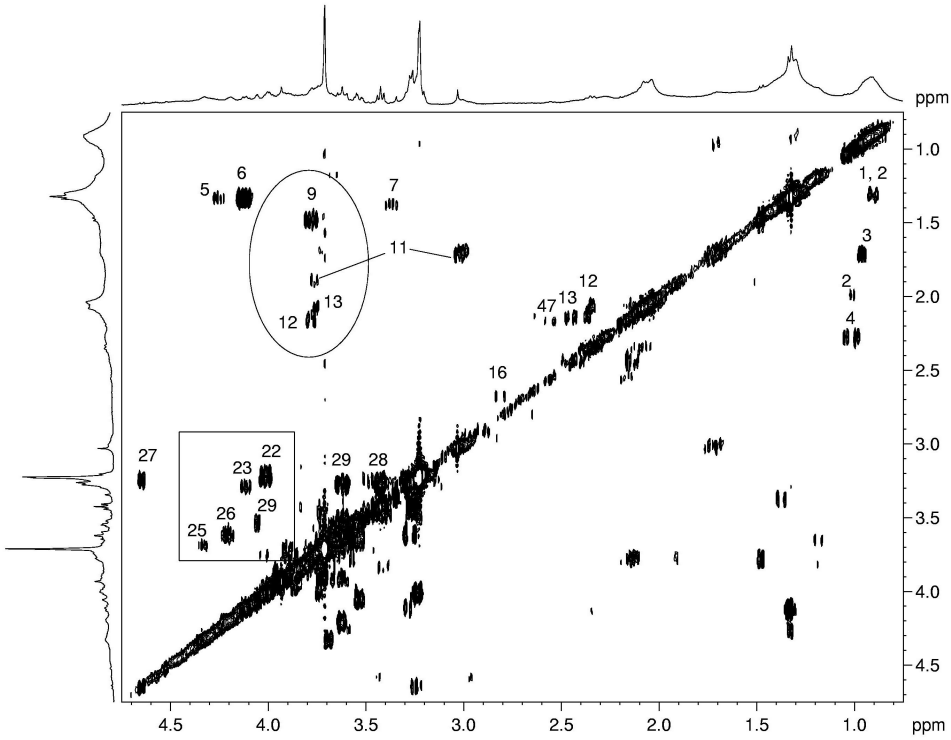

Figure 18. COSY NMR spectrum of healthy gastric mucosa. This COSY spectrum is particularly useful for the distinction of Lac (labeled as number 6) and threonine (Thr, labeled as 5), whose doublets at 1.33 ppm overlap, and for the detection of α-hydrogens of several amino acids (circled). It also permits to distinguish glycerophosphocholine (GPC, labeled as 25) from phosphorylcholine (PC, labeled as 26), whose $N^+(CH_3)_3$ signals are usually unresolved, and to detect phosphorylethanolamine (PE, labeled as 22), whose signals are found in a very crowded region and often hidden under those of other metabolites (squared).

TOCSY (82,83) experiments (Figure 19) enable all the components of a spin system to be detected (at least in principle). The core of these experiments is a spin-lock time, which allows transfer of information from one spin to another belonging to the same coupling network, even if these spins are separated by many bonds (Figure 20). The mixing time must be held long enough (from 60 to 140 ms) to complete the transfer process to all the spins. In our studies we have selected a mixing time of 100 ms. The TOCSY spectra permit the identification of $^1H,^1H$ connectivities up to five or six bonds.

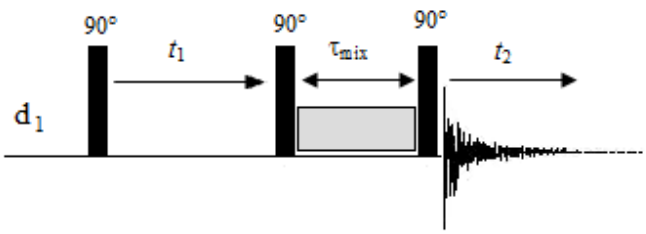

Figure 19. Pulse sequence for the TOCSY experiment. The heart of the sequence is the period of isotropic mixing, indicated by the rectangle, which transfers magnetization between spins which are connected via an unbroken network of couplings.

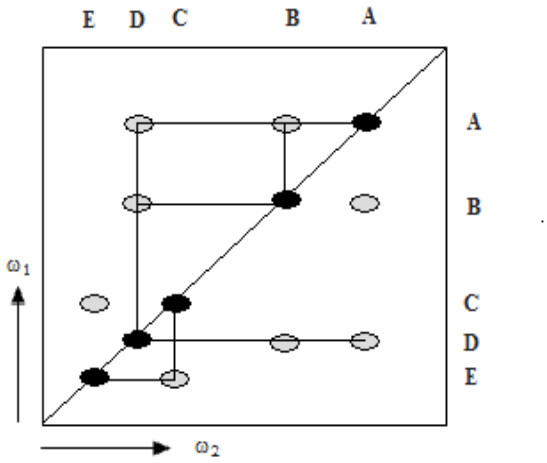

Figure 20. Schematic TOCSY spectrum for the same spin system as for the COSY spectrum show in Figure 17.

As example of the used of TOCSY in the characterization of the gastric mucosa are shown in Figure 21.

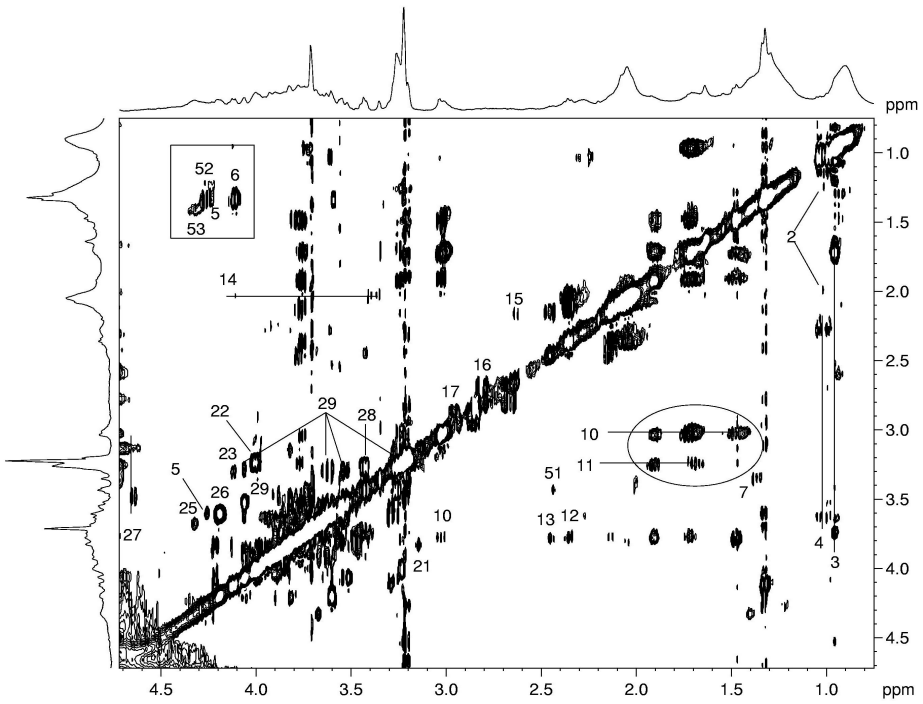

Figure 20. TOCSY NMR spectrum of healthy gastric mucosa. Some metabolites, such as lysine (Lys, labeled as 10) and arginine (Arg, labeled as 11) (circled), *myo*-Inositol (Myo) and β-glucosio (β-Glc) are better differentiated in TOCSY spectra that in the COSY one. More interestingly, some signals due to α-CH of bonded aminoacids [mainly alanine (Ala) and Thr] are detected in the region of the 2D spectrum close to the correlations of Lac and Thr (squared, labeled as 6 and 5, respectively).

Heteronuclear chemical shift correlation experiments HMBC and HSQC, are basically heteronuclear COSY experiments that allow us to obtain information about directly connected or long-range relayed protons and heteronuclei. By heteronucleus I mean ^{13}C, but the experiment can be applied to other nuclei, such as ^{15}N, ^{31}P, etc. In heteronuclear two-dimensional NMR experiments the nucleus that evolves during t_1 is different from that which is detected in t_2. Classical 2D HETero-CORrelated experiments (HETCOR) (84) are based on the acquisition of the heteronucleus, whereas information about the proton is obtained in the second dimension, ω_1. Conversely, inverse-detection experiments (Heteronuclear Multiple Quantum Coherence HMQC (85), Heteronuclear Single Quantum Coherence HSQC (86), and Heteronuclear Multiple Bond Correlation HMBC (87) relay on the acquisition of the more receptive nucleus, *i.e.* the proton, whereas the chemical shift of the heteronucleus is found in ω_1. The two-dimensional heteronuclear NMR experiments are based on the existence of coupling constants between heteronuclei and protons, and due to the difference between one-

bond and long-range coupling constants, it is possible to obtain separately spectra depending only on ^{1}J(CH) or on ^{n}J(CH). The inverse-detection method produces more information, spectra of a higher quality and in less time with respect to classical hetero-correlated experiments, even though it requires good suppression of the signals of protons bonded to the not-magnetic isotopomer of the X nucleus (*e.g.* ^{12}C), and, when working in aqueous solution, the suppression of water signal. The pulse sequence for HSQC experiment is reported in Figure 21. The HSQC experiment is based on a double INEPT (88) polarisation transfer, first from proton to carbon, then from carbon back to proton after a time t_1, during which the carbon chemical shift evolves. The experiment is usually applied in its decoupled (from heteronucleus) version. The knowledge of the carbon chemical shift associated to the proton one represents a key step in the identification of a metabolite.

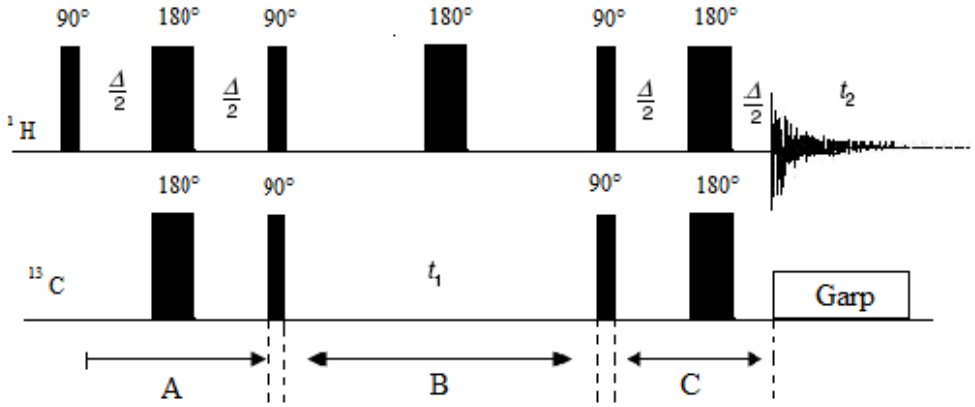

Figure 21. Pulse sequence for HSQC experiment. Decoupling from ^{13}C carbon is achieved through a GARP pulse sequence (89).

An example of HSQC spectra of gastric mucosa are reported in Figure 22.

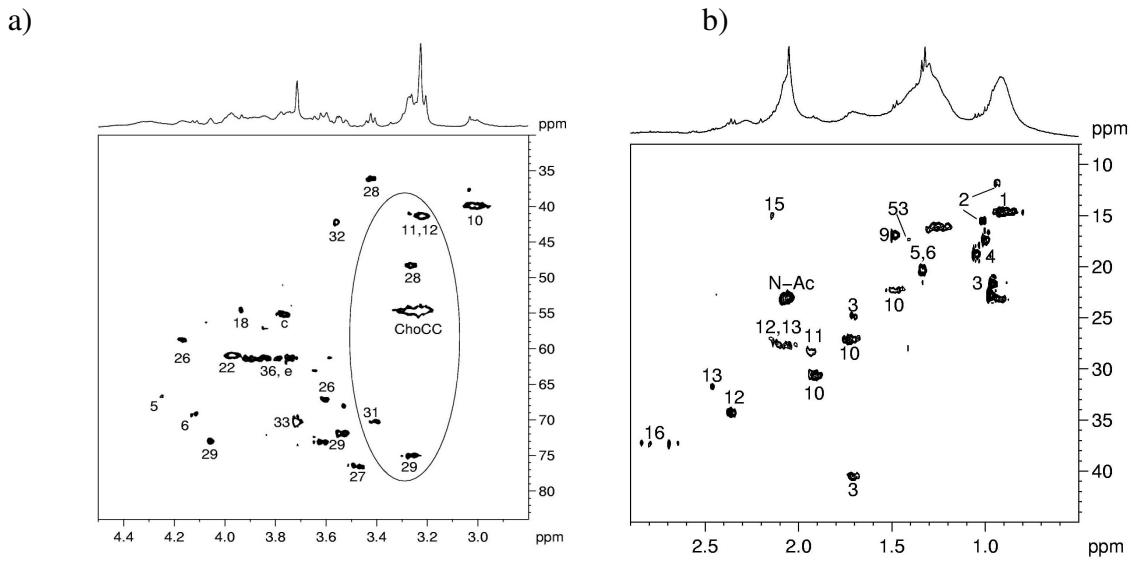

Figure 22. HR-MAS HSQC spectrum of healthy gastric mucosa. a) One region of the major interest is usually that corresponding to the $N^+(CH_3)_3$ of ChoCC, Tau, Arg, Myo and PE, which all contribute to the 3.2 ppm signal in the proton spectra. These molecules can readily be distinguished in HSQC spectra due to the large differences in their ^{13}C chemical shifts (circled) and also to their multiplicity (CH_3 *vs* CH_2), if edited sequences are employed (90). Some problems are encountered in the interpretation of the region between 3.6 and 4.0 ppm, for the presence of overlapped correlations around 62 ppm, presumably due to glycerols and CH_2OH of Glc. b) At low ppm the ^{13}C chemical shifts dispersion is also useful for the assignment of the signals of aliphatic amino acids isoleucine (Ile), valine (Val) and leucine (Leu).

To acquire a complete set of good-quality 2D spectra, 15–20 hours of acquisition are required.

Details of the experiment used in the characterization of tissues

Proton HR-MAS spectra were recorded with a Bruker Avance400 spectrometer equipped with a $^1H/^{13}C$ HRMAS probe (operating at 400.13 and 100.61 MHz, respectively) and with a Bruker Cooling Unit (BCU) for temperature control. Samples were spun at 4000 Hz, and three different types of 1D proton spectra were acquired using sequences implemented in the Bruker software: (i) a standard sequence with 1.5 s water presaturation during relaxation delay, 8 kHz spectral width, 32k data points, 32–64 scans, (ii) a water-suppressed spin-echo CPMG sequence with 1.5 s water presaturation during relaxation delay, 1 ms echo time (τ) and 360 ms total spin-spin relaxation delay (2nτ), 8 kHz spectral width, 32k data points, 256 scans, and (iii) a sequence for diffusion measurements based on stimulated echo and bipolar-gradient pulses with big delta 200 ms, eddy current delay Te 5ms, little delta 2*2 ms, sine-shaped gradient with 32 G/cm followed by a 200 μs delay for gradient

recovery, 8 kHz spectral width, 8k data points, and 256 scans. Two-dimensional COSY spectra were acquired using a standard pulse sequence and 0.5 s water presaturation during relaxation delay, 8 kHz spectral width, 4k data points, 32 scans per increment, and 256 increments. Two-dimensional TOCSY spectra were acquired using a standard pulse sequence and 1 s water presaturation during relaxation delay, 100 ms mixing (spin-lock) time, 4 kHz spectral width, 4k data points, 32 scans per increment, and 128 increments. Two-dimensional HSQC spectra were acquired using a standard pulse sequence echo-antiecho phase sensitive and 0.5 s relaxation delay, 1.725 ms evolution time, 4 kHz spectral width in *f*2, 4k data points, 128 scans per increment, 17 kHz spectral width in *f*1, and 256 increments. It is not necessary to add a reference standard for the chemical shift scale, such as TSP (trimethylsilylpropansulfonate), but our suggestion is to use a well known resonance as internal standard, such as H-1 of α-glucose (α-Glc) (a doublet at 5.24 ppm, J 3.8 Hz) or the methyl of Ala, Lac (doublets at 1.48 ppm, J 7.2 Hz, and 1.33 ppm, *J* 6.9 Hz, respectively). Attention should be paid when using the signal of HDO to calibrate the chemical shift scale, for it is highly temperature dependent.

TEMPERATURE EFFECTS

The samples were studied under temperature control conditions, at 278° K. This was necessary to slow down tissue degradation processes, which are found to be more evident at room temperature. As example, two sets of representative 1D proton spectra obtained at 300° and 278° K at different times (0 and 18–21 h) from two samples of normal gastric mucosa are reported in Figure 23. They were all acquired using a water-presaturation sequence and are informative of small and large metabolites present in the tissue. The two spectra at t=0 (a and c) are similar, except for a different intensity of the signal at 3.72 ppm due to polyethylene glycol (PEG), used as an excipient in pharmaceutical preparations, and for a slightly better spectral resolution in the case of c). After almost 1 day, an increase in the signals of small metabolites, more evident at the higher work temperature (see b versus d), can be observed. These spectral changes are attributable to the increased mobility of some metabolites and to the partial disruption of subcellular structures, probably due to both temperature and spinning. Degradation symptoms only slightly affect the samples in the first hour of analysis and, in the view of future applications of HR-MAS with diagnostic purposes, they do not have to be

overemphasized. Nevertheless, these findings suggested to work at 278° K, especially to safely acquire 2D spectra, which are more time-consuming than the 1D ones.

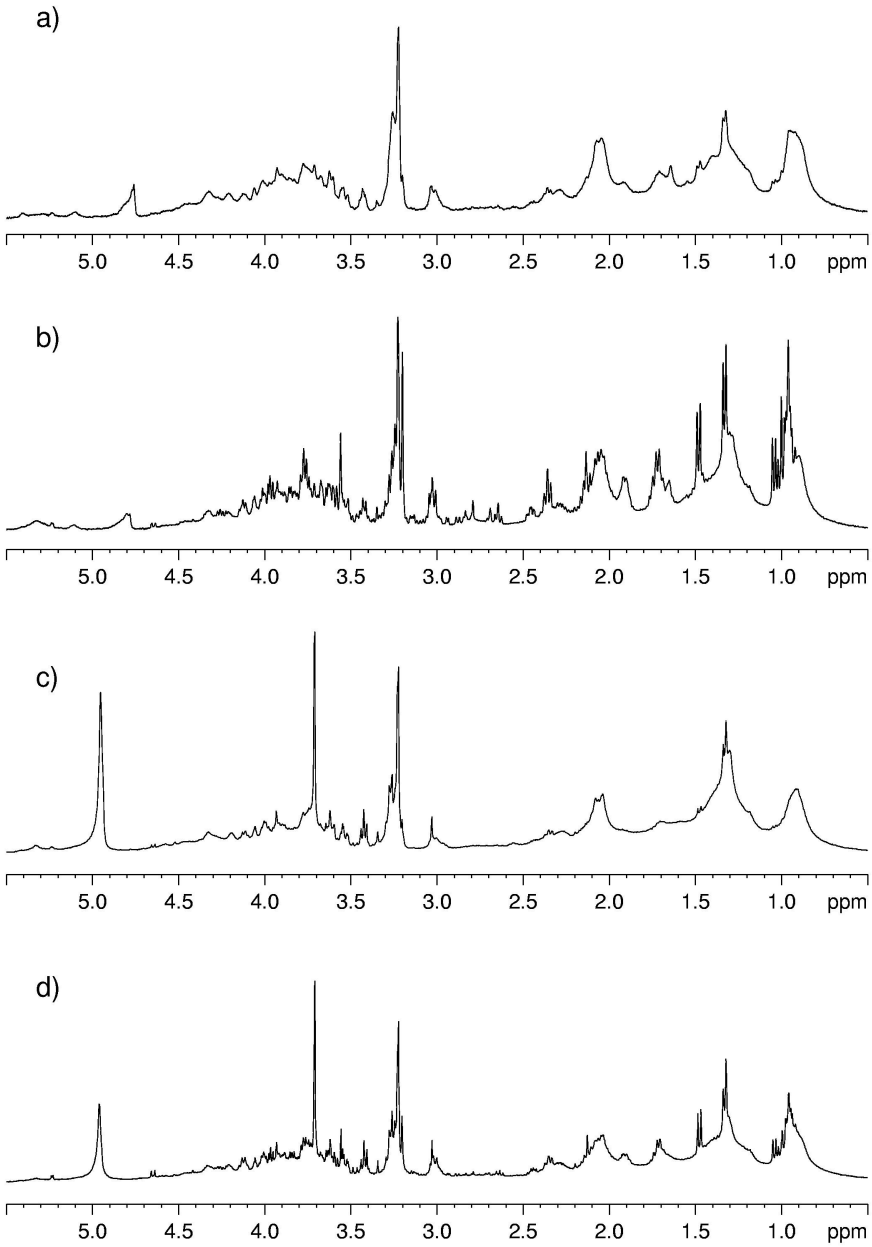

Figure 23. 1D water-presaturated ^{1}H NMR spectra of healthy gastric mucosa: a) sample 1 at 300° K, t = 0 h; b) sample 1 at 300° K, t = 21 h; c) sample 2 at 278° K, t = 0 h; d) sample 2 at 278° K, t = 18 h.

References

1. Kreis R. Quantitative localized ^{1}H MR spectroscopy for clinical use. *Prog. Nucl. Magn, Reson*. 1997; **31**: 155-195.
2. Rudkin TM, Arnold DL. MR Spectroscopy and the Biochemical Basis of Neurological Disease. *Magnetic resonance Imaging of the Brain and Spine* Atlas SW. (eds), Lippincott Williams & Wilkins, 2002; **35**, 2021-2040.
3. Smith ICP, Stewart LC. Magnetic resonance spectroscopy in medicine: clinical impact. *Prog. Nucl. Magn. Reson*. 2002; **40**: 1-34.
4. Rijpkema M, Schuuring J, van der Meulen Y, van der Graaf, Bernsen H, Boerman R, van der Kogel A, Heerschap A. Characterization of oligodendrogliomas using short echo time ^{1}H MR spectroscopic imaging. *NMR Biomed*. 2003; **16**: 12-18.
5. Tugnoli V, Tosi MR, Bertoluzza A, Barbarella G, Ricci R, Fini G. In vitro magnetic resonance spectroscopy of healthy and neoplastic brain tissues. *J. Mol. Struct*. 1999; **482-483**: 365-369.
6. Tosi MR, Tugnoli V, Bottura G, Lucchi P, Battaglia A, Giorgianni P, Ferri C, Mannini D, Reggiani A. In vitro MRS and HPLC studies on human renal cell carcinomas. *Oncol. Rep*. 2000; **7**: 1355-1358.
7. Tosi MR, Tugnoli V, Bottura G, Lucchi P, Battaglia A, Giorgianni P. Biochemical characterization of human renal tumors by in vitro nuclear magnetic resonance. *J. Mol. Struct*. 2001; **565-566**: 323-327.
8. Tosi MR, Tugnoli V, Bottura G, Lucchi P. Multinuclear magnetic resonance spectroscopy of human healthy and neoplastic renal tissues. *Appl. Spectr*. 2001; **55**: 908-912.
9. Tugnoli V, Tosi MR, Tinti A, Trinchero A, Bottura G, Fini G. Characterization of lipids from human brain tissues by multinuclear magnetic resonance spectroscopy. *Biopolymers (Biospectroscopy)* 2001; **62**: 297-306.
10. Tosi MR, Bottura G, Lucchi P, Reggiani A, Trinchero A, Tugnoli V. Cholesteryl esters in human malignant neoplasms. *Int. J. Mol. Med.* 2003; **11**: 95-98.
11. Tugnoli V, Bottura G, Fini G, Reggiani A, Tinti A, Trinchero A, Tosi MR. ^{1}H-NMR and ^{13}C-NMR lipid profiles of human renal tissues. *Biopolymers (Biospectroscopy)* 2003; **72**: 86-95.
12. Tosi MR, Reggiani A, Tugnoli V. Are molecular features of a chromophobic cell renal cell carcinoma correlated with clinical findings? *Int. J. Mol. Med.* 2003; **12**: 99-102.
13. Tosi MR, Trinchero A, Poerio A, Tugnoli V. Fast NMR evaluation of lipids in human tissues. *Italian J. Biochem*. 2003; **52**: 141-144.
14. Tugnoli V, Reggiani A, Beghelli R, Tomaselli V, Trinchero A, Tosi MR. Magnetic resonance spectroscopy and high performance liquid chromatography of neoplastic human renal tissues. *Anticancer Res*. 2003; **23**: 1541-1548.

15. Tosi MR, Fini G, Tinti A, Reggiani A, Tugnoli V. Molecular characterization of human healthy and neoplastic cerebral and renal tissues by in vitro ^{1}H NMR spectroscopy (review). *Int. J. Mol. Med.* 2002; **9**; 299-310.
16. Tugnoli V, Tosi MR, Barbarella G, Bertoluzza A, Ricci R, Trevisan C. In vivo ^{1}H MRS and in vitro multinuclear MR study of human brain tumors. *Anticancer Res.* 1996; **16**: 2891-2900.
17. Tugnoli V, Tosi MR, Barbarella G, Ricci R, Calbucci F, Bertoluzza A. In vitro and in vivo MRS study of human glioma metabolites. *Int. J. Oncol*. 1997; **11**: 319-324.
18. Barbarella G, Ricci R, Pirini G, Tugnoli V, Tosi MR, Bertoluzza A, Calbucci F, Leonardi M, Trevisan C, Eusebi V. In vivo single voxel ^{1}H MRS of glial brain tumors: correlation with tissue histology and in vitro MRS. *Int. J. Oncol*. 1998; **12**: 461-468.
19. Tugnoli V, Tosi MR, Barbarella G, Ricci R, Leonardi M, Calbucci F, Bertoluzza A. Magnetic resonance spectroscopy study of low grade extra and intracerebral human neoplasms. *Oncol. Rep*. 1998; **5**: 1199-1203.
20. Tosi MR, Ricci R, Bottura G, Tugnoli V. In vivo and in vitro nuclear magnetic resonance spectroscopy investigation of an intracranial mass. *Oncol. Rep*. 2001; **8**: 1337-1339.
21. Moka D, Vorreuther R, Schicha H, Spraul M, Humpfer E, Lipinski M, Foxall PJD, Nicholson JK, Lindon JC. Magic Angle Spinning Proton Nuclear Magnetic Resonance Spectroscopic Analysis of Intact Kidney Tissue Samples. *Anal. Commun*. 1997; **34**: 107-109.
22. Cheng LL, Chang IW, Louis DN, Gonzalez RG. Correlation of high-resolution magic angle spinning proton magnetic resonance spectroscopy with histopathology of intact human brain tumor specimens. *Canc. Res*. 1998; **58**: 1825-1832.
23. Cheng LL, Chang IW, Smith BL, Gonzalez RG. Evaluating human breast ductal carcinomas with high-resolution magic-angle spinning proton magnetic resonance spectroscopy. *J. Magn. Reson*. 1998; **135**: 194-202.
24. Tomlins AM, Foxall PJD, Lindon JC, Lynch MJ, Spraul M, Everett JR, Nicholson JK: High resolution magic angle spinning ^{1}N nuclear magnetic resonance analysis of intact prostatic hyperplastic and tumour tissues. *Anal. Commun*. 1998; **35**: 113-115.
25. Millis K, Weybright P, Campbell N, Fletcher JA, Fletcher CD, Cory DG, Singer S. Classification of Human Liposarcoma and Lipoma Using Ex Vivo Proton NMR Spectroscopy. *Magn. Res. Med.* 1999; **41**: 257-267.
26. Cheng LL, Anthony DC, Comite AR, Black PM, Tzika AA, Gonzalez RG. Quantification of microheterogeneity in glioblastoma multiforme with ex vivo high-resolution magic-angle spinning (HRMAS) proton magnetic resonance spectroscopy. *Neuro-oncology* 2000; **2**, 87-95.
27. Cheng LL, Wu C, Smith MR, Gonzalez RG. Non-destructive quantitation of spermine in human prostate tissue samples using HRMAS ^{1}H NMR spectroscopy at 9.4 T. *FEBS Lett.* 2001; **494**: 112-116.

28. Griffin JL, Williams HJ, Sang E, Nicholson JK. Abnormal lipid profile of dystrophic cardiac tissue as demonstrated by one- and two-dimensional magic-angle spinning (1)H NMR spectroscopy. *Magn. Reson. Med*. 2001; **46**: 249-255.
29. Shockcor JP, Holmes E. Metabonomic applications in toxicity screening and disease diagnosis. *Current Topics Med. Chem.* 2002; **2**: 35-51.
30. Rooney OM, Troke J, Nicholson JK, Griffin JL. High-resolution diffusion and relaxation-edited magic angle spinning ^{1}H NMR spectroscopy of intact liver tissue. *Magn. Reson. Med*. 2003; **50**: 925-930.
31. MG Swanson, Vigneron DB, Tabatabai ZL, Males RG, Schmitt L, Carroll PR, James JK, Hurd RE, Kurhanewicz J. Proton HR-MAS spectroscopy and quantitative pathologic analysis of MRI/3D-MRSI-targeted postsurgical prostate tissues. *Magn. Reson. Med*. 2003; **50**: 944-954.
32. Wang Y, Bollard ME, Keun H, Antti H, Beckonert O, Ebbels TM, Lindon JC, Holmes E, Tang H, Nicholson JK. Spectral editing and pattern recognition methods applied to high-resolution magic-angle-spinning ^{1}H nuclear magnetic resonance spectroscopy of liver tissues. *Anal. Biochem.* 2003; **323**: 26-32.
33. Sitter B, Bathen T, Hagen B, Arentz C, Skjeldestad FE, Gribbestad IS. Cervical cancer tissue charaterized by high-resolution magic angle spinning MR spectroscopy. *Magn. Reson. Mat. Phys. Biol. Med*. 2004; **16**: 174-181.
34. Cheng LL, Ma MJ, Becerra L, Ptak T, Tracey I, Lackner A, Gonzalez RG. Quantitative neuropathology by high resolution magic angle spinning proton magnetic resonance spectroscopy. *Proc. Nat. Acad. Sci. USA* 1997; **94**: 6408-6413.
35. Barton SJ, Howe FA, Tomlins AM, Cudlip SA, Nicholson JK, Bell BA, Griffiths JR. Comparison of *in vivo* ^{1}H MRS of human brain tumours with ^{1}H HR-MAS spectroscopy of intact biopsy samples *in vitro. Magn. Reson. Mat. Phys. Biol. Med*. 1999; **8**: 121-128.
36. Tzika AA, Cheng LL, Goumnerova L, Madsen JR, Zurakowski D, Astrakas LG, Zarifi MK, Scott RM, Anthony DC, Gonzalez RG, Black PM. Biochemical characterization of pediatric brain tumors by using in vivo and ex vivo magnetic resonance spectroscopy. *J. Neurosurg*. 2002; **96**: 1023-1031.
37. Sitter B, Sonnewald U, Spraul M, Fjösne HE, Gribbestad IS. High-resolution magic angle spinning MRS of breast cancer tissue. *NMR Biomed*. 2002; **15**: 327-337.
38. Levitt MH. *Spin Dynamics - Basics of Nuclear Magnetic Resonance,* John Wiley & Sons, Ltd. Chichester, 2002.
39. Derome AE. *Modern NMR Techniques for Chemistry Research*. Pergamon Press Ltd. Oxford, 1987.
40. Croasmun WR, Carlson RMK (eds. *Two-Dimensional NMR Spectroscopy Applications for Chemists and Biochemists*. 2nd edition, VCH Publishers, Inc., NY, 1994.

41. Breitmaier E, Voelter W. Carbon-13 NMR spectroscopy. *High-resolution methods and applications in organic chemistry and biochemistry.* Weinheim, VCH Publishers,1987.
42. Hu H, Shaka AJ. Composite pulsed field gradients with refocused chemical shifts and short recovery time. *J. Magn. Reson.* 1999; **136**:54–62.
43. Pretsch E, Bühlmann P, Affolter C. *Structure Determination of Organic Compounds - Tables of Spectral Data*. Springer-Verlag, Berlin, 2000.
44. Fan TWM. Metabolite profiling by one- and two-dimensional NMR analysis of complex mixtures. *Progr. Magn. Reson. Spectr*. 1996; **28**: 161-219.
45. Willker W, Engelmann J, Brand A, Leibfritz D. Metabolites Identification in Cell Extracts and Culture Media by Proton-detected 2D-H,C-NMR Spectroscopy. *J. Magn. Res. Anal.* 1996; **2**: 21-32.
46. Bentrude WG, Setzer WN, in *Phosphorus-31 NMR Spectroscopy in Stereochemical Analysis*, , Verkade JG, Quin LD (eds), VCH Publishers, Inc. NY. 1987.
47. Gorenstein DG, Shah DO, in *Phosphorus-31 NMR*, D. G. Gorenstein (ed.), Academic Press, Inc. NY, 1984.
48. Andrew ER, Bradbury A, Eades RG. Removal of dipolar broadening of nuclear magnetic resonance spectra of solids by specimen rotation. *Nature,* 1959; **183**: 1802–1803.
49. Stejskal EO, Schaefer J, Waugh JS. Magic-angle spinning and polarization transfer in proton-enhanced NMR. *J. Magn. Reson.* **1977**; **28**: 105–112.
50. Andrew ER, Bradbury A, Eades RG. Removal of dipolar broadening of nuclear magnetic resonance spectra of solids by specimen rotation. *Nature* 1959; **183**: 1802-1803.
51. Lowe IJ. Free induction decays of rotating solids. *Phys. Rev. Lett.* 1959; **2**: 285-287.
52. Tugnoli V, Schenetti L, Mucci A, Nocetti L, Toraci C, Mavilla L, Basso G, Rovati R, Tavani F, Zunarelli E, Righi V, Tosi MR. A comparison between in vivo and ex vivo HR-MAS ^{1}H MR spectra of a pediatric poster fossa lesion. *Int. J. Mol. Med.* 2005; **16**: 301-307.
53. Sitter B, Bathen T, Hagen B, Arentz C, Skjeldestad FE, Gribbestad IS. Cervical cancer tissue characterized by high-resolution magic angle spinning MR spectroscopy. *MAGMA.* 2004; **16**: 174-181.
54. Martinez-Granados B, Monleon D, Martinez-Bisbal MC, Rodrigo JM, del Olmo J, LluCh P, Ferrandez A, Marti-Bonmati L, Celda B. Metabolite identification in human liver needle biopsies by high-resolution magic angle spinning 1H NMR spectroscopy. *NMR Biomed*. 2006; **19**: 90-100.
55. Beckonert OP, Nicholson JK, Lindon JC. High resolution magic angle spinning and MR spectroscopy of tumor tissues: Techniques and Applications. In: *Nuclear Magnetic Resonance Spectroscopy in the Study of Neoplastic Tissues*. Tosi R, Tugnoli V, (eds). Nova Science Publisher Inc., New York, 2005, 397-437.

56. Duarte IF, Stanley EG, Holmes E, Lindon JC, Gil AM, Tang H, Ferdinand R, McKee CG, Nicholson JK, Vilca-Melendez H, Heaton N, Murphy GM. Metabolic assessment of human liver transplants from biopsy samples at the donor and recipient stages using high-resolution magic angle spinning 1H NMR spectroscopy. *Anal. Chem.* 2005; **77**: 5570-5578.
57. Li W, Lee REB, Lee RE, Li J. Methods for acquisition and assignment of multidimensional high-resolution magic angle spinning NMR of whole cell bacteria. *Anal. Chem.* 2005; **77**: 5785- 5792.
58. Martinez-Bisbal MC, Marti-Bonmati L, Piquer J, Revert A, Ferrer P, Llàcer JL, Piotto M, Assemat O, Celda B. ^{1}H and ^{13}C HR-MAS spectroscopy of intact biopsy samples *ex vivo* and *in vivo* 1H MRS study of human high grade gliomas. *NMR Biomed.* 2004; **17**: 191-205.
59. Sitter B, Autti T, Tyynelae J, Sonnewald U, Bathen TF, Puranen J, Santavuori P, Haltia MJ, Paetau A, Polvikoski T, Gribbestad IS, Haekkinen AM. High-resolution magic angle spinning and ^{1}H magnetic resonance spectroscopy reveal significantly altered neuronal metabolite profiles in CLN1 but not in CLN3. *J. Neurosci. Res.* 2004; **77**: 762-769.
60. Tzika AA, Astrakas L, Cao H, Mintzopoulos D, Andronesi OC, Mindrinos M, Zhang J, Rahme LG, Blekas KD, Likas AC, Galatsanos NP, Carroll RS, Black PM. Combination of high-resolution magic angle spinning proton magnetic resonance spectroscopy and microscale genomics to type brain tumor biopsies. *Int. J. Mol. Med.* 2007; **20**: 199-208.
61. HolmesE, Tsang TM, Tabrizi SJ. The Application of NMR-Based Metabonomics inNeurological Disorders. *J. Amer. Soc. Exper. NeuroTherapeutics* 2006; **3**: 358–372.
62. Wang Y, Holmes E, Comelli EM, Fotopoulos G, Dorta G, Tang H, Rantalainen MJ, Lindon JC, Corthésy-Theulaz IE, Fay LB, Kochhar S, Nicholson JK. Topographical variation in metabolic signatures of human gastrointestinal biopsies revealed by high-resolution magic-angle spinning 1H NMR spectroscopy. *J. Proteome Res.* 2007; **6**: 3944-3951.
63. Yang Y, Li C, Nie X, Feng X, Chen W, Yue Y, Tang H, Deng F. Metabonomic studies of human hepatocellular carcinoma using high-resolution magic-angle-spinning ^{1}H NMR spectroscopy in conjunction with multivariate data analysis. *J. Proteome Res*. 2007; **6**: 2605-2614.
64. Opstad KS, Bell BA, Griffiths JR, Howe FA. An investigation of human brain tumour lipids by high-resolution magic angle spinning (1)H MRS and histological analysis. *NMR Biomed*. 2008 **9**:
65. Waters NJ, Garrod S, Farrant RD, Haselden JN, Connor SC, Connelly J, Lindon JC, Holmes E, Nicholson JK. High-Resolution Magic Angle Spinning ^{1}H NMR Spectroscopy of Intact Liver and Kidney: Optimization of Sample Preparation Procedures and Biochemical Stability of Tissue during Spectral Acquisition. *Anal. Biochem.* 2000; **282**: 16-23.
66. Hu JZ, Wind RA. The evaluation of different MAS techniques at low spinning rates in aqueous samples and in the presence of magnetic susceptibility gradients. *J. Magn. Reson.* 2002; **159**: 92-100.

67. Wu CL, Taylor JL, He W, Zepeda AG, Halpern EF, Bielecki A, Gonzalez RG, Cheng LL. Proton high-resolution magic angle spinning NMR analysis of fresh and previously frozen tissue of human prostate. *Magn. Reson. Med*. 2003; **50**: 1307-1311.
68. Michaelis T, Helms G, Frahm J. Metabolic Alterations in Brain Autopsies: Proton NMR Identification of Free Glycerol. *NMR Biomed*. 1996; **9**: 121-124.
69. Petroff OAC, Ogino T, Alger JR. High-Resolution Proton Magnetic Resonance Spectroscopy of Rabbit Brain: Regional Metabolite Levels and Postmortem Changes. *J. Neurochem*. 1988; **51**: 163-171.
70. Middleton DA, Bradley DP, Connor SC, Mullins PG, Reid DG. The effect of sample freezing on proton magic-angle spinning NMR spectra of biological tissue. *Magn. Reson. Med.* 1998; 40: 166-169.
71. Price WS. Water signal suppression in NMR spectroscopy. *Annual Reports on NMR Spectroscopy*.Webb GA ed. Academic Press, London. 1999; 290-354.
72. Meiboom S, Gill D. Modified spin-echo method for measuring nuclear relaxation times. *Rev. Sci. Instrum.* 1958; **20**: 688-691.
73. Wu DH, Chen A, Johnson CS. An improved diffusion-ordered spectroscopy experiment incorporating bipolar-gradient pulses. *J. Magn. Reson. Series A* 1995; 115: 260-264.
74. Aue WP, Bartholdi E, Ernst RR. Two-dimensional spectroscopy. Application to nuclear magnetic resonance. *J. Chem. Phys.* 1976; **64**: 2229-2246.
75. Bax A, Davis DG. MLEV-17-based two-dimensional homonuclear magnetization transfer spectroscopy. *J. Magn. Res.* 1985; **65**: 355-360.
76. Braunschweiler L, Ernst RR. Coherence transfer by isotropic mixing: application to proton correlation spectroscopy. *J. Magn. Reson.* 1983; **53**: 521-528.
77. Bodenhausen G, Freeman R, Turner DL. Two-dimensional J spectroscopy: Proton-coupled carbon-13 NMR. *J. Chem. Phys*. 1976; **65**: 839-840.
78. Bodenhausen G, Ruben DJ. Natural abundance nitrogen-15 NMR by enhanced heteronuclear spectroscopy. *Chem. Phys. Lett*. 1980; **69**: 185-189.
79. Jeener J. Pulse Pair Techniques in High Resolution NMR. *Ampere International Summer School*, Basko Polje, Yugoslavia. 1971.
80. Aue WP, Bartholdi E, Ernst RR. Two-dimensional spectroscopy. Application to nuclear magnetic resonance. *J. Chem. Phys.* 1976; **64**: 2229-2246.
81. Kumar A, Wagner G, Ernst RR, Wüthrich K. Studies of J-connectives and selective ^{1}H-^{1}H Overhauser effects in H_2O solutions of biological macromolecules by two-dimensional NMR experiments. *Biochem. Biophys. Res. Commun.* 1980; **96**: 1156-1163.
82. Braunschweiler L, Ernst RR. Coherence transfer by isotropic mixing: application to proton correlation spectroscopy. *J. Magn. Reson.* 1983: **53**: 521-528.

83. A. Bax, D. G. Davis: MLEV-17-based two-dimensional homonuclear magnetization transfer spectroscopy. *J. Magn. Res.* **1985**, *65*, 355-360.
84. Müller L, Ernst RR. Coherence transfer in the rotating frame. Application to heteronuclear cross-correlation spectroscopy. *Mol. Phys*. 1979; **38**: 963-992.
85. A. Bax, R. H. Griffey, B. L. Hawkins: Correlation of proton and nitrogen-15 chemical shifts by multiple quantum NMR. *J. Magn. Reson.* 1983; **55**: 301-315.
86. Bodenhausen G, Ruben DJ. Natural abundance nitrogen-15 NMR by enhanced heteronuclear spectroscopy. *Chem. Phys. Lett*. 1980; **69**: 185-189.
87. Bax A, Summers MF. Proton and carbon-13 assignments from sensitivity-enhanced detection of heteronuclear multiple-bond connectivity by 2D multiple quantum NMR. *J. Am. Chem. Soc.* 1986; **108**: 2093-2094.
88. Morris GA, Freeman R. Enhancement of nuclear magnetic resonance signals by polarization transfer. *J. Am. Chem. Soc.* 1979; **101**: 760-762.
89. Shaka AJ, Barker PB, Freeman R. Computer-optimized decoupling scheme for wideband applications and low-level operation. *J. Magn. Reson*. 1985; **64**: 547-552.
90. Willker W, Leibfritz D, Kerssebaum R, Bermel W. Gradient selection in inverse heteronuclear correlation spectroscopy. *Magn. Reson. Chem.* 1993; **31**: 287-292.

Chapter 3

MULTIVARIATE DATA ANALYSIS

GENERAL INTRODUCTION

The data collected in science, technology, and almost everywhere else are *multivariate*, with multiple variables measured on multiples samples or at multiple time points (1-14). Multivariate data, accurately obtained on intelligently selected observations and variables, contain much more information than univariate data and, for this reason, an adequate multivariate characterization is a necessary first step in the investigation in both basic research and applied technology. Multivariate Data Analysis (MVDA) results have to be interpreted and related to the objectives of the investigation and the scientific-technical context. Nowadays, tables and data are abundant in all parts of research and development and the high quantity of data necessitates the use of appropriate analytical tools for extracting significant information from the large amount of raw data, capturing the systematic variation without throwing away useful notions intrinsic to the original nature of the experimental data set (14-17).

Pattern-recognition tools are an important part of the process of metabolomics and are being used to fully analyse the large multivariate data sets that are produced by other '-omic' technologies (18-20). Both supervised and unsupervised techniques (Figure 1) can be used to derive metabolic profiles. Supervised techniques use the information of class membership, such as disease status, to classify a given data set and therefore should be tested by data that are not used to build the pattern-recognition model. To investigate the innate variation in a data set in an unsupervised manner, techniques such as principal components analysis or hierarchical cluster analysis have been applied. However, in situations in which specific questions are being posed, supervised techniques might be more appropriate to either force classification (such as in determining which metabolites distinguish between groups) or regress a pattern against a trend (such as correlating a temporal progression with metabolic changes). Methods for supervised pattern recognition include for example prediction to latent structures through partial least squares (PLS). For all the supervised techniques it is necessary to test the sensitivity and reproducibility of the models produced, although the biological function of the metabolites identified can also indicate the success of the particular pattern-recognition tool.

Multivariate data analysis was applied to different types of high resolution ^{1}H NMR data ranging from 1D or 2D spectra. Several new approaches to data analysis of NMR data

have been studied and compared (21,22).

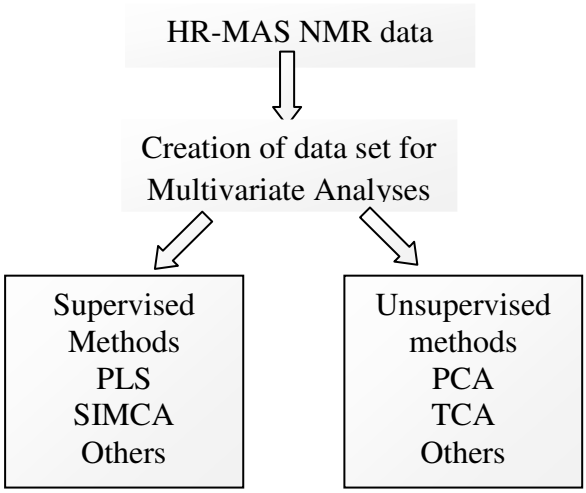

Figure 1. Exemple of chemometric methods that can be utilized during the analysis of HR-MAS NMR spectral data. (PLS: partial least squares, SIMCA: soft independent modeling of class analogies, PCA principal components analysis, TCA: tree cluster analysis.)

In particular we combined ^{1}H NMR data obtained with HR-MAS spectra and advanced chemometrics methods including multi-way methods in attempting to enhance the interpretation and to obtain quantitative information on the biological tissue samples. This combination seems to be very useful for the extraction of relevant information for the study of human diseases.

In particular I utilised two multivariate projection methods:

- Principal Components Analysis, PCA.
- Partial Least Squares-Discriminant Analysis PLS-DA, that is a variant of PLS, projections to latent structures (23).

One of the remarkably simple approach to multivariate data analysis is based on the so-called *projection methods.* This approach represents the "case" as a swarm of points in a K-dimensional space (K = number of variables), and then projects the point swarm down onto a lower dimensional plane or hyper-plane. The coordinates of the points on this hyper-plane provide a compressed representation of the observations, and the direction vectors of the

hyper-plane provide a corresponding representation of the variables (24). The projection approach can be adapted to a variety of data-analytical objectives and to any shape of multivariate values.

In the early stage of a project, when little is known about a problem, a simple overview of the information in a data table is often required. Such an overview can be obtained with principal components analysis, which produces a summary showing how the observations are related and if there are any deviating observations or groups of observations in the data. In addition, PCA is also able to describe the relationship among the measured variables: which variables contribute similar information to the PCA model, and which provide unique information about the observations. In other words, PCA describes the correlation structure of a matrix **X** (N x K), in which observations, N_i, are arranged in rows and variables, K_i, in columns. Often, an initial PCA of a data set reveals groupings among observations and this may indicate the need for further PCA modelling of each such group (*class*) in order to fine-tune the analysis and to understand the characteristic features of the different groups. Then, the last stage of data analysis could be represented by the regression modelling between two blocks of data, usually denoted **X** and **Y**, with the aim of predicting **Y** from **X** for new observations. This kind of modelling is accomplished with the PLS method. In process modelling and monitoring the **X**-*factors* or *predictors* are the signals which are frequently sampled, at regular time intervals, to monitor the status of the process, whereas the **Y**-*responses* mirror properties like yield or quality of a product, and which are measured less frequently (23).

Principal Components Analysis

Principal components analysis forms the basis for multivariate data analysis. As shown in Figure 2, the starting point for PCA is a matrix of data with N rows (*observations*) and K columns (*variables*), here denoted by **X**.

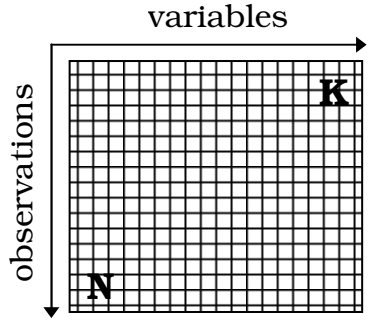

Figure 2. Schematic representation of a data matrix **X**.

The observations can be analytical samples, chemical compounds or reactions, process time points of a continuous process, batches from a batch process, and so on. Variables may be spectra or chromatographic signals (NIR, MIR, UV, etc.), parameters like temperatures, pressures, flows curves, etc.

As previously mentioned, the most important use of PCA is indeed to represent a multivariate data set as a low dimensional plane, usually consisting of 2 to 5 dimensions, such that an overview of the data is obtained. Statistically, PCA finds lines, planes and hyper-planes, in the K-dimensional space that approximate as well as possible in the least squares sense the original data. This means that a line or plane, that is the least squares approximation of a set of data points, makes the variance of the co-ordinates on the line or plane as large as possible. In particular, principal components analysis is able to decompose the initial matrix **X** (*N* x *K*) into a small number of components, *J*:

$$\mathbf{X} = \mathbf{A}\mathbf{P}^{\mathbf{T}} + \mathbf{E}$$

where **A** (*N* x *J*) is the *score* matrix, **P** (*J* x *K*) is the *loading* matrix and both describe the systematic variation within the **X** data, and **E** is the stochastic component or, simpler, the residual matrix.

These new matrices, **A** and **P**, can be analyzed graphically by means of two plots, the *score* and the *loading* ones. The score plot is a summary of the relationships among the observations and shows how they are projected in the new low dimensional hyper-plane. The loading plot is a similar summary of the variables and displays the relationships among them in the new PCs space. The two plots are complementary and super imposable, and a direction in one plot corresponds to the same direction in the other one. This means that an interesting pattern seen in the score plot can be interpreted by looking along that interesting direction in the loading plot. An important aspect of any PCA application is the choice of *J*, *i.e.* the number of components to be used in order to obtain a model representative of the real system. Several tests for determining the optimal value have been developed (25). Among them, *cross-validation (CV)*, the one employed in this work, is a useful tool to chose the correct number of components to use and it provides more realistic residuals than those obtained by ordinary residuals of the fitted model. It consists of an internal resembling method. In particular, one, *venetian blind*, or some samples are left out at time and the model is built up again on the remaining data value. The model is used to predict the left out samples. The procedure is iteratively repeated until each data value has been left out once. The estimation

of the "internal" prediction is expressed through the Root Mean Square Error in Cross-Validation, RMSECV, and the percent of captured variance by the model in cross-validation, R^2_{CV}, computed respectively by (1):

$$RMSECV = \sqrt{\frac{1}{n-1}\sum_{i=1}^{n}\sum_{j=1}^{k}\left(\hat{x}_{ij} - x_{ij}\right)^2} \qquad R^2_{CV} = 1 - \frac{\sum_{i=1}^{n}\sum_{j=1}^{k}\left(\hat{x}_{ij} - x_i\right)^2}{\sum_{i=1}^{n}\sum_{j=1}^{k}\left(x_{ij} - \bar{x}_j\right)^2}$$

where n is the number of objects, k is the number of variables, $\hat{x}_{ij}$ is the predicted value of variable j for the i-left out sample, x_{ij} is the i-row value of the **X** original data and $\bar{x}_j$ is the average value over samples for variables j. The lower the RMSECV and the higher R^2_{CV}, the better the prediction ability of the model is. Nevertheless, the right compromise between RMSECV and the cumulative variance explained by the model in fit has to be chosen. Furthermore, where scores and loadings are examined graphically, it is usually possible to assess if a component is meaningful or not from visual inspection.

Partial Least Squares-Discriminant Analysis

All PLS methods build a regression model between two blocks (data matrices) independent variables (**X**) and dependent variables (**Y)** using as a representation of these matrices latent variables calculated so that they explain the directions of maximum covariance. **Y** can be a vector (in PLS1) or a matrix (in PLS2). The general equation of all inverse calibration methods as PLS is:

Y_XB (2)

where **X** and **Y** are represented by their latent variables and **B** contains the determined regression coefficients in the calibration step. Different algorithms have been developed to calculate PLS models (26-29).

PLS-DA is a variant of PLS used as a classification tool (30,32).

Finally, prior to PCA and PLS-DA analyses, data are pre-treated, in order to transform them into a form suitable for the analysis. Sometimes, pre-processing techniques can make difference between a useful model and no model at all. There are several kind of pre-processing that can be used depending on the nature and properties of the data sets. Among the various pre-processing tools available, *mean-centering* of data and *block-scaling*, which

are the pre-treatments used during my work, are briefly described.

Mean-centering

Mean-centering is a pre-treatment generally used to eliminate the systematic local difference between objects. With mean-centering the average value of each variable is calculated and then subtracted from the data (24).

$$x_{n,k}^{cent} = x_{n,k} - \sum_{k=1}^{K} \frac{x_{n,k}}{K}$$

This simply corresponds to moving the system coordinates in the origin of the multivariate space, conserving, at the same time, the geometry, i.e. the real information contained in the initial data matrix.

Block-Scaling

When there is the risk of dramatically up-weighting components present in very small amounts and showing little variation (such as spectral background or baseline) working with unscaled X arrays is preferable. However, *e.g.* when there are some compounds at concentration at least of one order to of magnitude higher with respect to every other components comparable influence in the data analyses (32). In order to do this, different blocks of variables are defined and Block-scaling (32) is accomplished. For multi-way arrays Block-scaling, *e.g.* within the second mode (variables mode) is accomplished by rearranging the three-way array to a bideimensional IK x J matrix and then weighting each variable belonging to the same block by:

$$wj_B = \sqrt{SS_{TOT}/SS_{BLOCK} \cdot n_{BLOCK}}$$

where SS_{TOT} is the total sum of squares over all J's variables, SS_{BLOCK} is the sum of squares over the J's variables belonging to the given block and n_{BLOCK} is the number of defined blocks. Also in the block-scaling case, the same general considerations drawn for scaling hold. In fact, the only difference between autoscaling and block-scaling is the definition of the weighting factor not how it is applied.

References

1. Smilde A, Bro R, Geladi P. Multi-way analysis. *Application in the chemical sciences.* WILEY, John Wiley & Sons, Ltd, England, 2004.
2. Wold S, Sjöström M. .Chemometrics, present and future success *Chemom. Intell. Lab. Syst.* 1998; **44**: 3-14.
3. Munck L, Nørgaard L. Chemometrics in food science: a demonstration of the feasibility of a highly exploratory, inductive evaluation strategy of fundamental scientific significance *Chemom. Intell. Lab. Syst.* 1998; **44**; 31-60.
4. Devos A, Simonetti AW, van der Graaf M, Lukas L, Suykens JAK, Vanhamme L, Buydens LMC, Heerschap A, van Huffel S. The use of multivariate MR imaging intensities versus metabolic data from MR spectroscopic imaging for brain tumour classification *J. Magn. Reson.* 2005; 173: 218-228.
5. Brown M, DunnWB, Ellis DI, Goodacre R, Handl J, Knowles JD, Hagan SO, Spasic' I, Kell DB. A metabolome pipeline:from concept to data to knowledge. *Metabolomics.* 2005; **1**: 39.
6. Nguyen V, Rocke DMtumor classification by partial least quares using micro aray gene expression data. *Bioinformatics*. 2002; **18**: 39-50.
7. Nilsson J, De Jong S, Smilde AK. Multi-way calibration in 3D QSAR. *J. Chemom.* 1997; **11**: 511-524.
8. Dyrby M, Petersen M, Whittaker AK, Lambert L, Nørgaard L, Bro R, Engelsen SB. Analysis of lipoproteins using 2D diffusion-edited NMR Spectroscopy and multiway chemometrics. *Anal. Chim. Acta*. 2005; **531**: 209-216.
9. Garcia I, Sarabia L, Cruz Ortiz M, Aldama JM. Three-way models and detection capability of a gas chromatography-mass spectrometry method for the determination of clenbuterol in several biological matrices: the 2002/657/EC European Decision. *Anal. Chim. Acta.* 2004; **515**: 55-63.
10. Baunsgaard D, Nørgaard L, Godshall MA. Specific screening for colour precursors and colorant in beet and cane sugar liquors in relation to model colorants using spectrofluorimetry evaluated HPLC and multiway analysis. *J. Agriculture and Food Chem.* 2001; **49**: 1687-1694.
11. Bro R. Exploratory study of sugar production using fluorescence spectroscopy and multiway analiyis. *Chemom. and Intell. Lab. Syst.* 1998: **46**: 133-147.
12. Gurden SP, Westerhuis JA, Smilde AK. Monitoring of batch processes using spectroscopy. *AIChE Journal.* 2002; **48**: 2283-2295.
13. Theodora K, Nomikos P, MacGregor JF. Analysis, monitoring and fault diagnosis of bacth processes using multiblock and multi-way PLS. *J. Proc. Control*. 1997; **5**: 277-284.
14. Pravdova V, Boucon C, De Jong S, Walczak B, Massart DL. Three-way principal components analysis applied to food analysis: an example. *Anal. Chim. Acta*. 2002; **462**: 133-148.

15. Bro R. Multivariate calibration: What is in chemometrics for the analytical chemist? *Anal. Chim. Acta*. 2003; **500**: 185-194.
16. .Bodecchi LM, Cocchi M, Malagoli M, Manfredini M, Marchetti A. Application of infrared spectroscopy and multivariate quality control methods in PVC manufacturing *Anal. Chim. Acta*. 2005; **554**: 207-217.
17. Cocchi M, Durante C, Grandi M, Lambertini P, Manzini D, Marchetti A. Simultaneous determination of sugars and organic acids in aged vinegars and chemometric data analysis. *Talanta*. 2006; **69**: 1166.
18. Trygg J, Holmes E, Lundstedt T. Chemometrics in metabonomics. *J. Proteome Res.* 2007; **6**: 469-479.
19. Lindon, JC, Holmes E, Nicholson JK. Pattern recognition methods and applications in biomedical magnetic resonance. *Prog. Nuc. Magn. Reson*. 2001; **39**: 1-40.
20. Valafar F. Pattern recognition techniques in microarray data analysis. *Ann. NY Acad. Sci*. **980**, 41–64 (2002).
21. Cloarec O, Dumas ME, Trygg J, Craig A, Barton RH, Lindon JC, Nicholson JK, Holmes E. Evaluation of the orthogonal projection on latent structure model limitations caused by chemical shift variability and improved visualization of biomarker changes in 1H NMR spectroscopic metabonomic studies. *Anal Chem* 2005; **77**: 517-526.
22. Cloarec O, Dumas ME, Craig A, Barton RH, Trygg J, Hudson J, Blancher C, Gauguier D, Lindon JC, Holmes E Nicholson J. Statistical total correlation spectroscopy: an exploratory approach for latent biomarker identification from metabolic 1H NMR data sets. *Anal Chem* 2005; **77**:1282-1289.
23. Wold S, Albano C, Dunn WJ, Edlund U, Esbensen K, Geladi S, Helberg E, Johansson W, Lindberg W, Sjöström. Multivariate data analysis in Chemistry. *Chemometrics: Mathematics and Statistics in Chemistry.* B.R. Kowalski (ed). Reidel D. Publishing Company, Dordrecht, Holland, 1984.
24. Eriksson L, Johansson E, Kettaneh-Wold N, Trygg J, Wikström C, Wold S. *Multi- and Megavariate Data Analysis. Basic Principles and Applications.* Umetrics AB. 2006; 44-47
25. Malinoski ER. *Factor Analysis in Chemistry*. Second ed. Wiley, New York. 1991.
26. Boardman AE, Hui BS, Wold H. The partial least-squares fix point method of estimating interdependent systems with latentvariables. *Commun Statistics Theory Methods.* 1981; **10**: 613-639.
27. de Jong S. Simpls an alternative approach to partial least-squares regression. *Chemom. Intell. Lab. Sys*t. 1993; **18**: 251-263.
28. Wold S, Martens H, Wold H. The multivariate calibration-problem in chemistry solved by the PLS method. *Lecture Notes Math*. 1983; **973**: 286-293.

29. Esbensen KH. Multivariate data analysis-in practice. An introduction to multivariate data analysis and experimental design. Oslo. CAMO. 2000.
30. Briandet R, Kemsley EK, Wilson RH. Discrimination of Arabica and Robusta in instant coffee by Fourier transform infrared spectroscopy and chemometrics. *J Agri Food Chem* 1996; **44**: 170-174.
31. Barker M, Rayens W. Partial least squares for discrimination. *J Chemom*. 2003; **17**: 166-173.
32. Wold S, Johansson E, Cocchi M. 3D QSAR in drug design: theory, methods and applications, Hugo Kubinyi, ESCOM Science Publischer, Leiden. 1993; p.523.

Chapter 4

BRAIN TUMOURS

GENERAL INTRODUCTION

The clinical presentation of brain tumors varies greatly depending on tumor type and location. Seizure, hemiplegia, visual or hearing loss, diploidia, headache are common neurologic findings related to reised intracranial pressure. Neuroradiologic techniques represent the main tool in the diagnosis of brain tumours. Computed Tomography (CT) and digital angiography, have been widely used for clinical diagnoses and continue useful for tumors screening and for definition of calcified lesion. The advent of MRI greatly improved tumor characterization. The MRI technique is adequate for morpho-anatomical description, but it specificy is low (1). The information obtained from tomography and MRI examinations provide a precise histology in the majority of cases, non-distinctive images can be found difficulties in differentiation between malignant tumors and tipical benign tumor or abscess. This demonstrates the need for additional tools enabling non invasive histological diagnosis of a cranial lesion with a significantly higher degree of certainty than attainable from imaging modalities. There is a growing body of evidence that ^{1}H NMR (or MRS) may contribute to the clinical evaluation of a number of pathologies and/or therapeutically induced changes in metabolite concentrations (2). *In vivo* MRS is a non-invasive method to detect the biochemical changes accompanying the disease. The clinical impact of MRS in medicine has been widely reviewed by Smith *et al* (3) and shows promise as a method to complement routine diagnostic investigation. However, the *in vivo* method suffers from some internal and external limitations that may strongly influence the results (4,5). In particular the poor *in vivo* spectral resolution leads to limited characterization of the real biochemical composition of explored tissue. Moreover, even among metabolites that are detectable with *in vivo* MRS, subtle concentration differences between normal and pathological tissue, such as a neoplasm, can go unnoticed and result in a diagnostic error. The detailed biochemical picture of tissue is the basis of correct interpretation by *in vivo* MRS, and can be used when the molecular markers are well established. A deep knowledge of the biochemical composition of tissue have been obtained by spectroscopic analysis on extracts obtained from tissue (*in vitro* MRS). The analysis is generally carried out of chemical extracts of tissue samples because the extraction procedure produces a homogenous, macromolecule-free solution with a low viscosity, which yields narrow, well-resolved ^{1}H NMR spectra. Consequently, a large number of cellular metabolic databases have been compiled from ^{1}H NMR studies of extracted tissues (6-9). Nevertheless, there are potential problems in the use of extracts. One drawback is that

histopathological structures are not preserved prohibiting pathological analysis of the same sample. Another disadvantage is that important molecular components may be lost by the extraction procedure. Nowadays, the biochemical composition of tissue can be obtained by spectroscopic analysis directly from tissue specimens through *ex vivo* HR-MAS NMR. The HR-MAS technique is a powerful analytical tool introduced in 1997 for the study of human tissue, potentially bridging the divide between *in vitro* and *in vivo* MRS. *Ex vivo* HR-MAS might help for brain tumor diagnosis. Cheng *et al.* (10) demonstrated that proton magnetic resonance spectroscopy (^{1}H MRS) with HR-MAS can preserve tissue histopathology features while producing well-resolved spectra of cellular metabolites. HR-MAS can be very helpful for the assignment of the resonances *in vivo* of human brain cancer.

Classification of Brain Tumor

Brain tumour are the most frequent cause of death for CNS (Central Nervous System) pathology after stroke. The overall incidence of primary and secondary brain tumors in the European countries and in the United State is approximately 16 new case/100000 persons per year, with only slight variations among the different regions in the world and among different races (11-14). Primary intar-cranial tumor account for about 5-10% of all neoplasms. They represent the second most frequent category of tumors in young children after blood malignancies; as a metter of fact primary brain tumors show a first peak of incidence between 0 and 4 year, then decrease from 15 to 24 years and subsequently a steady rise that reaches a plateau between 65 and 79 years.

Intra-cranial tumors represent a complex and heterogeneus group of neoplastic lesions. They include primary and secondary tumors of the encephalon, tumors arising from meninges, hypophysal and pineal glands, cranial nerves and intracranial blood vessels, from the skull and embryonic vestiges. Since this great and complex variety of neoplastic lesions, many classifications have been proposed, each based on a different criterion and conceived with a distinctive purpose. Brain tumors can be classiefied on their pathological, epidemiological, prognostic, topographic or neuroradiological features. However, the simplest way to categorize intra-cranial neoplasms is to distinguish between primary brain neoplasms and metastatic tumors. Brain metastase are more common than primary brain tumors since metastatic spread of the tumor to the brain and its coverings from extra-cranial sites (lung, breast, gastrointestinal, melanoma, etc.) is a relatively common occurrence, with intra-cranial metastases found in up to 24% of all patients who die from cancer. Among primary brain

neoplasms, the classification that is usually referred to, is the one proposed by the World Health Organization (WHO), which relies on the cellular origin of each tumor type and distinguishes among five different main groups: tumor originating from neuro-epitelial cells (gliomas, ependymal tumors, choroida plexus tumors, neuronal ,neoblastic, pineal and embryonic tumors), tumors arising from cranial and spinal nerves, from meningis, from lymphatic and haemathopoietic tissue and from germ cells (15,16). This new classification considers not only the clinical course and histological appearance of neoplasms but also their immunophenotypic features and molecular and cytogenetic profile, which are more likely to correlate with MRS metabolic patterns rather than with conventional MRI.

References

1. Falini A, Politi LS, Vezzulli P. Clinical Applications of MR Spectroscopy in Neuroncology. In *Nuclear Magnetic Resonance Spectroscopy in the study of Neoplastic Tissue.* Tosi R, Tugnoli V, (eds). Nova Science Publisherets, Inc. New York, 2005; 59-93.
2. Sokol M. High Resolution NMR Studies of Brain Tumors. In *Nuclear Magnetic Resonance Spectroscopy in the study of Neoplastic Tissue.* Tosi R, Tugnoli V, (eds). Nova Science Publisherets, Inc. New York, 2005; 167-210.
3. Smith ICP, Stewart LC. Magnetic resonance spectroscopy in medicine: clinical impact. *Prog. Nucl. Magn. Reson. Spect.* 2002; **40**: 1-34.
4. Martinez-Bisbal MC, Marti-Bonmati L, Piquer J, Revert A, Ferrer P, Llàcer JL, Piotto M, Assemat O, Celda B. ^{1}H and ^{13}C HR-MAS spectroscopy of intact biopsy samples *ex vivo* and *in vivo* 1H MRS study of human high grade gliomas. *NMR Biomed.* 2004; **17**: 191-205.
5. Poullet JB, Martinez-Bisbal MC, Valverde D, Monleon D, Celda B, Arus C, Van Huffel S. Quantification and classification of high-resolution magic angle spinning data for brain tumor diagnosis. *Proceedings of the 29th Annual Intern. Conf. of the IEEE EMBS Cité Internationale*, Lyon, France. 2007; SaC **11.2**: 5407-5410.
6. Govindaraju V, Young K, Maudsley AA. Proton NMR chemical shifts and coupling constants for brain metabolites. *NMR Biomed.* 2000; **13**: 129–153.
7. Wevers RA, Engelke U, Heerschap A. High resolution H-1-NMR spectroscopy of blood-plasma for metabolic studies. *Clin. Chem*. 1994; **40**: 1245–1250.
8. Wevers RA, Engelke U, Wendel U, Dejong JGN, Gabreels FJM, Heerschap A. Standardized method for high-resolution H-1-NMR of cerebrospinal-fluid. *Clin. Chem.* 1995; **41**: 744–751.
9. Schiebler ML, Miyamoto KK, White M, Maygarden SJ, Mohler JL. In vitro high resolution 1H-spectroscopy of the human prostate: benign prostatic hyperplasia, normal peripheral zone and adenocarcinoma. *Magn. Reson. Med.* 1993; **29**: 285–291.

10. Cheng LL, Anthony DC, Comite AR, Black PM, Tzika AA, Gonzalez RG. Quantification of microheterogeneity in glioblastoma multiforme with ex vivo high-resolution magic-angle spinning (HRMAS) proton magnetic resonance spectroscopy. *Neurooncol*. 2000; **2**: 87–95.
11. Walker AE, Robins M, Weifield FD. Epidemiology of brain tumors: the national survey of intracranial neoplams. *Neurology.* 1985; **35**: 219-226.
12. Stiller CA, Parkin DM. Geographic and ethnic variations in the incidence of childhood cancer. *Br. Med. Bull*. 1996; **52**: 682-703.
13. Kuratsu J, Ushio Y. Epidemiological study of primary intracranial tumours in elderly people. *J. Neurol. Neirosurg. Psychiatru*. 1997; **63**: 116-118.
14. Stiller CA, Allen MB, Eatock EM. Childhood cancer in Britain: the National Registry of childhood tumours and incidence rates 1978-1987. *Eur. J. Cancer.* 1995; **31**: 2028-2034.
15. Smirniatopulos JG. The new WHO classification in brain tumors. *Neuroimanig Clin. North Am.* 1999; **9**: 559-613.
16. Biernat W. 2000 World halt Organization classification of tumours of the nervous system. *Pol. J. Pathol.* 2000; **51**: 107-114.

MEDULLOBLASTOMA

Medulloblastoma is classified under the embryonal PNET (primitive neuroectodermal tumor), childhood medulloblastoma alter survival likelihood. The WHO classification of brain tumors recognizes desmoplastic/nodular medulloblastoma, medulloblastoma with extensive nodularity, large cell medulloblastoma, and anaplastic medulloblastoma, in addition to medulloblastoma with no other distinguishing features. All the tumors originate from primitive or undifferentiated neuroephitelial cells, so they are typically considered pediatric brain tumors (1). Brain tumors in paediatric patients are proportionally much more common malignancies diagnosed in this age group than those in adults. A large body of paediatric brain tumors show low degree of malignancy and therefore respond to therapy, but their anatomical localization, often adjacent to vital structures, makes diagnosis challenging. Histologically similar tumor types to those in adults, such as benign and malignant astrocytomas, and dissimilar ones, such as PNET, neuroblastomas and retinobaslatomas, are found.

Clinical material. A 3-year-old child was admitted to the hospital because of persistent headaches, which started one month previously, and a refusal to eat due to persistent nausea. He underwent MRI and *in vivo* ^{1}H MRS of the head on a 1.5 Tesla clinical imager (Philips Intera, Best, Netherlands), which revealed an intracranial tumor occupying most of the left portion of the posterior fossa. Compared to brain parenchyma, the lesion was predominantly hyperintense on T2-weighted images and slightly hypointense on T1-weighted images with restricted apparent diffusion coefficient (ADC). After intravenous gadolinium injection, the mass was enhanced strongly, but not uniformly due to internal small cystic components (Figure 1). Extension to supratentorial space through the Pacchioni foramen was clearly visualized, and an extra-axial subarachnoid location was initially suggested. Compression of the fourth and third ventricles and the aqueductus caused marked hypertensive triventricular hydrocephalus. Spine imaging revealed diffused leptomeningeal tumor localizations. The very large dimension of the tumor combined with the high cellular density, as suggested by the restricted ADC, and the apparent extra-axial localization into the subarachnoid space, raised the diagnostic hypotheses of a rare case of lymphoma to be differentiated from medulloblastoma. After MR examination, a ventricular-peritoneal shunt was positioned. Twelve days after MRI, the child underwent brain surgery, which revealed an intra-axial

tumor. Extemporaneous histological examination on a sample was diagnostic for medulloblastoma and extensive, but only partial resection of the tumor was possible. Subsequent histopathological analysis revealed apoptotic elements, necrosis, high proliferation activity (MIB1 =70%) and highly positive CD56 immunoassay. No nodular aspect was reported. *In vivo* ^{1}H MR spectra were performed using a spin-echo sequence with 144 ms echo time (TE), 2 sec repetition time (TR), and averaging the signal of 128 consecutive scans, 512 data points and point resolved spectroscopy (PRESS) localization technique. Two volumes of interest (VOI) (3x2x2 cm) were placed respectively on the tumor mass (Figure 1) and on normal appearing cerebellar parenchyma. Water signal suppression was performed using a standard chemical shift selective saturation standard (CHESS) sequence with two Gaussian chemical shift selective pulses of 70 Hz. The data were processed using CSX2 (Kennedy Krieger Institute, Baltimore, USA). DC Correction, Zero Filling factor 2, Gaussian Filter with L.B. 3.0 Hz (time domain), High Pass Filter Bandwith 50 Hz (to suppress water peak) and baseline correction was applied to both the spectra data.

For the NMR experiments details see chapter II.

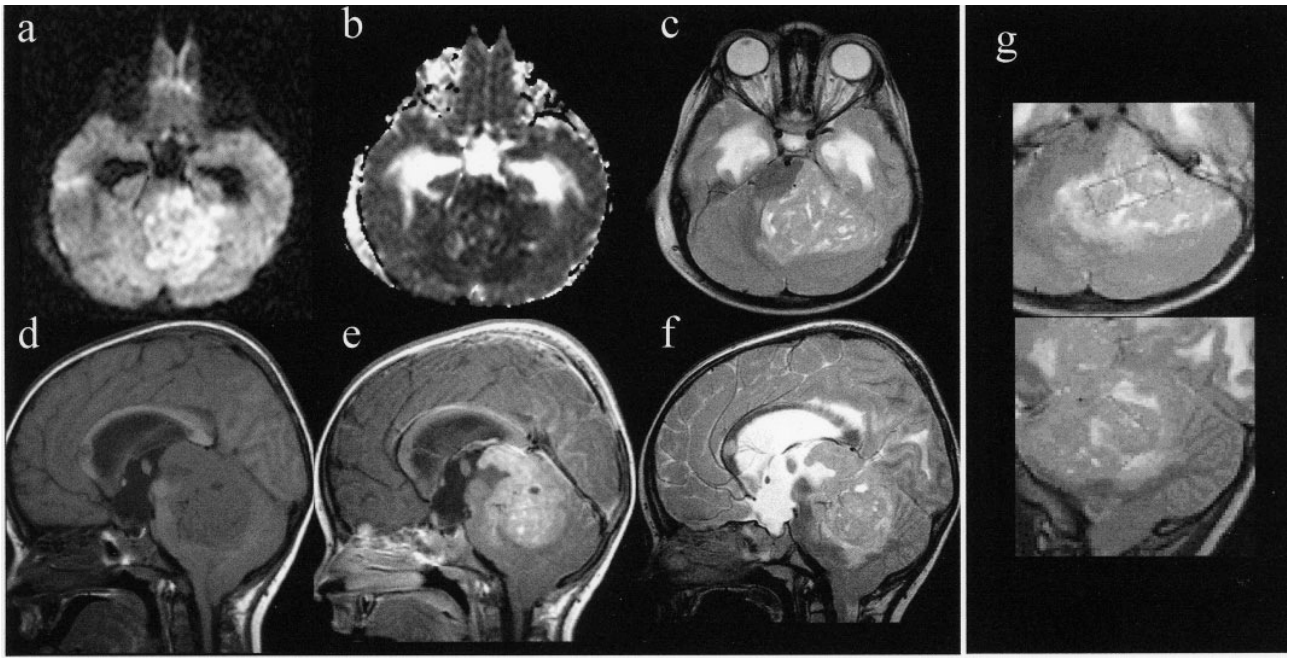

Figure 1. Conventional MR imaging. (a) Axial diffusion weighted; (b) apparent diffusion coefficient; (c) axial T2 weighted; (d) saggital T1 weighted;(e) post-gadolinium sagittal T1 weighted; (f) sagittal T2 weighted; and (g) single voxel localizer displayed in green over T2 weighted axial and sagittal images.

Results and Discussion

The single voxel *in vivo* ^{1}H MR spectra obtained from the medulloblastoma and contralateral healthy cerebellum are reported in Figure 2a and b, respectively. The spectrum of the lesion (Figure 2a) displays one predominant signal at 3.2 ppm, which is usually attributed to ChoCC, accompanied by low intensity peaks at 3.0 ppm, attributable to Cr derivatives, at 2.3 ppm, attributable to glutamate plus glutamine (Glx); and at 2.0 ppm, attributable to NAA and Glx (2). The high ChoCC/Cr ratio found in the present case can be associated with the synthesis of new cell membranes. Several MRS studies correlate the increase of such compounds to the cell neoplastic proliferation (3,4). Moreover, it can be noted that signals downfield from ChoCC are nearly absent in the MR spectrum of the lesion with respect to that of the contralateral healthy cerebellum (Figure 2b). In fact, the *in vivo* MR spectrum of the contralateral VOI shows high signals from NAA at 2.0 ppm, Cr at 3.0 ppm, ChoCC at 3.2 ppm, and Myo at 3.5 ppm. Lower signals due to NAA at 2.5 ppm and to Glx at 2.3 ppm are also observed. The signal at 3.5 ppm could receive contributions from both Myo and glycine (Gly). Signals at higher frequencies are poorly resolved. ChoCC/Cr metabolite signal intensity ratio is within the range measured for the cerebellar tissue of healthy children, while a reduction of NAA/ChoCC and NAA/Cr ratios is evident (5-7). We hypothesized that the reduction of NAA was an expression of mild oedema and neuronal dysfunction in the otherwise normal appearing brain tissue chosen for MRS, an effect in agreement with the high compression exerted by the tumor.

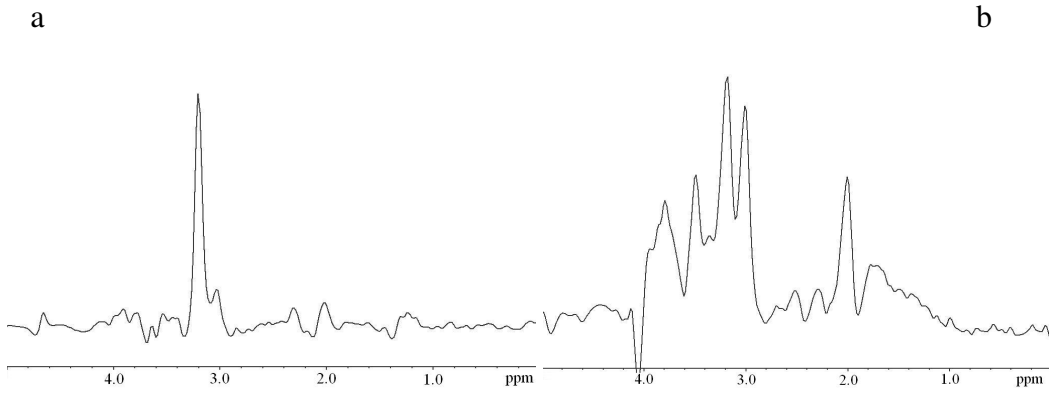

Figure 2. *In vivo* ^{1}H MR spectra of (a) medulloblastoma and (b) contralateral healthy cerebellum.

Figure 3 reports the *ex vivo* ^{1}H HR-MAS NMR spectra of the medulloblastoma performed with different experiments. A conventional presaturated 1D spectrum, which highlights both

lipid and small metabolite contribution, is displayed in panel a. Figure 3b shows a spectrum obtained using a CPMG spin-echo sequence, in order to separate signals according to their different T_2 and enhance the resonance of metabolites with respect to those of macromolecules. Figure 3c represents the diffusion-edited spectrum displaying contributions from mobile lipids and macromolecules.

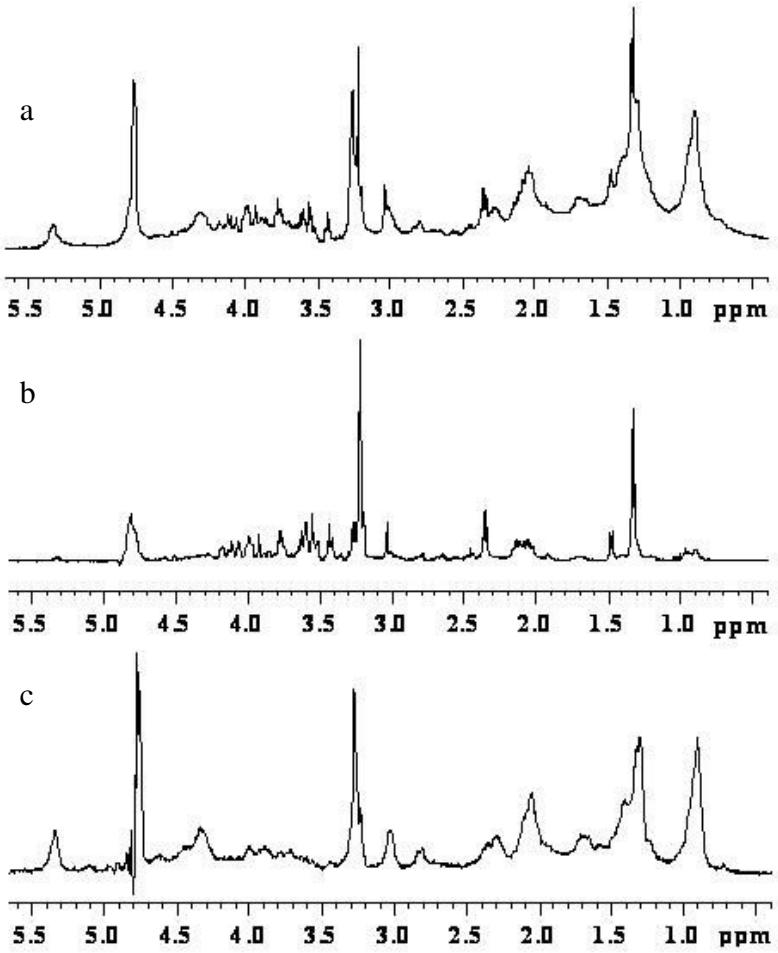

Figure 3. ^{1}H HR-MAS spectra of the medulloblastoma. (a) Conventional ^{1}H spectrum obtained with water presaturation and composite pulse, (b) CPMG spectrum obtained with 360 ms total spin-echo time and (c) diffusion edited spectrum obtained with Δ= 200 ms, δ= 4 ms and gradient strength of 32 G/cm.

The most abundant metabolites can be assigned by comparison with literature data, but a complete assignment requires the acquisition of selected 2D experiments such as COSY, TOCSY and HSQC. These experiments enable a complete and unambiguous identification of the metabolic pattern characterizing the examined tissue. The principal metabolites are labelled in Figure 4, and the ^{1}H and ^{13}C assignments of the observed pool of metabolites, particularly osmolites, free amino acids and a fraction of mobile lipids, are reported in Table

I. A look at the HR-MAS spectra shows that the spectral detail is much higher than that obtainable *in vivo,* and that Myo, taurine (Tau) and PE, and a trace of arginine, contribute to the *in vivo* signal at 3.2 ppm, usually attributed to ChoCC [GPC, PC free choline (Cho)]. The H-5 proton signal of Myo at 3.28 ppm (triplet) is detected through the correlation with H 4,6 at 3.63 ppm in the COSY spectrum, and the correlations with other protons of its spin system (4.06, 3.63, and 3.53 ppm) in the TOCSY spectrum (Figure 5a). The CH_2N protons of PE at 3.23 ppm (triplet) are detected in both homonuclear correlation spectra, through a correlation with CH_2O at 4.00 ppm (a double triplet, which resembles a quartet), which shows a coupling with the phosphorous nucleus. Similarly, the CH_2N protons of Tau at 3.26 ppm (triplet) are detected through the correlation with CH_2S at 3.42 ppm (triplet). An estimation of relative contributions of these metabolites to the integral value of signals between 3.32 and 3.15 ppm, usually attributed to the *in vivo* spectra of ChoCC, can be derived from the evaluation of areas of selected signals (weighted on the basis of the relative proton numbers). This calculation leads to the presence of 20% PE, 18% Tau, 55% PC + Cho, and 7% Myo. The same experiments highlight a contribution from the CH_2N Lys and CH_2COO^- asparagines (Asn) signals to the *in vivo* signal at 3.0 ppm, usually attributed to NCH_3 Cr protons (Figure 5b). Cr participates in 60% of the total area of the region 3.10-2.90 ppm, as deduced by comparison of the integral of the signal at 3.92 ppm (CH_2 protons of Cr). Finally, *ex vivo* ^{1}H NMR experiments indicate the presence of alanine (Ala) and lactate (Lac) and the absence of NAA. The absence of NAA in the HR-MAS spectra and presence of only a trace of acetate suggest that the peak at 2.0 ppm in the *in vivo* spectrum could be principally due to the $CH_2(\beta)$ and $CH_2(\alpha)$ signals of glutamate plus glutamine. A direct comparison between the *in vivo* and *ex vivo* MR profiles of medulloblastoma can be made after applying a broadening processing function to the HR-MAS signal which, although implying the loss of a higher degree of information furnished by the HR-MAS spectrum, shows the close correspondence between the two spectra (Figure 6), especially when the region of ChoCC and Cr signals is considered. The highest signal is that usually attributed to ChoCC, which we have shown above to receive contributions from a number of other metabolites, accompanied by low intensity peaks due to glutamate plus glutamine at 2.3 and 2.0 ppm, and Cr (plus Lys and asparagine) at 3.0 ppm. More difficult is the comparison between regions at higher frequencies of the two spectra, where signals due to Tau, Myo, Gly and PE are expected. These signals are evident in the *ex vivo* spectrum, but they are less clear *in vivo* because of more distortions from the evolution of coupling constants. The estimation of the ratio ChoCC/Cr from the *in vivo* spectrum (5/1)

compares well with that from the HR-MAS spectrum (6.5/1) obtained, considering the regions 3.15-3.32 and 3.10-2.90 ppm. Myo, Tau, Gly and PE have already been reported as significant metabolites from *in vitro* MRS studies on medulloblastoma (8,9). Accordingly, prominent Tau, Gly and PE peaks are easily observed in our *ex vivo* spectrum (Figure 4), and the presence of Tau in *in vivo* spectra of the medulloblastoma has been reported (10,11). Further considerations can be argued from the analysis of *ex vivo* MR spectra. Mobile lipids, which are already visible in the standard presaturated 1D spectrum (Figure 3a), are further evidenced in the diffusion-edited spectrum (Figure 3c) by the broad signals at 0.89, 1.30, 3.26 and 5.32 ppm. In particular, the 3.26 ppm resonance, deriving from the trimethylammonium of the choline residue, strongly suggests that phospholipids are present in substantial amounts in the examined medulloblastoma. It is worthwhile to underline the presence of broad signals at 3.02 and 1.72 ppm (which are correlated by the TOCSY experiments also to the 1.48 and 1.91 ppm signals), attributable to Lys in non-negligible amounts and possibly involved in lysyl-phosphatidylglycerols. These findings provide a deeper insight into the lipid composition of brain neoplasms to be pursued. It has been reported that the presence of mobile lipids, both in *ex vivo* and *in vivo* MR spectra of brain neoplasms, is correlated to necrosis in the lesions (12,13). This spectroscopic datum directly correlates to a morphological aspect of the histopathological assessment. Moreover, Tzika *et al* reported that *in vivo* and *ex vivo* MR spectra of several pediatric brain tumors exhibited substantial levels of lipids, which may be due to apoptosis and/or necrosis (14). As a consequence, the histological features of apoptosis and necrosis, evidenced in the histological analysis of this medulloblastoma, are reflected by the presence of lipid signals in our *ex vivo* HR-MAS MR spectra.

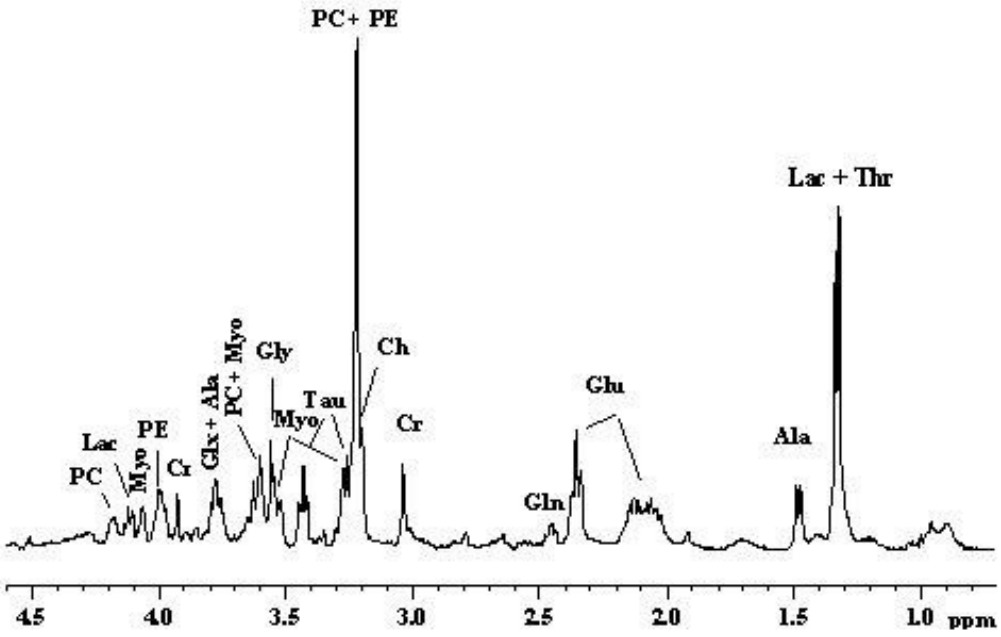

Figure 4. HR-MAS ^{1}H spectrum of the medulloblastoma. CPMG spectrum obtained with 360 ms total spin-echo time; the major metabolites are labelled.

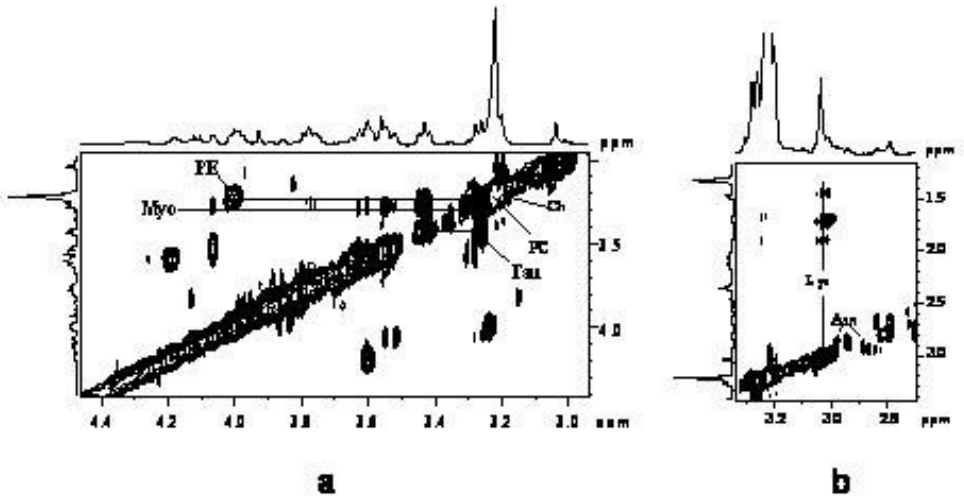

Figure 5. Partial regions of the TOCSY spectrum of the medulloblastoma.

In this case report, we have demonstrated that the *ex vivo* HR-MAS NMR spectroscopy can reach a high resolution degree, thus providing a link between *in vivo* MRS and neuropathological analysis. The present study demonstrates that e*x vivo* HR-MAS ^{1}H NMR is able to strongly improve the clinical possibility of *in vivo* MRS and can be used in conjunction with *in vivo* spectroscopy for clinical purposes, in which case a large number of samples can be analyzed and histologically classified.

The identified metabolites are denoted with labels according to Table I.

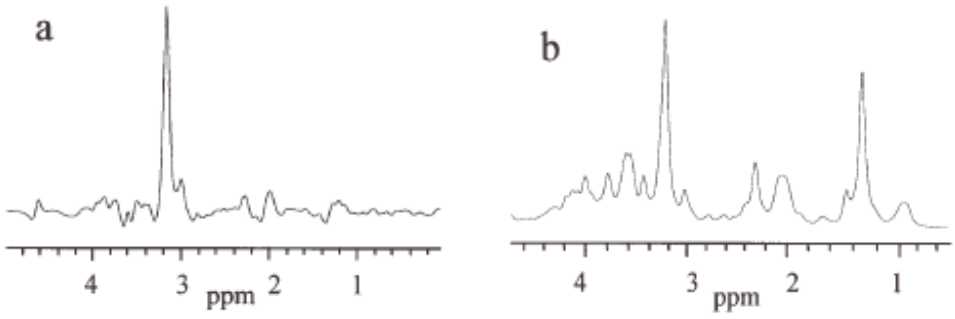

Figure 6. Comparison of the *in vivo* ^{1}H spectrum, recorded at 1.5 T, of the medulloblastoma (a) and its *ex vivo* ^{1}H HR-MAS spectrum, recorded at 9.4 T (b); an exponential function with a 30-Hz line broadening (LB) was applied prior to the Fourier transformation with the aim of having a spectrum line width comparable to the *in vivo* spectrum.

References

1. Verma S, Tavare C, Gilles F. Histologic Features and Prognosis in Pediatric Medulloblastoma. *Pediatr. Dev. Pathol*. 2008; **17**: 1.
2. Barton SJ, Howe FA, Tomlins AM, Cudlip SA, Nicholson JK, Bell BA, Griffiths JR. Comparison of *in vivo* 1H MRS of human brain tumors with ^{1}H HR MAS spectroscopy of intact biopsy samples *in vitro*. *Magn Res Mat Phys Biol Med (MAGMA)* 1999; **8**: 121-128.
3. Barbarella G, Ricci R, Pirini G, Tugnoli V, Tosi MR, Bertoluzza A, Calbucci F, Leonardi M, Trevisan C, Eusebi V. *In vivo* single voxel 1H MRS of glial brain tumors: correlation with tissue histology and *in vitro* MRS. *Int. J. Oncol*. 1998; **12**: 461-468.
4. Shimizu H, Kumabe T, Yoshimoto T. Correlation between Choline level measured by proton MR spectroscopy and Ki-67 labeling in gliomas. *AJNR Am. J. Neuroradial*. 2000; **21**: 659-665.
5. Wang Z, Sutton L, Cnaan A, Haselgrove JC, Rorke LB, Zhao H, Bilaniuk LT, Zimmerman RA. Proton MR spectroscopy of pediatric cerebellar tumors. *Am. J. Neuroradiol.* 1995; **16**: 1821-1833.
6. Tedeschi G, Bertolino A, Righini A, Campbell G, Raman R, Duyn JH, Moonen CT, Alger JR, Di Chiro G. Brain regional distribution pattern of metabolite signal intensities in young adults by proton magnetic resonance spectroscopic imaging. *Neurology* 1995; **45**: 1384-1391.
7. Van der Knaap MS, Van der Grond J, Van Rijen PC, Faber JA, Valk J, Willemse K. Age-dependent changes in localized proton and phosphorus MR spectroscopy of the brain. *Radiology* 1990; **176**: 509-515.
8. Kinoshita Y, Yokota A. Absolute concentrations of metabolites in human brain tumors using *in vitro* proton magnetic resonance spectroscopy. *NMR Biomed.* 1997; **10**: 2-12.

9. Sutton LN, Wehrli SL, Gennarelli L, Wehrli SL, Gennarelli L, Wang Z, Zimmerman R, Bonner K, Rorke LB. High-resolution 1H-magnetic resonance spectroscopy of pediatric posterior fossa tumors *in vitro*. *J. Neurosurg*. 1994; **81**: 443-448.
10. Wilke M, Eidenschink A, Muller-Weihrich S, Auer DP. MR diffusion imaging and 1H spectroscopy of a child with medulloblastoma. A case report. *Acta Radiol.* 2001; **42**: 39-42.
11. Moreno-Torres A, Martinez-Perez I, Baquero M, Campistol J, Capdevila A, Arús C, Pujol J. Taurine detection by proton magnetic resonance spectroscopy in medulloblastoma: contribution to noninvasive differential diagnosis with cerebellar astrocytoma. *Neurosurgery* 2004; **55**: 824-829.
12. Kusel AC, Donnelly SM, Halliday W, Sutherland GR, Smith IC. Mobile lipids and metabolic heterogeneity of brain tumors as detected by *ex vivo* ^{1}H MR spectroscopy. *NMR Biomed.* 1994; **7**: 172-180.
13. Negendank W and Sauter R. Intratumoral lipids in 1H MRS *in vivo* in brain tumors: experience of Siemens cooperative clinical trial. *Anticancer Res.* 1996; **16**: 1533-1538.
14. Tzika AA, Cheng LL, Goumnerova L, Madsen JR, Zurakowski D, Astrakas LG, Zarifi MK, Scott RM, Anthony DC, Gonzalez RG, Black PM. Biochemical characterization of pediatric brain tumors by using in vivo and ex vivo magnetic resonance spectroscopy. *J. Neurosurg*. 2002; **96**: 1023-1031.

MENINGIOMAS

The most frequent tumors of the central nervous system are represented by meningiomas. They typically manifest in adults and they are more common in women than in men. Meningiomas are generally slow-growing, benign tumors attached to the dura mater and composed of neoplastic meningothelial (arachnoidal) cells. Meningiomas have a wide range of histopathological appearances, among which meningothelial and fibrous are by far the most common. Moreover, 10-15% of meningiomas present an atypical pattern with rim like enhancement, cyst formation, intralesion hemorrhage and metaplasia. Meningiomas with these morphological features resemble metastases or malignant gliomas with cystic or necrotic aspects (1). Although meningiomas have characteristic neuroimaging features, hemangiopericytomas, schwannomas, and dural metastatic tumors may mimic meningiomas (2).

The purpose of this study was: to identify the metabolic patterns of meningiomas; to assess the presence and the relevance of the metabolic alterations linked to different subtypes of meningiomas; to compare the *ex vivo* and the *in vivo* spectra to clarify and validate the *in vivo* MRS.

Clinical Materials. This study was approved by the local ethics committee and the patients provided a written informed consent. Six patients underwent surgical resection of the tumors and the specimens were snap-frozen in liquid nitrogen and stored at -80˚C until *ex vivo* MRS analysis. Histopathological analysis of the 6 lesions identified them as meningiomatous in nature. According to the WHO 2000 criteria (3), three out of the six meningiomas were classified as classic meningothelial, grade I, one as classic fibrous, grade I, and one as classic transitional, grade I. One of them showed oncocytic differentiation, demonstrated both by conventional histology and immunohistochemistry (4). The neoplastic cells showed prominent nucleoli and focally high nucleus/cytoplasm ratio. The mean mitotic index (total counts per ten high-power fields) was 6/10 HPF, increasing up to 12/10 HPF in some areas. The lesion was therefore classified as grade II. The cellular proliferation index, determined by MIB-1, and expressed as LI, ranged from 1-3% for 4 meningiomas of the meningothelial, transitional and fibrous subtypes, consistent with grade I lesions. In one meningioma of the meningothelial subtype MIB-1 LI was slightly increased to 5%, but was still in keeping with a

grade I lesion. The MIB-1 LI for the oncocytic meningioma was much higher; its mean value was 5%, and approached 14% in some areas, thus classified as a grade II lesion. The clinical data and MRS experiment types of the 6 patients are shown in Table II.

Table II. Patients' clinical data and NMR experiments.

Patients	Age (sex)	Meningioma Subtype and grade MIB-1 LI 1%	*In vivo* ^{1}H-MRS		*Ex vivo* HR-MAS MRS		
			TE 38 ms	TE 144 ms	1D ^{1}H zgcppr	1D ^{1}H cpmgpr	1D ^{1}H led
1	66 (M)	Meningothelial, grade I MIB-1 LI 1%			1a	1b	1c
2	53 (F)	Meningothelial, grade I MIB-1 LI 3%	X	X	2a	2b	2c
3	61 (F)	Fibrous, grade I MIB-1 LI 1%	X	X	3a	3b	3c
4	26 (M)	Oncocytic, grade II MIB-1 LI 5%, up to 14%	X	X	-	-	-
5	50 (F)	Meningothelial, grade I MIB-1 LI 5%	X	X	5a	5b	5c
6	74 (M)	Transitional, grade I MIB-1 LI 2%			6a	6b	6c

In vivo ^{1}H MRS. The patients underwent MRI and *in vivo* ^{1}H MRS of the head on a 3T clinical imager (Philips Intera, Best, The Netherlands). I*n vivo* ^{1}H MR spectra were performed using a spin-echo sequence with 38 and 144 ms TE, 2s TR, 2048 data points, PRESS localization technique and averaging the signal of 128 scans. The VOIs (6-8 cm3) were placed and shaped according to the size of the lesion. Water signal suppression was performed using a CHESS sequence with two Gaussian chemical shift selective pulses of 70 Hz. The data were processed and analyzed using software developed by one of the authors (C.T.) on IDL platform (Research System, Inc., Boulder, CO, USA). DC correction, zero filling factor 2, Gaussian filter with LB 3.0 Hz (time domain), high pass filter bandwith 50 Hz (to suppress water peak) and baseline correction were applied to the spectral data.

For the NMR experiments details see Chapter II.

Results and Discussion

HR-MAS spectra. Figure 1 shows the *ex vivo* 1D ^{1}H conventional HR-MAS MR spectra of three subtypes of meningiomas diagnosed as meningothelial (patient 2), fibrous (patient 3) and transitional (patient 6).

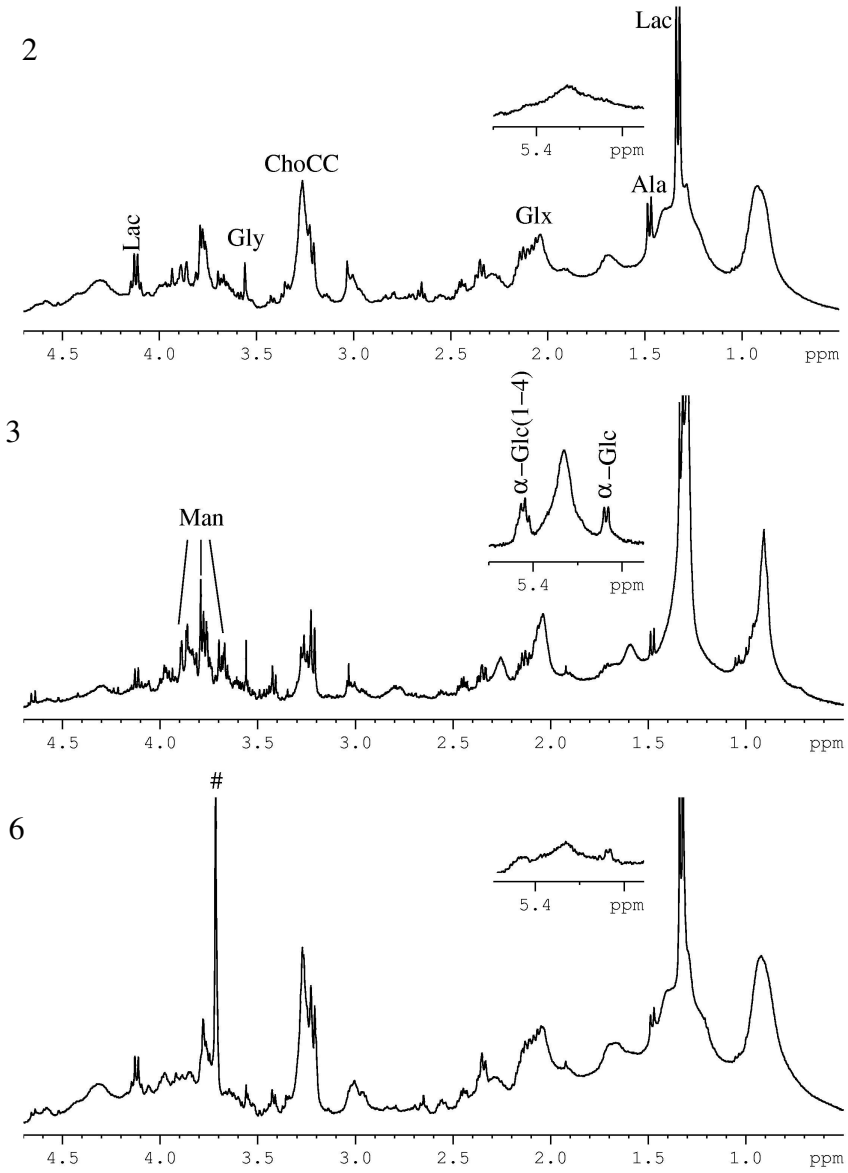

Figure 1. *Ex vivo* 1D ^{1}H conventional presaturated HR-MAS MR spectra of samples: 2, meningothelial; 3, fibrous; and 6, transitional. #, denotes PEG.

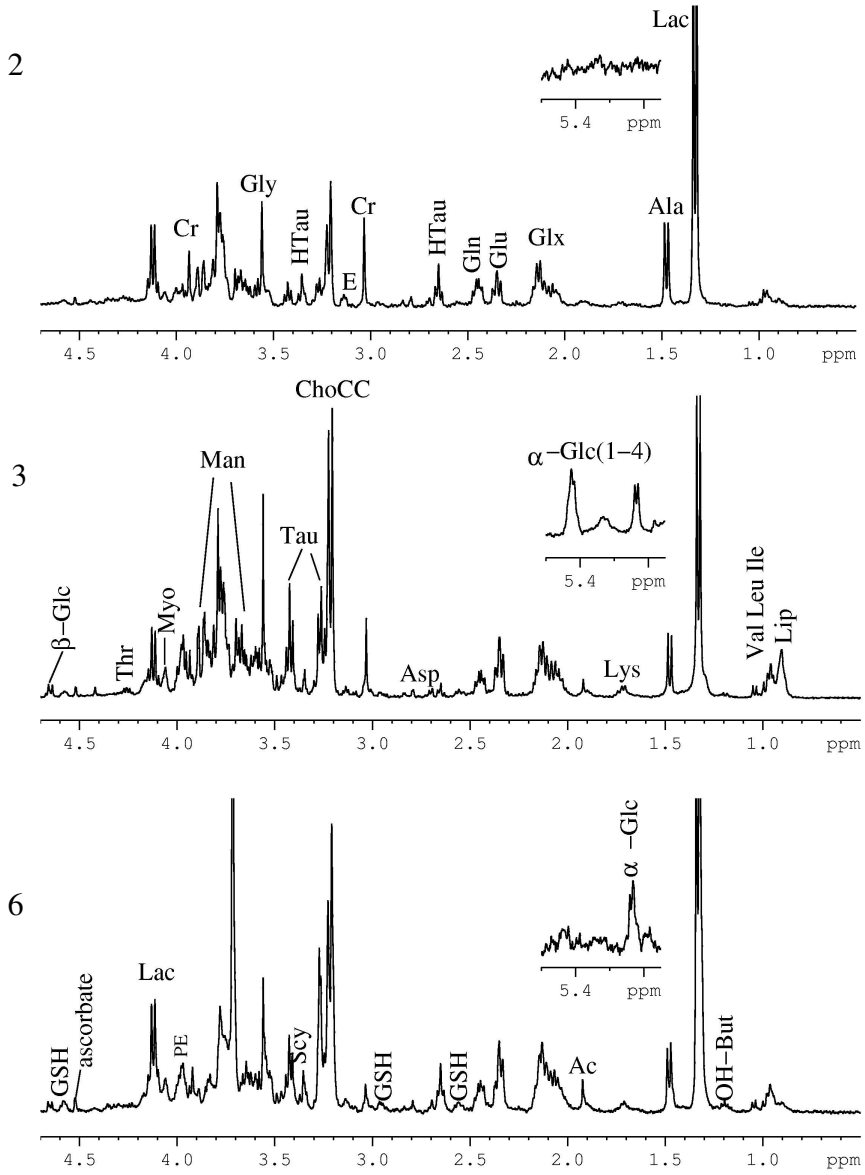

Figure 2. *Ex vivo* CPMG spectra of samples 2, 3 and 6 obtained with a 360 ms total spin-echo time.

The spectra highlight both narrow and broad signals, which can be separated by using a CPMG spin-echo and a diffusion-edited sequence. Figure 2 shows the spin-echo spectrum displaying signals due to the resonances of small metabolites, and Figure 3 displays the diffusion-edited spectrum in which contributions from mobile lipids and macromolecules were found. The labels were chosen to indicate the more abundant and visible metabolites (Figures 1 and 2) and macromolecules (Figure 3) in each spectrum. The efficacy of the above sequences at clarifying tissue components is remarkable when considering the region at ~3.2 ppm, which is of great importance in *in vivo* spectroscopy, because it contains signals due to ChoCC. This region, as is particularly evident in samples 2 and 6 (Figure 1), is formed by overlapping broad and narrow signals. In the CPMG experiment (Figure 2) the narrow signals

due to Cho, GPC, PC, Tau, and a low percentage Myo, are highlighted, whereas the broad component due to the $N^+(CH_3)_3$ of phospholipids is evident in the diffusion-edited spectrum (Figure 3). The detection of metabolites was obtained, not only through 1D ^{1}H NMR spectra, but also through selected 2D experiments such as COSY, TOCSY and HSQC, and their assignment was confirmed by comparison with literature data. The full experiments provided complete and unambiguous identification of the metabolic pattern characterising the examined tissues. The main metabolites are labeled in Figures 1-6 and the pool of metabolites especially osmolites, free amino acids and mobile lipids are reported in Table I.

Low molecular-weight metabolites. Abundant metabolites such as Lac, Ala, glutamate (Glu), glutamine (Gln), Cr, ChoCC, Tau and Gly can be identified by direct inspection of the 1D ^{1}H NMR spectra obtained using the spin-echo sequence, whereas, the identification of metabolites hidden under the more abundant ones can be obtained through COSY, TOCSY and HSQC spectra. For example, the presence of the glutathione (GSH), particularly abundant in sample 1, was established by the COSY cross peaks between the signals at 8.57 and 8.36 ppm with signals at 4.57 and 3.77 ppm, respectively (Figure 4). These correlations are attributed to the NH/CH(α) pair of cysteine (Cys) and NH/CH_2 of Gly in GSH and their detection indicates that the NH protons of glycyl and cysteinyl amidic groups are in slow-exchange with water. This assignment was confirmed by a TOCSY spectrum (showing a further correlation between NH at 8.57 ppm and CH_2 at 2.96 ppm of Cys), and by the HSQC spectrum, showing the H,C correlation at 3.77/44.0 ppm, attributable to the CH_2 group of a bonded Gly, clearly distinguishable from free Gly, whose H,C correlation is found at 3.56/42.3 ppm (Figure 6). It is also to be noted that the resonances of the glutamyl moiety of GSH were well distinguished from those of free Gln and Glu (Figure 5, left). The other resonances due to cysteinyl and glutamyl moieties of GSH are reported in Table I. HTau was identified by the triplet at 2.65 ppm, which correlated with a triplet at 3.35 ppm in the COSY spectrum, whereas β-Ala, which is the major product of uracil catabolism, displayed a correlation between a triplet at 2.55 ppm and a triplet at 3.18 ppm.

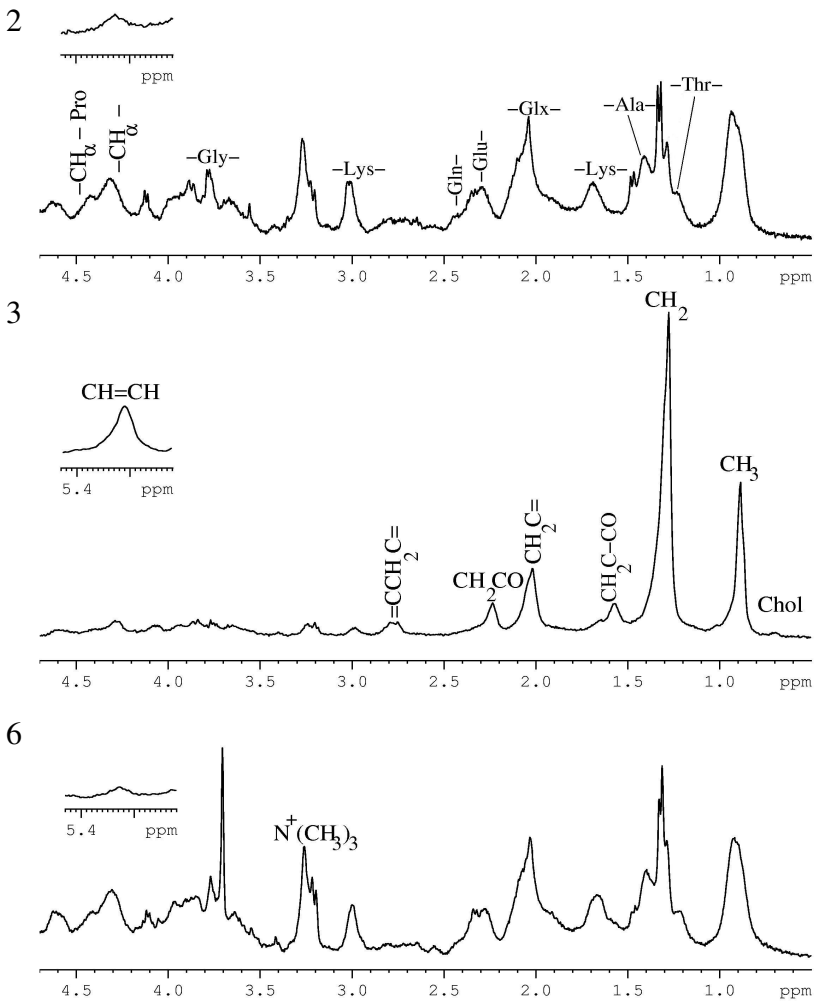

Figure 3. *Ex vivo* diffusion-edited spectra of samples 2, 3 and 6 obtained with ¢=200 ms, ‰=4 ms and a gradient strength of 32 G/cm.

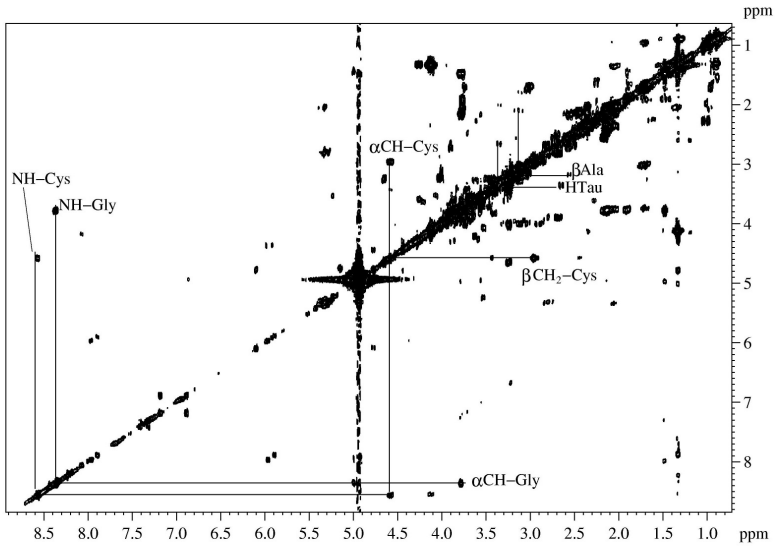

Figure 4. COSY spectrum of sample 1.

The resonances of the methyl groups of Leu, Ile, Val were in the range between 0.94-1.04 ppm and appeared, in 1D ^{1}H spectra, as a shoulder of a broad band at 0.9 ppm due to methyl resonances of lipids and macromolecules. The identification of these amino acids was easily obtained through the COSY and TOCSY spectra. Val was identified by the correlation between the methyl resonances at 0.99 and 1.04 ppm with the β-CH at 2.25 ppm. Ile was characterized by the resonances at 1.02 ppm and 1.97 ppm, and Leu was identified by the correlations between the signals at 0.95 and 0.97 ppm with that at 1.72 ppm. The signals of Lys, more evident in sample 3, and Arg were partially overlapped with those of Leu and Ile; their clear identification was achieved, from COSY spectra, by the correlations at 3.02/1.73 ppm for Lys and at 3.23/1.70 ppm for Arg. Further confirmation came from the correlations in the TOCSY spectra (Figure 5, right). The same 2D homonuclear experiments revealed the methyl doublet of Thr at 1.33 ppm (hidden in all samples under that of Lac) by its correlation with α·-CH at 4.26 ppm. The region of the ^{1}H spectra at around 3.2 ppm, which displayed resonances usually attributed to ChoCC (GPC, PC and Cho) in the *in vivo* spectra, received contributions, in the reported samples, from PE, Myo, β-Glc, Tau, Arg and GPE, as already observed in the case report of medulloblastoma. Regarding ChoCC, Cho and PC were the main metabolites, whereas GPC was not detected. In all meningiomas, traces of ascorbate (a doublet at 4.52 ppm correlating with a signal at 4.01 ppm), aromatic metabolites such as phenylalanine (Phe), adenosine, uracil, uridine-monophosphate (UMP), uridine-diphosphate (UDP), tyrosine (Tyr), histidine (His) and fumarate were found in varying percentages.

Samples 1 and 6 were the richest ones in GSH, whereas it was present only at trace level in samples 3 and 5. GSH is expected to be present in meningiomas, but it is difficult to find in extracts (2,5). The detection of GSH in tumoral tissues is important in relation to its documented tumor chemoresistance (6-8). Moreover, GSH is metabolically linked to Ala, Gln and Glu (5) and this correlation probably indicates why these metabolites are present in appreciable amounts in the meningiomas studied. GSH participates in many cellular reactions and its metabolism is implicated for health (9) and with respect to cancer, it is able to play both protective and pathogenic roles (6). The presence of hipoturine (HTau) together with Tau is probably due to the redox balance in these metabolites; indeed HTau is a precursor of Tau, the main end product of Cys metabolism in mammals, and is thought to share the same physiological function (10). Tau is the most abundant amino acid found in the mammalian brain and seems to play a role in a wide range of basic physiological functions (11). The

presence of these metabolites with antioxidant activity (GSH and HTau) needs further investigation, performed by multidisciplinary analytical approaches, to gain new insight into the redox state in neoplastic tissues.

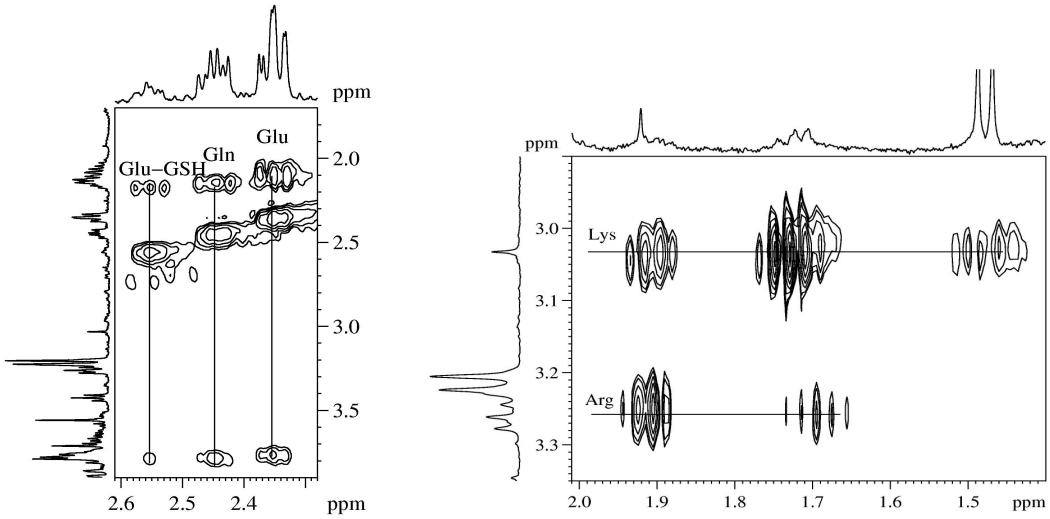

Figure 5. Partial TOCSY spectra of sample 1 (left) and sample 3 (right).

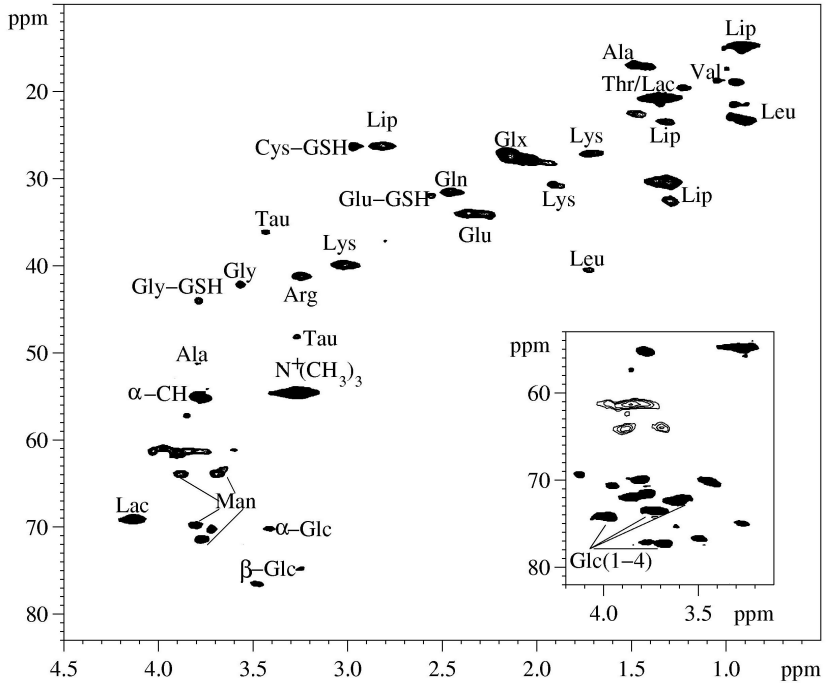

Figure 6. HSQC spectrum of sample 1. The insert shows a selected region of sample 3.

It is worth noting that the *ex vivo* 1D and 2D ^{1}H HR-MAS experiments showed the absence of NAA in all the examined samples, in accordance with the extracerebral origin of these lesions. Table III shows the integral ratios with respect to Ala=1 of the main metabolites detected in *ex vivo* CPMG spectra; Ala was chosen since it is a well-known metabolite

characteristic of meningiomas (12). It should be noted that Ala intracellular level is intrinsic to the identity of the meningeal cell type and it is maintained through neoplastic transformation (13). The high amount of Ala in human meningiomas can be explained in light of this connection. Glx, free Cho, ChoCC, Ala, Gly, and Tau are known to be the main components of meningiomas together with relatively low amounts of Cr, as derived by the high Ala/Cr ratio typical of meningiomas (14).

Lipids and macromolecules. The most significant differences among the meningiomas appear to be in the large components of 1D ^{1}H presaturated (Figure 1) and in 1D ^{1}H diffusion-based MR spectra (Figure 3). The profiles of samples 2 and 3 represent two limit situations. Sample 2 displays large components due to phospholipids (identified by the signals of $N^{+}(CH_3)_3$ at 3.23/54.8 ppm) and mobile peptidic residues. The amino acidic components of these residues were found from the resonances of bonded amino acids CH- (broad signal centered at 4.35 ppm) (15) and their correlations with the relevant protons. An accurate analysis of TOCSY and HSQC spectra permitted the following amino acids to be found: Thr (1.22 ppm), Ala (1.41/17.1 ppm), Lys (3.02, 1.80 and 1.68 ppm), Glx (2.50÷2.20, and 2.10 ppm), Gly (3.92/43.5 ppm) and proline (Pro) (4.44/61.2 ppm, 2.28 ppm). A similar profile is displayed by sample 5 (meningothelial) and sample 6, identified by the histopathological analysis as transitional. The profile of sample 3 is characterised by the dominant resonances of triglycerides and by a trace of cholesterol (Chol) (identified by the methyl resonances at 1.04 and 0.73 ppm). The analysis of the spectrum showed that the triglycerides were formed by saturated, mono- and polyunsaturated fatty acids. Unsaturated acids were identified by the signals at 5.33 ppm, due to the ethylenic protons, and by the signals at 2.02 ppm, due to the methylenic protons of the $-CH_2-CH=$ moiety of mono- and poly-unsaturated fatty acids. The signals centered at 2.78 ppm are attributable to the methylenic protons between two double bonds ($=C-CH_2-C=$) in poly-unsaturated acids (linoleic and γ-linolenic). The spectrum of sample 1 (meningothelial) is characterised by bonded amino acids and phospholipids, and by a large amount of triglycerides and represents an intermediate situation between that of sample 2 and 3.

Polyols. All spectra show the presence of mannitol (Man), which was given to the patients before surgery for cerebral decompression, in varying amounts. Man is identified by a characteristic group of signals in the region 3.4 ÷3.9 ppm, and through $^{1}H,^{13}C$ correlations [3.68, 3.88/63.3 ppm (CH_2OH); 3.76/71.3 ppm and 3.80/69.7 ppm] (Fig. 6). The H-1 signals of α- and β-glucose (Glc) (at 5.24 and 4.67 ppm, respectively) are clearly detected in samples

3 and 6. In addition, sample 3 displays resonances attributable to α-Glc-(1→4) units, embedded in small oligosaccharides. The two doublets at 5.41 and 5.39 ppm are due to H-1 of α-Glc-(1→4), as confirmed by the C-1 chemical shift at 100.2 ppm (16). Other signals due to α-Glc-(1→4) units are found by the inspection of the TOCSY and HSQC spectra (Figure 6): H-1 protons correlate with H-2 protons at 3.64 and 3.55 (C-2 at 72.2 ppm), and with H-3 protons at 3.97 and 3.68 ppm (C-3 at 74.0 ppm). The pairs H-4/C-4 at 3.68/77.2 and at 3.43/70.0 ppm are attributable to central α-Glc-(1→4) units and the nonreducing terminal unit, respectively. The resonances of the reducing terminal unit are hidden under the signals of α- and β-Glc and only the signal due to H-1 (4.66 ppm) of the reducing β-Glc unit can be detected. The resonances of CH_2OH in Glc and α-Glc-(1→4) are found at 3.85/61.7 ppm. These data suggest the presence of oligosaccharides, probably maltotriose or maltotetraose. To our knowledge, it is the first time that these small sugars have been detected by MRS in human meningiomas. Other minor signals due to Myo and scillo-inositol are found in all samples, whereas ribose signals, bonded to UMP and UDP nucleotides were detected, especially in samples 1 and 2.

In vivo MR spectra. The *in vivo* MR spectra (TE=38 ms) of three different subtypes of meningioma, 3 (fibrous), 4 (oncocytic) and 5 (meningothelial), are reported in Figure 7.

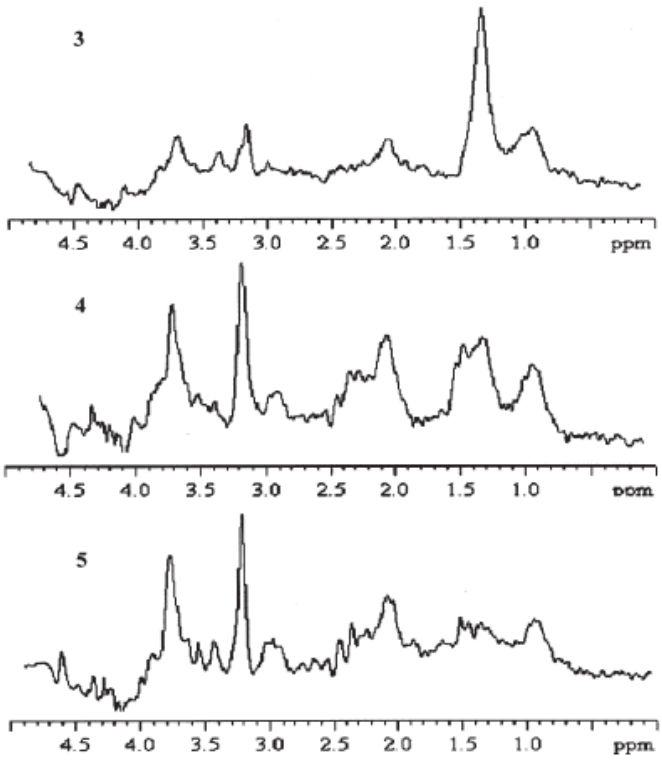

Figure 7. *In vivo* MR spectra of meningiomas: 3, fibrous; 4, oncocytic; and 5, meningothelial recorded at 3 T with TE=38 ms.

The three subtypes of meningioma are characterised by different metabolic profiles and on the basis of the analysis of the corresponding *ex vivo* spectra, it is possible to interpret the main features of each spectrum. The *in vivo* resonances at 0.9, 1.3, 2.1 and 2.8 ppm of sample 3 are mainly due to lipids and the broad signal around 2.1 ppm, besides triglycerides, receives a contribution from Glx, but not from NAA.

Regarding the ChoCC at 3.2 ppm, it should be underlined that this signal, usually assigned in the *in vivo* spectrum to ChoCC, receives substantial contributions from Tau, Myo and PE, and minor ones from Arg and β-Glc. Furthermore, in the *in vivo* spectrum the abundant signal at 3.4 ppm is recognizable due to Tau, and low signals at 3.0 ppm due to Cr and Lys. A direct comparison between *in vivo* (TE=38 ms) and conventional (zgcppr) *ex vivo* spectra (after a suitable broadening processing) of sample 3 shows a close correspondence between the two profiles (Figure 8).

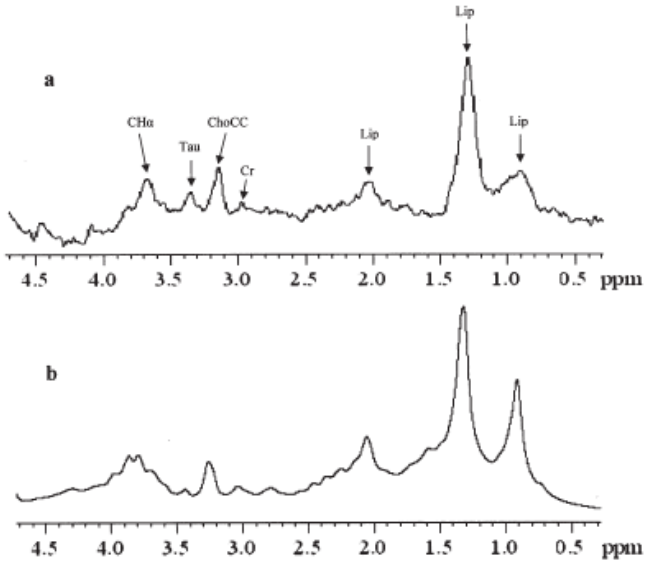

Figure 8. *In vivo* (a) (TE = 38 ms) and *ex vivo* (b) MR spectra of sample 3, fibrous.

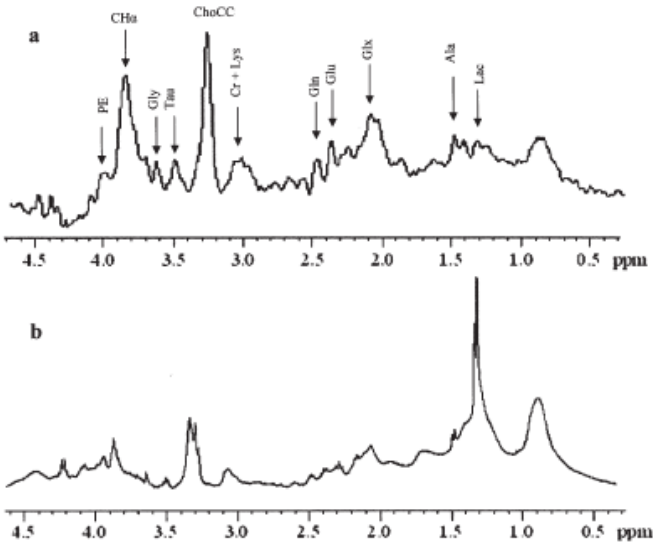

Figure 9. *In vivo* (a) (TE = 38 ms) and *ex vivo* (b) MR spectra of 5, meningothelial.

The slight difference between the *in vivo* and the *ex vivo* signal at around 3.8 ppm is explainable by considering that while the *in vivo* signal receives contributions from PE and -CH amino acids, the *ex vivo* shows additional contribution from Man. The *in vivo* spectrum of sample 5 (meningothelial) in comparison with that of sample 3 (fibrous) (Figure 7) is characterised by the lack of the resonances pertaining to triglycerides and by the presence of phospholipids and macromolecules. It is to be underlined that in the *in vivo* spectrum of 5, the signals due to Ala and Lac are well recognisable as doublets at 1.47 and 1.33 ppm, respectively. A direct comparison between the *in vivo* (TE=38 ms) and the conventional (zgcppr) *ex vivo* spectra (after a suitable broadening processing) of sample 5 shows a good correspondence between the two profiles (Figure 9), the only difference being the increased amount of Lac in the *ex vivo* spectrum. The metabolic profile of *in vivo* MR spectrum of sample 4 (oncocytic; its *ex vivo* spectrum is not available) is between those of 3 and 5 and displays an increased amount of triglycerides with respect to 5. Other well-identified metabolites in samples 3 and 5 are marked on the corresponding spectra. The *in vivo* spectra obtained with an echo time of 144 ms, and routinely used for diagnostic purposes, should be compared to the CPMG *ex vivo* ones, permitting evaluation of the ChoCC/Cr ratio. These ratios derived from *in vivo* measurements are 2.3, 7.9 and 9.3 for samples 2, 3 and 5, respectively, and are in good accordance with the *ex vivo* ones: 3.1, 8.0 and 11.0.

Table III. Abundance o metabolites. [a]

Sample	Ala 1,48[b]	Glx 2.35+2.44[b]	Cr 3.04[b]	Cho 3.20[b]	ChoCC 3.20-3.23[b]	Tau 3.23[b]	Gly 3.56[b]	Ala/Cr	ChoCC/Cr
1	1	2.31	0.18	1.14	2.87	0.72	0.63	5.6	16.0
2	1	1.24	0.50	0.87	1.56	0.29	0.54	2.0	3.1
3	1	2.72	0.65	2.74	5.34	2.32	1.02	1.5	8.1
5	1	1.48	0.40	2.26	4.50	1.10	0.95	2.5	11.2
6	1	2.48	0.20	2.80	4.95	1.54	0.60	5.0	24.8

[a] The integrals evaluated with respect to that of Ala=1. [b] The chemical shift values denote the signals used for the integration.

In conclusion, *ex vivo* HR-MAS MRS allowed us to make an accurate description of the metabolic profile of different meningiomas. By using 1D (composite pulse, water suppressed spin-echo Carr-Purcell-Meiboom-Gill and diffusion-edited sequences) and 2D (COSY, TOCSY and HSQC) experiments, we were able to evidence the presence of several metabolites in different histological subtypes of meningioma. The HR-MAS results agree with the findings in several reports on the major metabolites (Ala, ChoCC, Glx, together with a marked decrease or absence of Cr) found in *in vitro* and *in vivo* MRS spectra of meningiomas (14, 17- 20). Whereas several *in vivo* studies on human meningiomas are well documented (1, 2, 5, 12, 21-23) only one report (24) exists on the ^{1}H HR-MAS MR spectrum of a meningioma in comparison with different brain tumors. The spectroscopic data, obtained from the six samples of meningiomas, confirmed the presence of the typical metabolites of these benign neoplasms and, at the same time, that meningiomas with different morphological characteristics have different metabolic profiles, particularly regarding macromolecules and lipids. The *ex vivo* spectra, permitting a better understanding and interpretation of the *in vivo* MR spectra, show that the HR-MAS MRS technique is a complementary method to strongly support *in vivo* MR spectroscopy and increase its clinical potentiality.

References

1. Harting I, Hartmann M, Bonsanto MM, Sommer C, Sartor K: Characterization of necrotic meningioma using diffusion MRI, perfusion MRI, and MR spectroscopy: case report and review of the literature. *Neuroradiology* 2004; **46**: 189-193.
2. Cho YD, Choi GH, Lee SP, Kim JK. 1H-MRS metabolic patterns for distinguishing between meningiomas and other brain tumors. *Magn. Reson. Imag*. 2003; **21**: 663-672.
3. Pathology and Genetics. Tumours of the Nervous System. *World Health Organization Classification of Tumours.* Kleihues P and Cavenee WK (eds), IARC Press 2000; **1**.
4. Roncaroli F, Riccioni L, Cerati M, Capella C, Calbucci F, Trevisan C, Eusebi V. Oncocytic meningioma. *Am. J. Surg. Pathol*. 1997; **21**: 375-382.
5. Opstad KS, Provencher SW, Bell BA, Griffiths JR, Howe FA. Detection of elevated glutathione in meningiomas by quantitative *in vivo* 1H MRS. *Magn. Reson. Med*. 2003; **49**: 632-637.
6. Balendiran GK, Dabur R, Fraser D. The role of glutathione in cancer. *Cell. Biochem. Funct.* 2004; **22**: 343-352.
7. Locigno R, Castronovo V. Reduced glutathione system: Role in cancer development, prevention and treatment. *Int. J. Oncol.* 2001; **19**: 221-236.
8. Townsend DM, Tew KD. The role of glutathione-S transferase in anti-cancer drug resistance. *Oncogene* 2003; **22**: 7369- 7375.
9. Wu G, Fang YZ, Yang S, Lupton JR, Turner ND: Glutathione metabolism and its implications for health. *J. Nutr.* 2004; **134**: 489-492.
10. Huxtable RJ. Physiological actions of taurine. *Physiol. Rev.* 1992; **72**: 101-163.
11. Dominy J, Eller S, Dawson Jr R. Building biosynthetic schools: Reviewing compartmentation of CNS taurine synthesis. *Neurochem. Res*. 2004; **29**: 97-103.
12. Preul MC, Caramanos Z, Collins DL, Villemure JG, Leblanc R, Olivier A, Pokrupa R, Arnold DL. Accurate non invasive diagnosis of human brain tumors by using proton magnetic resonance spectroscopy. *Nat. Med.* 1996; **2**: 323-325.
13. Florian CL, Preece NE, Bhakoo KK, Williams SR, Noble MD. Type-specific fingerprint of meningioma and meningeal cells by proton nuclear magnetic resonance spectroscopy. *Cancer Res.* 1995; **55**: 420-427.
14. Gill SS, Thomas DGT, Van Bruggen N, Gadian GD, Peden CJ, Bell JD, Cox IJ, Menon DK, Iles RA, Bryant DJ, Coutts GA. Proton NMR spectroscopy of intracranial tumors: *in vitro* and *in vivo* studies. *J. Comput. Assist. Tomogr*. 1990; **14**: 497-504.
15. Richarz R, Wuthrich K. Carbon-13 NMR chemical shifts of the common amino acid residues measured in aqueous solutions of the linear tetrapeptides H-Gly-Gly-X-L-Ala-OH. Biopolymers 1978; **17**: 2133-2141.

16. Degn P, Larsen KL, Duus JØ, Petersen BO, Zimmermann W. Two-step enzymatic synthesis of maltooligosaccharide esters. *Carbohydr. Res*. 2000; **329**: 57-63.
17. Peeling J, Sutherland G. High-Resolution 1H NMR spectroscopy studies of extracts of human cerebral neoplasms. *Magn. Reson. Med.* 1992; **24**: 123-136.
18. Kinoshita Y, Yokota A. Absolute concentrations of metabolites in human brain tumors using *in vitro* proton magnetic resonance spectroscopy. *NMR Biomed.* 1997; **10**: 2-12.
19. Tugnoli V, Tosi MR, Barbarella G, Ricci R, Leonardi M, Calbucci F, Bertoluzza A. Magnetic resonance spectroscopy study of low grade extra and intracerebral human neoplasms. *Oncol Rep* 1998; **5**: 1199-1203.
20. Lehnhardt FG, Bock C, Rohn G, Ernestus RI, Hoehn M. Metabolic differences between primary and recurrent human brain tumors: a 1H NMR spectroscopic investigation. *NMR Biomed.* 2005; **18**. 371-382.
21. Howe FA, Opstad KS. 1H MR spectroscopy of brain tumours and masses. *NMR Biomed.* 2003; **16**: 123-131.
22. Majòs C, Alonso J, Aguilera C, Serralonga M, Coll S, Acebes JJ, Arùs C and Gili J: Utility of proton MR spectroscopy in the diagnosis of radiologically atypical intracranial meningiomas. *Neuroradiology* 2003; **45**: 129-136.
23. Majòs C, Julià-Sapè M, Alonso J, Serralonga M, Aguilera C, Acebes JJ, Arùs C, Gili J. Brain tumor classification by proton MR spectroscopy: comparison of diagnostic accuracy at short and long TE. *AJNR* 2004; **25**: 1696-1704.
24. Barton SJ, Howe FA, Tomlins AM, Cudlip SA, Nicholson JK, Bell BA, Griffith JR. Comparison of *in vivo* 1H MRS of human brain tumors with 1H HR-MAS spectroscopy of intact biopsy samples *in vitro*. *MAGMA* 1999; **8**: 121-128.

Table I. List of ^{1}H and ^{13}C chemical shift (δ, ppm) of metabolites found in HR-MAS spectra of brain tumours [a,b].

entry	Metabolite	δ ^{1}H	δ ^{13}C		Medullobastoma	Meningima
1	Fatty acids	0.89	14.13-14.17	CH_3	y	y
		1.31	29.4-32.2	$(CH_2)_n$		
		1.59-1.60	25.2	$CH_2CC=O$		
		2.02	27.8	$CH_2C=$		
		2.24	34.2	$CH_2C=O$		
		2.78	26.2	$=CCH_2C=$		
		5.30-5.32	130.2; 128.4	CH=CH		
2	Isoleucine	0.94 (t)	11.7	δ-CH_3	y	y
		1.02(d)	15.5	γ-CH_3		
		1.29,1.48	25.1	γ-CH_2		
		1.97		β-CH		
		3.69		α-CH		
3	Leucine	0.95(d)	21.5	δ-CH_3	y	y
		0.97(d)	22.8	δ-CH_3		
		1.70	24.8	γ-CH		
		1.72	40.4	β-CH_2		
		3.74		α-CH		
4	Valine	0.99(d)	17.3	γ-CH_3	y	y
		1.04(d)	18.7	γ-CH_3		
		2.25		β-CH		
		3.61	d	α-CH		
5	Threonine	1.33(d)	20.3	γ-CH_3	y	y
		4.26	66.58	β-CH		
		3.60	61.22	α-CH		
6	Lactate	1.33(d)	20.3	CH_3	y	y
		4.11	69.1	CH		
7	Alanine	1.48(d)	16.8	β-CH_3	y	y
		3.78	51.1	α-CH		
8	Lysine	3.02(t)	39.9	ε-CH_2	y	y
		1.71	27.1	δ-CH_2		
		1.48	22.56	γ-CH_2		
		1.91	30.6	β-CH_2		
		3.79	c	α-CH		
9	Arginine	3.23	41.3	δ-CH_2	y	y
		1.69	24.9	γ-CH_2		
		1.92	28.1	β-CH_2		
		3.78	c	α-CH		
10	Glutamate	2.36(t)	34.0	γ-CH_2	y	y
		2.06, 2.14	27.9	β-CH_2		
		3.77	c	α-CH		
11	Glutamine	2.44(td)	31.5	γ-CH_2	y	y
		2.14	27.2	β-CH_2		
		3.78	c	α-CH		
12	Proline	3.43, 3.34		δ-CH_2	y	n
		2.01		γ-CH_2		
		2.34, 2.07		β-CH_2		
		4.12		α-CH		
13	Aspartic acid	2.68, 2.82	37.2	β-CH_2	y	y
		3.90		α-CH		
14	Asparagine	2.85, 2.96	26.30	β-CH_2	y	y
		4.01		α-CH		
15	Creatine	3.04(s)	37.5	NCH_3	y	y
		3.92(s)	54.5	CH_2		
16	Tyrosine	3.06, 3.20		β-CH_2	y	y
		3.93	56.7	α-CH		
		6.89	116.5	H*ortho*		
		7.23	131.5	H*meta*		
17	Phenylalanine	3.11, 3.28		β-CH_2	y	y
		3.99		α-CH		

		7.34	130.1	H*ortho*		
		7.43	129.6	H*meta*		
		7.37	128.2	H*para*		
20	Ethanolamine	3.15(t)	42.1	CH_2	y	y
		3.82(t)	58.2	CH_2		
21	Phosphoryl-ethanolamine	3.23	41.1	CH_2	y	y
		4.00	61.1	CH_2		
22	Glycerophosphoryl-ethanolamine	3.30		CH_2	y	y
		4.10		CH_2		
23	free Choline	3.20	54.6	$N(CH_3)_3$	y	y
		3.53	68.2	NCH_2		
		4.08	56.5	OCH_2		
24	Glycerophosphoryl-choline	3.22	54.7	$N(CH_3)_3$	y	n
		3.68		NCH_2		
		4.33		OCH_2		
25	Phosphorylcholine	3.22	54.7	$N(CH_3)_3$	y	y
		3.61	67.3	NCH_2		
		4.22	59.0	OCH_2		
26	β-Glucose	4.67(d)	96.6	1-CH	n	y
		3.26	74.8	2-CH		
		3.49	76.8	3-CH		
		3.40	69.9	4-CH		
		3.47	76.8	5-CH		
		e	e	6-CH_2		
27	Taurine	3.26(t)	48.1	SCH_2	y	y
		3.42(t)	35.9	NCH_2		
28	Myo-inositol	3.53(dd)	71.8	1,3-CH	y	y
		4.06(t)	72.9	2-CH		
		3.63(t)	73.1	4,6-CH		
		3.29(t)	75.0	5-CH		
29	Scyllo-inositol	3.35 (s)	73.9	CH	y	y
30	α-Glucose	5.24(d)		1-CH	n	y
		3.54	72.5	2-CH		
		3.73	73.8	3-CH		
		3.42	70.7	4-CH		
		e	e	6-CH_2		
31	Glycine	3.56	42.3	CH_2	y	y
33	Glycerol (in lipids)	4.10, 4.30		1,3-CH_2	n	y
		5.26		2-CH		
34	Glycerol	3.56, 3.65	63.3	1-CH_2	-	y
		3.81	72.7	2-CH		
35	UDPG	5.92		1-CHrib	y	y
		4.35		2-CHrib		
		5.90(d)		5-CHur		
		7.89(d)		6-CHur		
36	Uracil	5.80(d)		5-CHur	n	y
		7.54(d)		6-CHur		
38	Fumarate	6.52		CH	n	y
39	Tryptophane	7.73		4-CH		
		7.19		5-CH		
		7.29		6-CH		
		7.52		7-CH		
40	Adenine	8.23(s)		2-CH	y	y
		8.36(s)		8-CH		
		6.10		1'-CH		
		4.77		2'-CH		
		4.43		3'-CH		
41	N-Ac	2.01-2.12	23.0	$NC{=}OCH_3$		
42	Acetate	1.92	24.8	$CH_3C{=}O$	y	y
43	Hypotaurine	2.65(t)	38.73	CH_2	-	y
		3.35(t)	41.19	CH_2		
44	UMP	5.98		1-CHrib	n	y

		4.37		2-CHrib		
		5.97(d)		5-CHur		
		8.11(d)		6-CHur		
45	α-Glu-(1→4)	5.39,5.41	100.2	1-CH	n	y
		3.62	72.2	2-CH		
		3.98	74.0	3-CH		
		3.68	77.2	4-CH		
		3.73	73.5	5-CH		
46	Glutathione	4.57	56.18	α-CH-Cys	n	y
		2.96	26.3	β-CH_2-Cys		
		3.80		α-CH-Glu		
		2.16		β-CH_2-Glu		
		2.55		γ-CH_2-Glu		
		3.77	44.0	CH_2-Gly		
		8.57		NH-Cys		
		8.36		NH-Gly		
47	OH-butyrate	1.18		CH_3	n	y
		4.14				
48	Histidine	7.78 (s)		2-CH	n	y
		7.05(s)		4-CH		
49	Ascorbate	4.52(d)		4-CH	-	y
		4.01		5-CH		
50	β-Alanine	2.56	32.14	CH_2	-	y
		3.18	40.01	CH2		
51	Serine	3.96	61.2	1,3-CH_2	n	y
		3.84	57.0	2-CH		

a ^{1}H chemical shift are referred to alanine doublet at 1.48 ppm.
b ^{13}C chemical shift are referred to alanine at 16.8 ppm.
c C_ probably contributes to the 3.77, 55.1 ppm cross-peak.
d C_ probably contributes to the 3.61, 61.1 ppm cross-peak.
e Contribute to the broad correlation between CH_2 protons in the region 3.9-3.6 ppm and carbons around 62 ppm in HSQC spectra.

HIGH- AND LOW-GRADE GLIOMAS

Glioma is a type of primary central nervous system (CNS) tumour that arises from glial cells. The most common site of involvement of gliomas is the brain, but gliomas can also affect the spinal cord or any other part of the CNS, such as the optic nerves (1). Gliomas can be either benign (slow growing) or malignant (fast growing). Gliomas are further categorized according to their grade, which is determined by pathologic evaluation of the tumour. Low grade gliomas are well-differentiated (not anaplstic); these are begnin and portend a better prognosis of the tumour. High-grade gliomas are undifferentiated or anaplastic; these are malignant and carry a worse prognosis.

Adequate discrimination between high and low glioma grade remains a vital diagnostic decision determining the most effective chemotherapeutic or surgical treatment and having an important impact in patient management and outcome (2-5). *In vivo* ^{1}H NMR spectroscopy examinations are often used to assign glioma grade, many times based on the relative intensities of the total Choline (tCho) and Cr resonances in the tumour (6-8). This diagnostic decision has been helped more recently through the implementation a variety of pattern recognition methodologies (9). The accuracy of these methods is increasing progressively, but difficulties remain currently in the unambiguous classification of high and low grade gliomas. This may be due to the fact that *in vivo* ^{1}H NMR spectroscopy approaches as available in the clinic, are normally limited in sensitivity and resolution, resulting in relatively large voxel volumes and insufficient precision in the spectral assignments. In particular, the *in vivo* tCho peak, normally found to increase in high and low grade gliomas, contains contributions from a variety of choline containing metabolites including mainly, free choline (Cho), phosphorylcholine (PC) and glycerolphosphorylcholine (GPC). In spite of the crucial information that these metabolites could provide on the alterations of phospholipid metabolism underlying transformation and progression of astrocytomas, their relative contribution to the combined Cho peak cannot be derived from the *in vivo* detected tCho resonance. HR-MAS approaches have been recently proposed to investigate normal and diseased tissues, to overcome some of the limitations of *in vivo* spectroscopy (10,11). The HR-MAS approach uses small biopsies of the tumours, providing similar sensitivity and resolution to that previously obtained from the high resolution ^{1}H NMR analyses of tumour

extracts. However, few studies to date have investigated the metabolism of choline derivatives in human gliomas using this methodology (12,13).

Genomic approaches in tumours are currently envisioned to provide complementary information to the metabolic pattern obtained by HR-MAS, revealing the genomic "finger print" of the tumour (14). In this respect, DNA microchips provide comprehensive information on complete genome expression but the analysis of the fifty seven thousand genes dataset normally investigated is complex, and much of the information obtained is unrelated to the genes controlling choline transport and metabolism (15). The use of microfluidic cards containing exclusively the genetic probes for the pathway of interest may provide a valuable alternative, thus reducing the complexity of the genomic analysis and interpretation.

In this work we hypothesized that HR-MAS could improve the performance of *in vivo* clinical ^{1}H NMR because of its enhanced resolution of the choline compounds and that the microfluidic card analysis of the expression of choline metabolism genes could provide complementary information to interpret the observed HR-MAS alterations. Our results indicate that it is possible to discriminate unambiguously between high grade and low grade gliomas on the basis of the choline metabolite profile as detected by HR-MAS and quantified with the LCModel program. The increased choline peak observed in high grade gliomas is shown to be derived from an increase in phosphorylcholine while the increase in the tCho peak detected in low grade gliomas is caused by augmented glycerolphosphorylcholine content. The changes detected by ^{1}H HR-MAS are consistent with the upregulation of the choline kinase β or phospholipase C genes and the downregulation of the cytidyltransferase gene in high grade gliomas or the upregulation of Phospholipase A and lysophospholipase and the downregulation of phosphoilipase D detected in low grade gliomas.

Methods

Clinical Materials. Tumour specimens were provided by the Department of Neurosurgery, Univerisity Hospital "La Paz", Madrid, complying with all bioethical criteria of the local ethics committee of the Hospital. Tumour biopsies were obtained from the patients in the operating room following intracranial surgery, immediately frozen in liquid nitrogen and stored at -70° C until ^{1}H HR-MAS analysis. An adjacent biopsy of the tumour was obtained for histological classification. Tumour specimens from 23 patients were histologically classified according to the revised WHO criteria. The samples included 9 low-grade astrocytomas (WHO grade II), 6 anaplastic astrocytomas (WHO grade III) and 8

glioblastoma multiforme (WHO grade IV) (16). Grades III and IV were grouped as "high grade" gliomas, to favour a more robust clinical classification between low and high grade gliomas. Normal brain samples were obtained from patients undergoing partial lobotomy indicated in the treatment of epileptic seizures (17). The main goal of our work was to distinguish between low and high grade gliomas of our work was to classify gliomas between low and high grades.

Quantification. Quantification of tumor metabolites detectable in the *ex vivo* spectra was performed using the software program LCModel (Linear Combination of Model Spectra, (18)). LCModel fits spectra as a linear combination of model spectra from twenty eight brain metabolites and optional contributions for lipids and macromolecules. For the analysis of our *ex vivo* data a customized set of cerebral metabolites was prepared using the model solutions recommended by Dr. S. Provencher including; alanine, lactate, taurine, phosphocreatine, creatine, choline, glycerolphosphorylcholine, phosphorylethanolamine, phosphorylcholine, glycine, aspartic acid, glutamine, glutamate, myo inositol, N-acetyl-aspartate, acetate, threonine, glutathione, valine, isoleucine, leucine, glucose and GABA. The LC Model program found the best fit between the spectrum of the biopsy and the linear combination of the metabolite components, yielding values of metabolite content (μmol/g wet weight), with the fitting error expressed as the SD. Only metabolite fittings with errors below 20% SD were included in the final analysis. Since accurate tissue content and volume distribution in the HR-MAS rotor is difficult to determine, relative concentrations to the total choline or creatine peaks were used in the calculations.

Sample preparation and RNA extraction. Total experimental RNA was prepared from biopsies of normal brain and tumours using the RNAspin Mini RNA Isolation Kit (GE Healthcare). Approximately 20 mg biopsies were used. The purity and integrity of the labelled cRNA was evaluated from the A_{260}/A_{280} ratio and on an Agilent 2100 bioanalyzer, being always between 1.9-2.1. RNA integrity number was evaluated using the Agilent 2100 bioanalyzer, assuming appropriate intensities as those depicting 28S:18S ratio higher than 2. RNA Integrity Number (RIN) values were normally ≥7.

The human tissues are solid (preserved at -80° C) and must therefore be broken up mechanically as well as lysed. About 20 mg of biopsy are uded and it is grinding with a pestle and mortar for disruption. Grid the sample to a fine powder in the presence of liquid N_2. Add 350 μl buffer RA1 and 3,5 μl β-mercaptoethanol to ground tissue and vortex vigorously, filtered the lysate for clear and reduce viscosity through RNAspin Mini Filter

units, centrifuge for one minute at 11000g, add 350 µl ethanol (70%) to the homogenized lysate and mix by vortexing. For each preparation use one RNAsion Mini column placed in a 2 ml microcentrifuge. Pipet lysate up-and-down 2-3 times and then load the lysate onto the colum. Centrifugate for 30s at 8000g. Add 350 µl MDB (Membrane Desalting Buffer) and centrifuge at 11000g for 1 minute to dry the membrane. (Prepare the DNase reation mixture in a sterile microcentrifuge tube: for each isolation, add 10 µl reconstituted DNase I to 90 µl DNase reaction buffer). Apply 95 µl of DNase reaction mixture directly into the center of the silica membrane of the column and the incubate at room temperature for 15 min. Wash and dry silica membrane with 200 µl buffer RA2 and centrifuge at 11000g for 1 minute (the RA2 will inactive DNase I), a second wash with 600 µl buffer RA3 and centriguge at 11000g for 1 minute, and another wash with 250 µl buffer of RA3 and centrifuge at 11000g for 2 minute to dry the membrane completely. Elute the RNA in 100 µl H_2O and centrifuge at 11000g for 1 minute. Eluted RNA was immediately placed on the ice to prevent potential degradation and stored at -80° C.

Analysis of gene expression using microfluidic cards. The expression of the genes of the choline pathway was assayed using the individual probes for each gene as commercialized by Applied Biosystems using the Agylent 2100 analyzer (Foster City, CA, USA). TaqMan® probes for Gene Expression provide the most comprehensive set of pre-designed Real-Time PCR assays available including specifically most genes of the Kennedy pathway. All TaqMan® Gene Expression Assays were run with the same PCR protocol, eliminating the need for primer design or PCR optimization. Table I summarizes the transporters or enzymes of choline metabolism and the corresponding genes investigated in this study. The expression profiles of the different genes in tumor and healthy brain tissue were compared, assuming as a unit the value of the corresponding gene expression in the healthy brain.

Statistical analysis. From the LCModel analysis 6 variables were selected and tested as possible classifiers to differentiate between Low and High grade gliomas: Cho/tCho, GPC/tCho, PC/tCho, Cho/Cr, GPC/Cr, PC/Cr. For this purpose a Logistic Regression (LR) was applied. LR regresses a dichotomous dependent variable (Low or High Grade) on a set of independent variables (19,20)(Cho/tCho, GPC/tCho, PC/tCho, Cho/Cr, GPC/Cr, PC/Cr). Backward stepwise was used to select independent variables. Basically, the method enters all the variables (or interaction terms) together into the model and then the variables are tested for removal one by one. Also, another variable (tCho/Cr), which is assumed to be an

approximation to the *in vivo* situation, was tested by the same LR method to differentiate between Low and High Grade.

For NMR experiment details see Chapter 2

Table I. Transporters or enzymes of choline metabolism and the corresponding genes investigated.

	Enzyme or Transporter	Abbreviation	Gene Name	Assay ID
1	Choline transporter		CTL1	Hs00223114_m1
			CTL2	Hs00220814_m1
2	Choline kinase (EC 2.7.1.32)	ckα	CHKA	Hs00608045_m1
		ckβ	CHKB	Hs00193219_m1
3	Phosphocholine cytidylyltransferase (EC 2.7.7.15)	ctα	PCYT1A	Hs00192339_m1
		ctβ	PCYT1B	Hs00191464_m1
4	Phosphocholine transferase (EC 2.7.8.2)	ptc	CHPT1	Hs00220348_m1
5	Phospholipase D (EC 3.1.4.4)	plD1	PLD1	Hs00160118_m1
		plD2	PLD2	Hs00160163_m1
6	Lysophospholipase (EC 3.1.1.5)	lpl	LYPLA1	Hs00272216_s1
7	Glycerol-3-phosphate acyltransferases (EC 2.3.1.15 and EC 2.3.1.51)	at	GPAM	Hs00326039_m1
8	Phospholipase C (EC 3.1.4.3)	plC	PLCG1	Hs00234046_m1
10	Phospholipase A2 (EC 3.1.1.4)	plA2 VI	PLA2G6	Hs00185926_m1
		plA2 IV	PLA2G4A	Hs00233352_m1
11	Phospholipase A1 (EC 3.1.1.32)	plA1	PLA1A	Hs00210729_m1
12	Phosphatidate Phosphohydrolase (EC 3.1.3.4)	pap	PPAP2A	Hs00170356_m1

Results and Discussion

Figure 1 shows representative ^{1}H HR-MAS 1D spectra of healthy brain (1a), low and high grade gliomas (1b and 1c), respectively. The main metabolites observed include: Lac, γ-amino butyric acid (GABA), of NAA, Glx, creatine/phosphocreatine (Cr/PCr), Cho, GPC, PC, Myo. The broadened signals in the spectra originate from the presence of lipids and

macromolecules (MM).

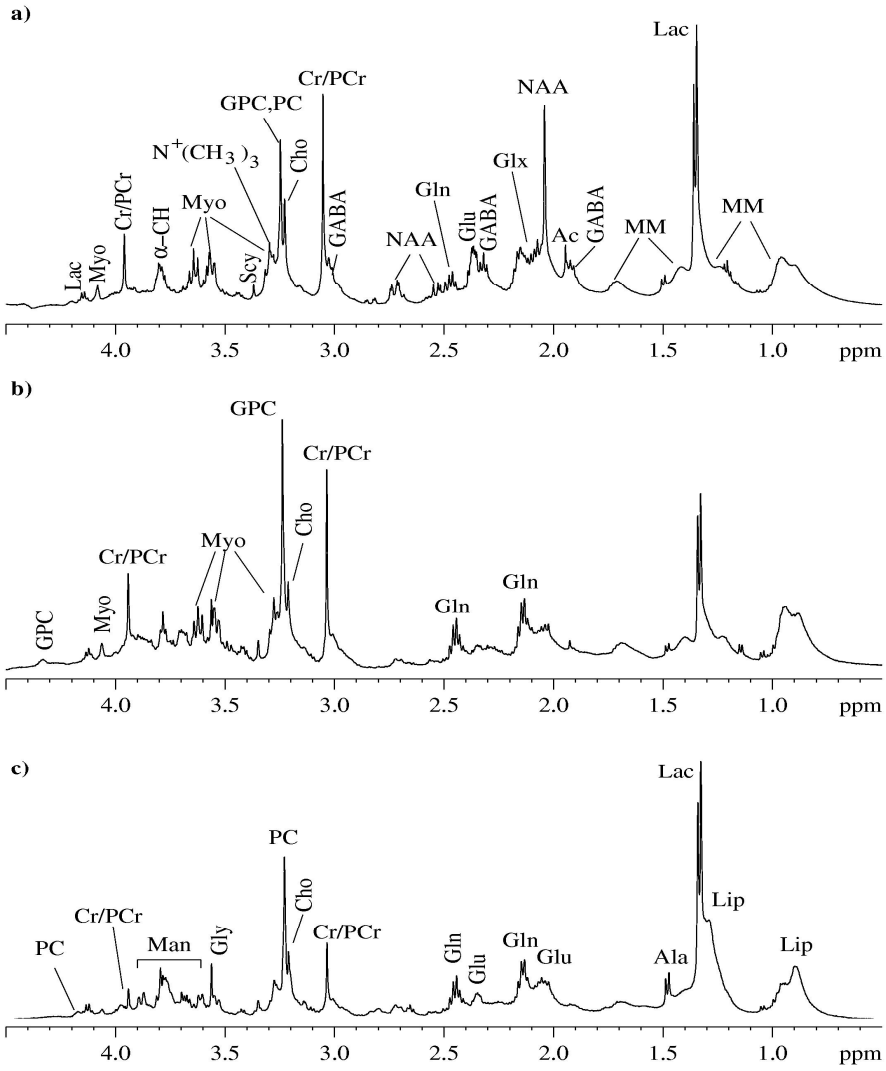

Figure 1. *Ex vivo* 1D water-presaturated ^{1}H HR MAS NMR spectra: a) healthy brain tissue, b) low glioma and c) high glioma grade.

The comparison between the glioma and the normal brain spectra show the decrease, or absence, of the neuronal markers NAA and GABA and a progressive increase in the lipid content (see resonances ca. 0.89 ppm), from low to high grade gliomas.

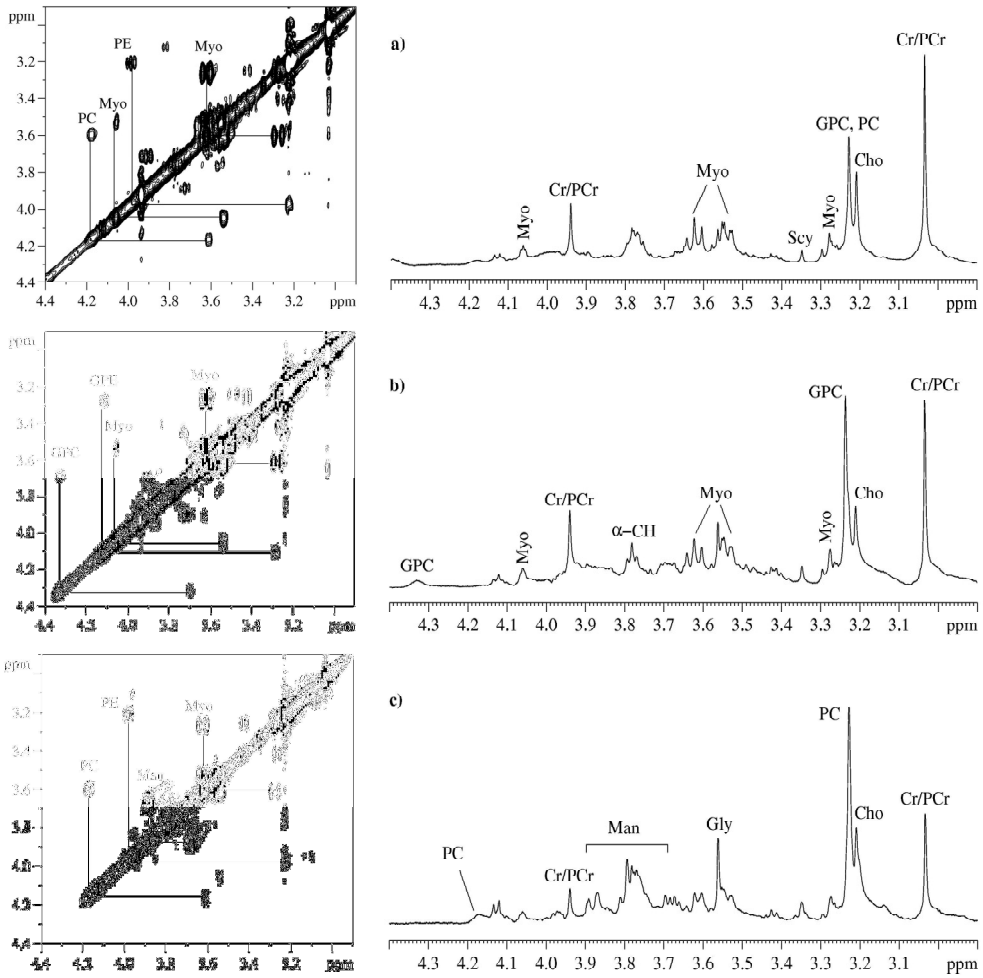

Figure 2. Left: the partial COSY spectra of a) healthy brain, b) low grade and c) high grade. Right: the partial CPMG spectra of a) healthy brain, b) low grade and c) high grade.

The spectra show significant differences in the 3.22 ppm region corresponding to choline metabolites. This region is expanded in Figure 2, to better illustrate the increased resolution attained through the use of 1D CPMG spectra (total spin-echo time $2n\tau$ = 144 ms, figure 2 right panels). Under these conditions, the broad resonances from lipids or macromolecules are attenuated from the spectra, and mainly low molecular weight metabolites become observable. Figure 2 illustrates the typical metabolic profile of healthy brain (2a), low (2b) and high (2c) grade gliomas in the region from 3.0 to 4.4 ppm. The most noticeable difference between healthy and diseased tissue is the increased of the Cho-containing metabolites both in low and high grade gliomas. GPC appeared to be the main contributors to the total choline increase in low grade gliomas, whereas in high grade gliomas, PC depicted the dominant contribution. A more detailed inspection of the corresponding 2D COSY ^{1}H HR-MAS spectra (left panels) confirmed GPC as the dominant contributor to the

total choline peak in low grade and PC in the high grade gliomas. It is interesting to show that the 2D approach allows the identification of additional metabolites like ethanolamine (E), Tau, and PE, not detectable in 1D spectra of the same biopsies. Interestingly, Mannitol (Man), a compound normally used during surgery of high grade gliomas to decrease cerebral oedema, is clearly detected in many of these spectra. However, these spectra provide only qualitative information on the choline containing metabolites of each tumour. To achieve a more quantitative interpretation we adapted the LC Model approach, currently used for in vivo spectroscopy (21,22), to the quantitative processing of ^{1}H HR-MAS spectra.

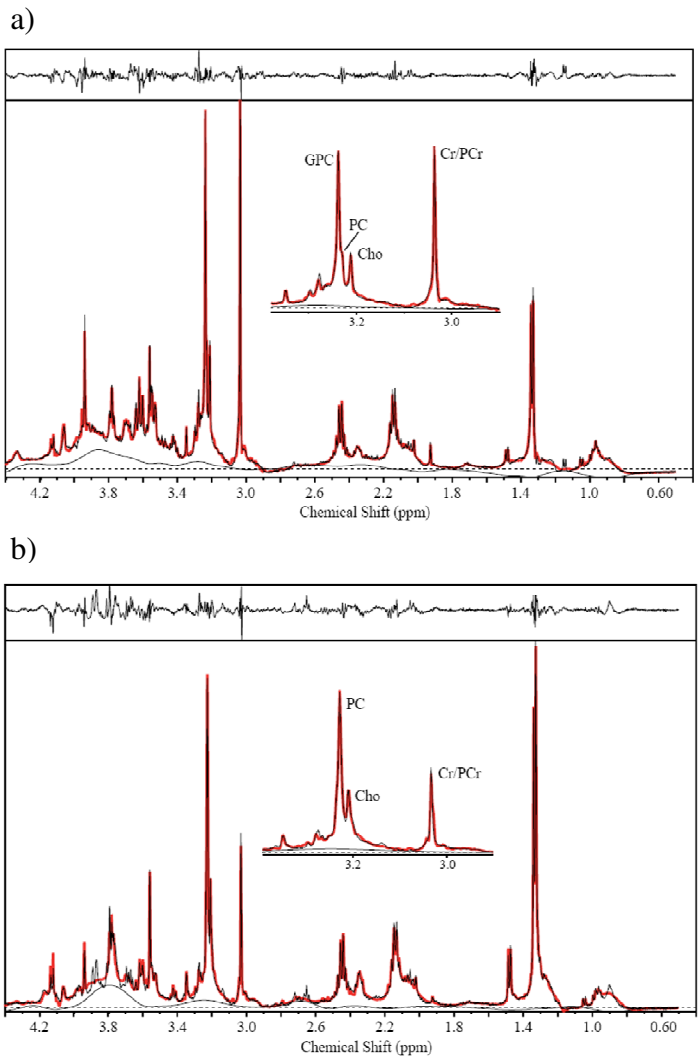

Figure 3. ^{1}H CPMG spectra acquired from low glioma grade (a) and a high glioma grade (b). Top row: differences between spectrum obtained from biopsis and the simulated spectrum obtained using the new metabolites data set.

Figure 3 illustrates representative LCModel fits of HR-MAS spectra from low (panel a) and high (panel b) grade glioma biospies, respectively. The corresponding inserts show the

expanded regions containing the choline and creatine resonances. The use of LCModel allows the correct quantification of the complete metabolite profile of the tumour, rather than providing isolated deconvolutions of specific resonances. This allows the proper fit of partially overlapping resonances, such as those of PC, GPC and Cho. In particular, the insert to Figure 3a depicts more clearly the higher contribution of GPC to the tCho resonances, the PC contribution remaining very low. In this case, the GPC content, appears to reach the same intensity as the Cr/PCr combined resonance. The metabolic profile shown in the insert to Figure 3b is clearly different, showing a dominant contribution of the PC peak with a virtually undetectable contribution of GPC. In the high grade tumours, the combined Cr/PCr resonance is decreased.

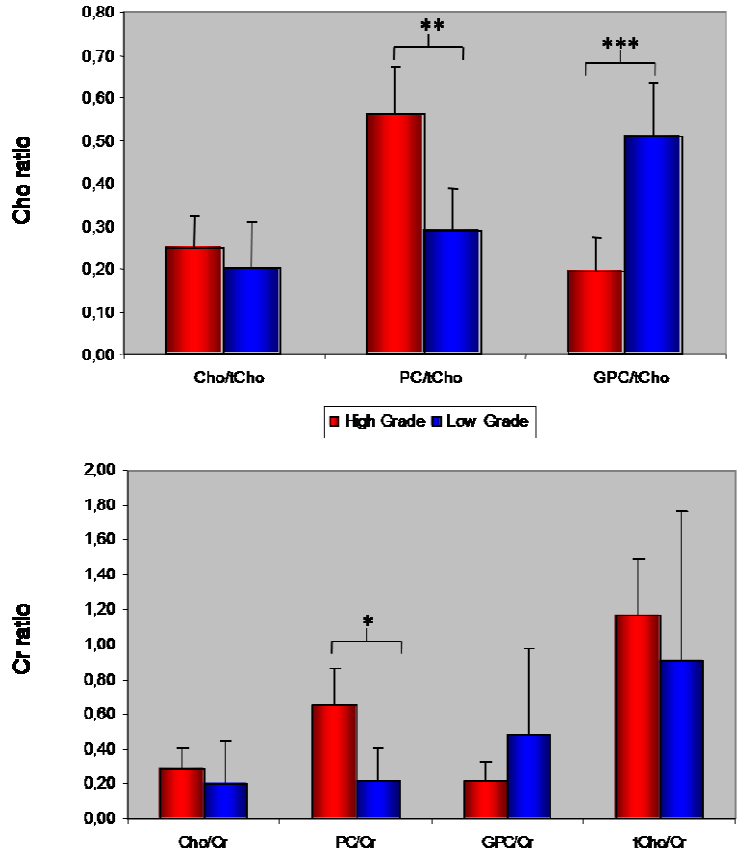

Figure 4. Report a relative contribution of Cho, PC and GPC respect to tCho (a) and to Cr (b). Mean differences were statistically compared by performing a Student t-test. *(P<0.05), **(P<0.005), ***(P<0.001).

Figure 4 summarizes the results obtained in the LC Model quantification of the ratios of free choline, PC and GPC to either total choline (panel a) or total creatine (panel b) peaks. While the ratios to the creatine peak do not provide an accurate differentiation between low

and high grade gliomas, the relative contributions of PC and GPC to the total choline resonance depict statistically significant differences between low and high grade gliomas.

Up till now it has been shown that the means of PC/tCho and GPC/tCho are statistically different when comparing low and high grade glioma. However, in order to find classifiers that discriminate between both tumours types, Logistic Regression analysis was performed. The independent variables tested by the LR analysis were Cho/tCho, PC/tCho, GPC/tCho, Cho/Cr, PC/Cr and GPC/Cr. From these, Cho/tCho, PC/tCho and GPC/tCho were selected as classifiers (Table II). The combination of these three variables allows the 100% of the tumours to be discriminated between low and high grade glioma (Table III and Figure 5).

Table II. Selected Variables for Classification

		B
Step 4(a)	Cho/tCho	8132,223
	PC/tCho	9118,222
	GPC/tCho	7775,408
	Constant	-8359,676

Table III. Classification based on Logistic Regression analysis.

		Observed	**Predicted Groups**		**Percentage Correct**
			Low	High	
Step 4	Grade	Low	8	0	100,0
		High	0	7	100,0
		Overall Percentage			100,0

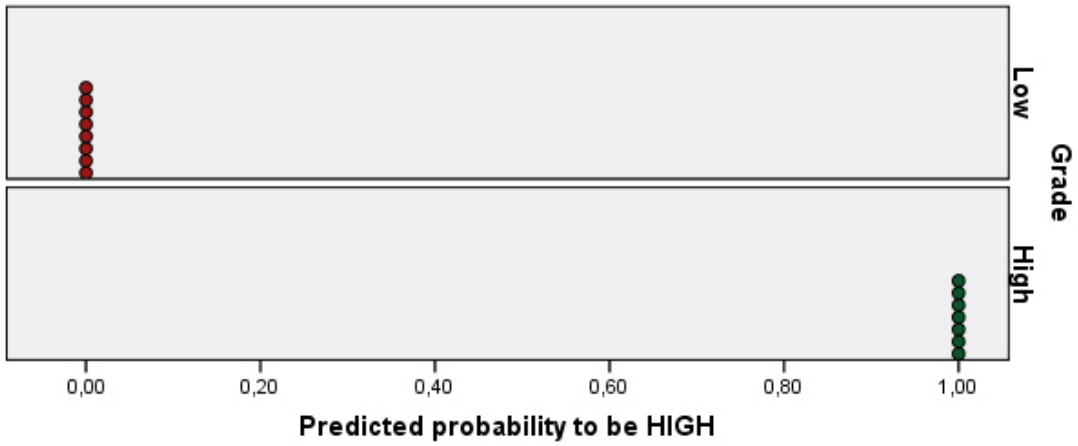

Figure 5. Predicted probability obtained from the LR analysis for the classification of Low and High Grade Gliomas using Cho/tCho, GPC/tCho and PC/tCho ratios as a classification variables.

The classification using the relative contributions of Cho, PC and GPC to tCho, which can only be calculated from high resolution spectroscopic data, was compared with the classification provided by the tCho/Cr ratio. This last variable was chosen as an approximation to the information obtainable from *in vivo* spectra (23). For this purpose a similar LR analysis was performed, yielding a much worse classification for Low and High grade Gliomas (Table IV and V and Figure 6).

Table IV. Selected Variable (tCho/Ct) for Classification

		B
Step 1(a)	tChoCr	1,053
	Constant	-1,164

(a) Variable(s) entered on step 1: tChoCr.

Table V. Classification based on Logistic Regression analysis.

Observed			**Predicted**		
			Grade		**Percentage Correct**
			Low	High	
Step 1	Grade	Low	7	1	87,5
		High	2	5	71,4
		Overall Percentage			80,0

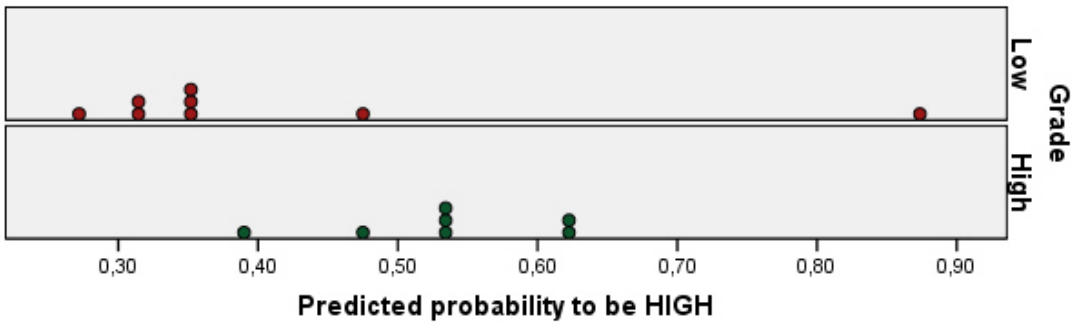

Figure 6. Predicted probability obtained from the LR analysis for the classification of Low and High Grade Gliomas using tCho/Cr ratio as the classification variable.

Figure 7 depicts the expression of the genes of choline metabolism in high grade (red) and low grade (blue) glioma biopsies relative to the expression found in normal brain, using the microfluidic cards approach.

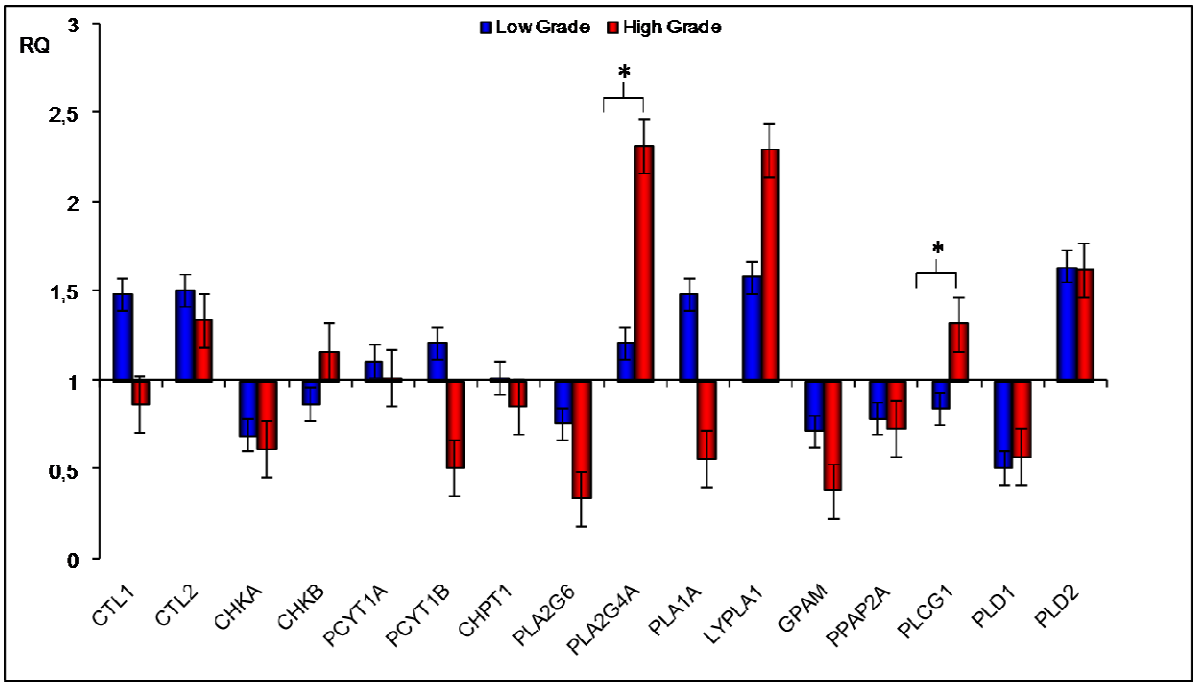

Figure7. Genes expression of the enzymes involve in the Choline Cycles in low and high grade of glioma tumours. X: the single gene, Y: the Relative Quantification (RQ) of the expression of the each gene. Mean differences were statistically compared by performing a Student t-test. *($P<0.05$). When RQ>1 the genes are upregulated, while RQ<1 the genes are downregulated, in comparison with healthy tissues RQ=1.

Ratios with values higher or lower than one reveal upregulation or downregulation of the corresponding gene as compared to its expression in the normal brain. In high grade gliomas, the following genes were found to be upregulated; choline transporter (CTL2),

choline kinase (CHKβ), phospholipases A, C and D (PLA2G4A, PLCG1 and PLD2) and lysophospholipase (LYPLA1), the upregulation being significant in phospholipases A and C. The remaining genes investigated in high grade gliomas were downregulated. In the low grade gliomas, upregulated genes were; choline transport (CTL1, CTL2), cytidylyl-transferase (PCYT1A, PCYT1B), phospholipases A and D (PLA2G4A, PLA1A and PLD2) and lysophospholipase (LYPLA1), the remaining being downregulated. Notably, some genes were upregulated in high grade gliomas and downregulated in low grade gliomas as choline kinase (CHKβ) and phospholipase C (PLCG1) while others were upregulated in low grade gliomas and downregulated in high grade gliomas as the choline transporter (CTL1), citydyltransferase (PCYT1B) and phospholipase A (PLA1A). Of these, only the differences in phospholipase C (PLCG1) upregulation and downregulation between high grade and low grade gliomas, became statistically significant. In general, high grade gliomas depicted significantly upregulated phospholipase A_2 and C expression as compared to low grade gliomas.

The present work illustrates how *ex vivo* ^{1}H HR-MAS analysis of tissue biopsies can help in the discrimination of high grade and low grade human astrocytomas, by investigating quantitatively the profile of choline containing metabolites. Previous studies have used ^{1}H HR-MAS to investigate the metabolic profile of cerebral tumors (12,13,24). These initial studies described the methodology and provided the assignments, but the spectral information remained at the qualitative level without the implementation of multivariate statistical methodologies. In general, the analysis of the resonances from choline containing compounds remained limited, since they overlapped to some extent and it is not possible to obtain accurate quantification without the use of adequate spectral deconvolution algorithms.

The present work overcomes this limitation by implementing a robust procedure for the quantification of the different choline containing compounds in ^{1}H HR-MAS spectra using the LCModel approach. LC Model allows to obtain the relative quantification of the complete metabolite profile of the biopsy, using a linear combination of the spectra of the different metabolites. In our case, we used a database containing the spectra of twenty three cerebral metabolites to calculate the corresponding linear combination that would optimally fit the experimental spectrum. In this report we focus only in the profile of choline containing metabolites. Our results show that the total choline peak is elevated both in low grade and high grade gliomas, but the profile of choline containing metabolites underlying

this increase is different in both cases. We show here that the total choline peak increase is derived from an increase in phosphorylcholine in high grade gliomas and an increase in glicerolphosphorylcholine in low grade gliomas. This results in a characteristic choline metabolite pattern in high and low grade gliomas, that allows the unambiguous classification of our complete data base of sixteen biopsies of human gliomas.

An important aspect of the present study is the genetic basis of the metabolite alterations observed by ^{1}H HR-MAS. Current molecular biology concepts indicate that the sequence of genetic information proceeds from the genome, to the transcriptome, to the proteome and finally to the metabolome. On this basis, it seems reasonable to propose that the genome constitutes the ultimate determinant of the metabolic phenotype or metabolome. Few studies have investigated previously this aspect (25)(Cheng1997). In many cases, high resolution ^{1}H NMR spectra of body fluids were used to investigate global system dynamics in drug metabolism and its disturbances (26) or the relationship between HR MAS spectra of tumor biopsies and the complete genome analysis (14). Much less information is available on the relative expression of the genes of the Kennedy pathway and the pattern of choline metabolites as detected by ^{1}H HR MAS.

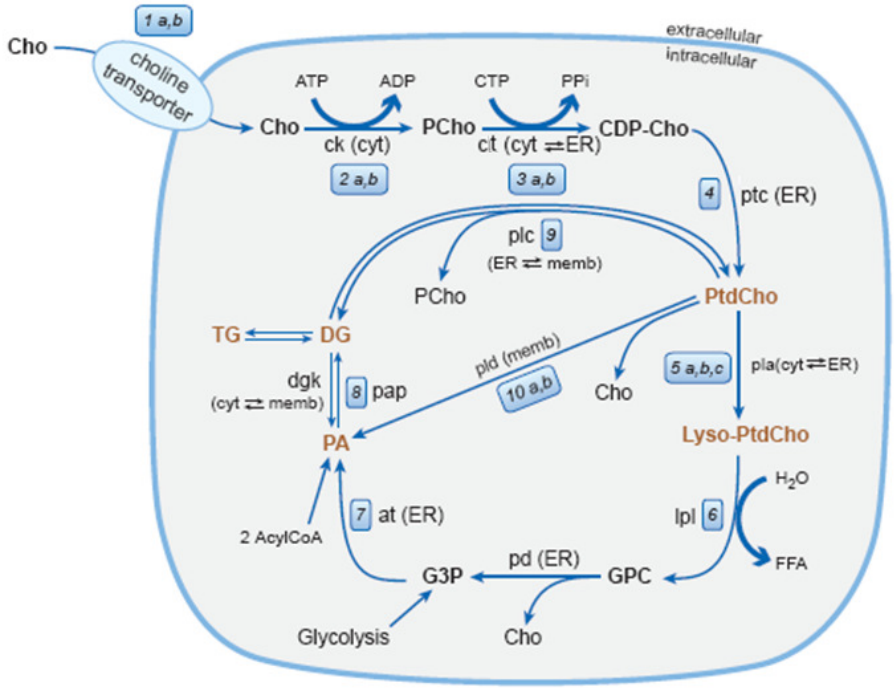

Figure 8. Choline metabolic patway. Cellular compartemnts: ER, endoplasmatic reticulum; cyt, cytosol; memb, membrane.

Figure 8 provides an adequate frame to discuss these aspects, by showing in more detail the metabolism of choline phospholipids, the enzymes involved and the different genes

coding for them (*ck,* choline kinase; *ct,* cytidylyl-transferase; *ptc,* phosphocholine cytidylyl-transferase; *pla,* phospholipase A_1 and A_2; *lpl,* lysophospholipase; *pd,* glycerophosphocholine phosphodiesterase; *at*, glycerol-3-phosphate acyltransferases; *plc,* phospholipase C; *pld,* phospholipase D).

Modern gene expression technologies allow to investigate specifically the genes related to a specific pathway, rather than the complete genome as previously done. In this work, we used microfluidic cards to investigate the expression of sixteen genes of the choline metabolism, to improve our understanding of the genetic basis of the metabolic profile of choline metabolites observed by ^{1}H HR-MAS. The most interesting changes found are those corresponding to genes depicting a crossover of genetic expression, becoming upregulated in one type of gliomas and downregulated in the other. The increase in PC in high grade gliomas can be explained by the increase in the expression of the choline kinase β gene and the phospholipase C gene, respectively. Several authors have described increases in the expression of the genes of choline transport (27) and choline kinase (28,29). Our results confirm these, suggesting that it is the gene of the choline transporter β or the choline kinase β are the ones responsible for the increase in the corresponding processes. In addition we show that there are significant increases in the expression of the phospholipase C gene in high grade gliomas, another potential source of PC. This is, to our knowledge a novel finding, indicating that the increase in PC is derived not only from an increase in its synthesis by choline kinase but by an increase degradation of phosphatodylcholine through the phosphoilipase C pathway. Taken together these results suggest an increase in the turnover rate of phosphatidylcholine with glioma grade. Moreover, some cancer therapies have proposed the use of choline kinase inhibitors (28,30,31). Present results indicate that the additional inhibition of the phospholipase C pathway, may provide a very useful complement of these therapies. The increase in GPC in the low grade gliomas reflects a positive balance between its production and degradation pathways. Net GPC synthesis is favoured by the increased expression of the choline transporter gene (α-isoform), cytidylyl-transferase gene (β isoform) and phospholipase A, respectively. GPC breakdown may be reduced because of the decrease in glycerol 3-phosphtae acyltransferase. In addition the relative amount of GPC to PC in low grade gliomas may be also favourable to the former, because of the reduced expression of the phospholipase C gene in low grade gliomas. Summarizing, the net balance between increased synthesis, reduced degradation and diminished PC synthesis through phospholipase C, may lead ultimately to relative GPC accumulation in low grade gliomas. This is an interesting

finding since only one previous study to our knowledge, reported on the genes regulating GPC metabolism in mammary tumours (32,33).

In summary, we provided a novel application of ^{1}H HR-MAS spectroscopy to the classification of human glioma biopsies. Our results show that high and low grade gliomas are characterized by increases in PC or GPC, respectively, and that these appear to be reflected by changes in the expression of the genes of the Kennedy pathway of choline metabolism.

References

1. Mamelak AN, Jacoby DB. Targeted delivery of antitumoral therapy to glioma and other malignancies with synthetic chlorotoxin (TM-601). *Expert. Opin. Drug Drliv.* 2007; **4**: 175-186.
2. Negendank WG, Sauter R, Brown TR, Evelhoch JL, Falini A, Gotsis ED, Heerschap A, Kamada K, Lee BC, Mengeot MM, Moser E, Padavic-Shaller KA, Sanders JA, Spraggins TA, Stillman AE, Terwey B, Vogl TJ, Wicklow K, Zimmerman RA. Proton magnetic resonance spectroscopy in patients with glial tumors: a multicenter study. *J Neurosurg* 1996; **84**: 449-458.
3. Lafuente JV, Alkiza K, Garibi JM, Alvarez A, Bilbao J, Figols J, Cruz-Sanchez FF. Biologic parameters that correlate with the prognosis of human gliomas. *Neuropathology* 2000; **20**: 176-183.
4. Narayana A, Chang J, Thakur S, Huang W, Karimi S, Hou B, Kowalski A, Perera G, Holodny A, Gutin PH. Use of MR spectroscopy and functional imaging in the treatment planning of gliomas. *Br J Radiol* 2007; **80**: 347-354.
5. Galanaud D, Chinot O, Metellus P, Cozzone P. Magnetic resonance spectroscopy in gliomas. *Bull Cancer* 2005; **92**: 327-331.
6. Yerli H, Agildere AM, Ozen O, Geyik E, Atalay B, Elhan AH. Evaluation of cerebral glioma grade by using normal side creatine as an internal reference in multi-voxel 1H-MR spectroscopy. *Diagn Interv Radiol* 2007; **13**: 3-9.
7. McKnight TR, Lamborn KR, Love TD, Berger MS, Chang S, Dillon WP, Bollen A, Nelson SJ. Correlation of magnetic resonance spectroscopic and growth characteristics within Grades II and III gliomas. *J Neurosurg* 2007; **106**: 660-666.
8. Chen CY, Lirng JF, Chan WP, Fang CL. Proton magnetic resonance spectroscopy-guided biopsy for cerebral glial tumors. *J Formos Med Assoc* 2004; **103**: 448-458.
9. McKnight TR. Proton magnetic resonance spectroscopic evaluation of brain tumor metabolism. *Semin Oncol* 2004; **31**: 605-617.
10. Tzika AA, Cheng LL, Goumnerova L, Madsen JR, Zurakowski D, Astrakas LG, Zarifi MK, Scott RM, Anthony DC, Gonzalez RG, Black PM. Biochemical characterization of pediatric brain

tumors by using in vivo and ex vivo magnetic resonance spectroscopy. *J Neurosurg* 2002; **96**: 1023-1031.

11. Cheng LL, Chang IW, Louis DN, Gonzalez RG. Correlation of high-resolution magic angle spinning proton magnetic resonance spectroscopy with histopathology of intact human brain tumor specimens. *Cancer Res* 1998; **58**: 1825-1832.
12. Martinez-Bisbal MC, Marti-Bonmati L, Piquer J, Revert A, Ferrer P, Llacer JL, Piotto M, Assemat O, Celda B. 1H and 13C HR-MAS spectroscopy of intact biopsy samples ex vivo and in vivo 1H MRS study of human high grade gliomas. *NMR Biomed* 2004; **17**: 191-205.
13. Valonen PK, Griffin JL, Lehtimaki KK, Liimatainen T, Nicholson JK, Grohn OH, Kauppinen RA. High-resolution magic-angle-spinning 1H NMR spectroscopy reveals different responses in choline-containing metabolites upon gene therapy-induced programmed cell death in rat brain glioma. *NMR Biomed* 2005; **18**: 252-259.
14. Tzika AA, Astrakas L, Cao H, Mintzopoulos D, Andronesi OC, Mindrinos M, Zhang J, Rahme LG, Blekas KD, Likas AC, Galatsanos NP, Carroll RS, Black PM. Combination of high-resolution magic angle spinning proton magnetic resonance spectroscopy and microscale genomics to type brain tumor biopsies. *Int J Mol Med* 2007; **20**: 199-208.
15. Podo F. Tumour phospholipidmetabolism. *NMR Biomed.* 1999; **12**: 413-439.
16. Biernat W. 2000 World Health Organization classification of tumors of the nervous system. *Pol J Pathol* 2000; **51**: 107-114.
17. Pascual JM, Carceller F, Cerdán S, Roda JM. Diagnóstico diferencial de tumores cerebrales "in vitro" por espectroscopía de resonancia magnética de protón. Método de los cocientes espectrales. *Neurocirugía* 1998; **9**: 4-10.
18. Provencher SW. Estimation of metabolite concentrations from localized in vivo proton NMR spectra. *Magn Reson Med* 1993; **30**: 672-679.
19. Agresti A. *Categorical Data Analysis*, 2nd ed. Nueva York: John Wiley and Sons. 2002.
20. Tatsuoka MM. *Multivariate analysis*. Nueva York: John Wiley & Sons, Inc.1971.
21. Opstad KS, Bell BA, Griffiths JR, Howe FA. An investigation of human brain tumour lipids by high-resolution magic angle spinning (1)H MRS and histological analysis. *NMR Biomed* 2008.
22. Kanowski M, Kaufmann J, Braun J, Bernarding J, Tempelmann C. Quantitation of simulated short echo time 1H human brain spectra by LCModel and AMARES. *Magn Reson Med* 2004; **51**: 904-912.
23. Kim JH, Chang KH, Na DG, Song IC, Kwon BJ, Han MH, Kim K. 3T 1H-MR spectroscopy in Grading of cerebral gliomas: comparison of short and intermediate echo time sequences. *AJNR J Neuroradiol.* 2006; **27**: 1412-1418.
24. Martinez-Bisbal MC, Celda-Munoz B, Marti-Bonmati L, Ferrer-Ripolles P, Revert-Ventura AJ, Piquer-Belloch J, Molla-Olmos E, Arana-Fernandez de Moya E, Dosda-Munoz R. The

contribution of magnetic resonance spectroscopy to the classification of high grade gliomas. The predictive value of macromolecules. *Rev Neurol* 2002; **34**: 309-313.

25. Cheng LL, Ma MJ, Becerra L, Ptak T, Tracey I, Lackner A, Gonzalez RG. Quantitative neuropathology by high resolution magic angle spinning proton magnetic resonance spectroscopy. Proc. Nat. Acad. Sci. USA. 1997; 94: 6408-6413.
26. Griffin JL, Scott J, Nicholson JK. The influence of pharmacogenetics on fatty liver disease in the wistar and kyoto rats: a combined transcriptomic and metabonomic study. *Journal of proteome research* 2007; **6**: 54-61.
27. Aboagye EO, Bhujwalla ZM. Malignant transformation alters membrane choline phospholipid metabolism of human mammary epithelial cells. *Cancer research* 1999; **59**: 80-84.
28. Glunde K, Bhujwalla ZM. Choline kinase alpha in cancer prognosis and treatment. *The lancet oncology* 2007; **8**: 855-857.
29. Mori N, Glunde K, Takagi T, Raman V, Bhujwalla ZM. Choline kinase down-regulation increases the effect of 5-fluorouracil in breast cancer cells. *Cancer Res* 2007; **67**: 11284-11290.
30. Ramirez de Molina R, Rodriguez-Gonzalez A, Gutierrez R, Martinez-Pinerio L, Sanchez J, Bonilla F, Rosell R, Lacal J. Overexpression of choline kinase is a frequent feature in human tumour-derived cell lines and lung, prostate, and colorectal human cancers. *Biochem. Biophys. Res. Commun.* 2002; **296**: 580-583.
31. Hernandez-Alcoceba R, Fernandez F, Lacal JC. In vivo antitumor activity of choline kinase inhibitors: a novel target for anticancer drug discovery. *Cancer Res.* 1999; **59**: 3112-3118.
32. Aboagye EO, Bhujwalla ZM. Malignant transformation alters membrane choline phospholipid metabolism of human mammary epithelial cells. *Cancer Res.* 1999; **59**: 80-84.
33. Glunde K, Jie C, Bhujwalla ZM. Molecular causes of the aberrant choline phospholipid metabolism in breast cancer. *Cancer Res.* 2004; **64**: 4270-4276.

Chapter 5

NEOPLASMS OF GASTROINTESTINAL TRACT

General Introduction

The neoplasms of the human gastrointestinal tract are an important public health problem due to their high incidence (1) and the high rates of recurrence and metastasis after resection. The outcome of treatment is highly dependent on correct and early diagnosis and the detection of early lesions, without lymph node involvement or distant metastases, results in a reduction of mortality (2). Thus the possibility to add new knowledge to the biochemistry of gastric and colon-rectal adenocarcinomas assumes great importance and the development of non conventional methods able to perform an early diagnosis based on the molecular composition instead of the morphology is highly desirable. Whereas organs, such as the brain, prostate, breast have been widely studied, and MRS is used routinely in clinical medicine to analyze them, MRS in the evaluation of neoplasms of human gastrointestinal mucosa is at the beginning. From this perspective my research work was to investigate the biochemical composition of normal and neoplastic human gastric and colorectal mucosa tissues by means *ex vivo* NMR, performed directly on biopsies or surgical tissues using HR-MAS NMR. The aim of this study is to relate the biochemical composition, obtained by using HR-MAS and quantitative histopathologic findings from the same gastrointestinal mucosa and to determine the metabolic profiles associated with functional, benign and malignant tissues.

The complete characterization of the metabolic composition of this tissue, will set the biochemical basis for the development and application of new protocols for the direct analysis of pathological tissues.

Considering the gastrointestinal tract my thesis work deal with the study of:

a) Stomach Mucosa
b) Colon Mucosa

STOMACH MUCOSAE

The Healthy Gastric Mucosa

Studies reported the application of *ex vivo* HR-MAS NMR in the characterization of the biochemical composition of human healthy and neoplastic gastric mucosa are rare in the international scientific literature.

The first step of my research was to investigate the biochemical composition of normal human gastric mucosa by *ex vivo* HR-MAS NMR.

Clinical materials. Selection of the patients: 5 patients were enrolled and gave written informed consent to participate in the study which was approved by the local research ethical committee. For each eligible patients, 6 biopsies have been taken (3 biopsies from the antrum and 3 biopsies from the gastric body) during endoscopy. Among them, 4 have been used for routinal histologic evaluation (hematoxilin-eosin) and 2 will be posed in liquid nitrogen and stored at -85°C. Endoscopy was performed using Olympus Instruments 140 series and biopsies forceps Olympus FB24Q, after sterilization in acetylacetic acid. The biopsies have been performed, on healthy tissues, in the subjects who do not present visible macroscopic alterations and the tissue is to be considered healthy only if the histological examination will confirm the macroscopic finding.

For the NMR experiments details see chapter II

Result and Discussion

The 1D proton spectra obtained from two representative samples of normal gastric mucosa (1 and 2), acquired by using a presaturation sequence with composite pulse (Bruker zgcppr), are reported in Figure 1.

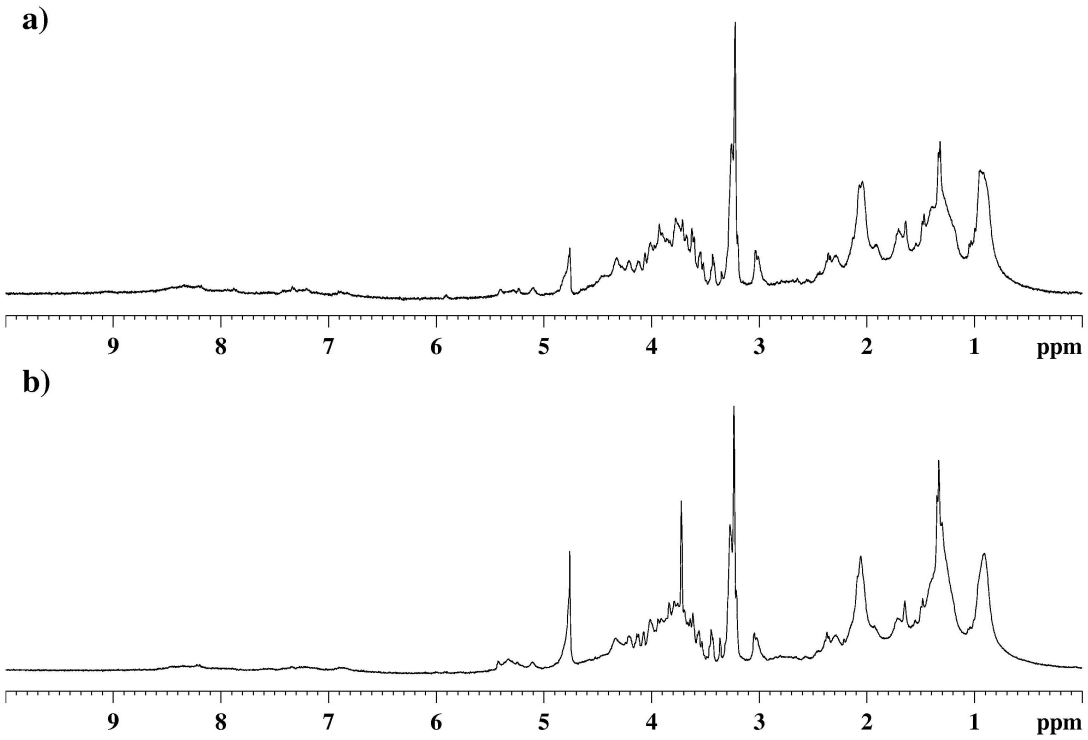

Figure 1. HR-MAS proton spectra of two representative samples of normal gastric mucosa: a) 1 and b) 2 samples, respectively.

The spectra of these samples, which are representative of the all that analysed, show the presence of the resonances deriving from metabolites and macromolecules with short T_2, but not so short to be NMR invisible, and are characterised by signals with a resolution comparable to that obtained for solution spectra. Furthermore, it is to note that in stomach tissues the lipid content is very low in comparison with that of other metabolites, as can be derived from the low intensity ratio between signals at 1.3 ppm $(CH_2)_n$, and at 0.89 ppm CH_3 (usually around 3:1). In order to evaluate the stability of the samples in the HR-MAS probe, the spectra were obtained at different times from their preparation. The spectra of sample 1 obtained after 3h (trace a) and after 6h (trace *b*) from the preparation are reported in Figure 2. These spectra evidence a progressive increase of spectral resolution probably related to the increasing mobility of some metabolites, as a consequence of the partial disruption of subcellular structures. In any case, the lactate content does not appreciably change, whereas changes related to the mobility enhancement of amino acidic fractions are detected: an increase of glycine, alanine, other aliphatic and aromatic amino acids, and free choline is observed. We are not able to give a straightforward explanation of this behaviour; however the prograstrin is cleaved at pairs of basic amino acids by a pro-hormone converter to form a

glycine intermediate (G-Gly) that serves as a substrate for peptide-glycine α-amidating mono oxigenase (3). Since on overexpression of gastrin, known to promote the growth of several neoplasms, in human gastric adenocarcinomas has been demonstrated (4), the presence of glycine could merit further investigations.

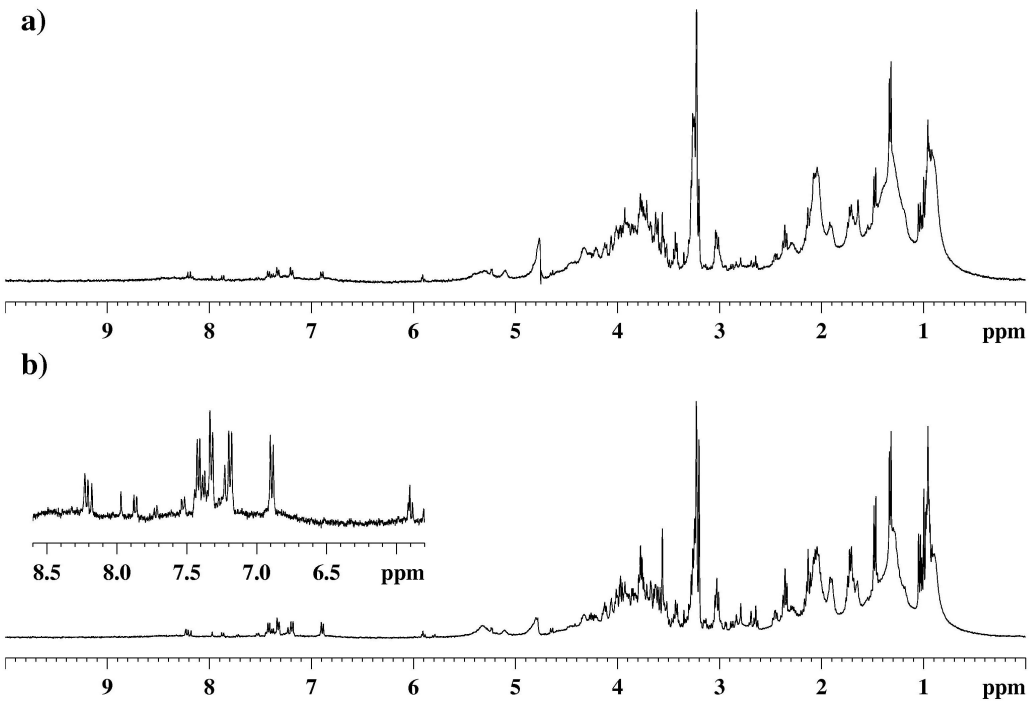

Figure 2: HR-MAS proton spectra of sample 1 a) after 3 hours and b) after 6 hours.

In order to separate the contribution of resonances due to macromolecules having short spin-spin relaxation times, spectra were acquired using a CPMG spin-echo sequence [90°- (τ-180°-τ)$_n$], choosing τ and n in order to separate signals according to their different T_2. Signals from macromolecules, having short T_2 (or large linewidth) are attenuated leaving only the resonances due to mobile small molecules. Diffusion-edited spectra were also acquired choosing a diffusion delay (Δ) and a gradient-field pulse duration (δ) and strength in order to observe components with low diffusion rates, deriving from lipids, glycogen and small proteins.

A conventional presaturated 1D spectrum with composite pulse (trace a), that highlights both lipids and small metabolites contribution, a CPMG spectrum (trace b),

showing the enhanced resonances of metabolites, and the diffusion-edited spectrum (trace c) of the same stomach sample 3 are reported in Figure 3.

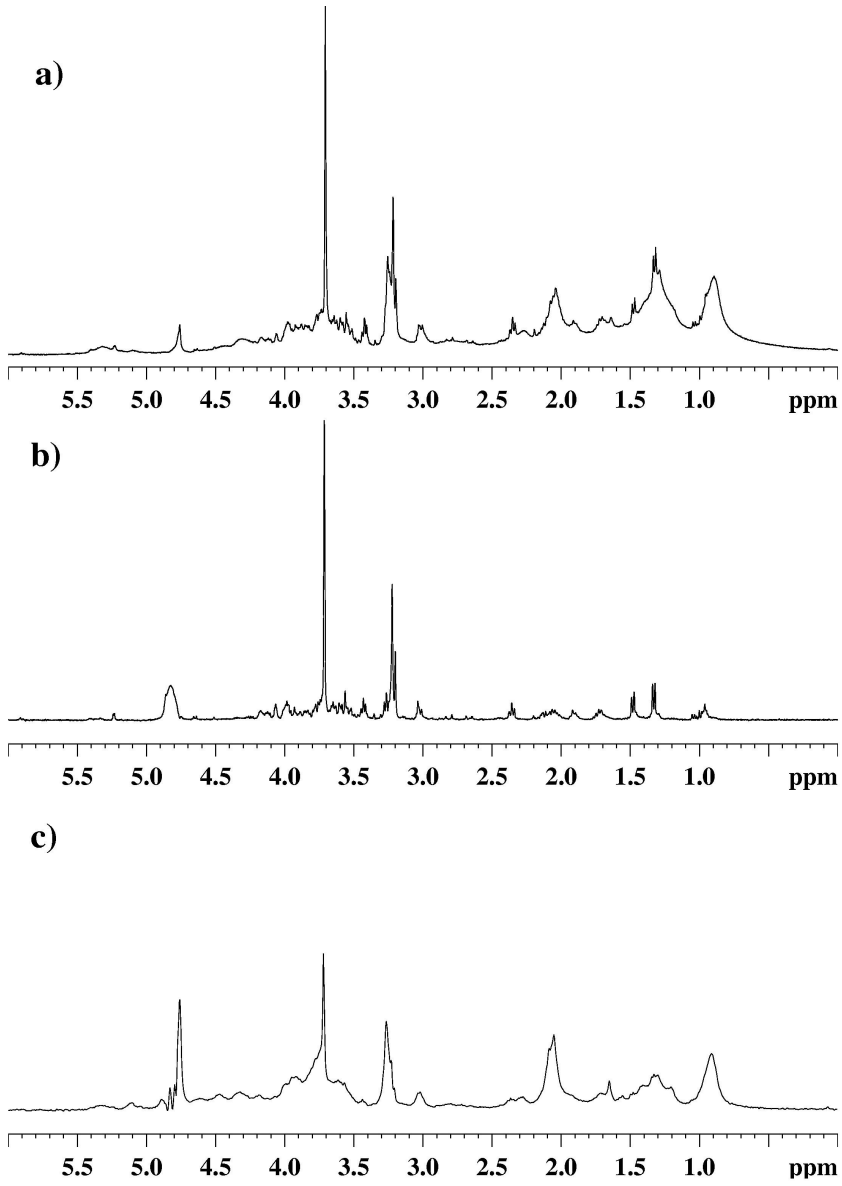

Figure 3 1D proton spectra of sample 3 a) conventional ^{1}H NMR spectrum obtained with water-presaturation and composite pulse, b) CPMG spectrum obtained with 360 ms total spin-echo time and c) diffusion-edited spectrum obtained with Δ = 200 ms, δ = 4 ms and gradient strength of 32 G/cm.

The analysis of the COSY spectrum (Figure 4) evidences the presence of a pool of metabolites, especially osmolites, free amino acids and a fraction of mobile lipids, whose assignments are reported in Table I

Some correlations, for example those due to glycerol (in lipids) protons at 5.24, 4.30 and 4.10 ppm are present in COSY spectra, but absent or attenuated in TOCSY spectra

(Figure 5). This difference can be explained by considering that in TOCSY spectra signals coming from large molecules relax during the mixing time and this, together with the characteristic chemical shifts, allows to say that this glycerol moiety is not involved in small but belongs to larger lipidic species. The COSY spectra are particularly useful for the detection and assignment of α-hydrogens of several amino acids, whereas the presence of lysine and arginine is better evidenced in TOCSY spectra. Both COSY and TOCSY experiments permit to establish that two metabolites, lactate and threonine, contribute to the doublet at 1.33 ppm found in ^{1}H NMR spectra.

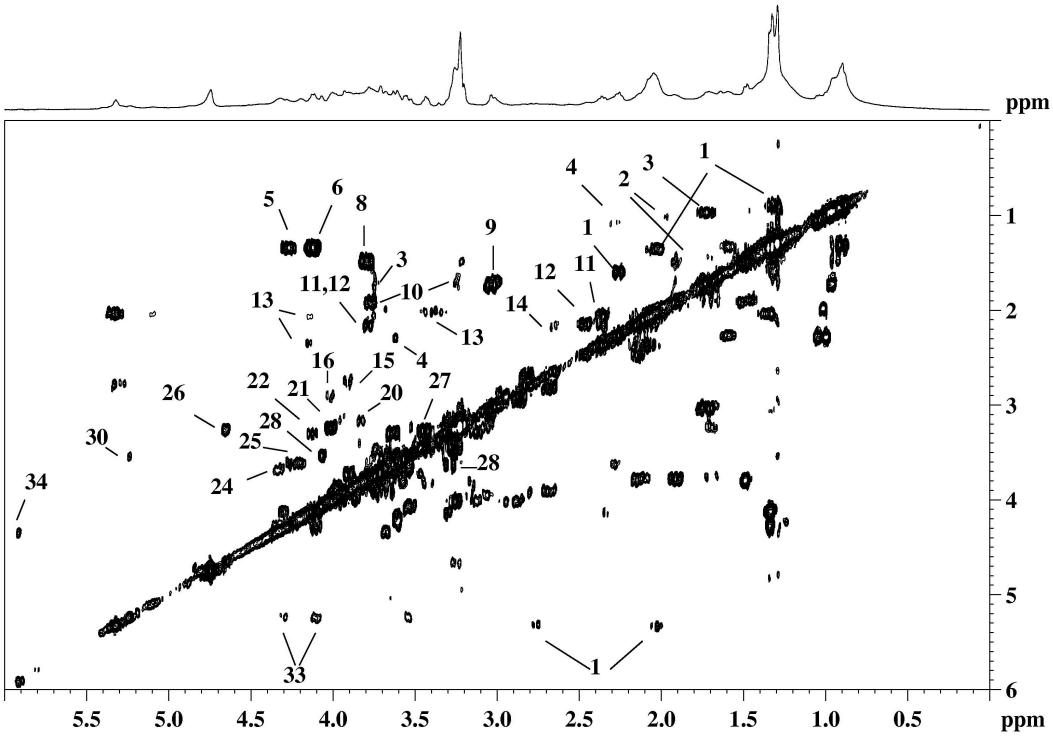

Figure 4. Partial COSY spectrum of sample 4. The identified metabolites are denoted with labels according to Table I.

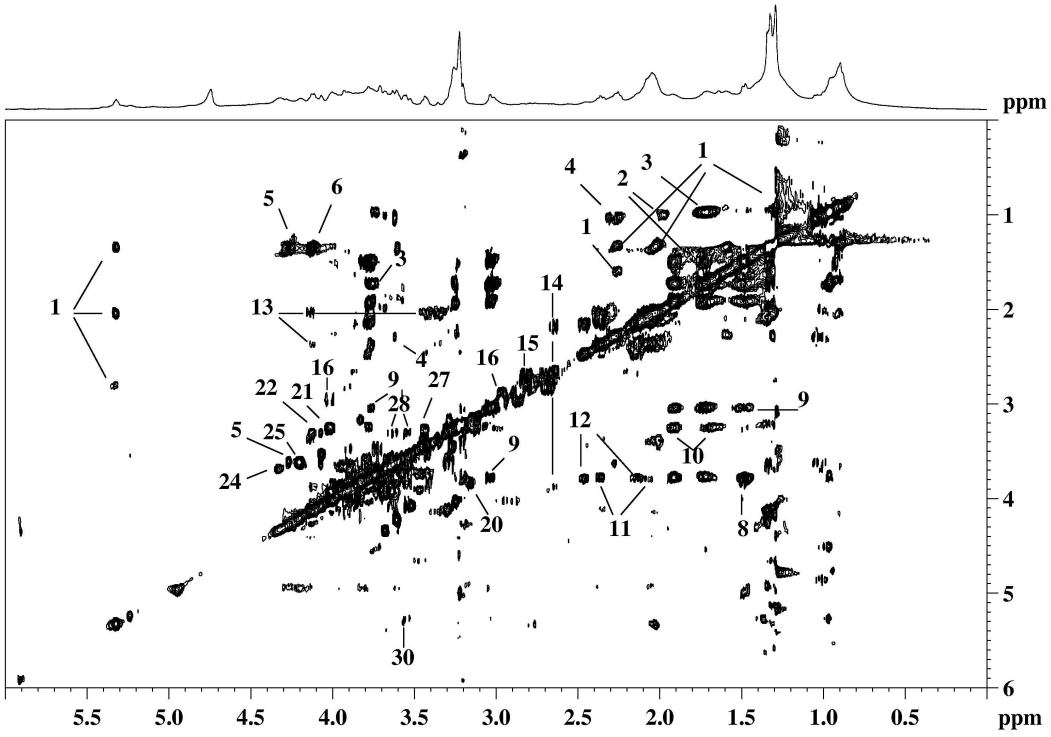

Figure 5. Partial TOCSY spectrum of sample 4. The identified metabolites are denoted with labels according to Table I.

The HSQC spectrum of sample 5 and relative assignments are reported in Figure 6. Some metabolites such as ChoCC, Arg and PE contribute all to the 3.2 ppm signal in the proton spectra but can be readily distinguished with HSQC due to the large difference in ^{13}C chemical shifts. The ^{13}C δ dispersion is also useful for the assignment of the signals of aliphatic amino acids (Ile, Val, Leu). The interpretation of the region between 3.4 and 4.0 ppm is more problematic, due to the presence of overlapped correlations around 62 ppm, presumably due to glycerols. All sample spectra show a strong resonance at 3.72 (s) ppm, attributable to PEG (confirmed by the ^{13}C resonance at 70.3 ppm).

The observed peaks seem to be principally related to the narrow components appearing in the CPMG spectrum (Figure 3b), with the exception of signals due to N-acetyl groups, which are instead evidenced in the diffusion-edited spectrum (Figure 3c).

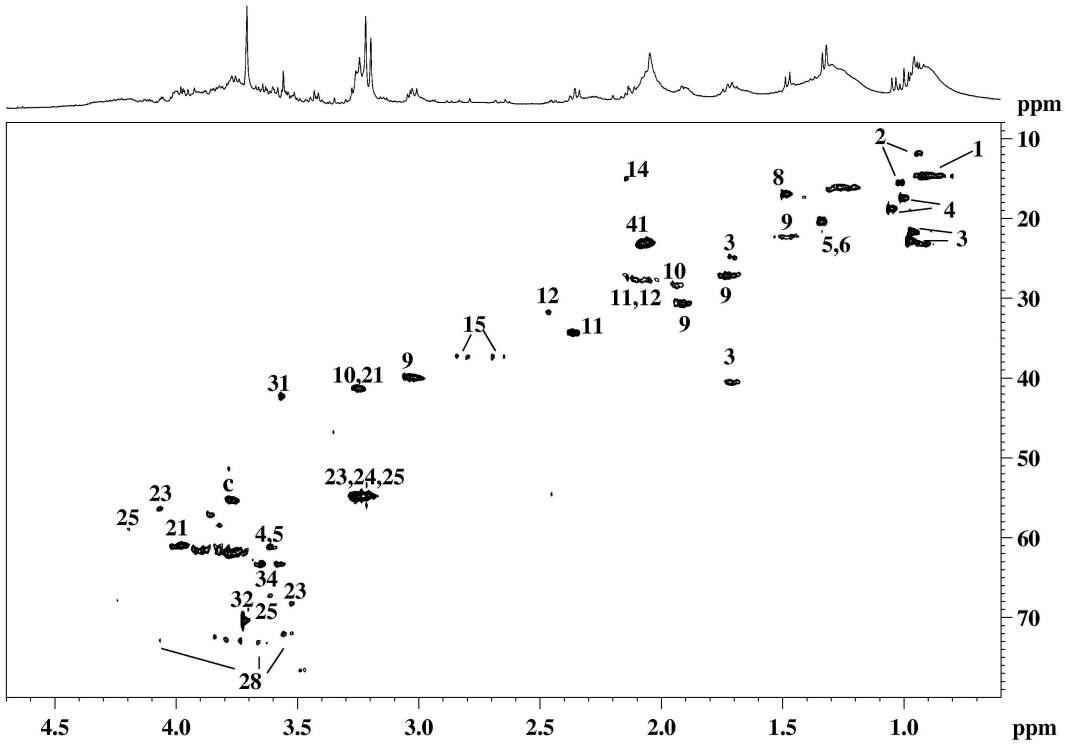

Figure 6. Partial $^{1}H,^{13}C$-HSQC spectrum of sample **5** (stomsan23). The identified metabolites are denoted with labels according to Table I.

All the samples analysed display the same resonances with only slight differences in the relative abundance. Through the use of one- and two-dimensional experiments it was possible to assign the NMR signals from more than forty species present in healthy human gastric mucosa. Among them only few components can to be confidently assigned by direct inspection of the ^{1}H NMR spectrum, namely, a doublet at 1.48 ppm is for Ala, a triplet at 2.36 ppm is for Glu, whereas a triplet at 3.43 ppm is for Tau. Instead, the doublet at 1.33 ppm, usually attributed to Lac, is due in our samples to the overlapping of Lac and Thr resonances, with the second species prevailing in the same cases. The presence of Lys is normally well evident in the one-dimensional ^{1}H spectrum from the triplet at 3.04 ppm (over-lapped to the singlet of Cr, while it is harder to distinguish the triplet of Arg from those of Tau and PE which are found very close in one-dimensional ^{1}H spectrum (and partially hidden under the choline containing compounds singlets). To our knowledge this study is the first one, aimed at elucidating the metabolic profile of normal human gastric mucosa by *ex vivo* HR-MAS NMR.

The characterization of the molecular pattern typical of the healthy gastric human mucosa will be the bases for the comparison with gastric neoplastic situations.

Human Gastric Adenocarcinomas

Gastric cancer is the leading cause of cancer related death in many parts of the world (5). Gastric carcinogenesis is a multistep and multifactorial process that in many cases involves a progression from normal mucosa through chronic gastritis, atrophic gastritis and intestinal metaplasia to dysplasia and carcinoma (6). A number of pre-cancerous conditions such as atrophic gastritis and intestinal metaplasia have been recognised due to *Helicobacter pylori* (*H. pylori*) infection or autoimmunity and there are putative associations with environmental agents such as dietary constituents and the formation of carcinogenic *N*-nitroso compounds within the stomach (7). The detection of early lesions, without lymph node involvement or distant metastases, would result in a
reduction of mortality (8). Thus, achieving a better understanding of the molecular features of gastric cancer and the development of reliable methods for early detection is highly desirable.
The NMR was used to elucidate the main metabolic characteristics of human adenocarcinomas. Only one paper (9) reports a study on gastric adenocarcinoma obtained from low resolution *ex vivo* MR spectrum of composite mucosal/submucosal layer and underlines that a decreased levels of lipids together with an increased of lactate and choline peaks were marker for malignancy.

Selection of the patients. Sixteen patients, 5 with gastric carcinoma (2 male, mean age 70.6 +/- 12.9 years, range 59-86 years) and 11 healthy subjects (7 male, mean age 49.3 +/- 17.3 years, range 30-86 years) were evaluated. Of the sixteen patients examined 14 underwent endoscopy, 2 underwent surgery for gastric adenocarcinoma; in all cases, sample of healthy gastric mucosa were collected.
All 5 patients with gastric cancer showed an *H. pylori* infection while no healthy subjects presented an *H. pylori* infection. Histological appearance was consistent with adenocarcinoma well differentiated in 3 patients, poorly differentiated and undifferentiated in one patient respectively.

The patients gave written informed consent to participate in the study which is approved by the local research ethics committee. For each eligible patient, 8 biopsies were taken (4 biopsies from the antrum and 4 from the gastric body) during endoscopy. Among

them, 4 were used for routine histologic evaluation (haematoxylin-eosin) and 4 were put in liquid nitrogen and stored at -85°C. Endoscopy was performed using Olympus Videoendoscope 140 series and biopsy forceps Olympus FB24Q, after sterilization in acetylacetic acid. The biopsies were obtained, on healthy tissues, in the subjects who did not present visible macroscopic alterations and the tissue were considered healthy only if the histological examination confirmed the macroscopic finding. It is reasonable that the tissue collections is performed on mucosa and submucosal layer. In the patients with gastric cancer the biopsies were taken from the lesion in clearly macroscopic aspect of carcinoma and in normal appearing mucosa far from lesion. The gastric biopsies were fixed in neutral buffered formalin, routinely processed and stained with Giemsa and haematoxylin-eosin. The Goseki classification (10) was used for grading adenocarcinoma.

Results and Discussion

Conventional presaturated 1D spectra, representative of the healthy (trace **a**) and neoplastic (trace **b**) gastric mucosa are reported in Figure 7. The healthy mucosa shows the presence of the resonances deriving from low molecular weight metabolites and macromolecules, whereas the adenocarcinoma is characterized by the presence of predominant signals due to triglycerides, which content is very low in healthy stomach. So it is possible to evidence the metabolic changes in the neoplastic human gastric mucosae. (For the metabolites assignment see table I)

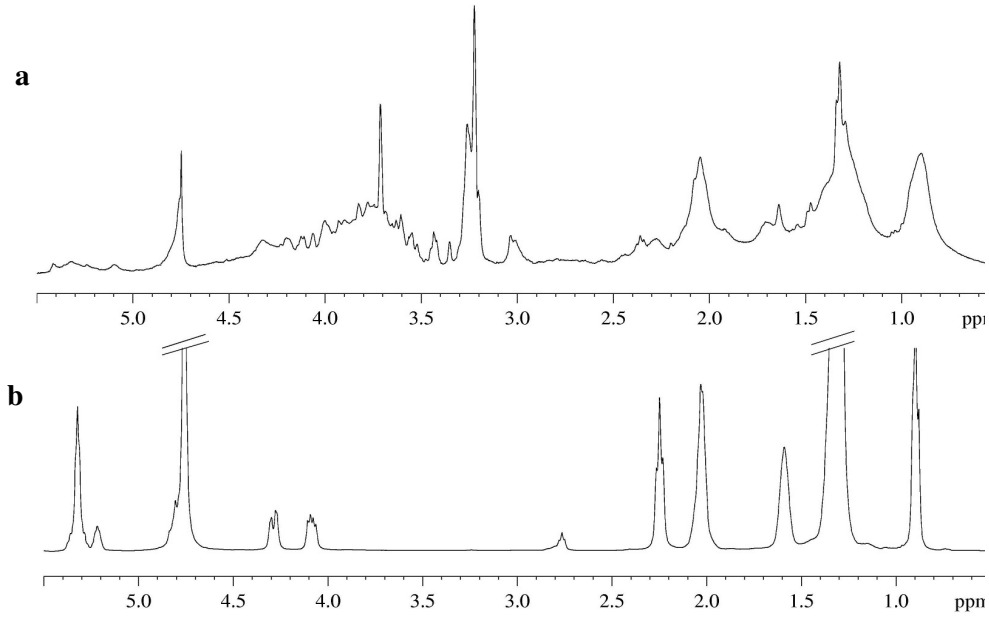

Figure 7. HR-MAS proton MR spectra of healthy (**a**) and neoplastic (**b**) samples.

As already observed, the ^{1}H MR spectra of gastric adenocarcinomas are dominated by the signals due to triglycerides. At first, we examined the type of fatty acids with the aims to characterise the relative content of saturated and unsaturated fatty acids.

Lipids. The proton spectrum of a neoplastic gastric mucosa, reported in Figure 8, shows the resonances characteristic of triglycerides, confirmed by the presence of signals due to glycerol (5.26, 4.30 and 4.10 ppm) and to long fatty acid chains. It is to remark that all the examined adenocarcinomas (5 patients, for the patient 2 nine spectra were obtained from sampling in different zone of the lesion tissues) show virtually identical spectral profile.

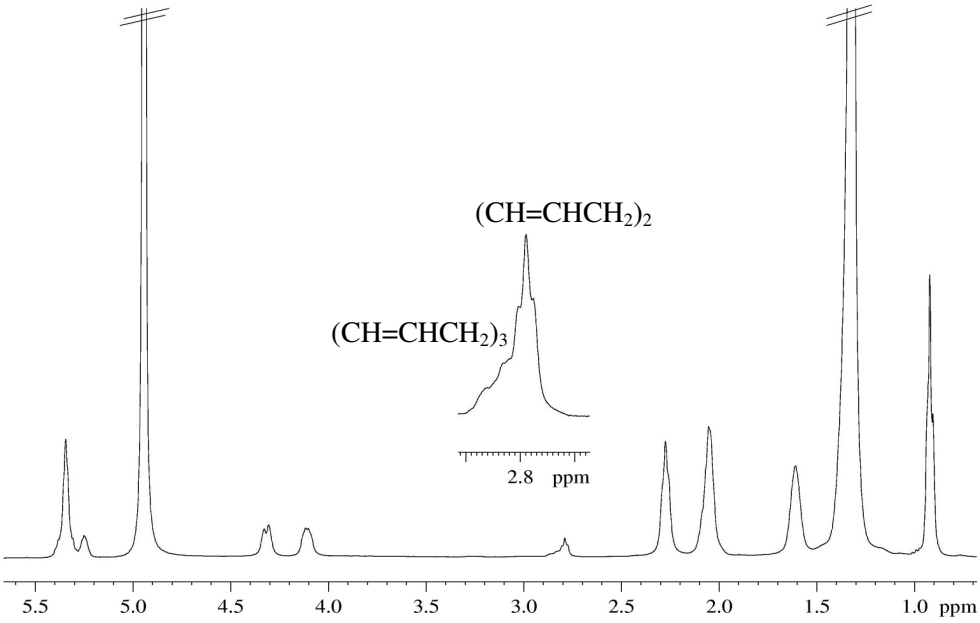

Figure 8. ^{1}H HR-MAS MR spectrum of cancerous gastric mucosa.

Signals at 2.02 ppm are to be assigned to methylene protons of C***H***$_2$-CH=CH moiety of mono- and poly-unsaturated fatty acids, whereas those at 2.78 ppm are attributable to methylene protons between two double bonds (=C-C***H***$_2$-C=) in poly-unsaturated acids. Furthermore, the unsaturated acids are identified by the signals at 5.33 ppm due to protons of -C***H***=C***H***- moiety.

The α-linolenic acid is identified by the signal of the methyl protons at 0.96 ppm and by its correlation with methylene protons of C***H***$_2$-CH=CH moiety at 2.06 ppm, detected in the COSY spectrum (Figure 9).

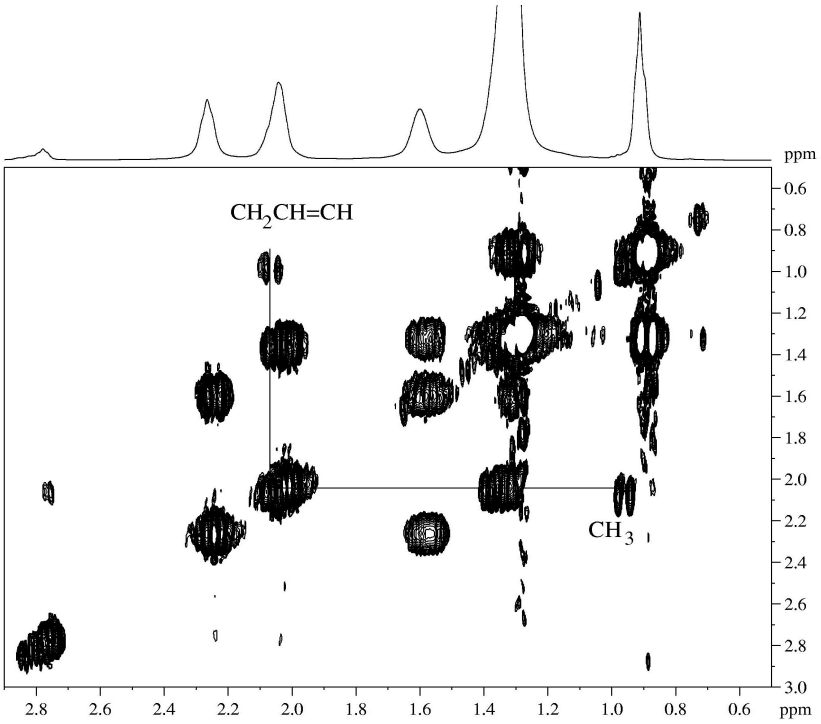

Figure 9. COSY spectrum of sample 2. The correlation CH_2-CH_3 of α-linolenic acid is evidenced.

The presence of linoleic acid is confirmed by the correlation between the triplet at 2.78 ppm (=C-C***H***$_2$-C=) and the signal at 2.02 ppm (C***H***$_2$-CH=CH) and by that with signal at 5.33 ppm (C***H***=C***H***).

The analysis of the fat components, in percentage of saturated, mono- and poly-unsaturated was performed through the integration of suitable signals: the starting point is represented by the integrated area of the CH_2(α) to C=O at 2.24 ppm. The percentage of unsaturated acids was evaluated by the ratio between the experimental and theoretical values of integrated area of CH_2(α) to double bond. The integrated area of CH_2(α) to double bond, due to mono- and poly-unsaturated acids was corrected by the contribution due to CH_2(α) of linoleic and α-linolenic acids, which is derived by the integrated area of the signal at 2.78 ppm, permitting to establish that the ratio of mono- and poly-unsaturated components is *ca*.3:1, in all the examined samples. The α-linolenic percentage was derived by the area of the terminal methyl signal at 0.96 ppm. The composition of triglycerides is reported in Table II.

Table II. Percentage of different fatty acid components in the adenocarcinoma samples.

Patients	Saturated	Unsaturated		
		mono-unsaturated	poly-unsaturated	
			linoleic	α-linolenic
1	20%	64%	14%	**2%**
2	28%	56%	13%	**3%**
3	23%	65%	10%	**2%**
4	26%	48%	24%	**2%**
5	28%	46%	24%	**2%**

Some considerations can be made on the ^{13}C MR spectra obtained with HR-MAS technique. A carbon spectrum representative of whole samples analysed is displayed in Figure 10.

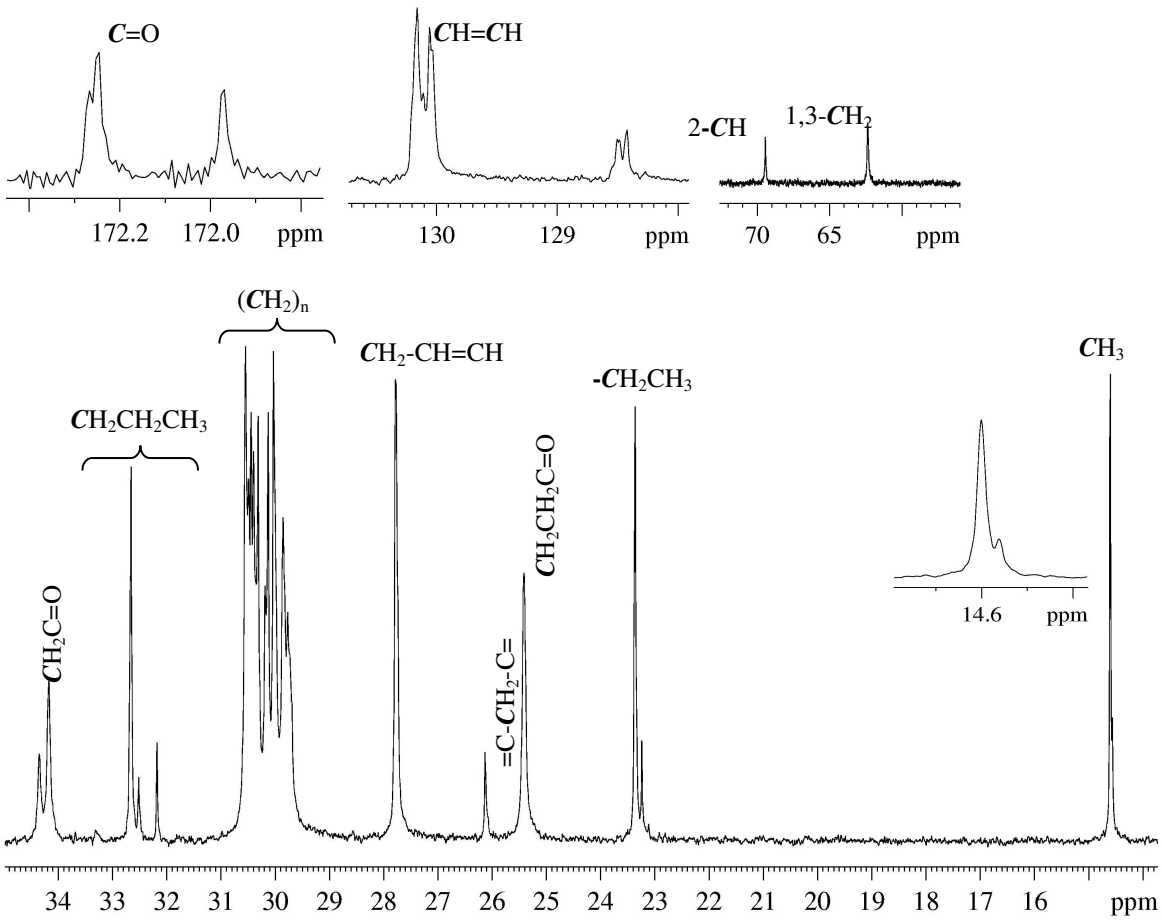

Figure 10. The ^{13}C HR-MAS spectrum of patient 2 biopsy. All ^{13}C resonance are reported in table III.

The spectrum is of good quality, with a resolution comparable to that obtained in solution, permitting the evaluation of the composition of triglycerides. Three signals are present in the carbonyl region, at 172.26, 172.24 and at 171.97 ppm: the more deshielded signals are due to the carbonyls in the 1,3 positions (*sn*1,3) and the other to the carbonyl in the 2 position (*sn*2) of glycerol. The slight difference of the carbonyl resonances in *sn*1,3 suggests that the triglycerides are mixed, even if no difference is observed in the *sn*2 carbonyl resonance. The two groups of signals centred at 130.1 and 128.5 ppm are due to olefinic carbons: in particular the latters are attributable to internal carbons of double bonds in linoleic and α-linolenic acid, whereas the formers are due to carbons of mono-unsaturated acids and to external carbons of double bonds in linoleic and α-linolenic acid. The identification of saturated fatty acids is obtained by the resonances of the $\boldsymbol{C}H_2\boldsymbol{C}H_3$ moiety at 23.2 and 14.60 ppm, whereas those of mono-unsaturated and poly-unsaturated acids is deducible from the resonances of $\boldsymbol{C}H_2$-CH=CH at 27.8 ppm, $\boldsymbol{C}H_2\boldsymbol{C}H_3$ at 23.3 ppm and 14.56 ppm. The linoleic acid is clearly identified by the resonance of =C-$\boldsymbol{C}H_2$-C= at 26.1 ppm. The ^{13}C resonances of the α-linolenic acid were not detected due to its low abundance.

The NMR date of lipids obtained through the MR analysis is reported in table III.

Triglyceride

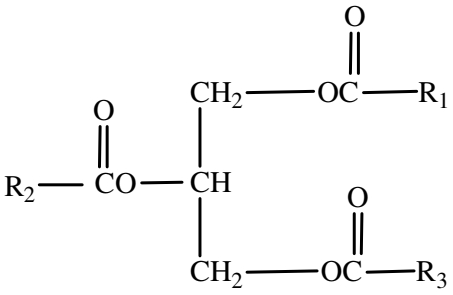

Glycerol	H	C
1,3-CH_2	4.10, 4.30	**62.4**
2-CH	5.22	**69.5**

—$CH_2CH_2CH_2CH_2(CH_2)_nCH_2CH_2CH_2CH_3$ Saturated Acids (S)

—$CH_2CH_2CH_2(CH_2)_3CH_2CH{=}CHCH_2(CH_2)_nCH_2CH_2CH_2CH_3$ Mono-unsaturated Acids (M)
χ ψ

—$CH_2CH_2CH_2(CH_2)_3CH_2CH{=}CH\text{-}CH_2\text{-}CH{=}CHCH_2CH_2CH_2CH_2CH_3$ Linoleic Acid (L)
α β γ

—$CH_2CH_2CH_2(CH_2)_3CH_2CH{=}CH\text{-}CH_2\text{-}CH{=}CH\text{-}CH_2\text{-}CH{=}CHCH_2CH_3$ α-Linolenic Acid (α-L)

Scheme 1. Triglycerides and relative numbering.

Table III. NMR data ($^{1}H,^{13}C$) of fatty acids in neoplastic gastric mucosa. For numbering see Scheme 1.

	C=O	**$CH_2(\alpha)$**	**$CH_2(\beta)$**	**$(CH_2)_n$**	**$CH_2CH=CH$**	**CH=CH**	**=C-CH_2-C=**	**$CH_2(\chi)$**	**$CH_2(\psi)$**	**CH_3**
C	172.26 172.24 171.97	34.2, 34.3	25.5	29.7÷30.6	27.8(M+L)	130.1, 128.5	26.1(L)	32.65, 32.51, 32.18(S)	23.3 (M+L), 23.2(S)	14.60 (M+L), 14.56(S)
H		2.24	-	1.60	2.02, 2.06(α-L)	5.33	2.78(L), 2.81 (α-L)	1.28÷1.32		0.89, 0.96(α-L)

The assignment of ^{13}C MR signals of the triglycerides was made through $^{1}H,^{13}C$ HSQC experiment and by comparison with the literature data (11). The detection of lipids in all the gastric adenocarcinomas examined differentiates them from the healthy mucosa in which their amounts is very low. This finding is in opposition with that of Mun *et al*. (9) who reported a decreased levels of lipids in gastric adenocarcinomas detected from low resolution *ex vivo* MR spectrum of composite mucosal/submucosal layer.

Within the panorama of the research on lipidic component of cell and tissues recognised as having a fundamental role in cell life and death (12), in recent years analytical studies performed by spectroscopic techniques have been gained importance. Indeed, deposits of neutral lipids in human cells and tissues have been revealed and identified by NMR. Recently, some authors have speculated that ^{1}H resonances, attributed to mobile lipids, originate from lipid droplets made of triglycerides and cholesteryl esters located both in the cytoplasm (13,14) and in the plasma membrane (15). The importance of these ^{1}H visible lipids in the life and death of cells has been highlighted by Hakumaki and Kauppinen (12) and the direct relationship between Nuclear Magnetic Resonance-visible lipids, lipid droplets and cell proliferation has been demonstrated by Barba *et al.* (16). Moreover, a positive correlation between the presence of lipid droplets detected *in vivo* by MRS and necrosis in rat brain glioma has been reported (17). All of these evidences show how these lipid droplet, formed by triglycerides, mainly, are closely involved in various aspects of tumor cell transformation.

In agreement with these findings, we have detected a lot of triglycerides in all the examined adenocarcinomas collected both by endoscopy or surgery. High amounts of lipids in clear cell renal carcinoma sample were detected, by *ex vivo* HR-MAS NMR, by Nicholson et *al.*(18). The result could be thus not surprising even if ultra-structural further investigations

are needed to better elucidate the localization of these compounds and to understand their role and significance in gastric adenocarcinomas.

Low molecular-weight metabolites in gastric adenocarcinoma. The CPMG experiment permits to attenuate the signal due to lipids and to evidence the signals arising from small metabolites in the neoplastic tissue; in this type of samples a good CPMG spectrum, *i.e.* a good suppression of lipid resonances, can be obtained using a total spin-echo time of 720 ms. The corresponding spectrum is reported in Figure 11.

Some metabolites can be identified by the comparison with the corresponding healthy tissues. In particular, adenosine, Ala, Phe, Tyr, His, α- and β-Glc, PC (trace), Myo, PE, Gly, Tau, HTau, Scy, ChoCC, Cho, E, succinate (Suc), Gln, Glu, methionine (Met), acetate (Ac), hydroxibutyrate (OH-But), Val and low amounts of Ile and Leu, are recognizable. Polyethylen glicole (PEG) is present in small amount in only some samples.

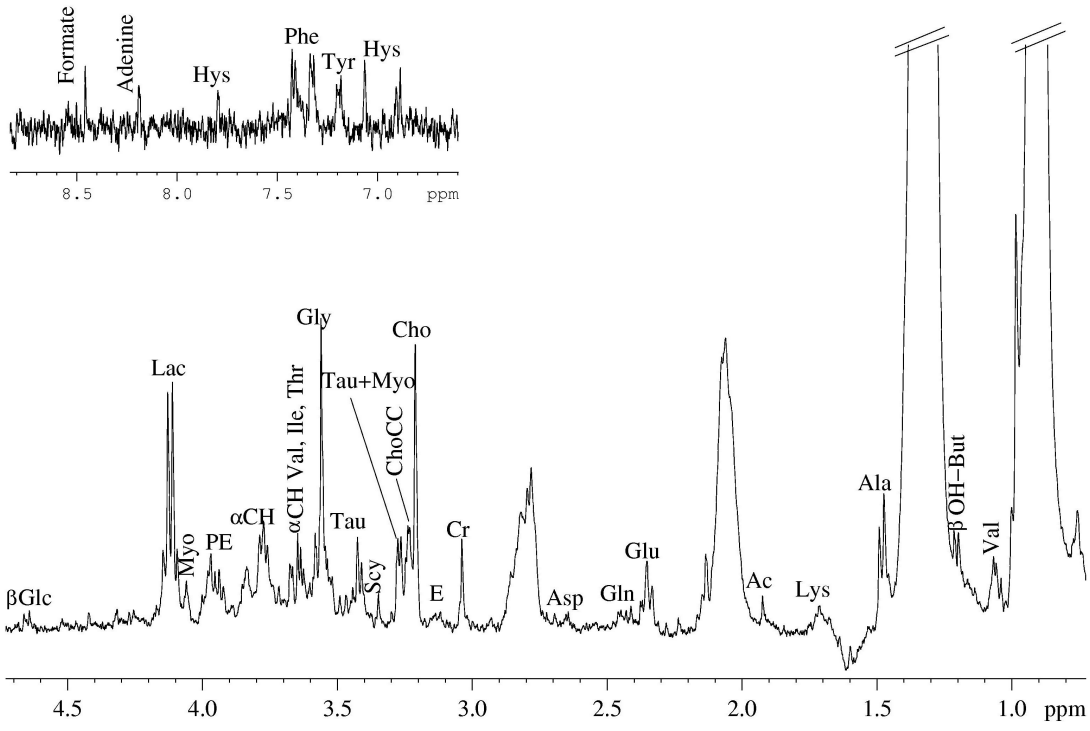

Figure 11. The CPMG spectrum of gastric adenocarcinoma tissue.

Different relative ratios of metabolites are found in the healthy and neoplastic tissues as clearly evident in the two spectra reported in Figure 12.

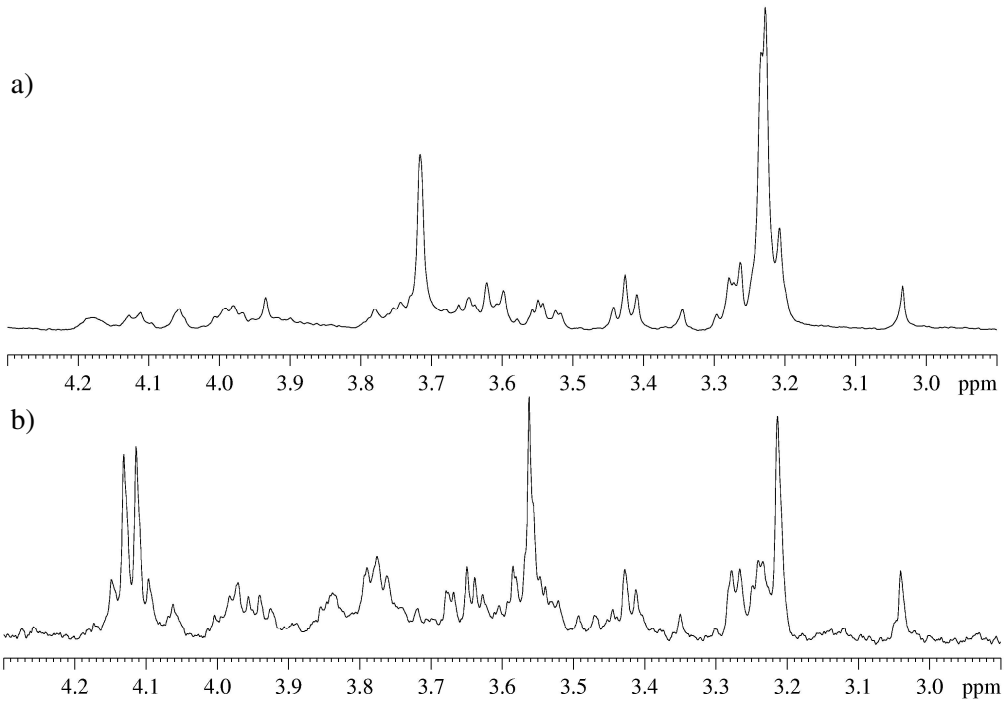

Figure 12. The CPMG spectra of healthy gastric mucosa (trace **a**) and adenocarcinoma (trace **b**).

At a glance, the major differences are found in the increased amount of Gly in neoplastic tissues with respect to the healthy ones. It has been suggested that intermediates of a more bioactive glycolitic pathway in neoplasms are responsible of an increasing of Gly amount, involving phosphoglycerate and serine (19). In agreement with these findings, several authors reported Gly as the most notable peculiarity in glioblastomas (20,21) and breast tumors (18). Moreover in the case of breast tumors, high amount of Gly were correlated to tumor size, cellularity and presence of positive lymph node (22).

Another difference, recurrent in all the examined adenocarcinomas, besides the change in the ChoCC/Cr ratio which passes from 16:1 in all the healthy samples to 2.5:1 in the neoplastic ones, is found in the relative abundance of Cho with respect to ChoCC. The healthy gastric mucosa is characterised by high amount of PC and low amounts of Cho and GPC, with a mean ratio Cho/ChoCC of 1:5. Instead, the adenocarcinoma samples are characterised by large amount of Cho and very low amounts of PC and GPC with a mean ratio Cho/ChoCC of 4:1.

PEG is a component of the anesthetic formulation administered to patients before endoscopy, and its presence was detected, through the strong singlet at 3.72 ppm only in healthy gastric mucosa; whereas it is absent or only in traces in all the gastric adenocarcinoma samples. It is interesting to note that this molecule is preferentially fixed in the healthy tissues only.

Evolution of normal mucosa to gastric cancer

Gastric carcinoma of the intestinal type originates from dysplastic epithelium, and may also develop from gastric adenomatous polyps, representing dysplastic epithelium arising in an elevated lesion (23). As already pointed out, the main causes of chronic atrophic gastritis and gastric atrophy are the autoimmune diseases (AAG) due to pernicious anemia or chronic *Helicobacter pylori* (*H. pylori*) infection (24,25). The intestinal metaplasia may be of the enteric (grade I), enterocolic (grade II), or colonic (grade III) type. Grade III intestinal metaplasia has traditionally been thought to be the riskiest, and the extent of atrophy and metaplasia could be a better marker for premalignancy than the mere identification of small intestinal metaplasia areas (26). Over the years, there has been much disagreement on the identification of the different grades of dysplasia and early gastric cancer. There is still a limited knowledge on metabolic alterations occurring in dysplastic/cancer cells, despite increasing indications of the involvement of some molecular components in tumor growth and invasiveness (15). Identifying molecular patterns of the different stages of gastric mucosa by advanced molecular techniques may result in rapid and effective methods for gastric adenocarcinoma diagnosis.

The metabolic profiles, associated with healthy and malignant human stomach tissue, can be now established through *ex vivo* HR-MAS NMR. The results of the study was to apply *ex vivo* HR-MAS NMR to human tissues, with the aim to have information on the molecular evolution of the gastric carcinogenesis. This data could be the basis for the development of *in vivo* MRS methodologies to diagnose gastric pathologies in clinical situations (9). Since *ex vivo* HR-MAS spectra allowed the detection of high lipid amount, especially in adenocarcinoma tissues, the study was continued with a microscopic investigation to identify and locate the lipids in the cellular and extra-cellular environments. The study try to correlate the morphological changes detected by transmission (TEM) and scanning (SEM) electron microscopy, with the metabolic profile of gastric mucosa in healthy, AAG, *H. pylori*-related gastritis and adenocarcinoma subjects.

Methods

Tissue protocols. We included 27 patients (15/12: male/female, mean age 56.6 ± 16.9 yrs): twelve normal subjects (7/5: male/female, mean age 53.2 ± 15.2 yrs); 5 with AAG (2/3: male/female, mean age 64.3 ± 17.6 yrs); 5 with *H. pylori* infection (4/1: male/female, mean age 46.2 ± 21.1 yrs) and 5 with adenocarcinoma (2/3: male/female, mean age 70.6 ± 12.9 yrs). Twenty-two patients underwent upper gastrointestinal endoscopy, and 5 gastrectomy for adenocarcinoma. Ten biopsies (antrum/gastric body), 4 for histologic evaluation, 4 for TEM and SEM and 2 for MRS analysis, were taken from each subject during endoscopy. The specimens (biopsies and surgical samples) in patients with gastric cancer were obtained exclusively from the carcinoma site, assuring the absence of any contaminants. The study was approved by the local ethics committee. All patients received detailed information regarding the procedure and written informed consent was obtained.

TEM. The biopsies were fixed in 5% glutaraldehyde in 0.1 M sodium phosphate buffer pH 7.2, post fixed in 1% osmium tetroxide in the same buffer, dehydrated and embedded in resin. Semithin sections (2 μm thick) cut with an ultramicrotome Reichert OM-2, were observed under a light microscope. Ultrathin sections (70 μm thick) were obtained from pathological areas chosen by light microscopy, stained with uranyl acetate and lead citrate were examined at TEM Philips CM10.

SEM. The biopsies were fixed in 5% glutaraldehyde in 0.1 M sodium phosphate buffer pH 7.2, critical point dried with Emitech K 850, coated with gold palladium film with an Emithech K500 sputter coater and observed under a Philips 515 SEM at 9-14 kV.

Statistical Analysis. NMR data were processed using the Bruker software applying 0.5 Hz line broadening, prior to Fourier transformation, phased and then the baseline was corrected. The results were based on a matrix consisting of 33 spectra. The NMR data points were reduced from 32k to 8k data points. The spectral width was selected to the chemical shift range δ 8.60-δ 0.78 by reducing the number of data points to 1600. The values of data points around the water signal in the range δ 5.03-δ 4.69 and δ 1.34-δ 1.29, were set to zero, where the lactate doublet occurs. Each data set was then normalized to unit area and analyzed by the statistical package SPSS (SPSS Inc., Chicago, IL) to get principal component analysis (PCA). The statistical method of PCA was used to differentiate spectra of gastritis from the healthy and neoplastic gastric mucosa. The number of principal component analyses (PCs), that gave the minimal total % variance, was considered to be the required number of PCs. The score

plot of the various PCs was interpreted, to reveal specific grouping and the relationship among samples.

In the present context, the eigenvalue represents the amount of the total test variance (%), accounted for a particular factor. However, the variance of the original data can be explained by the first few principal components and the remaining can be ignored. In this analysis three components with an eigenvalue greater than 1 were found and they account for about 70 % of the variance. A plot of PC1 against PC2 and PC2 against PC3 showed the maximum data spread in two dimensions. They included those data point intensities that were most correlated with the class and values of the PCs based on data point regions. Many of the data points were significantly ($p < 0.05$) correlated with the class index.

Results and Discussion

The 1D proton spectra of healthy, *H. pylori*–related gastritis, AAG and adenocarcinoma, acquired by using a presaturation sequence with composite pulse (Bruker zgcppr), are reported in Figure 13 (a-d, respectively). The spectra of these samples .show the presence of the resonances deriving from small metabolites and macromolecules with short T_2, but not so short to be MRS invisible. The profiles of the spectra in Figure 13a and 13b were quite similar, both displaying broad and narrow signals. The broad signals were due to lipids and macromolecules (MM). A progressive increase of fatty acids (FA) esterified in triglycerides (TG) passing from healthy tissue and *H. pylori*-related gastritis to AAG (Figure 13c), and adenocarcinoma (Figure 13d), was observed. In particular, the spectra of all the adenocarcinoma specimens analyzed, showed the exclusive presence of TG.

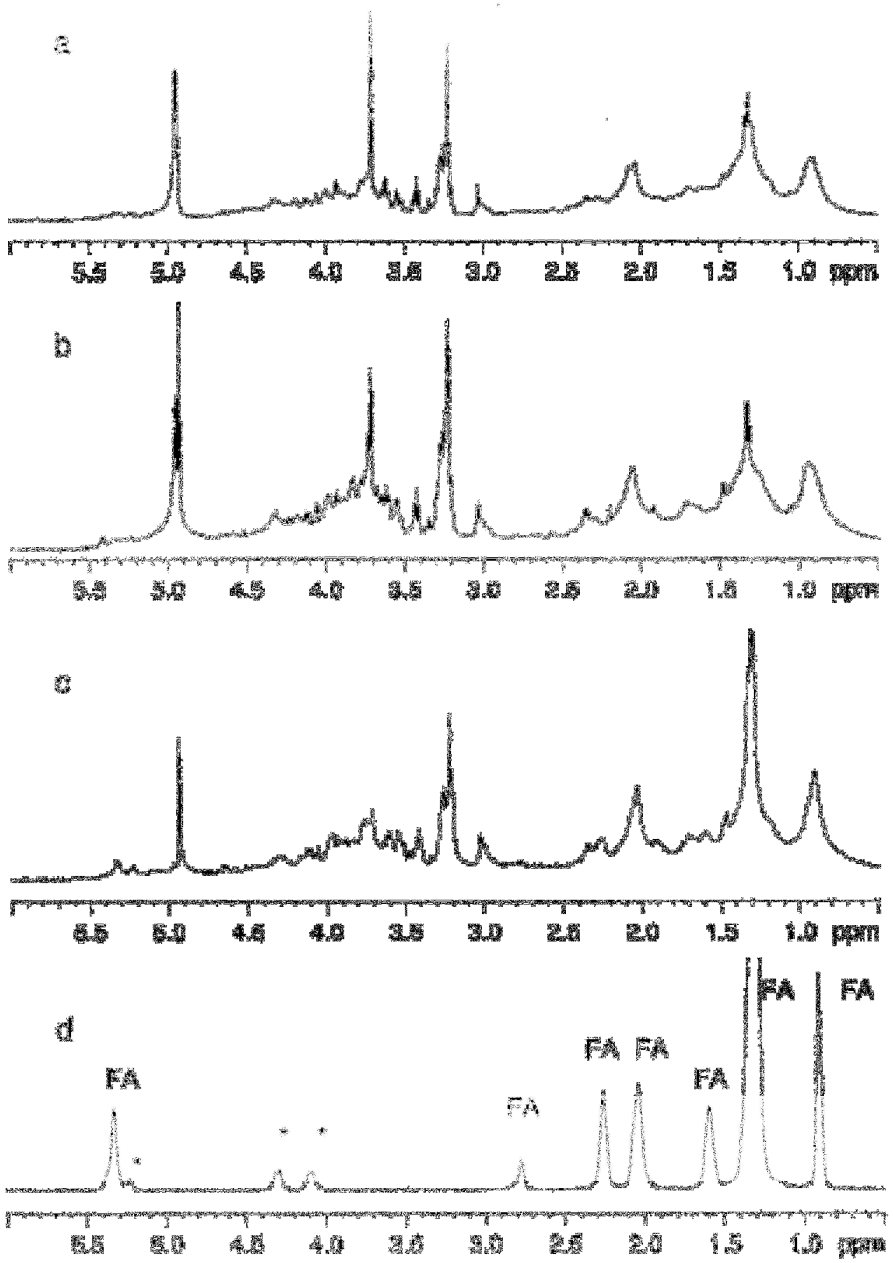

Figure 13. Proton HR-MAS MR spectra of: (a) healthy, (b) *H. pylori*- related gastritis, (c) AAG and (d) adenocarcinoma. * TG glyceryl residues, FA fatty acids chains.

Spectra acquired using a CPMG spin-echo sequence demonstrated the contribution due to mobile small molecules. The analysis of these spectra permitted a direct identification of a lot of metabolites (27,28) and their differences in percentage were obtained by the inspection of CPMG spectra reported in Figure 14a-d. The spectrum representative of *H. pylori*-related gastritis (Figure 2b) was very similar to that of the healthy gastric mucosa (Figure 14a).

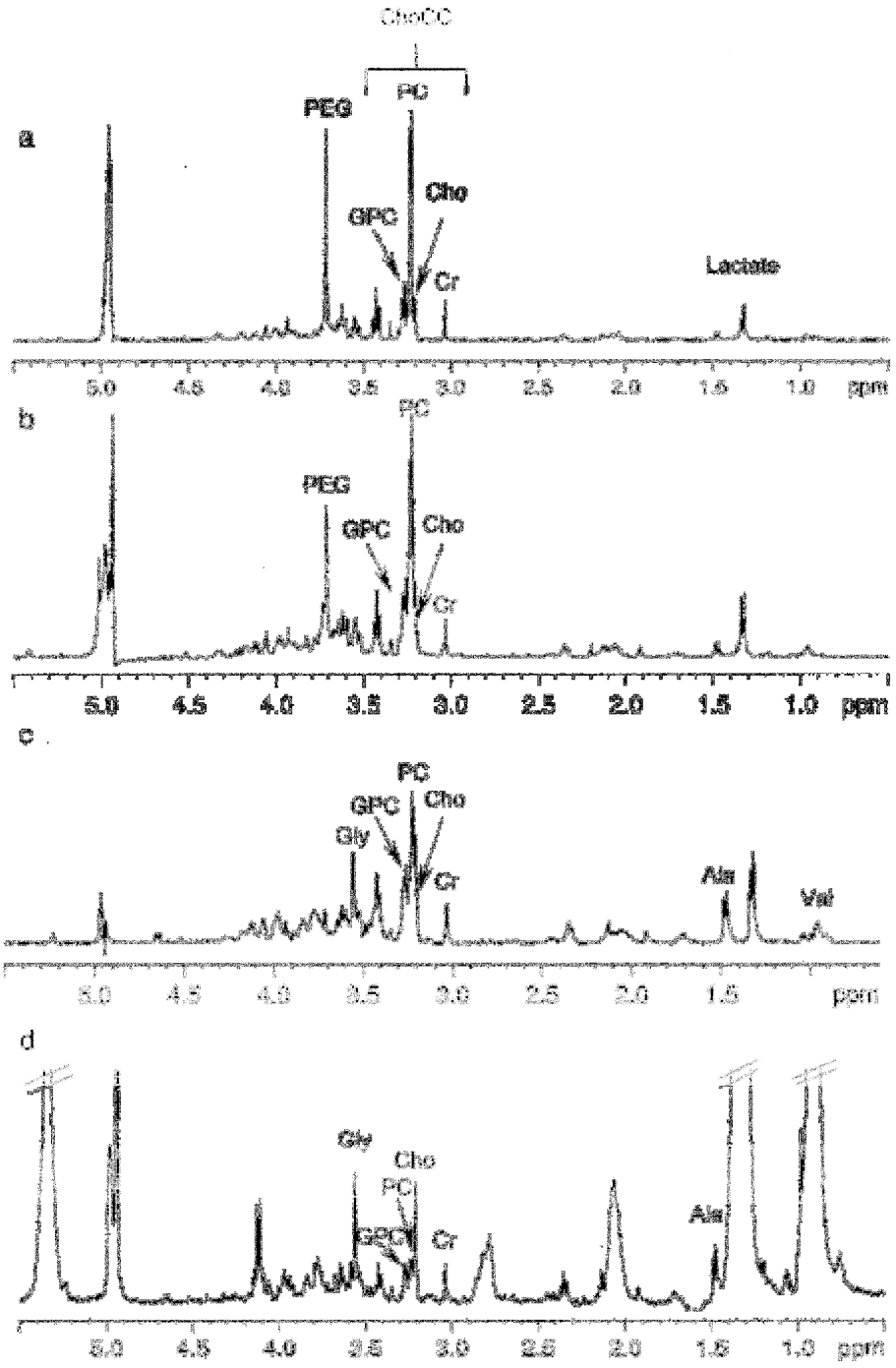

Figure 14. CPMG MR spectra of: (a) healthy, (b) *H. pylori*-related gastritis, (c) AAG and (d) adenocarcinoma.

The relative concentration of choline-containing compounds (ChoCC) and creatine (Cr) measured by the ChoCC/Cr ratio and the distribution of ChoCC [glycerophosphorylcoline (GPC), phoshorylcholine (PC) and free choline (Cho)], were similar. PC was the most

abundant in both situations. A slight increase of aliphatic aminoacids, valine (Val), leucine (Leu), isoleucine (Ile) at around 1.0 ppm, and Ala at 1.48 ppm, was revealed. The spectrum of AAG (Figure 2c) was instead characterized by enhanced resonances due to Val and Ala. In addition, strong signals due to Gly and free Cho could be detected along with the marked reduction of PC. The spectrum of the adenocarcinoma (Figure 14d) displayed a dramatic increase of free Cho, accompanied by very low amounts of GPC and PC and high amounts of Gly and Ala.

A progressive increase of free Cho, Gly and Ala, as already seen for TG, was observed passing from healthy tissue and *H. pylori*-related gastritis to AAG and adenocarcinoma (Figure 13). The behaviour of ChoCC and Gly is better shown in figure 15, reporting an enlarged region between 3.6 and 3.0 ppm of CPMG MR spectra of healthy gastric mucosa (Figure 15a), *H. pylori*-related gastritis (Figure 15b), AAG (Figure 15c) and adenocarcinoma (Figure 15d).

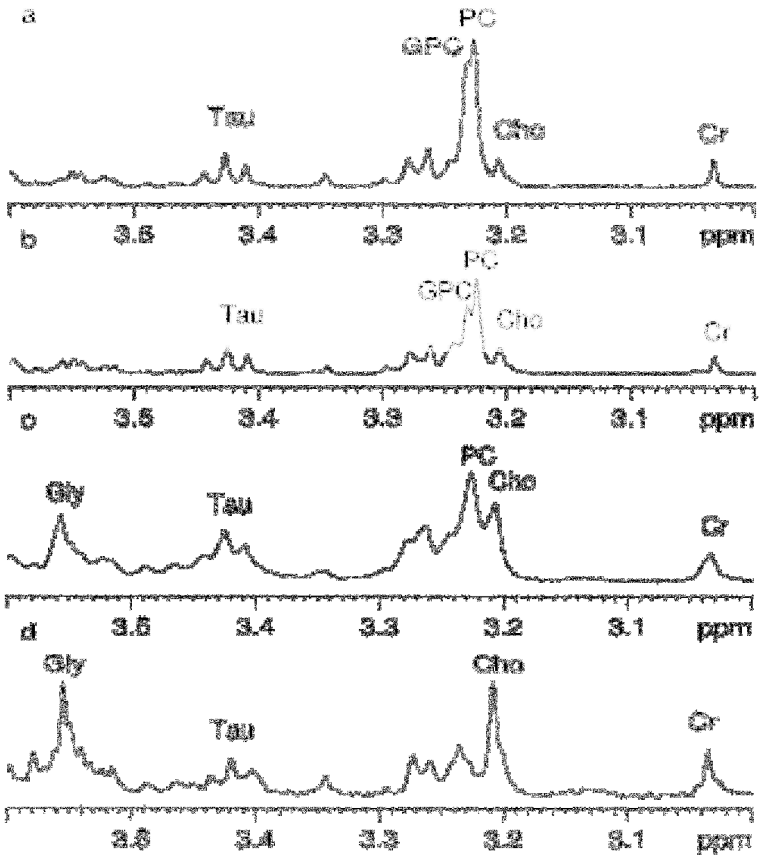

Figure 15. Enlarged region (3.6 ÷ 3.0 ppm) of CPMG MR spectra of: (a) healthy, (b) *H. pylori*-related gastritis, (c) AAG, (d) adenocarcinoma.

Diffusion-edited spectra (Figure 16a-d) were acquired in order to observe components with low diffusion rates deriving from lipids, carbohydrates and small proteins. The profile of the spectra 4a and 4b were very similar and characterized by phospholipids (Ph), MM, oligopeptides and polysaccharides. The Ph were identified, in particular, by the resonances of $N^+(CH_3)_3$ at 3.23 ppm (^{1}H MR spectra) and 54.8 ppm (^{13}C MR spectra) for phosphatidylcholine (Ptd-Cho). The remaining signals arose mainly from mobile peptidic residues and polysaccharides. The peptidic residues were recognizable by the broad signals around 4.30 ppm relative to the CH-α of bounded aminoacids, by the signals at 3.0 and 1.7 ppm for lysine (Lys), at 2.30 for glutamate (Glu), and they all contributed, with Ph, to the signals between 1.5 and 0.8 ppm (28). The broad signals between 3.5-4.0 ppm and the intense signal at 2.02 ppm suggested the presence of *N*-acetylated polysaccharides referable to mucin mucopolysaccharides.

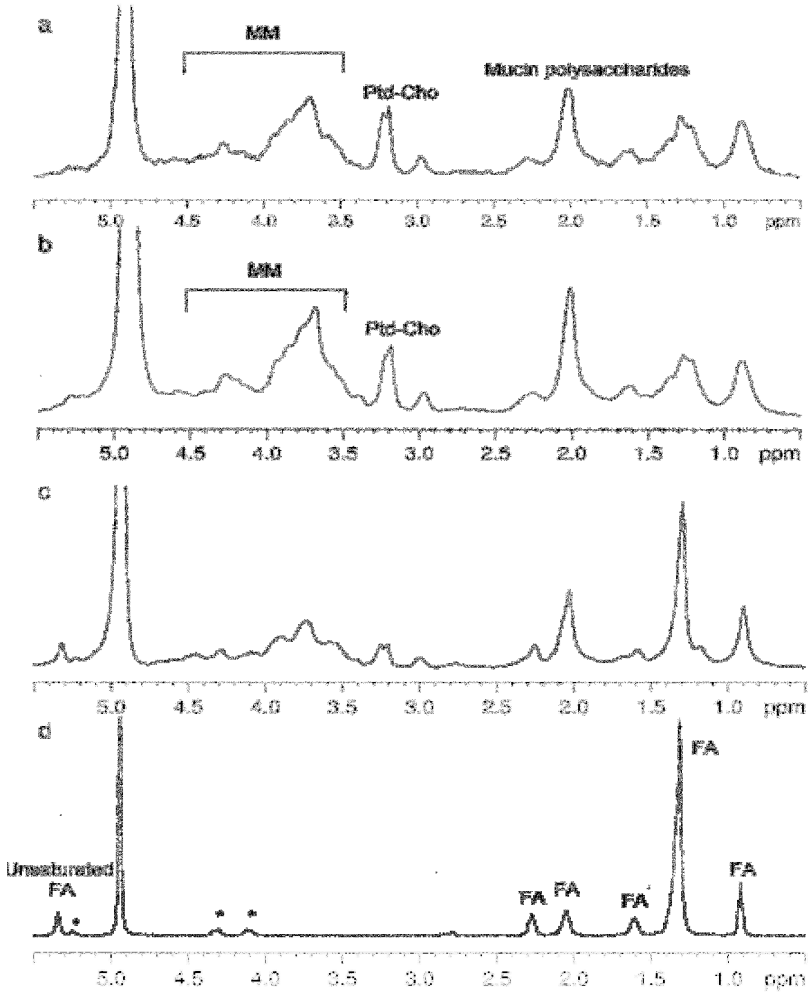

Figure 16. Diffusion-edited MR spectra of: (a) healthy, (b) H. pylori-related gastritis, (c) AAG, (d) adenocarcinoma. * TG glyceryl residues.

The spectrum in Figure 16c showed an increased amount of the components due to TG, signalling the molecular evolution of gastritis towards adenocarcinoma, characterized by the almost exclusive presence of TG (Figure 16d). The analysis of the spectrum showed that the TG were formed by saturated, mono- and poly-unsaturated FA. The unsaturated acids were identified by the signals at 5.33 ppm, assigned to the ethylenic protons, and by the signals at 2.02 ppm, due to the methylenic protons of the $-CH_2-CH=$ moiety of mono- and poly-unsaturated FA.

The *ex vivo* ^1H HR-MAS spectra (not shown) of the 9 specimens collected from the margin towards the core of a large adenocarcinoma sample, were all coincident and corresponded to those reported in Figures 13d and 13d. The only detectable resonances in all of these spectra were referable to TG.

The factor score plots PC1 versus PC2 and PC2 versus PC3 showed that there were clear differences ($p < 0.05$) between adenocarcinoma and healthy samples, *H. pylori*-related gastritis and AAG, but not between healthy and *H. pylori*-related gastritis samples (Figure 17).

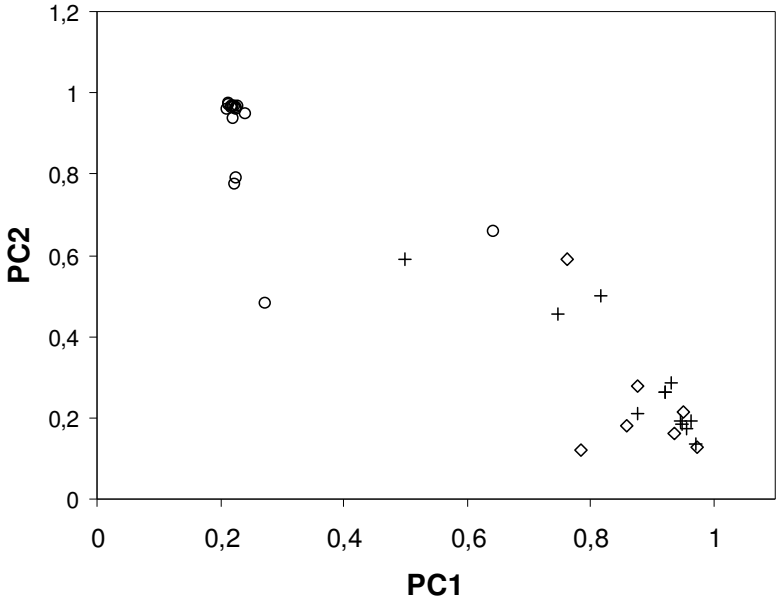

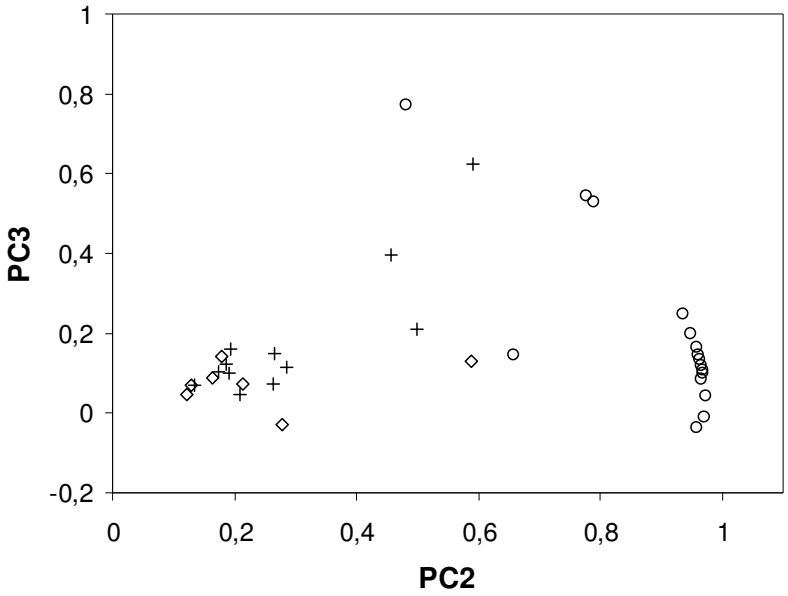

Figure 17. a) PC1 vs. PC2 and b) PC2 vs. PC3 score plots: clusters of adenocarcinoma vs. healthy and *H. pylori*-related gastritis samples. (○): adenocarcinoma, (◊) *H. pylori*-related gastritis and AAG, (+) healthy mucosa samples.

The TG, previously shown in AAG and adenocarcinoma samples by HR-MAS NMR, were detected as lipid bodies in gastric mucosa cells examined by TEM and SEM, but they were not visible in the light microscope (LM). AAG samples, by TEM, showed the presence of lipid vescicles, diffuse atrophy of parietal cell mass, disappearance of cell-cell contacts, cell shrinkage, mithocondria alteration, degradation of plasma and nuclear membranes. By SEM these lipid granules appeared quite often as grape-like shape (Figure 18a). All adenocarcinoma specimens by LM showed a low differentiated intestinal type characterized by cohesive neoplastic cells forming gland-like tubular structures in which cell cohesions were absent and in particular, no lipid granules were detected. Using TEM, a large number of globular structures in the cytoplasm were seen like those observed in the AAG samples. These lipid vesicles appeared well delimited and surrounded by a membrane-like layer and were mostly visible near the nuclei in most of the tumour cells (Figure 18b). Lipid vesicles, with a diameter ranging from 0.2 to about 1.5 μm were also revealed in tumour cells observed in the SEM (Figure 18c) but not were detected in the healthy samples.

a)

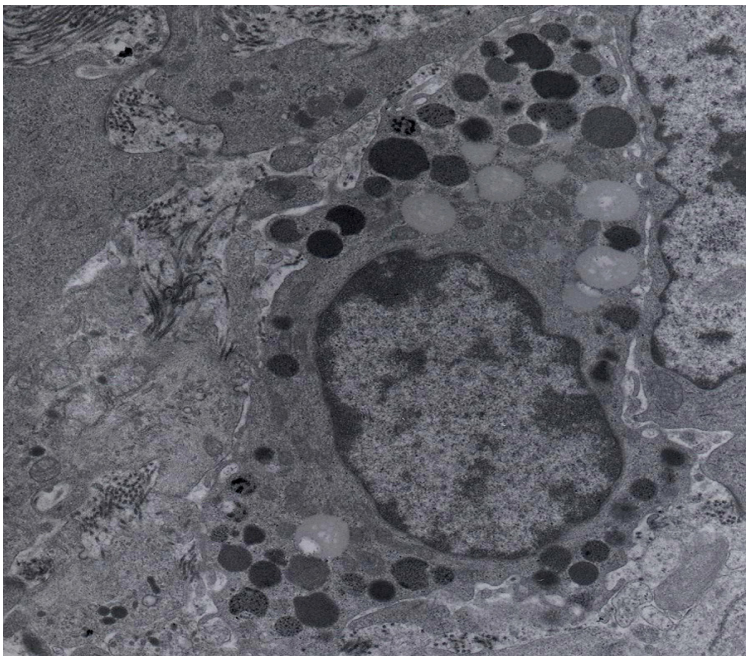

b)

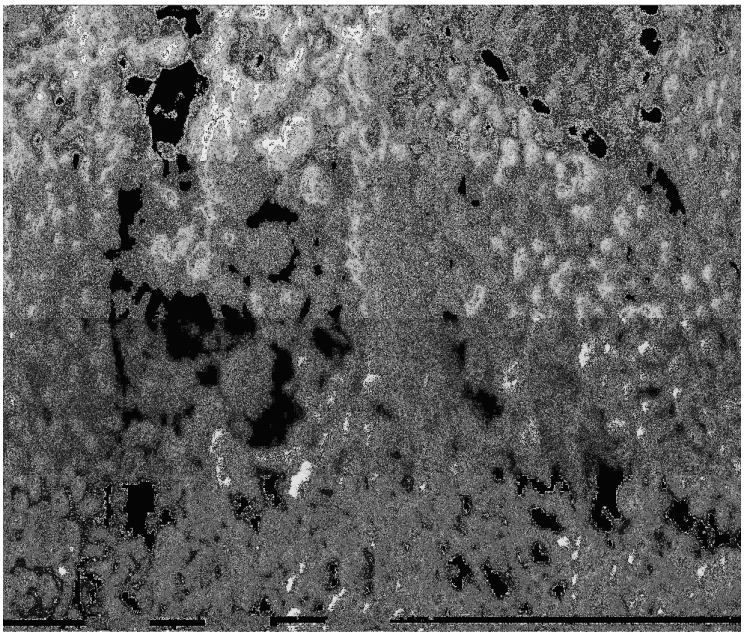

c)

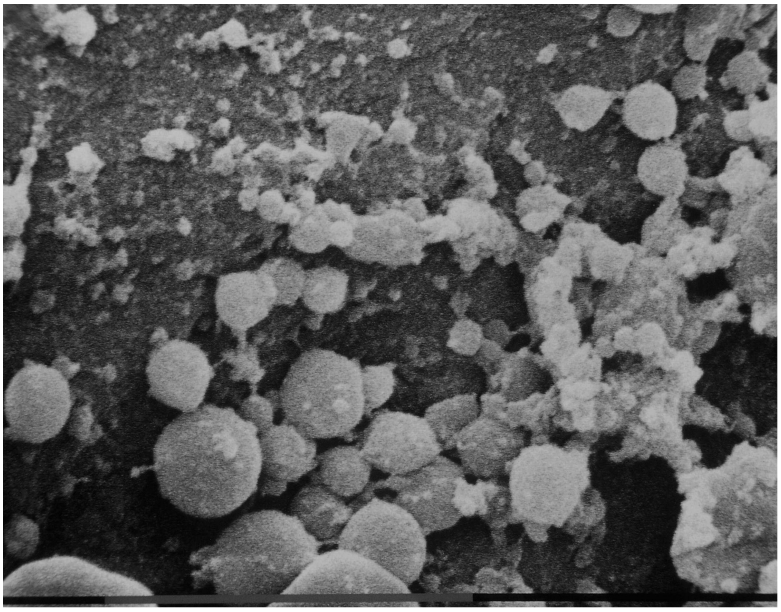

Figure 18. (a) TEM: ultrathin section of adenocarcinoma. Presence of intracellular electron dense globular bodies in the cytoplasm which could be identified as lipid bodies due to their osmiophilic nature. Scale bar = 0.95; (b) SEM: AAG. Globular lipid bodies singly or in clusters are visible. Scale bar = 1µm; (c) SEM: adenocarcinoma. Globular lipid bodies singly or aggregated are visible. Scale bar = 10µm.

Cancer exhibits a significant altered choline phospholipid metabolism compared with normal tissue (29). An increase of PC and ChoCC characterizes the aberrant choline phospholipid metabolism in cancers, as demonstrated by NMR studies (30,31).

This research confirms the previous data reporting that free Cho is the most abundant ChoCC metabolite in gastric adenocarcinomas. To our knowledge this is the first study reporting a strong elevation of free Cho in the AAG, when compared with *H. pylori*-related gastritis and healthy gastric mucosa. The complex Kennedy network, characterized by biosynthetic and breakdown pathways, regulates the choline phospholipid metabolism in which more enzymes lead changes in the overall choline metabolite profiles. The unexpected, high free Cho amount detected in the AAG and adenocarcinoma, led us to believe that the role of phosphatidylcholine specific phospholipase D (PC-PLD), which catalyses the hydrolysis of Ptd-Cho to free Cho and Phosphatidic acid (PA), is preminent in the development and progression of the gastric cancer. Indeed, PC-PLD has been implicated in cell proliferation and cancer (32). Its increased activity and expression has been reported in several human neoplasms (33-35), including gastric adenocarcinoma (36) where PC-PLD plays an important role in the promotion of cancer. These data could explain the high level of free Cho detected in the gastric adenocarcinoma samples examined. In addition, the formation of Cho and PA,

may be important in the molecular pathway of the gastric carcinogenesis, since these compounds are lipid derived second messengers involved in mitogenic signaling pathway (37). AAG, characterized also by a high level of free Cho, is evolving towards a pre-neoplastic condition and probably the high free Cho amount detected in gastric adenocarcinoma, is due to the synthesis of new cell membranes in the neoplastic cells. Further studies are needed to evaluate the activity and expression of the enzimatic pattern, associated to the synthesis and breakdown of membrane Ptd-Cho in these tissues.

The high amount of Gly we detected in gastric adenocarcinoma, has been already demonstrated in different human tumors. For example, Griffin and Shockor (38) suggested that a preeminent glycolytic pathway in cancer cells is responsible for the Gly increase and Finch et al. (39) showed an elevation of the level of the lactic dehydrogenase in AAG gastric wash samples. Moreover, other authors reported high level of Gly in glioblastomas, renal and breast tumors (18,21,22). Hypoxia could explain the high amount of Gly in gastric adenocarcinoma. A significant decrease in Gly, was detected in Hypoxia-Inducible Factor-1β (HIF-1β) deficient hepatomas (40). On the other hand, it is well known hypoxia in humans causes an up-regulation of different genes by activation of the Hypoxia-Inducible Factor-1α (HIF-1α) which has been demonstrated over-expressed in gastric cancer (41-43). In a similar way, a gastric cell line study has showed that reactive oxygen species, produced by *H. pylori* infection, lead to an increase of HIF1-α (44).

The Ala relative concentration was another peculiarity which differentiated AAG and adenocarcinoma samples from the healthy and *H. pylori*-related gastritis. Ala increase has been associated with different tumor types (38,45,46). Ala, in conjunction with lactate, increases in tissues during hypoxia, in fact, it is formed by pyruvate transamination to prevent further increase in lactate. Ben Yoseph et al. (47) showed a strong increase of lactate in mild hypoxia, while Ala increased in severe hypoxia. We hypothesize that the Ala increase in the AAG and adenocarcinoma samples, is related to a severe hypoxia conditions and could be a marker for new real-time metabolic molecular imaging for cancer diagnosis (48).

Ex vivo and *in vivo* MRS of most cancers are characterized by signals assigned to FA lipid mobile acyl chains. The appearance of mobile lipids in the spectra of intact cells is generally attributed to the formation of non-bilayer lipid structures, occurring either at the plasma membrane level or within cytoplasmic compartments (12,49). The resonances typical of mobile lipids, identified as TG, were detected in all the *ex vivo* ^{1}H HR-MAS MR spectra relative to AAG and adenocarcinoma, where the distribution of the mobile lipids appeared to

be homogeneous. The intra-and extra-cellular lipid accumulation and mitochondria degeneration, revealed by TEM and SEM, are probably associated to a severe perinecrotic hypoxia in AAG and adenocarcinoma samples. Our data are supported by Goto *et al.* (50) who demonstrated that the cytoplasmic accumulation of TG in human fibrosarcoma cells occurred in response to hypoxic conditions, and that mitochondria degeneration were probably caused by the reduction of β-oxidation of FA. A similar hypothesis was previously asserted by Freitas, who described lipid accumulation as a consequence of mitochondria degeneration in malignant solid tumors (51,52). Zoula *et al*. correlated lipid droplets in C6 rat brain glioma to a severe prenecrotic hypoxia (17). We suppose that the harmful effect of the increase of free FA concentration in gastric adenocarcima could be avoided by sequestring FA as TG in form of lipid droplets.

In conclusion, *ex vivo* HR-MAS MRS has been shown to be feasible even for small endoscopic biopsies and allows identification of Gly, Ala, Cho and TG, as the possible biochemical mediators for human gastric mucosa differentiation towards neoplastic conditions. Further studies on the enzymatic pathways of these metabolites will be useful. Moreover, the biochemical information obtained on gastric pathological tissue could represent the basis for clinical applications of *in vivo* MRS, which reliability is based on the identification of molecular markers.

References

1. Boring CC, Squires TS, Tong MS. Cancer statistic. *CA Cancer. J. Clin.* 1994; **44**: 7-26.
2. Rudy DRA, Zdon MJ. Update on colorectal cancer. *Am. Fam. Physician*. 2000; **61**: 1759-1769.
3. Stepan V, Sugano K, Yamada T, Park J, Dickinson CJ. Gastrin biosynthesis in canine G cells. *Am. J. Physiol*. 2002; **282**: G766-G775.
4. Tang Z, Zhao M, Ji J, Yang G, Yang G, Hu F, He J, Shen H, Gao Z, Zhao A, Li J, Lu Y. Overexpression of gastrin and c-met protein involved in human gastric carcinomas and intestinal metaplasia. *Oncol. Rep*. 2004; **11**: 333-339.
5. Murray CJ, Lopez AD. Alternative projections of mortality and disability by cause 1990-2000: Global Burden of Disease Study. *Lancet.* 1997; **349**: 1494-1504.
6. Correa P. Human gastric carcinogenesis. A multistep and multifactorial process. *Cancer Res*. 1992; **52**: 6735-6740.
7. Danesh J. *Helicobacter pylori* infection and gastric cancer: systematic review of the epidemiological studies. *Aliment. Pharmacol. Ther.* 1999; **13**: 851-856.
8. Rudy DRA, Zdon MJ. Update on colorectal cancer. *Am. Fam. Physician.* 2000; **61**: 1759-1769.
9. Mun CW, Cho JY, Shin WJ, Choi KS, Eun CK, Cha SS, Lee J, Yang YI, Nam SH, Kim J, Lee SY. Ex vivo proton MR spectroscopy (1H-MRS) for evaluation of human gastric carcinoma. *Magn Reson Imaging*. 2004; **22**: 861-870.
10. Goeseki N, Takizawa T, Koike M. Differences in the mode of extension of gastric cancer classified by histological type: new histological classification of gastric carcinoma. *Gut.* 1992; **33**: 606-612.
11. Mannina L, Luchinat C, Patumi M, Emanuele MC, Rossi E, Segre A. Concentration dependance of 13C NMR spectra of triglycerides: implications for the NMR analysis of olive oils. *Magn. Reson. Chem.* 2000; **38**: 886-890.
12. Hakumaki JM, Kauppinen RA. 1H NMR visibile lipids in the life and death of cells. *Trends Biochem. Sci.* 2000; **25**: 357-362.
13. Callies R, Sri-Pathmanathan RA, Ferguson DYP, Brindle KM. The appearance of neutral lipid signals in the 1H NMR spectra of a myeloma cell line correlates with the induced formation of cytoplasmatic lipid droplets. *Magn. Reson. Med.* 1993; **29**: 546-550.
14. Rèmy R, Fouilhè N, Barba I, Sam-Lai E, Lahrec H, Cucurella MG, Izquierdo M, Moreno A, Ziegler A, Massarelli R, Décorps M, Arús C. Evidence that mobile lipids detected in rat brain glioma by 1H nuclear magnetic resonance correspond to lipids droplets. *Cancer Res.* 1997; **57**: 407-414.
15. Ferretti A, Knijn A, Iorio E, Pulciani S, Giambenebetti M, Molinari A, Meschini S, Stringaro A, Calcabrini A, Freitas I, Strom R, Arancia G, Podo F. Biophysical and structural characterization of 1H-NMR-detectable mobile lipid domains in NIH-3T3 fibroblast. *Biochem. Biophys. Acta.* 1999; **1438**: 329-348.
16. Barba I, Cabanas ME, Arùs C. The relationship between nuclear magnetic resonance-visible lipids, lipid droplets and cell proliferation in cultured C6 cells. *Cancer. Res.* 1999; **59**: 1861-1868.
17. Zoula S, Hèrigault G, Ziegler A, Farion R, Dècorps M, Remy C. Correlation between the occurrence of 1H-MRS lipid signal, necrosis and lipid droplets during C6 rat glioma development. *NMR Biomed.* 2003; **16**: 199-212.
18. Tate AR, Foxall PJD, Holmes E, Moka D, Spraul M, Nicholson JK. Distinction between normal and renal cell carcinoma kidney cortical biopsy samples using pattern recognition of 1H magic angle spinning (MAS) NMR spectra. *NMR Biomed.* 2000; **13**: 64-71.

19. Peeling J, Sutherland G. High-resolution 1H NMR spectroscopy studies on extracts of human cerebral neoplasms. *Magn. Reson. Med.* 1992; **24**: 123-136.
20. Kinoshita Y, Yokota A. Absolute concentrations of metabolites in human brain tumors using *in vitro* proton Magnetic Resonance Spectroscopy. *NMR Biomed.* 1997; **10**: 2-12.
21. Lehnardt FG, Bock C, Rohn G, Ernestus RI, Hoehn M. Metabolic differences between primary and recurrent human brain tumors: a 1H NMR spectroscopic investigation. *NMR Biomed.* 2005; **18**: 371-382.
22. Sitter B, Lundgren S, Bathen Tone F, Halgunset J, Fjosne HE, Gribbestadt IS. Comparison of HR MAS MR spectroscopic profiles of breast cancer tissue with clinical parameters. *NMR Biomed.* 2006; **19**: 30-40.
23. Correa P. A human model for gastric carcinogenesis. *Cancer Res.* 1988; **48**: 3554-3560.
24. Helicobacter and Cancer Collaborative Group. Gastric cancer and Helicobacter pylori: A combined analysis of 12 case control studies nested within prospective cohorts. *Gut*. 2001; **49**: 347-353.
25. Meining A, Bayerdorffer E, Muller P, Miehlke S, Lehn N, Hölzel D, Hatz R, Stolte M. Gastric carcinoma risk index in patients infected with Helicobacter pylori. *Virchows Arch* 1998; **432**: 311-314.
26. Correa P. Chronic gastritis: a clinic-pathological classification. *Am. J. Gastroenterol*. 1988; **83**: 504-509.
27. Tugnoli V, Mucci A, Schenetti L, Calabrese C, Di Febo G, Rossi MC, Tosi MR. Molecular characterization of human gastric mucosa by HR-MAS magnetic resonance spectroscopy. *Int. J. Mol. Med*. 2004; **14**: 1065-1071.
28. Tugnoli V, Mucci A, Schenetti L, Parenti F, Cagnoli R, Righi V, Trinchero A, Nocetti L, Toraci C, Mavilla L,Trentini G, Zunarelli E, Tosi MR. Ex vivo HR-MAS MRS of human meningiomas: a comparison with in vivo 1H MR spectra. *Int. J. Mol. Med*. 2006; **18**: 859-869.
29. Podo F. Tumour phospholipid metabolism. *NMR Biomed.* 1999; **12**: 413-439.
30. Aboyage EO, Bujwalla ZM. Malignant transformation alters membrane choline phospholipid metabolism of human mammary epithelial cells. *Cancer Res* 1999; **59**: 80-84.
31. Iorio E, Mezzanzanica D, Alberti P, Spadaro F, Ramoni C, D'Ascenzo S, Millimaggi D, Pavan A, Dolo V, Canevari S, Podo F. Alterations of coline phospholipid metabolism in ovarian tumor progression. *Cancer Res*. 2005; **65**: 9369-9376.
32. Foster DA, Xu L. PhospholipaseD in Cell Proliferation and Cancer. *Mol. Canc. Res*. 2003; **1**: 798-800.
33. Noh DY, Ahn SJ, Lee RA, Park IA, Kim JH, Suh PG, Ryu SH, Lee KH, Han JS. Overexpression of phospholipase D1 in human breast cancer tissue. *Cancer Lett*. 2000; **161**: 207-214.
34. Uchida N, Okamura S, Nagamachi Y, Yamashita S. Increased phospholipase D activity in human breast cancer. *J. Canc. Res. Clin. Oncol.* 1997; **123**: 280-285.
35. Zhao Y, Ehara H, Akao Y, Shamoto M, Nakagawa Y, Banno Y, Deguchi T, Ohishi N, Yagi K, Nozawa Y. Increased activity and intranuclear expression of phpspholipase D2 in human renal cancer. *Biochem. Biophys. Res. Commun*. 2000; **278**: 140-143.
36. Uchida N, Okamura S, KuwanoH. Phospholipase D activity in human gastric carcinoma. *Anticancer Res*. 1999; **19**: 671-675.
37. Rodriguez-Gonzalez A, Ramirez de Molina A, Benitez-Rajal J, Lacal JC. Phospholipase D and choline kinase: their role in cancer development and their potential as drug target. *Prog. Cell Cycle Res.* 2003; **5**: 191-201.
38. Griffin JL, Shockor JP. Metabolic profiles of cancer cells. *Nat. Rev. Cancer* 2004; **4**: 551-561.

39. Finch PJ, Ryan FP, Rogers K, Holt S. Gastric enzymes as a screening test for gastric cancer. *Gut.* 1987; **28**: 319-322.
40. Griffiths JR, McSheehy PMJ, Robinson SP, Troy H, Chung YL, Leek RD, Williams KJ, Stratford IJ, Harris AL, Stubbs M. Metabolic Changes Detected by in Vivo Magnetic Resonance Studies of HEPA-1 Wild-Type Tumors and Tumors Deficient in Hypoxia-inducible Factor-1b (HIF-1b): Evidence of an anabolic Role for the HIF-1 Pathway. *Cancer Res.* 2002; **62**: 688-695.
41. Mizokami K, Kakeji Y, Oda S, Irie K, Yonemura T, Konishi F, Maehara Y. Clinicopathologic significance of hypoxia-inducible factor 1alpha over expression in gastric carcinomas. *J. Surg. Oncol*. 2006; **94**: 149-154.
42. Griffiths EA, Pritchard SA, Valentine HR, Whitchelo N, Bishop PW, Ebert MP, Price PM, Welch IM, West CM. Hypoxia-inducible factor-1alpha expression in the gastric carcinogenesis sequence and its prognostic role in gastric and gastro-oesophageal adenocarcinomas. *Br. J. Cancer* 2007; **96**: 95-103.
43. Zhong H, De Marzo AM, Laughner E, Lim M, Hilton DA, Zagzag D, Buechler P, Isaacs WB, Semenza GL, Simons JW. Overexpression of hypoxia-inducible factor 1alpha in common human cancers and their metastases. *Cancer Res.* 1999; **59**: 5830-5835.
44. Park JH, Kim TY, Jong HS, Kim TY, Chun YS, Park JW, Lee CT, Jung HC, Kim NK, Bang YJ. Gastric epithelial reactive oxygen species prevent normoxic degradation of hypoxia-inducible factor-1alpha in gastric cancer cells. *Clin. Cancer. Res*. 2003; **9**: 433-440.
45. Tosi MR, Fini G, Tinti A, Reggiani A, Tugnoli V. Molecular characterization of human healthy and neoplastic cerebral and renal tissues by in vitro 1H NMR spectroscopy. *Int. J. Mol. Med.* 2002; **9**: 299-310.
46. Bourne RM, Stanwell P, Stretch JR, Scolyer RA, Thompson JF, Mountford CE, Lean CL. In vivo and ex vivo proton MR spectroscopy of primary and secondary melanoma. *Eur. J. Radiol*. 2005; **53**: 506-513.
47. Ben Yoseph O, Baddar-Goffer RS, Morris PG, Bachelard HS. Glycerol 3-phosphate and lactate as indicators of the cerebral cytoplasmic redox state in severe and mild hypoxia respectively: A carbon-13 and phosphorus-31 NMR study. *Biochem. J.* 1993; **291**: 915-919.
48. Golman K, In't Zandt R, Thaning M. Real-time metabolic imaging. *Proc. Natl. Acad. Sci. USA*. 2006; **103**: 11270-11275.
49. Iorio E, Di Vito M, Spadaro F, Ramoni C, Lococo E, Carnevale R, Lenti L, Strom R, Podo F. Triacsin C inhibits the formation of 1H NMR-visible mobile lipids and lipid bodies in HuT 78 apoptotic cells. *Biochim. Biophys. Acta*. 2003; **1634**: 1-14.
50. Goto K, Asai T, Hara S, Namatame I, Tomoda H, Ikemoto M, Oku N. Enhanced antitumor activity of xanthohumol, a diacylglycerol acyltransferase inhibitor, under hypoxia. *Cancer Lett*. 2005; **219**: 215-222.
51. Freitas I. Lipid accumulation: the common feature to photosensitizer-retaining normal and malignant tissues. *J. Photochem. Photobiol. B* 1990; **7**: 359-361.
52. Freitas I, Bono B, Bertone V, Griffini P, Baronzio GF, Bonandrini L, Gerzeli G. Characterization of the metabolism of perinecrotic cells in solid tumors by enzyme histochemistry. *Anticancer Res*. 1996; **16**: 1491-1502.

COLON TISSUE

Colorectal cancer (CRC) is the fourth most common cancer and the second leading cause of cancer death in the United States with high morbidity and mortality. Currently, there are four tests for the early detection of CRC, including fecal occult blood testing (FOBT), sigmoidoscopy (SIG), colonoscopy (COL), and double contrast barium enema (DCBE) (1–3). The strongest evidence for a mortality reduction comes from three randomized controlled trials of FOBT (4–6), whereas three case-control studies have demonstrated support for SIG in reducing CRC mortality (7–9). Although the ability of COL to reduce mortality has not been determined from clinical trials, there is evidence to support the effectiveness of screening COL in reducing incidence and mortality (10 –12).

The recommendations of the American Cancer Society (ACS) have been shown to be those most widely recognized by primary care physicians (13). Currently, for CRC screening, the ACS recommends one of the following screening options: (*a*) annual FOBT by 3-day kit; (*b*) SIG every 5 years; (*c*) a combination of an annual FOBT plus SIG every 5 years; (*d*) a DCBE every 5–10 years; or (*e*) a COL every 10 years (2).

Complete "conventional" staging concepts require additional imaging procedures to assess potential metastatic spread to lymph nodes and solid organs (14-17). Of these conventional imaging procedures, contrast-enhanced computed tomography (CT) is the most common for both the abdomen and the thorax (16, 18-23). However, CT offers only morphological data for the evaluation of the tumor stage. Glucose analog [18F]-fluorodeoxyglucose-positron emission tomography (FDG-PET) can display functional information and has been found to be accurate in the detection of colorectal cancer and its distant metastases (24-29). Furthermore, based on its limited spatial resolution, FDGPET often makes difficult exact anatomical localization of the lesion. The combination of PET/CT scanners have been introduced into clinical practice because of their ability in detecting and characterizing malignant lesions, with advantages over morphology and function alone. The fusion of functional with morphological data, beneficial for the tumor staging, have been documented for different tumors including colorectal cancer (30-35). The stepwise multimodality diagnostic workup could be shortened by performing PET/CT colonography, as a whole-body imaging procedure. PET/CT protocols might not be specific enough to evaluate all clinically important aspects of the cancer entity (36-37).

The study of colon cancer by HR-MAS NMR has not been reported yet but to our knowledge, there is only one paper on the variation of the metabolic profile of healthy human gastrointestinal tract (GIT) (38).

We report a study on the *ex vivo* HR-MAS NMR of healthy and neoplastic colon tissues in combination with multivariate methods Principal Component Analysis (PCA) and Partial Least Squares Discriminant Analysis (PLS-DA). In particular PCA has been carried out as explorative analysis in order to obtain an overview on the whole data set without forcing any model and to extract relevant information. PLS-DA (39) has been used to build a classification model able to separate the classes of healthy and neoplastic human tissues on the basis of their *ex vivo* HR-MAS NMR spectra. Moreover, the biochemical data obtained on colorectal pathological tissue could represent the basis for accurate and non invasive clinical applications of *in vivo* MRS, which reliability is based on the identification of molecular markers.

Sample collection. Samples of 23 patients, 14 with colon cancer (7 male, range 52-78 years; and 7 women, range 48-90 years, and 9 healthy (9 male, range 30-86 years) were evaluated. Five biopsies, 4 for histologic evaluation and 1 for NMR analysis, were taken from each subject during endoscopy. The specimens (biopsies and surgical samples) in patients with colocancer were obtained exclusively from the carcinoma site, assuring the absence of any contaminants. Moreover, during surgery we also collected specimens at least 15 cm far from the adenocarcinoma, from the 14 colon cancer patients. The tissue samples were put in liquid nitrogen, after surgery, and stored at -80° C until MRS analyses.

Histologic evaluation. Four specimens from each patient fixed routinely with 10% buffered formalin and embedded in paraffin, after which the entire tumor was cut into serial 2- to 3-mm thick slices. Microscopic examination of hematoxylin and eosin-stained sections was performed by one pathologist unaware of other features of the case. Adenocarcinomas were classified as well (D), mild (MD) and poorly differentiated (PD). According to previously proposed measuring methods (40,41), the depth of submucosal invasion was determined using a micrometer under a microscope, and taken as the distance from the muscularis mucosae to the point of the deepest invasion (tumor apex). Demographic and histological data are reported in Table II.

For NMR experiments details see chapter II.

Table II. Demographic and histological data.

	Age	Sex	Type	Histology
Control subjects	60.89 ± 8.64	3 male	normal	Normal
Adenocarcinomas	63.33 ± 9.22	6 male	Adenocarcinomas	1D, 8MD, 2PD

Data handling and pretreatment. HR-MAS ^{1}H NMR data (normal ^{1}H sequence with water-presaturation) were processed by using the Bruker software, applying 0.5 Hz line broadening prior to Fourier transformation, then phased and baseline corrected (polynomial of order 6). The spectra, acquired for 31 samples of colon human tissues, are referenced to the chemical shift of the CH_3 peak of alanine at δ 1.48 ppm.

The NMR data points were reduced from 32k to 16k. The selected spectral width spans from δ 9.05 ppm to δ 0.05 ppm and the number of data points is 7500. The regions corresponding to water and PEG signals between δ 5.03-4.69 ppm and δ 3.75-3.68 ppm, respectively, were removed (6341 final data points), since these are regions of high variance that is mainly due to sample acquisition/manipulation and it is not interesting from the point of view of healthy-canceregenous tissues discrimination.

As is well known, pre-treatment of data is a critical and case dependent issue in multivariate analyses, above all as far as NMR spectra are concerned. In this study, several preprocessing were tested and the best performance was obtained by normalizing each spectrum to the sum of the intensity data. As far as scaling is concerned, working with unscaled data seems preferable, since in this case there is the risk of dramatically up-weighting components present in very small amounts and showing little variation (such as spectral background or baseline). However, given the presence of major and minor constituents, it is desiderable to give to different compounds a comparable influence in the data analysis. Taking into account this consideration, the data set was scaled using the block-scaling procedure called “block-adjusted non-scaled data (42). In particular, NMR spectra signals were divided in different regions (blocks) whose values were scaled in order to attain the same block-variance after pretreatment. In Figure 1, the block regions (figure 1a) and the pretreated signals (figure 1b) were reported, respectively.

As a first explorative tool, PCA was carried out on a data set organised as a bidimensional matrix of 31 (human colon samples) x 6341 points (ppm). Four samples seem to behave as outliers from PCA: samples c15 and c15t were not acquired with water-presaturation and samples c17 and c17t, that showed an higher signal at 2.0 ppm (not present

in the other samples); hence they were-excluded. Thus, these samples were excluded and PCA and PLS–DA analyses were carried out on the reduced data array of dimension 27 samples (9 healthy, 9 neoplastic and 9 peritumoral tissues) x 6341 points, *i.e.* δ 9.05 -δ 0.05 ppm. The PCA and PLS –DA analyses were carried out on the reduced data array of dimension 27 samples (9 healthy, 9 neoplastic and 9 peritumoral tissues) x 6341 points, *i.e.* δ 9.05 -δ 0.05 ppm. Six spectra acquired on 3 different patients tissues (3 spectra belonging to neoplastic and 3 to peritumoral section of colon region, respectively) were used as a test-set in order to validate and to test the performance of the different models.

PCA and PLS-DA analyses was carried out by using PLS-Toolbox 4.1 for MATLAB© (distributed by Eigenvector Research, WA, USA).

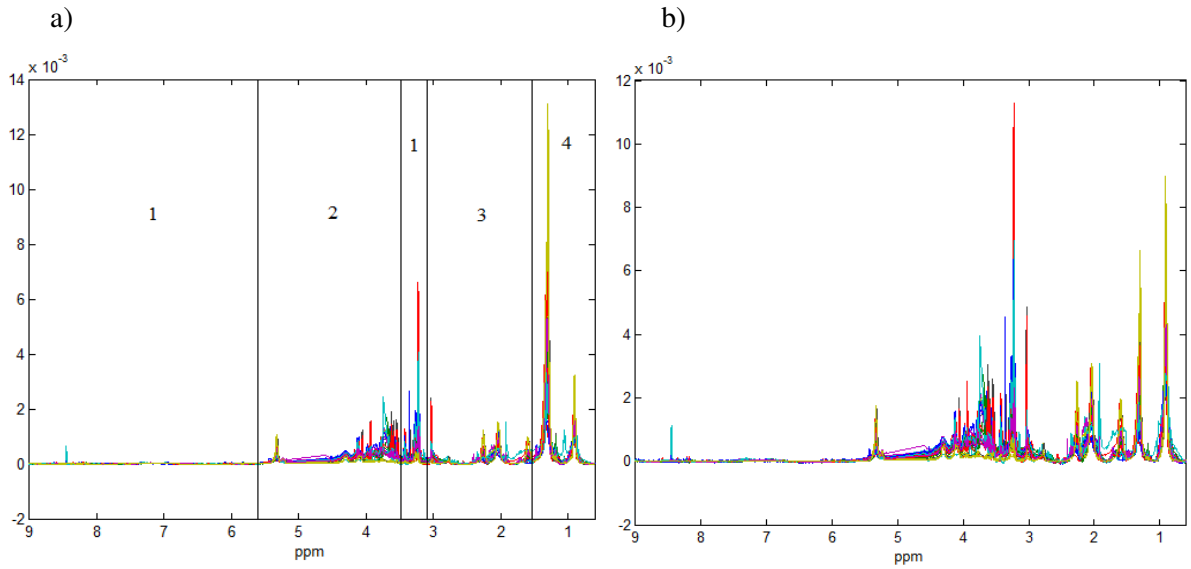

Figure 1. (a) Raw NMR spectra. The vertical line highlights the four regions selected for performing the block-scaling pre-treatment; (b) the corresponding 'blockscaled' signals.

Result and discussion

Representative 1D *ex vivo* HR-MAS ^{1}H NMR spectra of healthy colon tissues are shown in Figure 2: trace 2a displays a conventional 1D ^{1}H HR-MAS spectrum with water presaturation. The spectrum highlights both narrow and broad signals, which can be separated by using a CPMG spin-echo (trace 2b) and a diffusion-edited sequence (trace 2c). The spin-echo spectrum displays signals due to the resonances of small metabolites, whereas the diffusion-edited spectrum shows contributions from mobile lipids and macromolecules (MM).

The assignment of metabolites derives not only from the analysis of 1D ^{1}H NMR spectra, but also from that of selected 2D experiments such as COSY, TOCSY and HSQC,

and was confirmed by comparison with literature data. COSY and TOCSY spectra are very effective for the identification of hidden resonances: COSY spectra enable coupled proton-proton pairs to be found, whereas the TOCSY spectra permit $^{1}H,^{1}H$ connectivities up to five or six bonds and metabolite spin systems to be identified. HSQC spectra reveal directly bonded carbon-proton pairs, thus enabling the assignment of singlets (which do not give correlations in homonuclear COSY and TOCSY spectra), and the discrimination among compounds having similar proton but diverse ^{13}C chemical shifts. The full experiments provide complete and unambiguous identification of the metabolic pattern characterizing the examined tissues.

The TOCSY spectrum of a specimen obtained at least 15 cm far from a well differenziated adenocarcinoma with the deepest submucosal invasion (identified as 4h in figure 4) is reported as an example in figure 3. This experiment permits to detect hidden resonances, such as those of Lys, Arg, PE, and those due to bonded aminoacids (-Ala-, and -Thr-), to discriminate the resonances at 3.78 ppm due to the α-CH protons belonging to different α amino acids, and to distinguish PC, GPC and Cho.

The identification of metabolites can be improved exploiting the ^{13}C chemical shift dispersion in the second dimension of a HSQC experiment. The HSQC spectrum (Figure 5) permits to differentiate between free and bonded amino acids, (-Ala- , -Thr-, -Glu-, and –αCH-), between free glycerol and glycerol in lipids, and to better evidence signals due to proline (Pro).

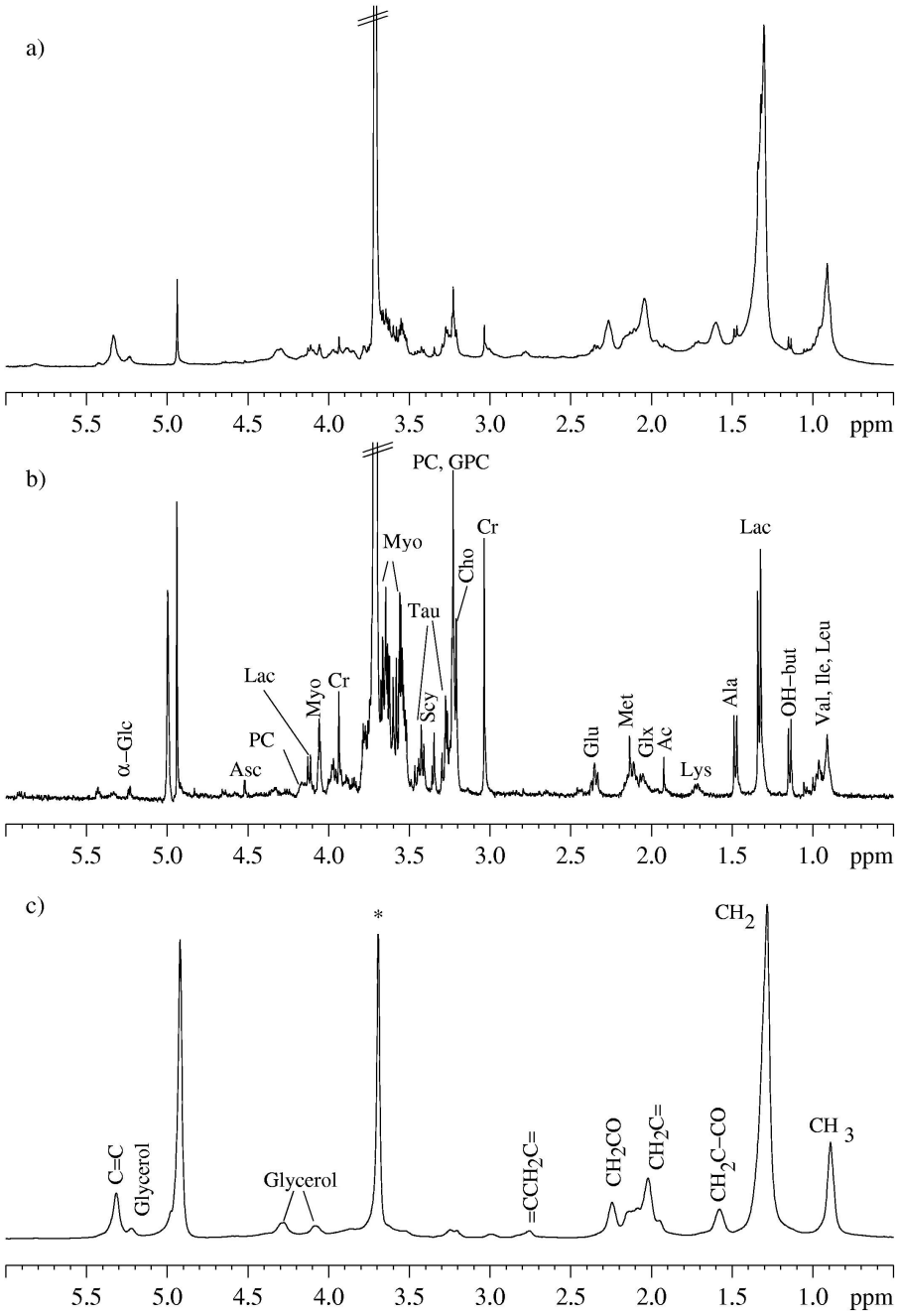

Figure 2. Representative *ex vivo* HR-MAS ^{1}H NMR spectra of colon biopsies: a) water-presaturated pulse sequence with composite pulse, b) CPMG spectrum and c) diffusion-edited spectrum. (*) Signal at 3.72 ppm due to PEG, an exogenous compound used as an excipient in pharmaceutical preparations before biopsies or surgery, is present in different amount in some samples.

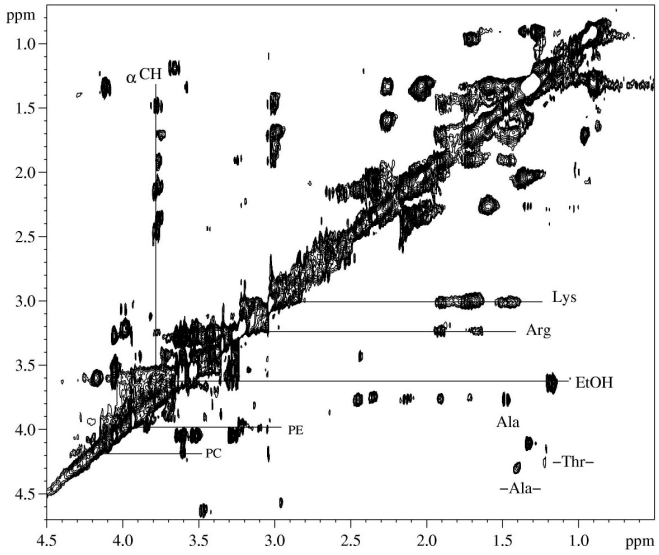

Figure 3: TOCSY spectrum of a colon specimens obtained at least 15 cm far from the adenocarcinoma (identified as 4h in figure 4).

The CPMG spectra of the healthy colon tissues permit to identify amino acids (Ala, Val, Leu , Ile, Glu and Lys), osmolites (Lac, Tau, Cr and ChoCC) and polyols (Myo and Scy). By inspection of the diffusion-edited spectra it is possible to assign resonances mainly due to fatty acid chains and to glycerol in triglycerides, but also to macromolecules, as already observed in other tissues (43). The main metabolites, characterizing the colorectal tissues are labeled in Figure 2 and the pool of metabolites especially osmolites, free amino acids and mobile lipids are reported in Table I.

The NMR spectra obtained, applying the same experimental set to neoplastic and peritumoral tissues, present different metabolic profiles with respect to the healthy ones. Furthermore, different metabolic profiles are also detected for the same tumour subtypes. As an example, we report in figure 4 (left), the spectra of two adenocarcinoma subtypes. The spectra 4a and 4b derive from two patients affected by well differenziated adenocarcinoma with the deepest submucosal invasion, whereas 4c and 4d are from two patients affected by undifferenziated adenocarcinoma with the deepest submucosal invasion.

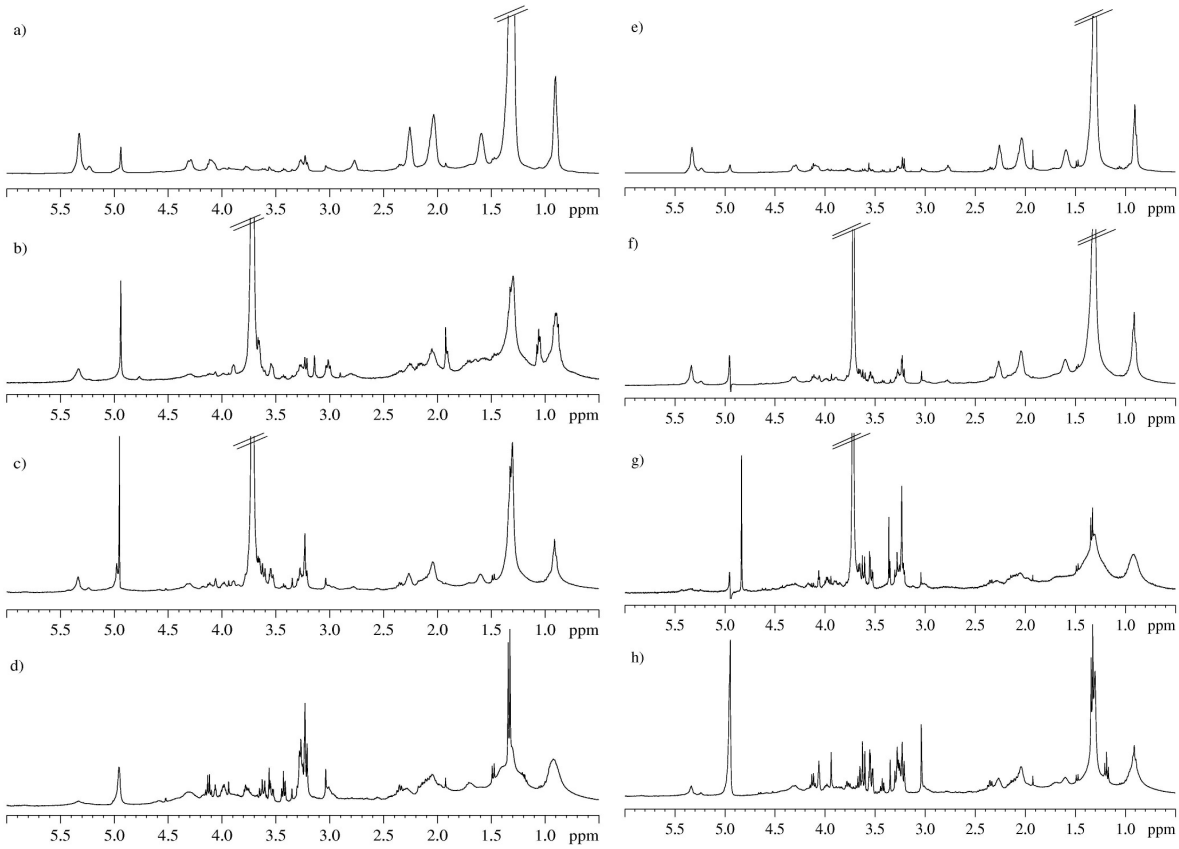

Figure 4. HR-MAS ^{1}H NMR water presaturated spectra of some colon biopsies: a) and b) well differenziated adenocarcinomas with the deepest submucosal invasion from two different patients; c) and d) undifferenziated adenocarcinomas with the deepest submucosal invasion from two different patients. e-h) tissue specimens obtained at least 15 cm far from the adenocarcinoma from the same patients.

The spectrum 4a (well differenziated adenocarcinoma with the deepest submucosal invasion) is characterized by a predominant amount of lipids, in particular triglycerides, whereas 4b well differenziated adenocarcinoma with the deepest submucosal invasion) and 4c (undifferenziated adenocarcinoma with the deepest submucosal invasion) reveal, besides the presence of lipids, that of metabolites. The 4d (undifferenziated adenocarcinoma with the deepest submucosal invasion) spectrum evidences the presence of metabolites and macromolecules, and the absence of lipids.

The spectra of the specimens obtained at least 15 cm far from the adenocarcinoma of the same patients, collected during surgery, are reported in Figure 4e-f (right). The inspection of the these spectra suggest that there is a great variability also among these samples. Even though the samples (e, f, g, h) are classified as healthy by the histological analysis, the NMR spectra reveal that metabolic profiles are quite different. Moreover, the comparison with the

corresponding neoplastic tissues does not reveal any systematic difference. In fact, spectrum 4e (classified as healthy) is quite similar to 4a (neoplastic), 4f and 4h (both classified as healthy) display an increased amount of triglycerides in different percentage with respect to 4b and 4d (neoplastic), whereas 4g (classified as healthy) shows the absences of triglycerides, in contrast to the other samples obtained at least 15 cm far from the adenocarcinoma.

Since the NMR spectra display variations in the metabolic profile not only for neoplastic tissues with different histological diagnosis, but also for those classified identical from the histological analysis, we conclude that the family of colon carcinoma is characterized at a certain degree by metabolic heterogeneity, also within the same subclass of tumours. As a consequence, a statistical multivariate approach to the analysis of HR-MAS NMR data is vital in order to find metabolic markers of the healthy and the neoplastic state of colorectal tissues, and to correctly classify the samples.

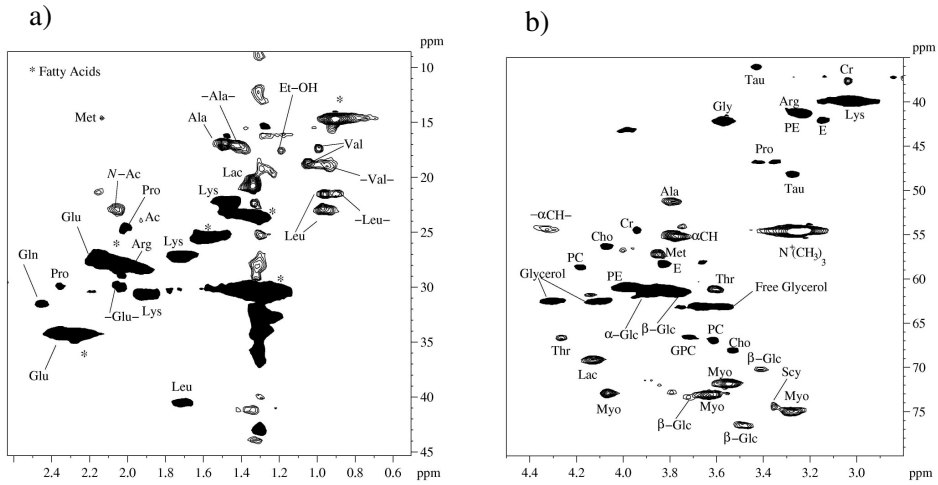

Figure 5. a) and b) partial region of $^{1}H,^{13}C$-HSQC NMR spectrum of colon specimens obtained at least 15 cm far from the adenocarcinoma. The identified metabolites are labelled according to Table I.

In order to extract as more information as possible by considering all the source of variability, *i.e.* healthy and tumoral tissues of all HR-MAS NMR spectra, PCA was performed on a pretreated data set.

PCA were carried out on zgcppr spectra acquired because these highlight both narrow and broad signals due to small metabolites and lipid plus macromolecules, respectively.

The PCA model was built by using 5 principal components (PC) according to venetian blinds cross-validation criterion. The performance of the model in terms of explained variance and root mean square error in cross validation is reported in Table III.

Table III. PCA results: PCs; number of components used; R^2 percentage of explained X-variance by the model; R^2cv percentage of of explained X-variance in cross validation.

PCs	R^2fit	R^2cv
5	88.06	74.88

Despite the applied pretreatments, the variability captured by the first two components (PC1 and PC2) is mainly due to lipids and macromolecules. By looking at PC1 *vs* PC2 scores plot, it is not present any discrimination among the samples on the basis of healthy cancer categories. On the contrary, a partial discrimination among the samples belonging to the different categories, could be provided by the analysis of the scores plots of PC3 *vs* PC4 *vs* PC5 (Figure 6).

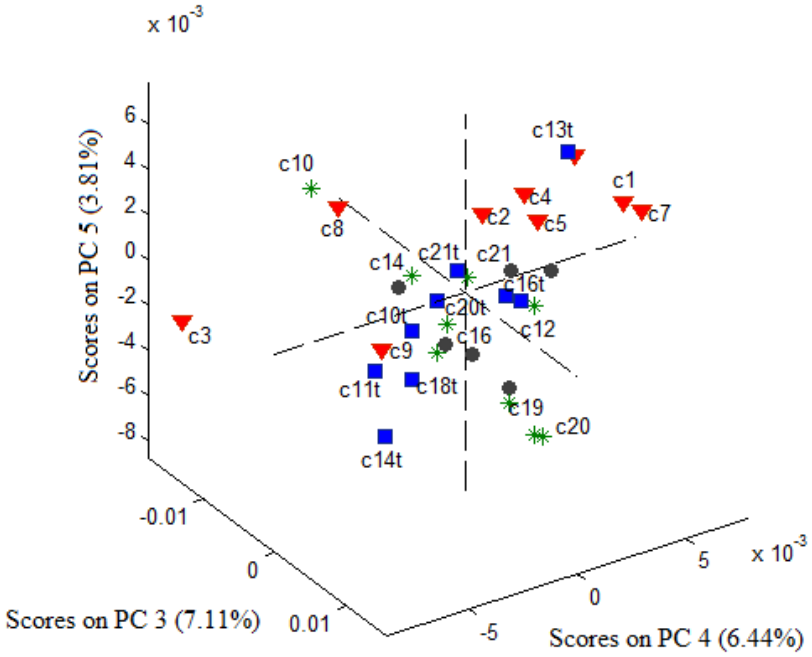

Figure 6. Scores plot of PC3 *vs.* PC4 *vs.* PC5. ▼ healthy samples, ■ adenocarcinomas, ✳ macroscopically normal colon specimens obtained at least 15 cm far from the adenocarcinoma, and ● test set samples (unknown samples). The number indicates the samples, and t indicates the tumoral samples.

In the scores plot of PC3 vs. PC4 vs. PC5 (Figure 6), it is possible to individuate two different groups: the first group includes the healthy samples, the second one includes the

neoplastic and colon specimens obtained at least 15 cm far from the adenocarcinoma. Furthermore, the healthy samples seem to be mainly discriminated for negative values of PC3 and positive values of PC4 and PC5. Although c3, c8 and c9 samples belong to the first group, they lie far away from it, above all for negative values of PC4. Within neoplastic and specimens obtained at least 15 cm far from the adenocarcinoma groups, all the samples are very close except for the c13t, which locates in the healthy group. As far as unknown samples is concerned, they are correctly predicted by the model as not healthy samples. In fact they are particularly close to the second group.

In Figure 7 are reported respectively a zoom of the loadings plot of PC3, PC4 and PC5 *vs*. the ppm region between 5.5 and 0.5 ppm, that show the highest absolute loadings values. The combined inspection of both scores and loadings plots (Figures 6 and 7) shows that the metabolic profile of healthy samples (negative PC3 score values and positive PC4 ones) seems to be characterized by a low contribution of lipids (positive PC3 loadings), a high percentage of sugars, such as Myo, Scy, Glc and -Glc- (positive PC4 loadings), and of Cr.
As far as neoplastic and specimens obtained at least 15 cm far from the adenocarcinoma tissues are concerned, they are characterized by an high amount of lipids (positive PC3 loadings values) and by a discrete presence of PC (phosphorilcholine) (negative PC4 loading values). Furthermore, the high contribution of these compounds seem to be the main responsible of c3, c8 and c9 sample's (healthy tissue) discrimination from their belonging group.

Finally, the loadings plot of PC3 confirms the high presence of the Ac moiety (high loadings values) in the neoplatic samples (in particular in c14t sample). The c3 sample is outlier, because it shows a higher amount of lipids and PC with respect to the healthy ones and a lower amount of Ac with respect to the tumoral ones.

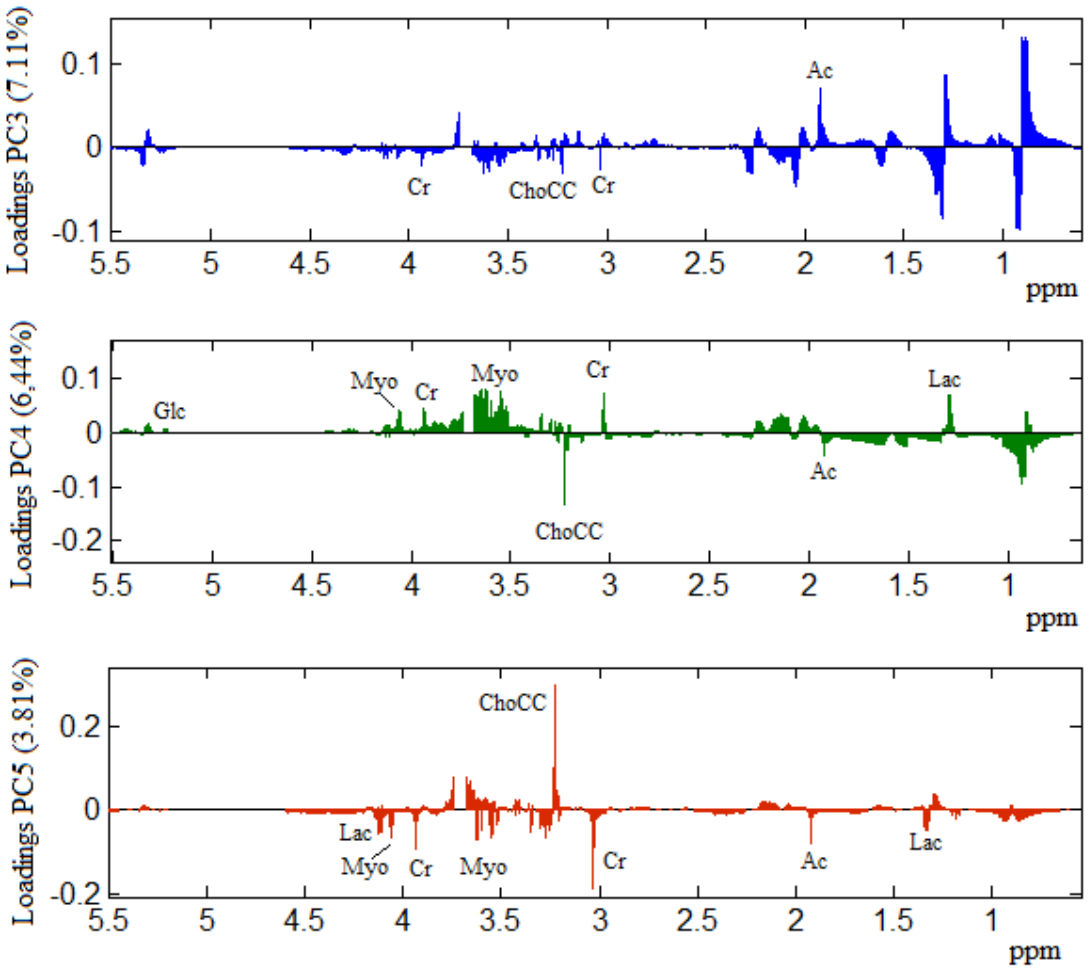

Figure 7. PC3, PC4 and PC5 loadings plots, respectively. The abscissa has been represented in ppm in order to better individuate the metabolites resonance.

By applying PLS-DA, a model describing the maximum possible separation of predefined classes is obtained. The validation step is used to predict the class of the test samples and compare these predictions to the known classes. A PLS-DA model has been built using the NMR data as the dependent X-variables and class information as the Y-variables, *i.e.* 9 healthy samples as class 1, and the 9 adenocarcinomas ones as class 2. Then, the 9 specimens obtained at least 15 cm far from the adenocarcinoma and the 6 unknown samples were used as test samples .

Determination of the optimal number of PLS latent variables was done by venetian blind cross-validation, using 6 numbers of data splits. Three latent variables was determined to be optimal. The total explained variation for the Y matrix was 82.50%. It can be also useful to known that a sample does not belong to any of the predefined classes.

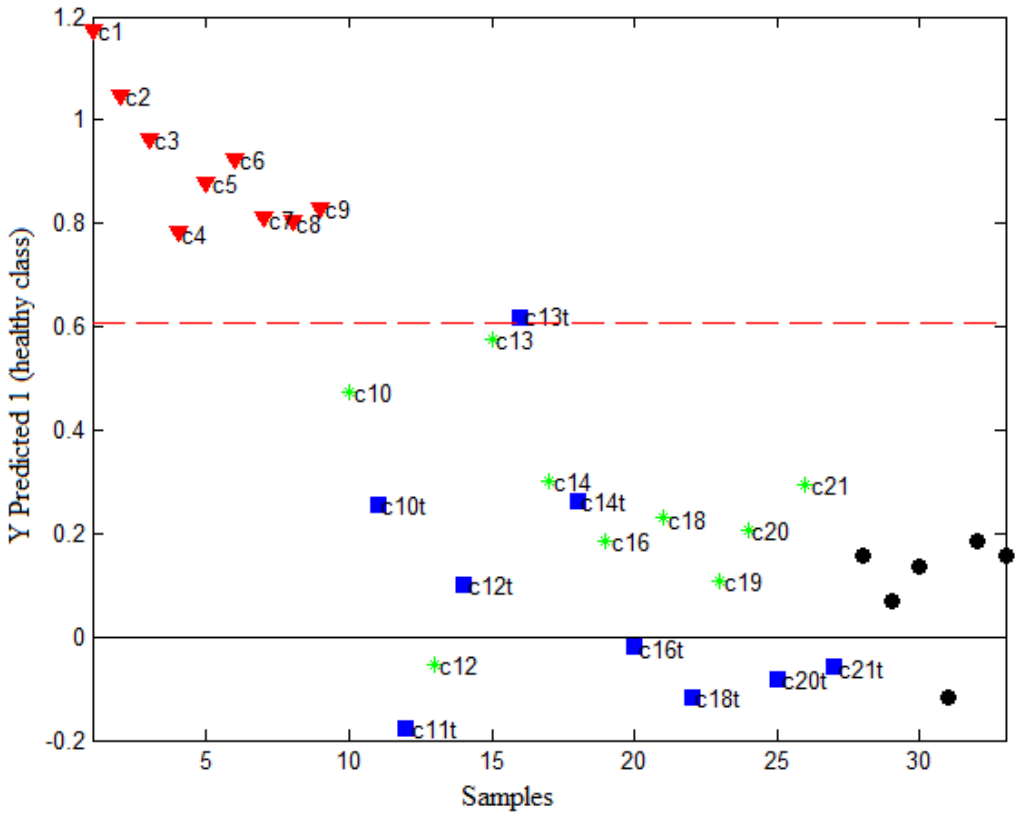

Figure 8. PLS-DA 3 latent variables. ▼ healthy samples, ■ adenocarcinomas, ✳ macroscopically normal colon specimens obtained at least 15 cm far from the adenocarcinoma, and ● unknown samples.

In figure 8, the results for the three latent variables PLS-DA model are shown for the prediction of the "healthy" class of the colon tissues. The calculated threshold between groups is shown as the horizontal dashed line. This threshold, is estimated by using the Bayes Theorem (PLS toolbox 4.0; Barry M. Wise, Neal B. Gallagher, Rasmus Bro, Jeremy M.Shaver, Willem Winding, R. Scott Koch. Eingenvector research incorporated) and it is obtained by minimizing the total classification errors for the training set samples. All healthly samples are correctly assigned, of nine samples belonging to the neoplastic class, eight are correctly assigned and one of them is predicted as a border line case.

Furthermore, to assess the behaviour of the model in estimating future samples, its performance was evaluated in cross validation too (figure 9). In Figure 9, five samples were misclassified, two belonging to healthy class (c8 and c9) and three to the tumorals (c13t, c14t and 10t) class, however c10t is just on the threshold value.

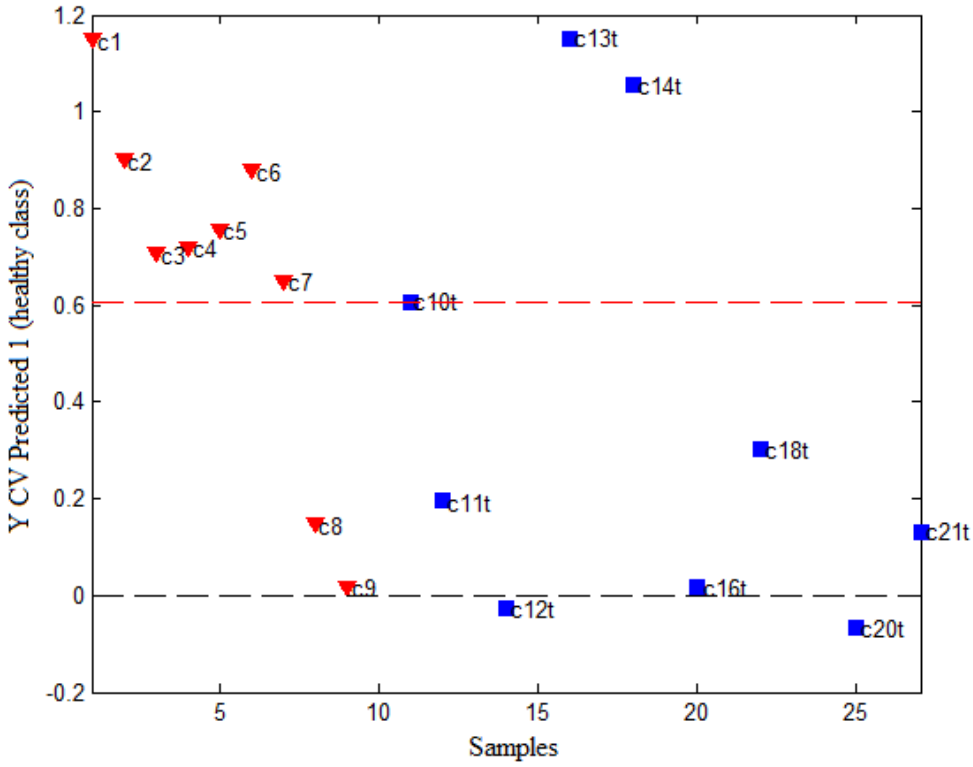

Figure 9: PLS-DA results in cross validation, 3 latent variables model for the healthy class. ▼ healthy samples, ■ adenocarcinomas.

As far as test samples are concerned all unknown samples are correctly assigned to the adenocarcinomas tissues class. Macroscopically normal colon specimens obtained at least 15 cm far from the adenocarcinoma tissues are also assigned to the adenocarcinomas tissues (their predicted values are below the threshold value), it can be noticed that in general they have y-values higher, *i.e.* towards the direction of the healthy class, than their corresponding tumoral tissues, *e.g.* c16, c18, c20 and c21 with respect to c16t, c18t, c20t and c21t. This confirms what observed from the NMR spectra that these colon specimens obtained at least 15 cm far from the adenocarcinoma share some feature of both classes but being more similar to the tumoral one.

In order to identify the metabolites which mainly contribute to the achievement of good prediction or which influence the given model, the pseudo regression coefficients plot (Figure 10a), corresponding to the characterization of healthy samples, was reported together, for efficacy of discussion, with representative NMR spectra for healthy (Figure 10b) and tumoral (Figure 10c) samples, respectively.

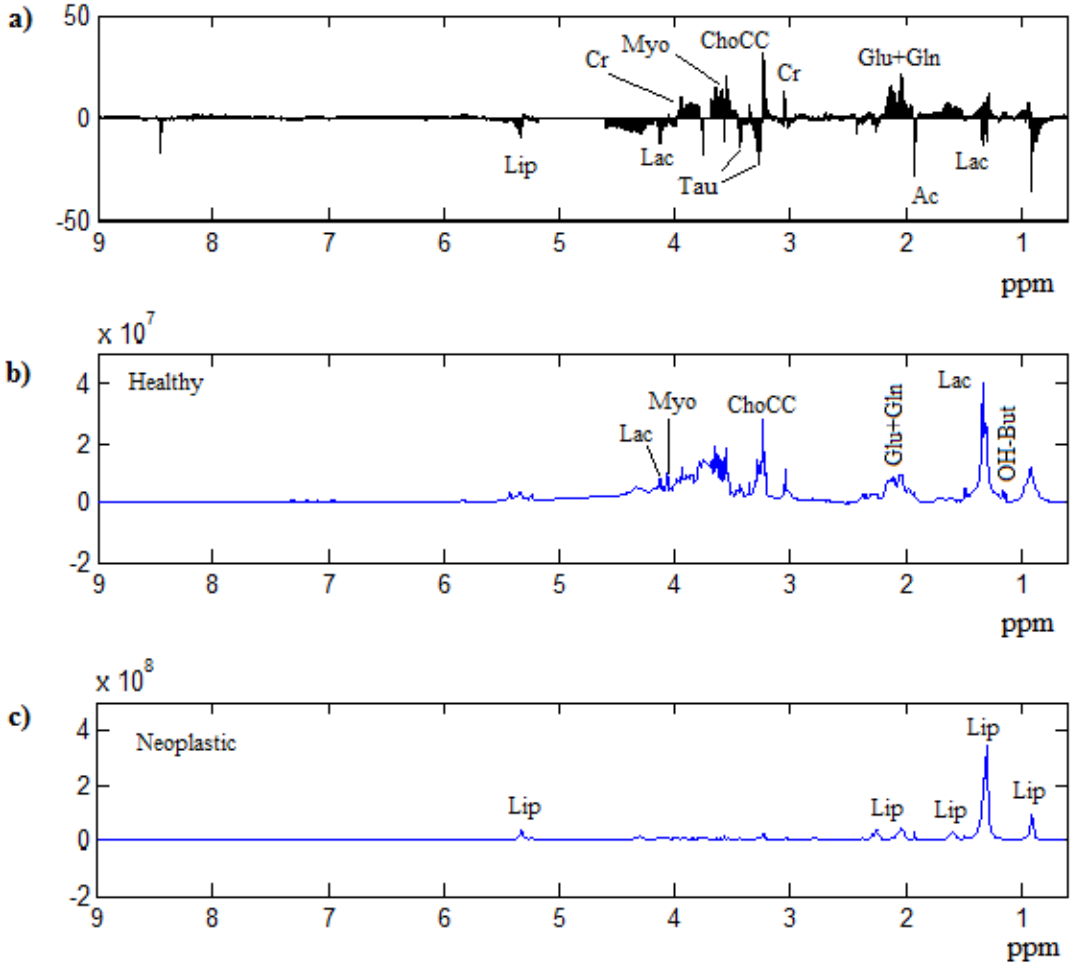

Figure 10. a) PLS-DA regression coefficient vs. ppm. NMR spectra of b) healthy and c) neoplastic colon tissues, respectively.

In figure 10a, the magnitude of loadings values is directly correlated with their influences in the prediction ability of the model, the loadings sign is related to the class discrimination: positive loadings values are associated with high y-values and hence healthly class and viceversa for negative loadings values. In other words, peaks corresponding to a positive loading values region indicate a relatively higher intensity of metabolites associated with healthy samples in comparison to all other regions.

Taking into account PCA results, the PLS-DA regression coefficients seem to select the same PCA loadings relevant regions. In addition, there is a further contribution of two metabolites in the discriminations of healthy and peritumoral classes: Tau (negative PLS-DA coefficients) is in low amount in the healthy class, whereas ChoCC (positive PLS-DA coefficients) are in high amount, in particular in the samples c8,c9, c10 c13 and c13t.

Conclusion. The last two decades have seen many works dealing with the use of Nuclear Magnetic Resonance (NMR) spectroscopic studies on healthy and neoplastic colorectal cells and tissues (44). These studies were motivated by a desire to refine tumor biochemistry with the aim to improve cancer detection, prognosis and categorization. The potential of *in vitro* NMR spectroscopy for grading human colorectal cancer has been explored on a set of increasingly tumorigenic cells. Low and highly tumorigenic malignant colorectal cell lines have been shown to be differenziated based on lipid, choline and fucose resonances (45,46). ^{1}H NMR spectroscopy performed on colorectal tumors and normal mucosa biopsies showed elevated taurine levels and reduced polyethyleneglycol absorption in neoplasms, which may have diagnostic significances (47). Later NMR studies by the same authors demonstrated that significant decreased levels of myo-inositol in colorectal tumors can be detected in intact biopsies (40). The study of Lean *et al.* (49), reported that ^{1}H NMR spectral profiles intermediate between normal and malignant situation in histologically normal tissue were of particular interest. Based on this spectroscopic datum, they were able to assess that NMR spectroscopy is sensitive to pre-malignant metabolic aspect prior to histological change. Although excellent spectroscopic data have been obtained from colorectal tissues, *in vivo* NMR studies on humans have not been reported until the recent work of Dzik-Jurasz *et al*. (50). They first demonstrated the feasibility of *in vivo* ^{1}H-NMR in locally advanced human colorectal adenocarcinoma, overcoming complications arising from tissue/air interface, thin dimension of the colon, its convoluted shape and peristalsis.

The NMR spectra of healthy tissues present different metabolic profiles with respect to neoplastic and peritumoral one. Furthermore, metabolic variations are detected not only for neoplastic tissues with different histological diagnosis, but also for those classified identical from the histological analysis. These findings suggest that the family of colon carcinoma is characterized at a certain degree by metabolic heterogeneity, also within the same subclass of tumours. The statistical multivariate approach applied to the NMR data is vital in order to find metabolic markers of the healthy and the neoplastic state of colo-rectal tissues, and to correctly classify the samples.

References

1. Pignone M, Rich M, Teutsch SM, Berg AO, Lohr KN. Screening for colorectal cancer in adults at average risk: a summary of the evidence for the U.S. Preventive Services Task Force. *Ann. Intern. Med.* 2002; **137**: 132–141.
2. Smith RA, Cokkinides V, von Eschenbach AC, Levin B, Cohen C, Runowicz CD, Sener S, Saslow D, Eyre HJ. American Cancer Society guidelines for the early detection of cancer. *CA Cancer J. Clin*. 2002; **52**: 8–22.
3. Ransohoff DF, Sandler RS. Clinical practice. Screening for colorectal cancer. *N. Engl. J. Med.* 2002; **346**: 40-44.
4. Mandel JS, Church, TR, Ederer F, Bond J. Colorectal cancer mortality: effectiveness of biennial screening for fecal occult blood. *J. Natl. Cancer Inst.* 199; **91**: 434–437.
5. Hardcastle JD, Chamberlain JO, Robinson MH, Moss SM, Amar SS, Balfour TW, James PD, Mangham CM. Randomised controlled trial of faecal-occult-blood screening for colorectal cancer. *Lancet* 1996, **348**: 1472–1477.
6. Kronborg O, Fenger C, Olsen J, Jørgensen OD, Søndergaard O. Randomised study of screening for colorectal cancer with faecal-occult-blood test. *Lancet* 1996, **348**: 1467–1471.
7. Newcomb PA, Norfleet RG, Storer BE, Surawicz TS, Marcus PM. Screening sigmoidoscopy and colorectal cancer mortality. *J. Natl. Cancer Inst.* 1993; **85**: 1311–1318.
8. Winawer SJ, Flehinger BJ, Schottenfeld D, Miller DG. Screening for colorectal cancer with fecal occult blood testing and sigmoidoscopy. *J. Natl. Cancer Inst.* 1993; **85**: 1311–1318.
9. Selby JV, Friedman GD, Quesenberry CP Jr, Weiss NS. A case-control study of screening sigmoidoscopy and mortality from colorectal cancer. *N. Engl. J. Med.* 1992; **326**: 653–657.
10. Lieberman DA, Weiss DG; Veterans Affairs Cooperative Study Group 380. One-time screening for colorectal cancer with combined fecal occult-blood testing and examination of the distal colon. *N. Engl. J. Med.* 2001; **345**: 555–560.
11. Anderson WF, Guyton KZ, Hiatt RA, Vernon SW, Levin B, Hawk E. Colorectal cancer screening for persons at average risk. *J. Natl. Cancer Inst*. 2002; **94:** 1126–1133.
12. Winawer S, Fletcher R, Rex D, Bond J, Burt R, Ferrucci J, Ganiats T, Levin T, Woolf S, Johnson D, Kirk L, Litin S, Simmang C; Gastrointestinal Consortium Panel. Colorectal cancer screening and surveillance: clinical guidelines and rationale-Update based on new evidence. *Gastroenterology* 2003; **124**: 544–560.
13. Klabunde CN, Frame PS, Meadow A, Jones E, Nadel M, Vernon SW. A national survey of primary care physicians' colorectal cancer screening recommendations and practices. *Prev. Med.* 2003; **36**: 352–362.
14. Byers T, Levin B, Rothenberger D, Dodd GD, Smith RA. American Cancer Society guidelines for screening and surveillance for early detection of colorectal polyps and cancer: update 1997.

American Cancer Society Detection and Treatment Advisory Group on Colorectal Cancer. *CA Cancer J. Clin.* 1997; **47**: 154–161.

15. Stevenson G. Colorectal cancer imaging: a challenge for radiologists. *Radiology*. 2000; **214**: 615-621.
16. Filippone A, Ambrosini R, Fuschi M, Marinelli T, Genovesi D, Bonomo L. Preoperative T and N staging of colorectal cancer: accuracy of contrast-enhanced multi-detector row CT colonography--initial experience. *Radiology*. 2004; **231**: 83-90.
17. Saunders TH, Mendes Ribeiro HK, Gleeson FV. New techniques for imaging colorectal cancer: the use of MRI, PET and radioimmunoscintigraphy for primary staging and follow-up. *Br. Med. Bull.* 2002; **64**: 81-99.
18. European Society for Medical Oncology Web site. http://www.esmo.org. Accessibility verified October 24, 2006.
19. National Comprehensive Cancer Network Web site. http://www.nccn.org. Accessibility verified October 24, 2006.
20. Mulhall BP, Veerappan GR, Jackson JL. Meta-analysis: computed tomographic colonography. *Ann. Intern. Med.* 2005; 142: 635-650.
21. Bipat S, Glas AS, Slors FJ, Zwinderman AH, Bossuyt PM, Stoker J. Rectal cancer: local staging and assessment of lymph node involvement with endoluminal US, CT, and MR imaging--a meta-analysis. *Radiology.* 2004; **232**: 773-778.
22. Sosna J, Morrin MM, Kruskal JB, Farrell RJ, Nasser I, Raptopoulos V. Colorectal neoplasms: role of intravenous contrast-enhanced CT colonography. *Radiology.* 2003; **228**: 152-156.
23. Sosna J, Kruskal JB, Bar-Ziv J, Copel L, Sella T. Extracolonic findings at CT colonography. *Abdom. Imaging* 2005; **30**: 709-713.
24. Rohren EM, Turkington TG, Coleman RE. Clinical applications of PET in oncology. *Radiology*. 2004; **231**: 305-332.
25. Kantorová I, Lipská L, Bêlohlávek O, Visokai V, Trubaĉ M, Schneiderová M. Routine (18)F-FDG PET preoperative staging of colorectal cancer: comparison with conventional staging and its impact on treatment decision making. *J. Nucl. Med*. 2003; **44**: 1784-1788.
26. Valk PE, Abella-Columna E, Haseman MK, Pounds TR, Tesar RD, Myers RW, Greiss HB, Hofer GA. Whole-body PET imaging with [18F]fluorodeoxyglucose in management of recurrent colorectal cancer. *Arch. Surg.* 1999; **134**: 503-511.
27. Kalff V, Hicks RJ, Ware RE, Hogg A, Binns D, McKenzie AF. The clinical impact of (18)F-FDG PET in patients with suspected or confirmed recurrence of colorectal cancer: a prospective study. *J. Nucl. Med.* 2002; **43**: 492-499.

28. Abdel-Nabi H, Doerr RJ, Lamonica DM, Cronin VR, Galantowicz PJ, Carbone GM, Spaulding MB. Staging of primary colorectal carcinomas with fluorine-18 fluorodeoxyglucose whole-body PET: correlation with histopathologic and CT findings. *Radiology.* 1998; **206**: 755-760.
29. Huebner RH, Park KC, Shepherd JE, Schwimmer J, Czernin J, Phelps ME, Gambhir SS. A meta-analysis of the literature for whole-body FDG PET detection of recurrent colorectal cancer. *J. Nucl. Med.* 2000; **41**: 1177-1189.
30. Cohade C, Osman M, Leal J, Wahl RL. Direct comparison of (18)F-FDG PET and PET/CT in patients with colorectal carcinoma. *J. Nucl. Med.* 2003; **44**: 1797-1803.
31. Bar-Shalom R, Yefremov N, Guralnik L, Gaitini D, Frenkel A, Kuten A, Altman H, Keidar Z, Israel O. Clinical performance of PET/CT in evaluation of cancer: additional value for diagnostic imaging and patient management. *J. Nucl. Med.* 2003; **44**: 1200-1210.
32. Selzner M, Hany TF, Wildbrett P, McCormack L, Kadry Z, Clavien PA. Does the novel PET/CT imaging modality impact on the treatment of patients with metastatic colorectal cancer of the liver? *Ann. Surg.* 2004; **240**: 1027-1034.
33. Kamel IR, Cohade C, Neyman E, Fishman EK, Wahl RL. Incremental value of CT in PET/CT of patients with colorectal carcinoma. *Abdom. Imaging*. 2004; **29**: 663- 668.
34. Antoch G, Saoudi N, Kuehl H, Dahmen G, Mueller SP, Beyer T, Bockisch A, Debatin JF, Freudenberg LS. Accuracy of whole-body dual-modality fluorine-18-2-fluoro-2-deoxy-D-glucose positron emission tomography and computed tomography (FDG-PET/CT) for tumor staging in solid tumors: comparison with CT and PET. *J. Clin. Oncol.* 2004; **22**: 4357-4368.
35. Kim JH, Czernin J, Allen-Auerbach MS, Halpern BS, Fueger BJ, Hecht JR, Ratib O, Phelps ME, Weber WA. Comparison between 18F-FDG PET, in-line PET/CT, and software fusion for restaging of recurrent colorectal cancer. *J. Nucl. Med.* 2005; **46**: 587-595.
36. Israel O, Yefremov N, Bar-Shalom R, Kagana O, Frenkel A, Keidar Z, Fischer D. PET/CT detection of unexpected gastrointestinal foci of 18F-FDG uptake: incidence, localization patterns, and clinical significance. *J. Nucl. Med.* 2005; **46**: 758-762.
37. Gutman F, Alberini JL, Wartski M, Vilain D, Le Stanc E, Sarandi F, Corone C, Tainturier C, Pecking AP. Incidental colonic focal lesions detected by FDG PET/CT. *Am. J. Roentgenol.* 2005; **185**: 495-500.
38. Wang Y, Holmes E, Comelli EM, Fotopoulos G, Dorta G, Tang H, Rantalainen MJ, Lindon JC, Corthésy-Theulaz IE, Fay LB, Kochhar S, Nicholson JK. Topographical variation in metabolic signatures of human gastrointestinal biopsies revealed by high-resolution magic-angle spinning 1H NMR spectroscopy. *J. Proteome Res.* 2007; **6**: 3944-3951.
39. Gavaghan CL, Holmes E, Lenz E, Wilson ID, Nicholson JK. An NMR-based metabonomic approach to investigate the biochemical consequences of genetic strain differences: application to the C57BL10J and Alpk: ApfCD mouse. *FEBS Lett.* 2000; **484**: 169-174.

40. Kitajima K, Fujimori T, Fujii S, Takeda J, Ohkura Y, Kawamata H, Kumamoto T, Ishiguro S, Kato Y, Shimoda T, Iwashita A, Ajioka Y, Watanabe H, Watanabe T, Muto T, Nagasako K. Correlations between lymph node metastasis and depth of submucosal invasion in submucosal invasive colorectal carcinoma: a Japanese collaborative study. *J. Gastroenterol.* 2004; **39**: 534-543.
41. Ueno H, Mochizuki H, Hashiguchi Y, Shimazaki H, Aida S, Hase K, Matsukuma S, Kanai T, Kurihara H, Ozawa K, Yoshimura K, Bekku S. Risk factors for an adverse outcome in early invasive colorectal carcinoma. *Gastroenterology*. 2004; **127**: 385-394.
42. Wold S, Johansson E, Cocchi M. 3D QSAR in drug design: theory, methods, and applications. Kubinyi H. (ed), ESCOM Scince Publischer, Leiden, 1993, 523.
43. Tugnoli V, Schenetti L, Mucci A, Parenti F, Cagnoli R, Righi V, Trinchero A, Nocetti L, Toraci C, Mavilla L, Trentini G, Zunarelli E, Tosi MR. Ex vivo HR-MAS MRS of human meningiomas: a comparison with in vivo 1H MR spectra. *Int. J. Mol. Med*. 2006; **18**: 859-869.
44. Smith ICP, Stewart LC. Magnetic resonance spectroscopy in medicine: clinical impact. *Prog. Nucl. Magn. Reson. Spectrosc.* 2002; **40**: 1-34.
45. Lean CL, Mackinnon WB, Delikatny EJ, Whitehead RH, Mountford CE. Cell-surface fucosylation and magnetic resonance spectroscopy characterization of human malignant colorectal cells. *Biochemistry* 1992; **20**: 306-311.
46. Mackinnon WB, Huschtscha L, Dent K, Hancock R, Paraskeva C, Mountford CE. Correlation of cellular differentiation in human colorectal carcinoma and adenoma cell lines with metabolite profiles determined by 1H magnetic resonance spectroscopy. *Int. J. Cancer.* 1994; **59**: 248-261.
47. Moreno A, Rey M, Montane JM, Alonso J, Arús C. 1H NMR spectroscopy of colon tumors and normal mucosal biopsies; elevated taurine levels and reduced polyethyleneglycol absorption in tumors may have diagnostic significance. *NMR Biomed.* 1993; **6**: 111-118.
48. Moreno A, Arús C. Quantitative and qualitative characterization of 1H NMR spectra of colon tumors, normal mucosa and their perchloric acid extracts: decreased levels of myo-inositol in tumours can be detected in intact biopsies. *NMR Biomed.* 1996; **9**: 33-45.
49. Lean CL, Newland RC, Ende DA, Bokey EL, Smith IC, Mountford CE. Assessment of human colorectal biopsies by 1H MRS: correlation with histopathology. *Magn. Reson. Med.* 1993; **30**: 525-533.
50. Dzik-Jurasz AS, Murphy PS, George M, Prock T, Collins DJ, Swift I, Leach MO, Rowland IJ. Human rectal adenocarcinoma: demonstration of 1H-MR spectra in vivo at 1.5 T. *Magn. Reson. Med.* 2002; **47**: 809-811.

Table I. List of ^{1}H and ^{13}C chemical shift (δ, ppm) of metabolites and exogenous molecules found in HR-MAS spectra of gastrointestinal mucosa[a,b].

entry	Metabolite	δ ^{1}H	δ ^{13}C		Stomach		Colon
					Healthy	Neoplastic	
1	Fatty acids	0.89	14.13-14.17	CH_3	y	y	y
		1.31	29.4-32.2	$(CH_2)_n$			
		1.59-1.60	25.2	$CH_2CC=O$			
		2.02	27.8	$CH_2C=$			
		2.24	34.2	$CH_2C=O$			
		2.78	26.2	$=CCH_2C=$			
		5.30-5.32	130.2; 128.4	CH=CH			
2	Isoleucine	0.94 (t)	11.7	δ-CH_3	y	trace	trace
		1.02(d)	15.5	γ-CH_3			
		1.29,1.48	25.1	γ-CH_2			
		1.97		β-CH			
		3.69		α-CH			
3	Leucine	0.95(d)	21.5	δ-CH_3	y	trace	y
		0.97(d)	22.8	δ-CH_3			
		1.70	24.8	γ-CH			
		1.72	40.4	β-CH_2			
		3.74		α-CH			
4	Valine	0.99(d)	17.3	γ-CH_3	y	y	y
		1.04(d)	18.7	γ-CH_3			
		2.25		β-CH			
		3.61	d	α-CH			
5	Threonine	1.33(d)	20.3	γ-CH_3	y	trace	y
		4.26	66.58	β-CH			
		3.60	61.22	α-CH			
6	Lactate	1.33(d)	20.3	CH_3	y	y	y
		4.11	69.1	CH			
7	Lidocaine	1.37(t)	9.2	CH3	y	n	n
	chlorohydrate	3.37(q)	50.6	CH2			
		2.20(s)	17.8	2,6-CH3			
8	Alanine	1.48(d)	16.8	β-CH_3	y	y	y
		3.78	51.1	α-CH			
9	Lysine	3.02(t)	39.9	ε-CH_2	y	y	y
		1.71	27.1	δ-CH_2			
		1.48	22.56	γ-CH_2			
		1.91	30.6	β-CH_2			
		3.79	c	α-CH			
10	Arginine	3.23	41.3	δ-CH_2	y	n	y
		1.69	24.9	γ-CH_2			
		1.92	28.1	β-CH_2			
		3.78	c	α-CH			
11	Glutamate	2.36(t)	34.0	γ-CH_2	y	y	y
		2.06, 2.14	27.9	β-CH_2			
		3.77	c	α-CH			
12	Glutamine	2.44(td)	31.5	γ-CH_2	y	trace	y
		2.14	27.2	β-CH_2			
		3.78	c	α-CH			
13	Proline	3.43, 3.34		δ-CH_2	y	n	y
		2.01		γ-CH_2			
		2.34, 2.07		β-CH_2			
		4.12		α-CH			
14	Methionine	2.13(s)	14.9	SCH_3	y	y	y
		2.62		γ-CH_2			
		2.16		β-CH_2			
		3.87		α-CH			
15	Aspartic acid	2.68, 2.82	37.2	β-CH_2	y	n	y
		3.90		α-CH			
16	Asparagine	2.85, 2.96	26.30	β-CH_2	y	n	trace
		4.01		α-CH			

17	Creatine	3.04(s) 3.92(s)	37.5 54.5	NCH_3 CH_2	y	y	y
18	Tyrosine	3.06, 3.20 3.93 6.89 7.23	 56.7 116.5 131.5	β-CH_2 α-CH H*ortho* H*meta*	y	y	y
19	Phenylalanine	3.11, 3.28 3.99 7.34 7.43 7.37	 130.1 129.6 128.2	β-CH_2 α-CH H*ortho* H*meta* H*para*	y	y	y
20	Ethanolamine	3.15(t) 3.82(t)	42.1 58.2	CH_2 CH_2	y	trace	y
21	Phosphoryl- ethanolamine	3.23 4.00	41.1 61.1	CH_2 CH_2	y	y	y
22	Glycerophosphoryl- ethanolamine	3.30 4.10		CH_2 CH_2	y	y	trace
23	free Choline	3.20 3.53 4.08	54.6 68.2 56.5	$N(CH_3)_3$ NCH_2 OCH_2	y	y	y
24	Glycerophosphoryl- choline	3.22 3.68 4.33	54.7	$N(CH_3)_3$ NCH_2 OCH_2	y	n	y
25	Phosphorylcholine	3.22 3.61 4.22	54.7 67.3 59.0	$N(CH_3)_3$ NCH_2 OCH_2	y	y	y
26	β-Glucose	4.67(d) 3.26 3.49 3.40 3.47 e	96.6 74.8 76.8 69.9 76.8 e	1-CH 2-CH 3-CH 4-CH 5-CH 6-CH_2	y	y	y
27	Taurine	3.26(t) 3.42(t)	48.1 35.9	SCH_2 NCH_2	y	y	y
28	Myo-inositol	3.53(dd) 4.06(t) 3.63(t) 3.29(t)	71.8 72.9 73.1 75.0	1,3-CH 2-CH 4,6-CH 5-CH	y	y	y
29	Scyllo-inositol	3.35 (s)	73.9	CH	y	y	y
30	α-Glucose	5.24(d) 3.54 3.73 3.42 e	 72.5 73.8 70.7 e	1-CH 2-CH 3-CH 4-CH 6-CH_2	y	y	y
31	Glycine	3.56	42.3	CH_2	y	y	y
32	PEG	3.72	69.9		y	trace	y
33	Glycerol (in lipids)	4.10, 4.30 5.26		1,3-CH_2 2-CH	y	y	y
34	Glycerol	3.56, 3.65 3.81	63.3 72.7	1-CH_2 2-CH	y	n	y
35	UDPG	5.92 4.35 5.90(d) 7.89(d)		1-CHrib 2-CHrib 5-CHur 6-CHur	y	n	y
36	Uracil	5.80(d) 7.54(d)		5-CHur 6-CHur	y	n	trace
37	Formiate	8.48			y	n	y
38	NADH	8.21			y	n	n
39	Tryptophane	7.73 7.19 7.29 7.52		4-CH 5-CH 6-CH 7-CH	y	n	y

40	Adenosine	8.36(s) 8.23(s)		8-CH 2-CH	y	y	y
41	N-Ac	2.01-2.12	23.0	$NC=OCH_3$	y	trace	y
42	Acetate	1.92	24.8	$CH_3C=O$	y	y	y
43	Hypotaurine	2.65(t) 3.35(t)	38.73 41.19	CH_2 CH_2	y	trace	n
44	UMP	5.98 4.37 5.97(d) 8.11(d)		1-CHrib 2-CHrib 5-CHur 6-CHur	y	n	trace
45	αGlc-1-X	5.40 3.61	100.2		y	n	trace
46	Glutathione	4.57 2.96 3.80 2.16 2.55 3.77 8.57 8.36	56.18 26.3 44.0	α-CH-Cys β-CH_2-Cys α-CH-Glu β-CH_2-Glu γ-CH_2-Glu CH_2-Gly NH-Cys NH-Gly	trace	n	n
47	OH-butyrate	1.18 4.14		CH_3	trace	y	y
48	Histidine	7.78 (s) 7.05(s)		2-CH 4-CH	y	y	trace
49	Ascorbate	4.52(d) 4.01		4-CH 5-CH	y	n	y
50	β-Alanine	2.56 3.18	32.14 40.01	CH_2 CH_2	y	n	n
51	Succinate	2.41(s)		α,β-CH_2	trace	y	y
52	Bonded Glycerols	3.95-3.70	61.3	1,3-CH_2	trace	n	
53	Bonded Ala	1.41 4,32	17.1	β-CH_3 α-CH	y	n	y
54	Bonded Val	0.93 2.08 4.11	23.0	γ-CH_3 β-CH α-CH	trace	n	n
55	Bonded Thr	1.22 4.24 4.31	16.2	γ-CH3 β-CH α-CH	trace	n	trace
56	Cetylpyridinium	5.08 2.03		NCH_2 β-CH_2	trace	n	n
57	Unknown	2.44 3.44			y	n	n
58	Unknown	1.63	23.5		y	n	n
59	Unknown	2.82 s		CH_2	n	n	y
60	Ethanol	1.18	17.5	CH_3	n	n	y

a ^{1}H chemical shift are referred to alanine doublet at 1.48 ppm.
b ^{13}C chemical shift are referred to alanine at 16.8 ppm.
c C_ probably contributes to the 3.77, 55.1 ppm cross-peak.
d C_ probably contributes to the 3.61, 61.1 ppm cross-peak.
e Contribute to the broad correlation between CH_2 protons in the region 3.9 _ 3.6 ppm and carbons around 62 ppm in HSQC spectra.

Chapter 6

RENAL CELL CARCINOMA

GENERAL INTRODUCTION

Renal cell carcinoma (RCC) is the sixth leading cause of cancer death. The frequency of RCC has constantly increased over the last 50 years, moving from 2-3% of all neoplasms to nearly 6% today: it is more frequent in men than in women, and have a higher incidence in the age group between 6^{th} and the 7^{th} decade, although onset is non-sporadic at any age (1). Specific incidence factors, which would enable the identification of the so-called risk groups, are not known. Smoking, obesity and exposure to asbestos, cadmium, vinyl chloride and trichloroethylene have been proposed as possible factors (2). Today, more than 50% of cases are diagnosed accidentally. Approximately one-third of patients present with disease which is already metastatic and for which there is currently no adequate treatment, furthermore no biofluid screening tests exist for RCC. The EAU (European Association of Urology) guidelines indicate abdominal CT, with or without contrast media, as a standard radiological procedure, as it provides an imaging scan of the controlateral kidney, as well as the diagnosis. Magnetic Resonance Imaging (MRI) is indicate as an additional diagnostic procedure.

It is now well established that kidney cancer does not represent a single disease, but rather a collection of different types of cancer (3). Five histological types of RCC are seen:

- Clear Cell (CCC): 60-85%
- Chromophil (ChL): 7-14%
- Chromophobic (ChC): 4-10%
- Oncocytic (ON): 2-5% (benign neoplasm);
- Collecting duct (CD): 1-2%

According to Fuhrman in 1982, four grades are determined as a function of nuclear anaplasia and cell morphology (4).

The identification of these different types of cancer requires the monitoring of their molecular signature and of their alterated metabolic profile.

In this field, basic MRS studies are needed to elucidate the main metabolic profiles in the comparison between healthy and neoplastic kidney. In the urological field, MRS has been applied to the study of the biochemical composition of biological fluids (5,6), as well as renal tissue metabolism and function (7-10). In previous studies (11,12), were described the

biochemical composition of human renal tissues with regards to both aqueous and lipid extracts studied by monodimensional low field *in vitro* MRS. *In vitro* studies yielded information on the marked decrease in renal osmolytes in nephrocarcinomas and on the cholesteryl ester content in malignant tumoral tissues.

Here, a preliminary *ex vivo* HR-MAS NMR study performed on human renal tumor tissue samples taken from five patients at the time of radical nephrectomy is reported. A sampling of macroscopically normal renal cortex and medulla from the same kidney was also performed. This study is performed in order to differentiate the full metabolic pattern of human intact renal cortex, medulla and tumor tissues.

Clinical materials. Specimens were collected from five patients undergoing radical nephrectomy for solid renal tumors. The clamping and/or division of the main renal artery was performed carefully immediately before collecting the specimens to minimize the warm ischemia time. In all cases, sample of normal cortex, normal medulla and tumor were taken.
Pathology. On microscopy, renal tumors were classified according to the WHO classification (13) (28) as clear cell (n=3) and papillary renal cell carcinoma (RCC) (n=2); tumor stage was based on TNM staging system (14) and grade was assessed according to the Furhman grading system (Table I) (4).

Table I. Patient characteristics.

Patients	Age (years)	Tumor size (cm)	Histological type	Fuhrman grade	TNM group stage
1	76	4	Clear cell RCC	G3	pT3a Nx
2	58	5	Clear cell RCC	G3	pT1bN0
3	77	9	Clear cell RCC	G3	pT3bNx
4	86	4	Papillary RCC	G2	pT1aNx
5	70	10	Papillary RCC	G2	pT3aN0

For NMR experimental details see Chapter II

Results and Discuss

Ex vivo 1D proton HR-MAS NMR spectra obtained from human normal cortex and medulla samples are shown in Figure 1 and 2, respectively. The spectra shown in Figure 1a and 2a, acquired using a 1D ^{1}H sequence with a water-presaturation, shows the presence of

narrow resonances derived from low molecular weight metabolites, and broad resonances mainly due to the presence of lipids and oligopeptides.

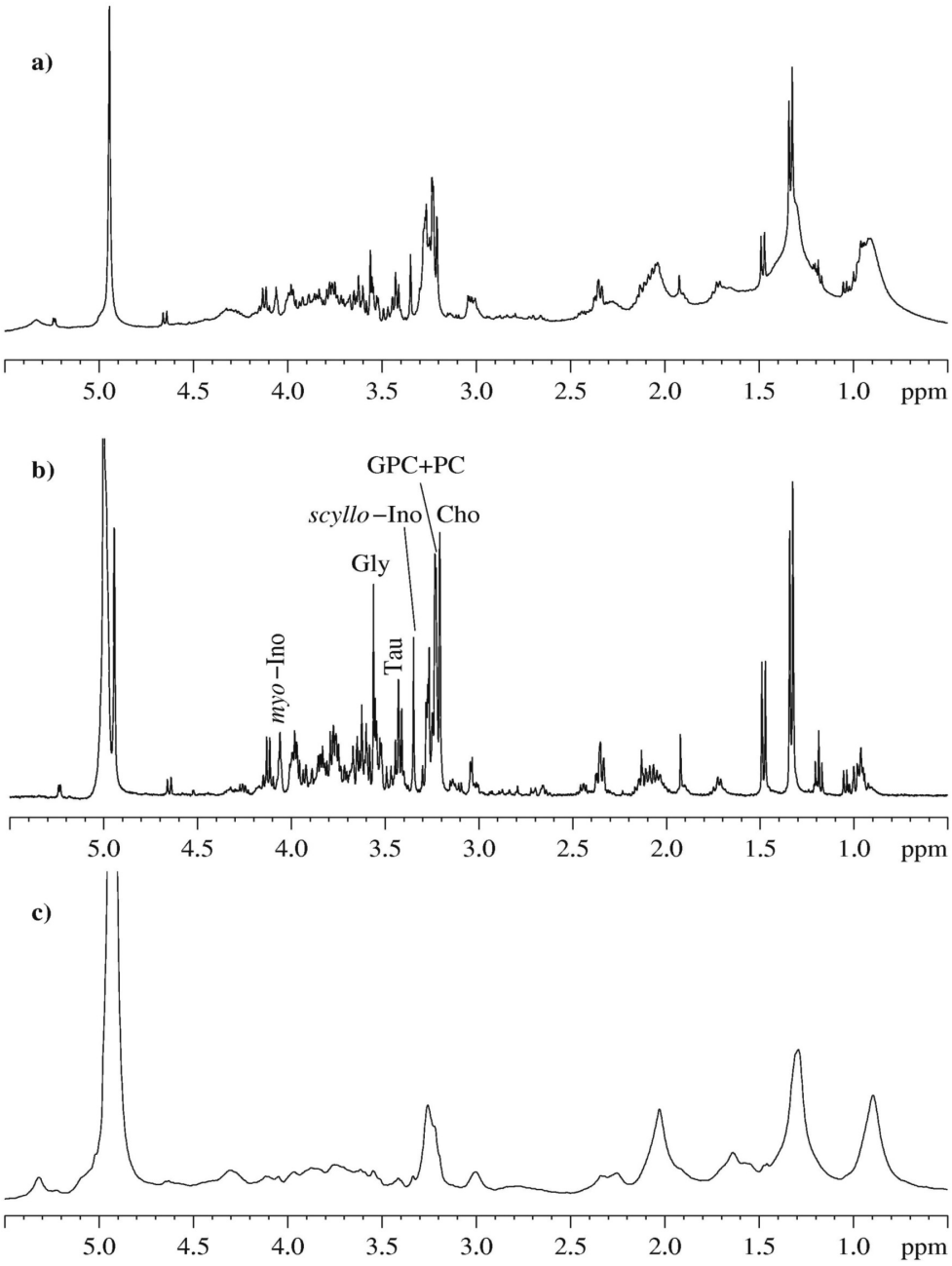

Figure 1. 1D ^{1}H HR MAS spectra of normal human cortex: a) Conventional proton spectrum with water-presaturation (the broad resonances are assigned to lipids and oligopeptides); b) CPMG spectrum; c) Diffusion-edited spectrum (the resonance at ~3.22 ppm is assigned to the trimethylammonium residue of phosphatidylcholine and the broad resonances are assigned to FA (fatty acids) esterified in TG (triglycerides) and Ph (phospholipids) with a lesser contribution of oligopeptides). Cho (free choline), Gly (glycine), GPC (glycerophosphorylcholine), myo-Ino (myo-inositol), PC (phosphorylcholine), scyllo-Ino (scyllo-inositol), (Tau) taurine.

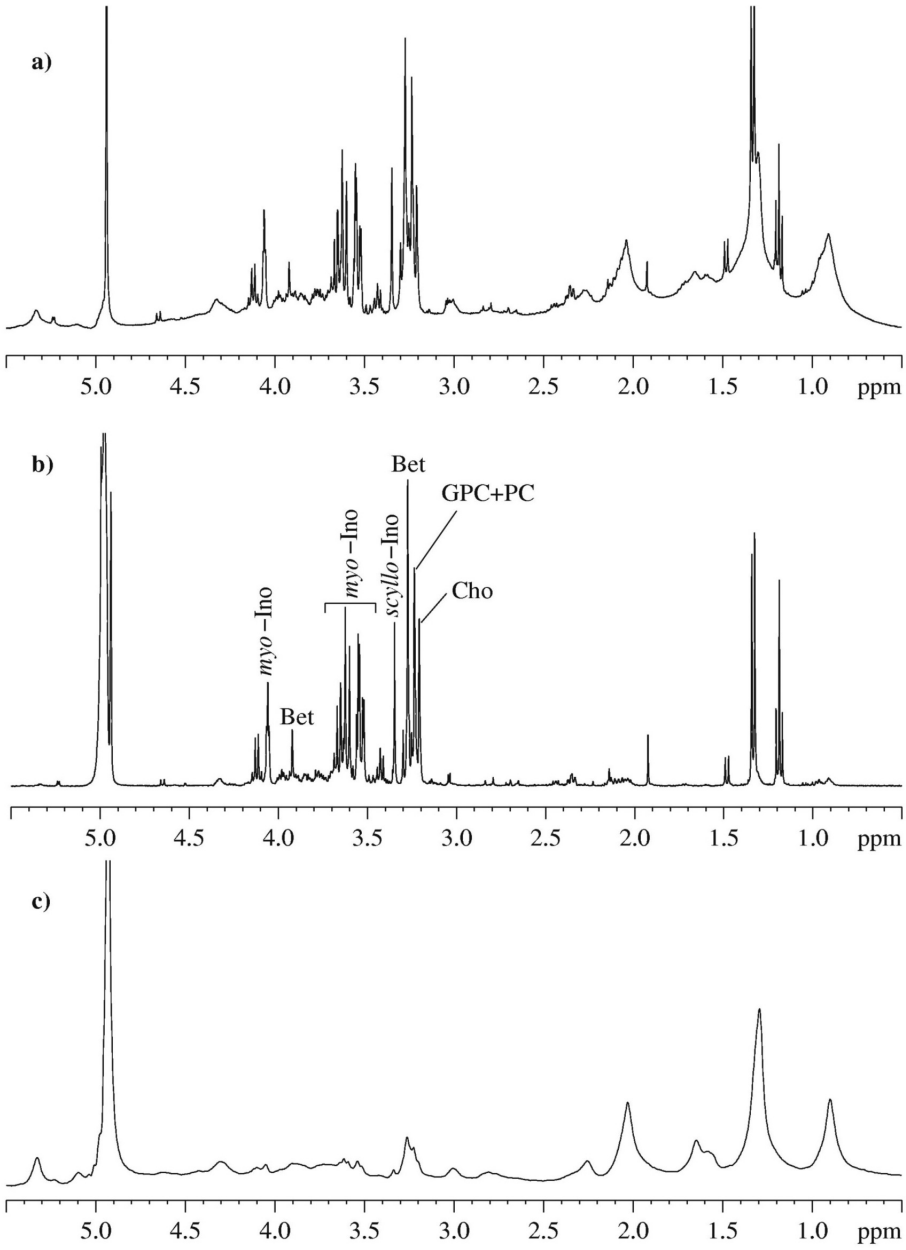

Figure 2. 1D ^{1}H HR MAS spectra of normal human medulla: a) Conventional proton spectrum with water-presaturation (the broad resonances are assigned to lipids and oligopeptides); b) CPMG spectrum; c) Diffusion-edited spectrum (the resonance at ~3.22 ppm is assigned to the trimethylammonium residue of phosphatidylcholine and the broad resonances are assigned to FA esterified in TG and Ph with a lesser contribution of oligopeptides) Bet (glycine-betaine), Cho, Gly, GPC, myo-Ino, PC, scyllo-Ino, Tau.

The HR MAS spectra obtained by using a CPMG sequence are given in Figure 1b and 2b. The cortex and medulla contain many small molecules with different distributions in the two kidney regions. Amino acids are present in higher amounts in the cortical tissue than in the medullary. In particular, the cortex is characterized by a high percentage of Gly and Tau, while the medulla by glycine-betaine (Bet) and *myo*-inositol (*myo*-Ino). Other osmolytes, such

as *scyllo*-inositol (*scyllo*-Ino) and ChoCC, GPC, PC and Cho, are present in approximately the same relative amounts in both kidney tissues. Diffusion-edited spectra, are shown in Figure 1c and 2c. The spectra of the cortex and medulla are quite similar and are dominated by the signals due to fatty acids (FA) of triglycerides (TG) and phospholipids (Ph), with a lesser contribution of oligopeptides. The same analyses were also performed on two different subtypes of renal cancer, namely clear cell RCC and papillary RCC. The corresponding spectra are shown in Figure 3 and 4, respectively. A marked difference between the two spectra is evident: the spectrum of the clear cell RCC displays predominant resonances due to lipids, whereas the papillary RCC shows a profile characterized by the presence of a large amount of amino acids. The analysis of the CPMG spectra (Figure 3b and 4b) indicate that the resonances of *myo*-Ino, *scyllo*-Ino and Bet drastically decrease or disappear in both the renal neoplasms in comparison with the normal cortex and medulla (Figure 1b and 2b) and show that Tau is present in high amounts in papillary RCC (Figure 4b), whereas ChoCC is the predominant component in the clear cell RCC (Figure 3b). The diffusion-edited spectra, shown in Figure 3c and 4c, further confirm that the neoplastic renal tissues present a different metabolic profile. That of the clear cell RCC (Figure 3c), is characterized by the exclusive presence of FA esterified in TG and cholesterol (CholE), while that of the papillary RCC (Figure 4c) shows weak signals due to bonded amino acids (MM), FA esterified in Ph (phosphatidylcholine).

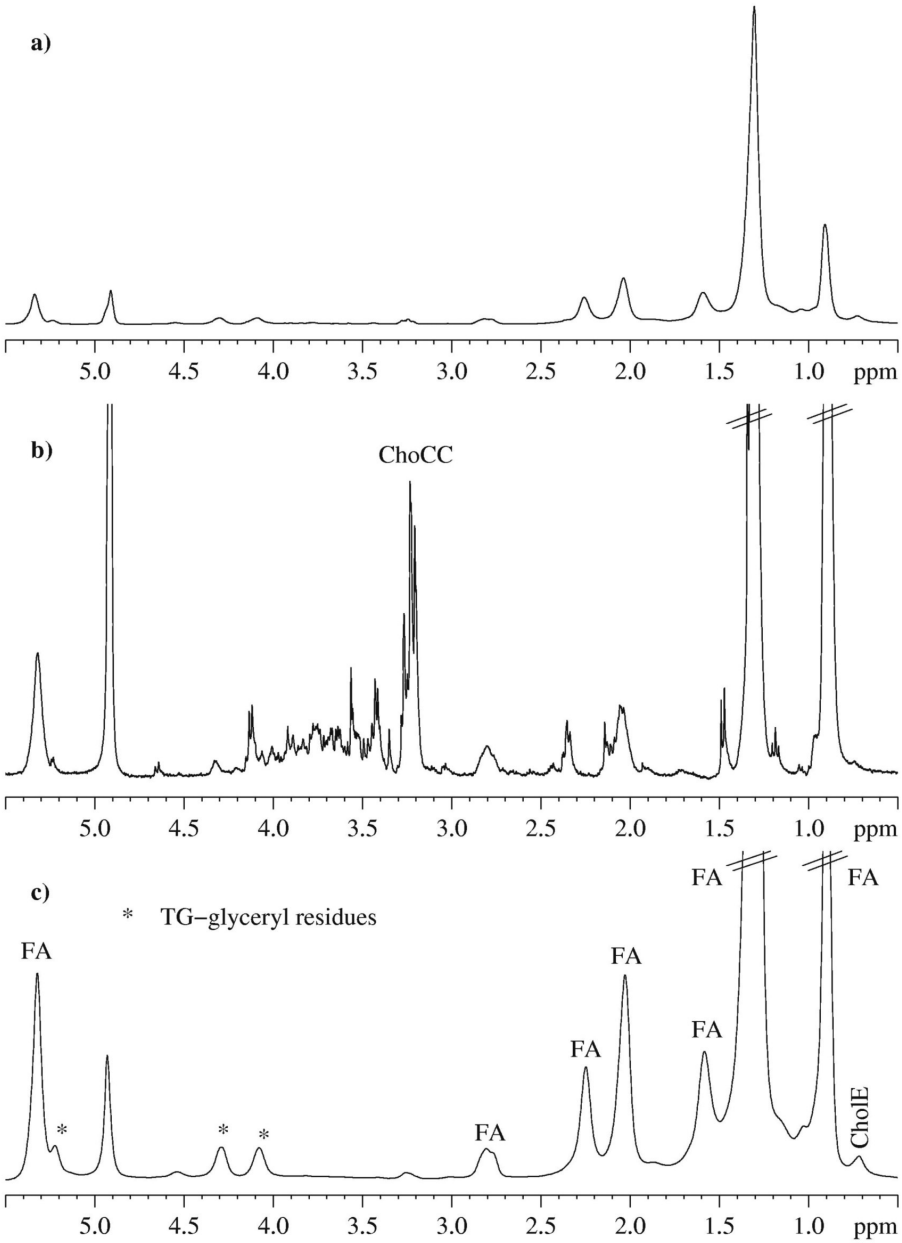

Figure 3. 1D ^{1}H NMR spectra of human clear cell renal cell carcinoma: a) Conventional proton spectrum with water-presaturation (the broad resonances are assigned to lipids); b) CPMG spectrum; c) Diffusion-edited spectrum.

In the biomedical field, *in vivo* volume-localized proton MRS has been used to assay the regional biochemistry in isolated perfused rat kidneys (15). The medullary region spectra were characterized by signals of osmolytes such as Bet, GPC and *myo*-Ino, while the spectra of the cortex were more complex and contained fewer osmolytes. In previous studies using ^{1}H HR-MAS NMR, a biochemical investigation of ten histologically unclassified human renal carcinomas has been reported (16) and a distinction between normal cortex and again

histologically unclassified eleven renal carcinoma biopsy samples (including 2 renal metastases) has been also published (17). Moreover ^{1}H HRMAS NMR studies on intact rat renal cortex and medulla have been performed (18). Previous paper, (11) reported the *in vitro* ^{1}H NMR spectra of the two different regions of healthy human kidney, *i.e.* the cortex and medulla and showed that many osmolytes, markers of normal renal function, were present in the healthy kidney, with a different distribution between the cortex and medulla. In particular, Bet and *myo*-Ino predominated in the medulla, while tetramethylammonium (TMA) and succinate (Suc) were predominant in the cortex. Further it reported that a marked decrease of these osmolytes was typical of clear cell RCCs with respect to the histological Fuhrman grade. On the contrary, the ChoCC signal intensity remained unchanged, assuming in the tumoral sample the significance of a cell proliferation marker. Renal cells under physiological conditions are exposed to extracellular NaCl and urea and respond to hypertonic stress by accumulating small organic molecules, the so called osmolytes. In the medulla of the concentrating kidney, the accumulation of osmolytes, which do not perturb cell function, permits the mantainance of normal intracellular concentrations of inorganic electrolytes and are thus termed "compatible osmolytes". It has been shown that in the mammalian kidney these include the trimethylamines Bet and GPC, the polyols sorbitol (Srb) and *myo*-Ino, and, quantitatively less important, free amino acids and their derivatives (19,20).

The *ex vivo* HR-MAS data permitted the evaluation of the different distribution of the metabolites in intact specimens of the human kidney cortex and medulla. Tau and Gly are the more important markers of the cortical region, whereas Bet, *myo*-Ino and GPC characterize the medulla. In the spectra, there is no evidence of any substantial amounts of Srb detected, in contrast to that in intact rat renal medulla (18). The data are in agreement with the findings of Schmolke *et al.* (21) who measured, by liquid chromatography, the osmolyte concentration in homogenates of five different human kidney zone from the cortex towards the papillary tips. The authors showed that the major osmolytes were *myo*-Ino, GPC and Bet, whereas Srb was detectable in negligible amounts. The spectroscopic data show that both kidney regions present signals ascribable to *scyllo*-Ino and *myo*-Ino. To our knowledge, the presence of *scyllo*-Ino has not yet been reported in normal human kidney. This metabolite may be involved in osmoregulatory processes as more abundant stereoisomer *myo*-Ino.

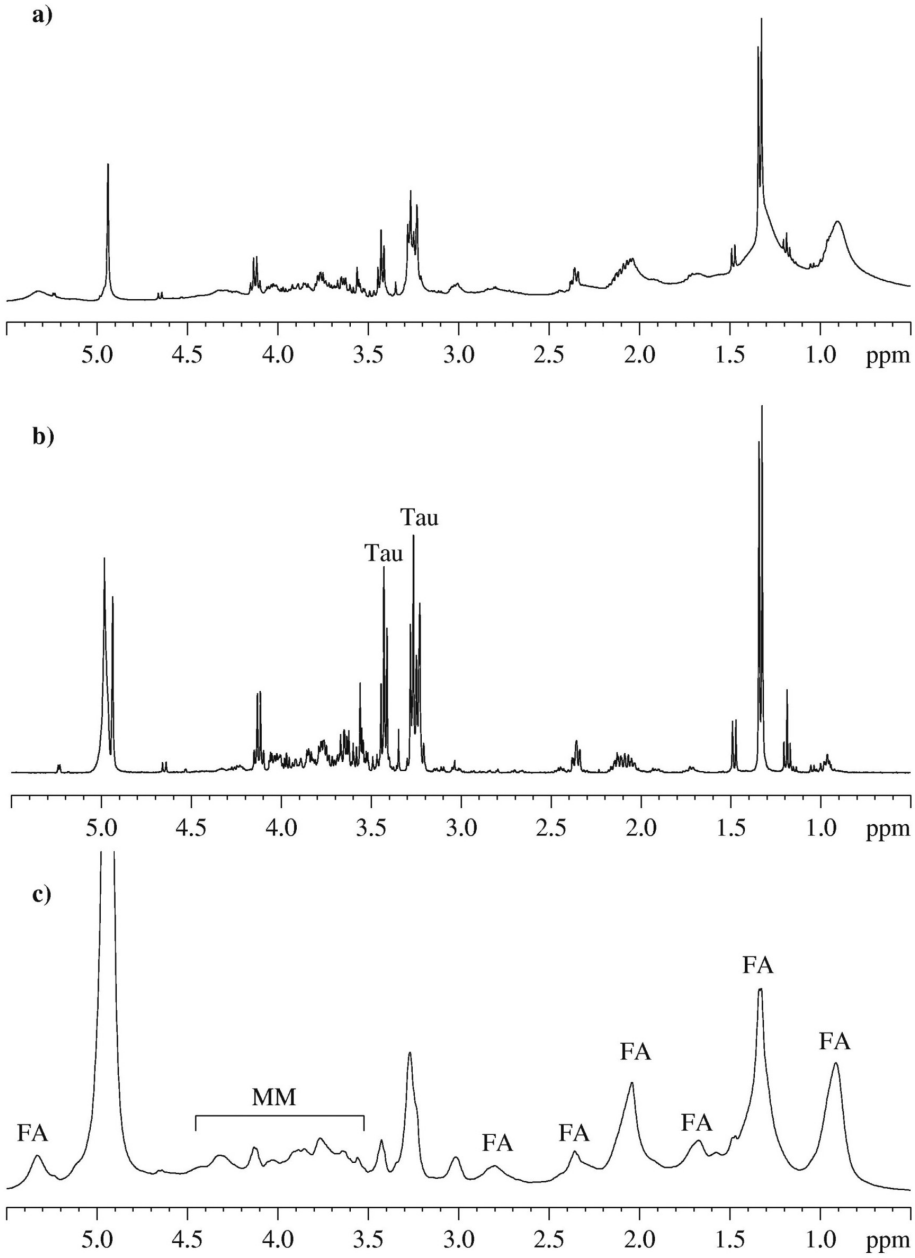

Figure 4. 1D ^{1}H NMR spectra of human papillary renal cell carcinoma: a) Conventional proton spectrum with water-presaturation (the narrow resonances are assigned to low molecular weight metabolites, and the broad resonances are due to lipids and bonded amino acids); b) CPMG spectrum; c) Diffusion edited spectrum (the broad resonance at ~3.22 ppm is assigned to the trimethylammonium residue of phosphatidylcholine).

As regards the presence of TMA and Suc, no traces were found in the intact cortical samples, indicating that they may have been generated by the extraction process. Clear cell and papillary RCCs are characterized by a metabolic pattern markedly different from those of cortical and medullary tissues not macroscopically affected by tumor invasion (Figure 3 and 4). By inspection of Figure 3b and 4b, relative to the resonances pertaining to the low

molecular weight metabolites, a marked decrease of Bet, *myo*-Ino and *scyllo*-Ino in the malignant lesions can be seen. The general decrease of the relative amounts of the osmolytes is a recurrent finding of all the tumors studied, thus confirming on intact specimens that these osmolytes are the markers of normal kidney function. Furthermore, ChoCC content is higher in clear cell RCC (Figure 3b) with respect to the papilla and the latter is characterized by a high level of Tau (Figure 4b), which participates in osmoregulation, stabilizes the membrane potential in skeletal muscle, affects calcium ion kinetics, has antioxidant and anti-inflammatory properties and acts as a neurotransmitter (19,20). The high amount of ChoCC may be attributed to the "nonphysiological" condition of neoplastic renal cells, considering that changes in osmolyte levels are not uniform when renal function is impaired (19). ChoCC, GPC in particular, behave differently from the other osmolytes, substantially maintaining their relative intensity in the *ex vivo* spectra of intact normal and tumoral renal tissues. It is difficult to account for this phenomenon, which is probably caused by multiple concomitant factors, but we assume that in the renal tissues ChoCC are not only implicated in osmotic balance. Since these compounds are also involved in cell membrane synthesis and breakdown processes and are thus related to cell replication, high levels in clear cell RCCs could be ascribed to tumor cell proliferation, as observed in brain malignancies (22-25). Another important difference between the normal and the neoplastic tissues arises from the analysis of Figure 1c, 3c and 4c. The spectrum in Figure 3c relative to a clear cell RCC shows a strong increment of the lipid component due to TG and confirms the presence, in the intact biopsies, of CholE, which we have previously demonstrated to be present as cholesteryl oleate in the extracts (12,26). These results are relevant in the light of theories that correlate the presence of CholE to cell proliferation in different experimental models and in several types of human neoplasms. Indeed, Batetta *et al.* (27) have hypothesized that "proliferative processes are characterized by a specific pattern of cholesterol metabolism, namely an increase in cholesterol synthesis and an accumulation of cholesterol esters in proliferating cells." The hypothesis that CholE play a leading role in the regulation of tumor growth, particularly within the tumor itself, thus find a possible explanation. Indeed, abnormal CholE storage in clear cell RCCs has already been reported in literature (28) and is paralleled by an increase in AcylCoA-cholesterol acyltransferase (ACAT) activity. Lipid components due to TG and CholE are present in a very low amounts or absent in the spectra of the papillary RCC (Figure 4 c). The spectroscopic comparison between clear cell and papillary RCC tissues shows important metabolic differences. Literature data (11,12,29,30) demonstrated that benign

oncocytomas and malignant chromophobe RCCs are characterized by a typical and different metabolic pattern if compared with clear cell RCC, the latter having a worse prognosis. Indeed, metabolic differences can be related to the different histological RCC types and nuclear Fuhrman grade, which are two of the most important prognosticators for survival (3). Further studies are needed to confirm the hypothesis that the metabolic profile of renal neoplasms are correlated with their prognosis. In conclusion, *ex vivo* HRMAS is a viable and powerful means of probing for molecular information on human normal and neoplastic renal tissues. This technique allows the identification of metabolic indicators of general renal condition in both the physiological and pathological situation, such as depleted osmolyte concentrations and increased lipid components. These observations are consistent with evident changes in renal tissue metabolic profiles. These preliminary results encourage further investigations on a wider range of kidney tumors of different histhological type and grade. Such research will constitute the basis for a biochemical classification of renal neoplastic pathologies which can thus be evaluated by *in vivo* MRS for clinical purposes. Moreover, these data contribute to a better knowledge of the molecular processes fundamental to the onset of renal carcinogenesis.

References

1. Mostofi FK, Coll E. Update on Pathology of renal tumors. New trends in diagnosis and treatment of renal cancer. *Acta Medica: Ed. Congressi,* 1991.
2. Dhote R, Coll E. Risk factors for adult renal cell carcinoma: a systematic reviews and implications for prevention. *BJV Int.* 2000; **86**: 7-20.
3. Gudbjartsson T, Hardarson S, Petursdottir V, Thoroddsen A, Magnusson J, Einarsson GV. Histological subtyping and nuclear grading of renal cell carcinoma and their implications for survival: A retrospective nation-wide study of 629 patients. *Europ Urol* 2005; **48**: 593-600.
4. Fuhrman SA, Lasky LC, Limas C. Prognostic significance of morphologycal parameters in renal cell carcinoma. *Am. J. Surg. Pathol*. 1982; **6**: 655-663.
5. Neild GH, Foxall PJD, Lindon JC, Holmes EC, Nicholson JK. Uroscopy in the 21st century: high-field NMR spectroscopy. *Nephrol. Dial. Transplant.* 1997; **12**: 404-417.
6. Hauet T, Mothes D, Goujon JM, Caritez JM, Carretier M, Eugene M. Evaluation of injury preservation in pig kidney cold storage by proton nuclear magnetic resonance spectroscopy of urine. *J. Urol.* 1997; **157**: 1155-1160.
7. Dixon RM, Frahm J. Localized proton MR spectroscopy of the human kidney *in vivo* by means of short echo time STEAM sequences. *Magn. Reson. Med*. 1994; **31**: 482-487.
8. Moka D, Vorreuther R, Schicha H, Spraul M, Humpfer E, Lipinski M, Foxall PJD, Nicholson JK, Lindon JC. Magic angle spinning proton nuclear magnetic resonance spectroscopic analysis of intact kidney tissue samples. *Anal. Commun.* 1997; **34**: 107-109.
9. Foxall PJD and Nicholson JK: Nuclear magnetic resonance spectroscopy: a non invasive probe of kidney metabolism and function. *Exp. Nephr.*1998; **6**: 409-414.
10. Hauet T, Goujon JM, Tallineau C, Carretier M, Eugene M. Early evaluation of renal reperfusion injury after prolonged cold storage using proton nuclear magnetic resonance spectroscopy. *Br. J. Surg.* 1999; **86**: 1401-1409.
11. Tugnoli V, Reggiani A, Beghelli R, Tomaselli V, Trinchero A, Tosi MR. Magnetic resonance spectroscopy and high performance liquid chromatography of neoplastic human renal tissues. *Anticancer Res.* 2003; **23**: 1541-1548.
12. Tugnoli V, Bottura G, Fini G, Reggiani A, Tinti A, Trinchero A, Tosi MR. ^{1}H-NMR and ^{13}C-NMR lipid profiles of human renal tissues. *Biopolymers* 2003; **72**: 86-95.
13. Eble JN, Togashi K, Pisani P. Renal cell carcinoma. In: *Pathology and Genetics of Tumors of the Urinary System and Male Genital Organs. World Health Organization Classification of Tumors*. Eble JN, Sauter G, Epstein JI, Sesterhenn IA (eds.). IARC Press. 2004; 12-43.
14. Wittekind C, Compton CC, Sobin LH. TNM residual tumor classification revisited. *Cancer* 2002; **94**: 2511-2516.

15. Cowin GJ, Leditschke, Crozier S, Brereton IM, Endre ZH. Regional proton nuclear magnetic resonance spectroscopy differentiates cortex and medulla in the isolated perfused rat kidney. *MAGMA* 1997; **5**: 151-158.
16. Moka D, Vorreuther R, Schicha H, Spraul M, Humpfer E, Lipinski M, Foxall PJD, Nicholson JK, Lindon JC. Biochemical classification of kidney carcinoma biopsy samples using magic-angle-spinning 1H nuclear magnetic resonance spectroscopy. *J Pharm. Biomed. Anal*. 1998; **17**: 125-132.
17. Tate AR, Foxall PJD, Holmes E, Moka D, Spraul M, Nicholson JD, Lindon JC. Distinction between normal and renal cell carcinoma kidney cortical biopsy samples using pattern recognition of 1H magic angle spinning (MAS) NMR spectra. *NMR Biomed*. 2000; **13**: 64-71.
18. Garrod S, Humpfer E, Spraul M, Connor SC, Polley S, Connelly J, Lindon JC, Nicholson JK, Holmes E. Highresolution magic angle spinning 1H NMR spectroscopic studies on intact rat renal cortex and medulla. *Magn. Reson. Med*. 1999; **41**: 1108-1118.
19. Burg M. Molecular basis of osmotic regulation. *Am. J. Physiol*. 1995; **268**: F983-F996.
20. Beck F-X, Burger-Kentischer A, Muller E. Cellular response to osmotic stress in the renal medulla. *Pflugers Arch-Eur. J. Pysiol.* 1998; **436**: 814-827.
21. Schmolke M, Schilling A, Keiditsch E, Guder WG. Intrarenal distribution of organic osmolytes in human kidney. *Eur. J. Clin. Chem. Clin. Biochem*. 1996; **34**: 499-501.
22. Nuclear Magnetic Resonance Spectroscopy in the Study of Neoplastic Tissue. Tosi R, Tugnoli V (eds.). New York, Nova Science Publishers, Inc., 2005; 1-444.
23. Kwock L, Smith JK, Castillo M, Ewend MG, Collichio F, Morris DE Bouldin TW, Cush S. Clinical role of proton magnetic resonance spectroscopy in oncology: brain, breast, and prostate cancer. *Lancet Oncol*. 2006; **7**: 859-868.
24. Martinez-Brisbal MC Marti-Bonmati L, Pique J, Revert A, Ferrer P, Llacer Jl, Piotto M Assemat O, Celda B. 1H and 13C HR-MAS spectroscopy of intact biopsy samples *ex vivo* and *in vivo* 1H MRS study of human high grade gliomas. *NMR Biomed.* 2004; **17**: 191-205.
25. Barbarella G, Ricci R, Pirini G, Tugnoli V, Tosi MR, Bertoluzza A, Calbucci F, Leonardi M, Trevisan C, Eusebi E. *In vivo* single voxel 1H MRS of glial brain tumors: correlation with tissue histology and *in vitro* MRS. *Int. J. Oncol.* 1998; **12**: 461-468,.
26. Tosi MR, Tugnoli V. Cholesteryl esters in malignancy. *Clin. Chim. Acta.* 2005; **359**: 27-45.
27. Batetta B, Pani A, Putzolu M, Sanna F, Bonatesta R, Piras S, Spano O, Mulas MF, Dessí S. Correlation between cholesterol esterification, *MDR1* gene expression and rate of cell proliferation in CEM and MOLT4 cell lines. *Cell. Prolif.* 1999; **32**: 49-61.
28. Gebhard RL, Clayman RV, Prigge WF, Figenshau R, Staley NA, Reesey C, Bear A. Abnormal cholesterol metabolism in renal clear cell carcinoma. *J. Lip. Res.* 1987; **28**: 1177-1184.

29. Tosi MR, Reggiani A, Tugnoli V. Are molecular features of a chromophobic cell renal cell carcinoma correlated with clinical findings? *Int. J. Mol. Med.* 2003; **12**: 99-102.

30. Tosi MR, Rodriguez-Estrada MT, Lercker G, Poerio A, Trinchero A, Reggiani A, Tugnoli V. Magnetic resonance spectroscopy and chromatographic methods identify altered lipid composition in human renal neoplasms. *Int. J. Mol. Med.* 2004; **14**: 93-100.

CONCLUDING REMARKS

CONCLUDING REMARKS

This thesis shows that HR-MAS NMR spectroscopy is well suited for clinical applications to cancer diagnosis and grading. I concentrated on the use of the technique in different types of tumour, in order to characterize the metabolic pathways of the tissues, to identify possible metabolic markers using statistical analysis and to explore the potentiality of a combined HR-MAS and genetic analysis.

HR-MAS NMR is an ideal method for the study of intact tissue samples. Sample preparation is easy and quick to perform and this makes me envisage the possible application of this technique as an alternative method or complementary to histopathology for immediate cancer diagnosis. It is possible to plan larger evaluation studies, in which split samples are taken for HR-MAS NMR and histopathological analysis. This would further test the reliability of the method which could then result in a rapid diagnostic mean to perform and which could help to guide surgical procedures. Statistical pattern recognition techniques would help to simplify the interpretation and, given the development of robotic sample preparation and data collection methods, the clinical application of high resolution MAS NMR spectroscopy in tumour diagnosis would become a new possibility.

Single 1D experiments can be performed in ~ 5-10 minutes, and a set of three experiments covering the different metabolic profile in cancer tissues takes currently about 30 minutes. Techniques like water presaturation (for detecting low- and high-molecular weight metabolites), CPMG (detecting mainly water-soluble, low-molecular weight metabolites) and diffusion-edited spectroscopy (mainly lipids and high-molecular weight metabolites such as oligopeptides) have been found to be most suitable for this work. This pool of experiments is further completed by the use of 2D NMR techniques for the identification of hidden resonances, helping the analysis of complex spectral pattern due to signal overlapping.

The *ex vivo* HR-MAS NMR analysis permits to relate the biochemical composition with quantitative histopathologic findings from the same tissues and to determine the metabolic profiles associated with functional, benign and malignant tissues. Furthermore, correlation between some metabolites and proliferative markers allows to gain insight into the relationship between cellular proliferation and the metabolic changes associated with the presence and aggressiveness of a neoplasia.

The selection of a certain tissue or area for HR-MAS NMR spectroscopic analysis is an essential step, as well as the selection of the size and location of the voxel(s) for *in vivo*

MRS. Generally the voxel or sample should contain at least 50% or more of the tissue under investigation. If there is not enough tumour for example in the volume, this could results in some degree of misinterpretation. With this method, the HR-MAS spectra obtained are comparable to *in vivo* MRS results, showing higher resolution and a signal-to-noise ratio similar to NMR spectra of tissue extracts.

It is also possible to take several samples either for statistical validation or for the study of tissue/tumour heterogeneity. *Ex vivo* ^{1}H HR-MAS of tissue sample improves the analysis of micro-heterogeneity in grade tumours, and can provide insights into the relationships between clinically relevant cell processes and specific metabolites, such as choline-containing compounds involved in phospholipid metabolism, or lipids involved in apoptosis leading to necrosis.

Currently, a major focus in cancer research is to identify genes, using DNA-microarrays, that are aberrantly expressed in tumour cells, and to use their abnormal expression as biomarkers. These approach facilitates precise diagnosis and/or therapy outcomes of malignant transformation. Furthermore, comprehensive understanding of gene expression changes in specific tumour types should also greatly support tumour analysis and the development of new treatment regimens. Notably, the HR-MAS and genomic data strongly correlate, further demonstrating the biological relevance of HR-MAS for tumour typing. The levels of specific metabolites, such as choline containing metabolites, that are altered in gliomas tissue. These changes correspond to the differential expression of Kennedy cycle genes. Kennedy cycle genes responsible for the biosynthesis of choline phospholipids (such as phosphatidylcholine) and appear to be altered by malignant transformation. These data demonstrate the validity of our combined approach to produce and utilize MRS/genomic biomarker profiles to type brain tumour tissue.

Ex vivo HR-MAS of human tissue samples offers a potential new goal for the characterization of human cancer. This new technique allows the pathological diagnosis and the detection of tumoural biomarker and seems to be promising in developing the management of cancer disease.

Ackowledgments/Ringraziamenti

Eccomi arrivata alla parte più difficile! In poche righe è veramente difficile ringraziare tutte le persone che hanno contribuito in modo diverso alla riuscita di questo lavoro.

Desidero ringraziare la Professoressa Luisa Schenetti, alla quale vorrei esprimere tutta la mia ammirazione, la stima e la gratitudine per essere stata la mia guida e per tutto il lavoro realizzato. Grazie per gli insegnamenti, l'appoggio, la pazienza, l'amicizia e la totale fiducia che ha posto in me in questo lungo tempo di convivenza.
Al Dottor Vitaliano Tugnoli un sincero grazie per avermi dato la possibilità di svolgere questa tesi e per la sua disponibilità a lasciarmi libera di esprimere e di mettere in gioco la mia capacità di ricerca!
Per la Professoressa Adele Mucci, sicuramente grazie per gli insegnamenti di risonanza, i saggi consigli, la pazienza, il tempo trascorso con me, le chiacchiere e tante cose condivise in questi tre anni.
Un grande e sincero grazie dal profondo del cuore va alle mie colleghe (vorrei far presente solo donne) e ai fantastici amici del terzo piano di Chimica Organica. Questi tre anni sono stati davvero intensi scientificamente ma anche umanamente. Quanti momenti passati insieme, sarà sempre un grande piacere ricordarli. Non farò ringraziamenti personificati (li farò direttamente), ma in queste poche righe alcuni nomi che rimarranno sempre nel mio cuore li voglio lasciare. Sandra, Stefania Francesca, Ferdinando, Lisa, Nicola, Rita, Claudia!! Insieme a loro aggiungo anche, Daniele, Francesca P, Gaele, Rosaria, Valerio. Un particolare ringraziamento a Caterina per l'amicizia e per il lavoro svolto insieme!
Grazie a tutto gruppo del CIGS!! La mia seconda dimora dopo l'ufficio della Schene. Un particolare ringraziamento a Cecilia e Cinzia!

Mi agradacimiento son también para algunas personas de Madrid.
Para el Doctor Sebastiàn Cerdàn, mi reconocimiento para haberme recibidos, para un periodo bastante largo qué me ha permitido de crecer científicamente y conocer muchas personas qué me han ayudado a entender el sentido de qué quiere decir ser científico si no también qué es amistad.
La Doctora Maria Luisa Garcìa-Martìn (alias Marisa). A ella mi admiracion, estima, gratitud para la colaboración y el trabajo realiazo. Gracias para su apoyo y sobretodo para su amistad

grande y encondicionada, has sido muy importante para mi. “he llegado y he empezado a buscar mi leyenda personal” ahora después de dos años creo de haber encontrado el camino!
À Professora Doutora Margarida Castro a minha gratidão, pela grande amizade, pelos seus conselhos. Muito obrigada por tudo! “Mi compañera de Colegio” no olvidaré esos momentos!!
Y como no agradecer mi companeros de laboratorio de Madrid!!! A todos Muchas Gracias para el apoyo, amistad, cofiancia y estima qué me habéis concedido, siempre todas las veces qué estuve allí con vosotros fue como estar en mi casa: Patricia, Pilar, Rui, Tiago, Laura, Ines, Rosa, Teresa N., David!! Un gracias my especial desde mi corazón para Teresa D. y Jesus.
Deseo agradecer también dos amigas: Elena y Mgiò, os amistad y cariño me ayudó mucho…!!!

Ringazio tutti gli amici della montagna, gli ex compagni di liceo: Claudia, Dani, Jessy, Rudy, Manuel, Richy, Monte, Marco e il grande Stefano (a te grazie perché in ogni momento, felice e non, ci sei sempre stato!!!!). E grazie a tutti quelli che in questi tre anni hanno incrociato il mio cammino che sono tantissimi, e che ognuno a modo suo ha lasciato qualcosa!!

Un grazie speciale a Paolo!

Grazie, infinitamente grazie ai miei genitori, in ogni momento siete stati presenti dandomi la forza e spronandomi sempre a dare il meglio. Un ringraziamento speciale al mio insostituibile fratello Fabio per essere riuscito a sopportarmi anche nei miei momenti peggiori!
Per voi non solo un grazie ma anche tutto il mio amore e la mia eterna riconoscenza! A voi dedico tutto questo lavoro!